AD-A231 804

DTIC FILE COPY

ANALYSIS OF HIGH FREQUENCY SEISMIC DATA

by

Hans Israelsson
Anne Suteau-Henson
Alan Ryall

Science Applications International Corporation
Center for Seismic Studies
1300 N. 17th Street, Suite 1450
Arlington, VA 22209

1 October 1990

Scientific Report No. 1

Approved for Public Release;
Distribution Unlimited

DTIC
ELECTE
FEB 0 6 1991
S
B
D
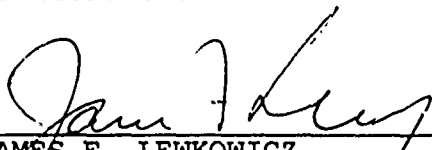
91 2 04 080
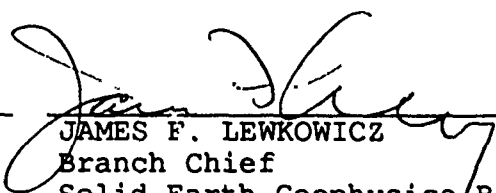
The views and conclusions contained in this document are those of
the authors and should not be interpreted as representing the
official policies, either expressed or implied, of the Defense
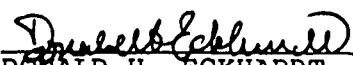Advanced Research Projects Agency or the U.S. Government.

This technical report has been reviewed and is approved for
publication.

JAMES F. LEWKOWICZ   JAMES F. LEWKOWICZ
Contract Manager   Branch Chief
Solid Earth Geophysics Branch   Solid Earth Geophysics Branch
Earth Sciences Division   Earth Sciences Division

FOR THE COMMANDER

DONALD H. ECKHARDT, Director
Earth Sciences Division

. REPORT DOCUMENTATION PAGE

Form Approved
OMB No 0704-0188
Exp Date: Jun 30, 1986

1a REPORT SECURITY CLASSIFICATION	1b RESTRICTIVE MARKINGS
UNCLASSIFIED	

2a SECURITY CLASSIFICATION AUTHORITY	3 DISTRIBUTION/AVAILABILITY OF REPORT
	Approved for public release;
2b DECLASSIFICATION/DOWNGRADING SCHEDULE	Distribution Unli'ted

4 PERFORMING ORGANIZATION REPORT NUMBER(S)	5. MONITORING ORGANIZATION REPORT NUMBER(S)
SAIC CSS Technical Report C89-01	GL-TR-90-0299

6a NAME OF PERFORMING ORGANIZATION	6b OFFICE SYMBOL (If applicable)	7a NAME OF MONITORING ORGANIZATION
Science Applications International Corporation		Geophysics Laboratory

6c. ADDRESS (City, State, and ZIP Code)	7b. ADDRESS (City, State, and ZIP Code)
Center for Seismic Studies, 1300 N. 17th Street, Suite 1450 Arlington, VA 22209	Hanscom AFB, MA 01731-5000

8a. NAME OF FUNDING/SPONSORING ORGANIZATION Defense Advanced Research Projects Agency	8b OFFICE SYMBOL (If applicable)	9. PROCUREMENT INSTRUMENT IDENTIFICATION NUMBER
		F19628-88-C-0159

8c. ADDRESS (City, State, and ZIP Code)	10 SOURCE OF FUNDING NUMBERS			
1400 Wilson Boulevard Arlington, VA 22209	PROGRAM ELEMENT NO	PROJECT NO.	TASK NO.	WORK UNIT ACCESSION NO
	62714E	8A10	DA	h

11. TITLE (Include Security Classification)

Analysis of High Frequency Seismic Data

12. PERSONAL AUTHOR(S)

H. Israelsson, A. Suteau-Henson, A. Ryall

13a TYPE OF REPORT	13b TIME COVERED	14 DATE OF REPORT (Year, Month, Day)	15 PAGE COUNT
Scientific #1	FROM 10/1/88 TO 10/1/89	1990 October 1	162

16. SUPPLEMENTARY NOTATION

17. COSATI CODES			18. SUBJECT TERMS (Continue on reverse if necessary and identify by block number)
FIELD	GROUP	SUB-GROUP	High Frequency Spectral Scaling
			Regional Waveforms NORESS
			Ripple-Fired Quarry Blasts NRDC

19 ABSTRACT (Continue on reverse if necessary and identify by block number)

See attached sheet.

20 DISTRIBUTION/AVAILABILITY OF ABSTRACT	21 ABSTRACT SECURITY CLASSIFICATION
☒ UNCLASSIFIED/UNLIMITED ☐ SAME AS RPT. ☐ DTIC USERS	Unclassified

22a NAME OF RESPONSIBLE INDIVIDUAL	22b TELEPHONE (Include Area Code)	22c OFFICE SYMBOL
James Lewkowicz	(617)377-3028	GL/LWH

DD FORM 1473, 84 MAR

83 APR edition may be used until exhausted
All other editions are obsolete

SECURITY CLASSIFICATION OF THIS PAGE

UNCLASSIFIED

19. Abstract

This report covers work completed by the Center for Seismic Studies research staff on high frequency seismology between 1 October 1988 and 1 October 1989. The focus of the research is on the detection, location, and identification of seismic events using high frequency seismic data. Data for these studies come primarily from the NORESS small aperture array in Norway and its high frequency (up to 125 Hz) central element, and the high-frequency stations installed by the Natural Resources Defense Council (NRDC) close to the Eastern Kazakhstan test sites in the Soviet Union.

The first section is an examination of the NORESS data to be used in this project. Mining is found to be a major source of seismic signal in Fennoscandia with large concentrations of activity on the Kola Peninsula, Southern Norway, and Central Sweden. There is evidence that the shooting practices (tonnage, charge distribution in time and space, etc.) at the Kola Peninsula mines are different than those at the Scandinavian mines. Detection thresholds and location errors for events at regional distances to NORESS based on two and one-half years of data are also given.

Spectral characteristics of the high frequency noise recorded at both NORESS and the KKL station of the NRDC network are discussed in section two. The decay of the power spectra with frequency do not follow a simple power law and spectral peaks, possibly generated by non-linear mechanical and electrical processes of the instruments and their recording systems, impose limits on the detection of weak signals.

In section three, a method is developed for estimating the rolloff and scaling parameter for corner frequency-seismic moment from spectral ratios of a suite of events from the same location and with the same source function.

Section four contains studies of the characterization of earthquakes and mine blasts. Inter-event correlation of mine blasts is shown to constrain the relative locations of events to very small distances (100m at 15 Hz). The effect of scatter in the delays of ripple fired quarry blasts are examined theoretically and illustrate that a 20% scatter can significantly attenuate the secondary harmonics of the spectrum and reduce the signal-to-noise ratio of the primary peak. A characterization of regional events recorded at NORESS and the NRDC stations using spectrograms shows that, while some mines exhibit classic spectral scalloping due to ripple firing, many do not. Low signal-to-noise ratios and small bandwidth due to high-frequency attenuation at regional distances (beyond 1000 km) limit the effectiveness of this method.

The final section is a short note on the instrument responses of the NRDC stations and the Special Data Collection System used to monitor the Nevada test site. Because the response of the two systems are similar in the teleseismic frequency band (1 to 3 Hz), magnitudes obtained from the two different systems can be compared in a gross sense.

TABLE OF CONTENTS

Accession For		
NTIS GRA&I	☑	
DTIC TAB	☐	
Unannounced	☐	
Justification		
By		
Distribution/		
Availability Codes		
Dist	Avail and/or Special	
A-1		

LIST OF FIGURES

FOREWORD

This report covers work completed by the Center for Seismic Studies research staff on high frequency seismology between 1 October 1988 and 1 October 1989. During this period, Dr. Alan Ryall was the Director of Research at the Center for Seismic Studies and it was under his direction that this work was performed. The focus of the research is on the detection, location, and identification of seismic events using high frequency seismic data. Data for these studies comes primarily from the NORESS small aperture array in Norway and its' high frequency (up to 125 Hz) central element, and the high-frequency stations installed by the Natural Resources Defense Council (NRDC) close to the Eastern Kazakhstan test sites in the Soviet Union. A brief description of the contents of the report are given below

The first section is an examination of the NORESS data to be used in this project. Mining is found to be a major source of seismic signal in Fennoscandia with large concentrations of activity on the Kola Peninsula, Southern Norway, and Central Sweden. There is evidence that the shooting practices (tonnage, charge distribution in time and space, etc.) at the Kola Peninsula mines are different than those at the Scandinavian mines. Detection thresholds and location errors for events at regional distances to NORESS based on two and one-half years of data are also given.

Spectral characteristics of the high frequency noise recorded at both NORESS and the KKL station of the NRDC network are discussed in section two. The most important observations of this work are that the decay of the power spectra with frequency do not follow a simple power law and that spectral peaks, possibly generated by non-linear mechanical and electrical processes of the instruments and their recording systems, impose limits on the detection of weak signals.

In section three, Israelsson develops a method for estimating the rolloff and scaling parameter for corner frequency-seismic moment from spectral ratios of a suite of events from the same location and with the same source function.

Section four, the largest section of this report, contains studies of the characterization of earthquakes and mine blasts. Israelsson correlated pairs of waveforms from a set of 137 events, to determine the similarities and differences between events as a function of distance. One of the results of this study is that high correlation at high frequencies can constrain the relative locations of events to very small distances (100m at 15 Hz). In another study, the effect of scatter in the delays of ripple fired quarry blasts were examined. This theoretical exercise illustrates that a 20% scatter can significantly attenuate the secondary harmonics of the spectrum and reduce the signal-to-noise ratio of the primary peak. The final report in section four is a characterization of regional events recorded at NORESS and the NRDC stations by Suteau-Henson. Spectrograms were used to characterize regional events recorded at NORESS and the NRDC stations. While some mines exhibited classic spectral scalloping due to ripple firing, many did not. Low signal-to-noise

viii

ratios and small band. idth due to high-frequency attenuation at regional distances (beyond 1000 km) limit the effectiveness of this method.

The final section is a short note on the instrument responses of the NRDC stations and the Special Data Collection System used to monitor the Nevada test site. Because the response of the two systems are similar in the teleseismic frequency band (1 to 3 Hz), magnitudes obtained from the two different systems can be compared in a gross sense.

Jerry Carter

1.1 REGIONAL EVENTS DETECTED AND LOCATED BY THE NORESS ARRAY

ABSTRACT

In this note we analyze regional seismic events reported in the NORESS seismic bulletin for a period of two and a half years. On the average, 9 events are detected and located each day on working days with few events reported on weekends. About 7 of the working day events occur at distances less than 400 km and about half of the 9 events are from two limited areas in Central Sweden and Southern Norway. Usually, 2 of the 9 events are in fact from the mining districts in Central Sweden, which occupy an area of only about 20 by 60 km. Magnitudes for events in a given region are approximately normally distributed with standard deviations between 0.2-0.35. Differences of more than one magnitude unit between the median magnitudes for events in the Baltic region and the Kola Peninsula on the one hand ($ML=2.7$) and Norway and Sweden on the other ($ML=1.1-1.5$) suggest major differences in the use of explosion tonnages in the mining industry and related fields. The temporal pattern of events detected on the Kola Peninsula differs from that of events in other regions. Most events are reported on weekends with a peak early Sunday morning. The fact that few events are detected during working days on the Kola Peninsula may partly be due to the pronounced temporal variation of the seismic noise at NORESS. Annual event activities of about 15 and 75 chemical explosions per million km^2 with $ML \geq 3.0$ and $ML \geq 2.0$ respectiv.ly are obtained for the operative area of NORESS.

1.1.1 Introduction

Seismic recordings at local and regional distances have been in the focus of seismic verification research for over a decade. The emphasis on regional recordings is due to the prospects for in-country seismic monitoring stations. Discussions on the number of seismic events that need to be identified by in-country station networks have been based on readily available occurrence rates for earthquakes (Hannon, 1983). However, a large number of mining and industrial chemical explosions are also recorded at local and regional distances, and masking of nuclear tests with large chemical explosions has indeed been considered as a possible evasion scenario. There are few systematic compilations of the occurrence of chemical explosions with regard to frequency, geographical location, and magnitude. The number of local and regional events that will be recorded at a station is of course entirely dependent on the routine use of chemical explosions by local mining and construction industries, and characteristics of such events vary with time and geographical region.

Mining and industrial chemical explosions are also of interest to the global seismic monitoring system developed by the GSE (CD/43, 1979). Although this system emphasizes detection at teleseismic distances, local and regional data are supposed to be exchanged as well. Concern has been expressed about the amount of data that has to be handled if all detected local and regional seismic events have to be reported by a seismic station. Some form of abbreviated reporting has therefore been considered for earthquake swarms and sequences. However, the reporting and handling of data for chemical explosions at local and regional distances also need to be addressed.

In this note we compile some statistics for the local and regional events reported in the NORESS seismic event bulletin. As emphasized above, the characteristics of local and regional events may vary strongly with geographical region as well as with time. Even if general conclusions can not be drawn from the analysis of events occurring in one region during a short period of time, it is felt that the "NORESS case" is a valuable illustration of the kind of statistics one may have for chemical explosions recorded at local and regional distances. Not only does the NORESS array have a high detection capability, but the NORESS seismic event bulletin is also compiled in a systematic and consistent manner.

1.1.2 The NORESS Seismic Event Bulletin

The NORESS bulletin is based on real time processing; automatically determined event solutions are reviewed and graded by an analyst from standard plots of associated record sections and f-k diagrams (Mykkeltveit, 1985). The bulletin has been reported since late 1985. The data used in this study covers the period from

Jan. 1, 1986 to June 30, 1988 and is limited to seismic events that were graded A (acceptable) in the analyst's review. A total of 5946 such events were reported for this period, which corresponds to a daily average of 6.5 events.

Geographical Distribution:

The map in *Figure 1* shows the geographical distribution of the events. The circular area within 500 km of NORESS is well covered with event epicenters from 80 ° to 330 ° north. At distances greater than 500 km most events occur to the east of NORESS. At distances greater than 1000 km there are virtually no events to the west of NORESS. Note that there are events distributed along fairly long profiles (out to 1500 km) to the east and northeast of NORESS. There is also rather complete azimuthal coverage at radii of around 200, 500, and 1000 km.

The perspective representation in *Figure 2* of the number of events as a function of location relative to NORESS is dominated by two major event clusters within about 200 km; one in central Sweden, east of the array, and one in Southern Norway, south of the array. These clusters stand out as sharp peaks in the figure. Even though there is a fairly high concentration of events in western Norway, the distribution is more spread out. In relation to these areas, the considerable activity in the Baltic area on the Kola Peninsula can barely be seen on a similar figure showing the entire region of this study.

The strong concentration of events at close distances is also illustrated by *Figure 3*, which shows the cumulative distribution of the epicentral distance for all the events. About 60 % of the events are at distances less than 200 km and 80 % of the events are within about 400 km.

Magnitude Distribution

The histogram in *Figure 4* shows the frequency distribution of the event magnitudes, ML. Most of the events are in the range $ML=1-2$ with a sharp peak at $ML=1.1$. There is also a small secondary broader peak around $ML=2.6$. The cumulative distribution function of the magnitudes of all events in *Figure 4* shows that about 80% of the events have a magnitude of $ML \leq 2.0$. The pronounced concentration of small magnitude events at short epicentral distances and of large magnitude events at large epicentral distances is illustrated by the cumulative distribution functions of the epicental distance for events with magnitude less than and greater than $ML=2.0$ in *Figure 5*. The two functions show that only 15% of the events with $ML>2.0$ occur at distances less than 400 km, and over 95% of the events with $ML<2.0$ occur at distances less than 400 km.
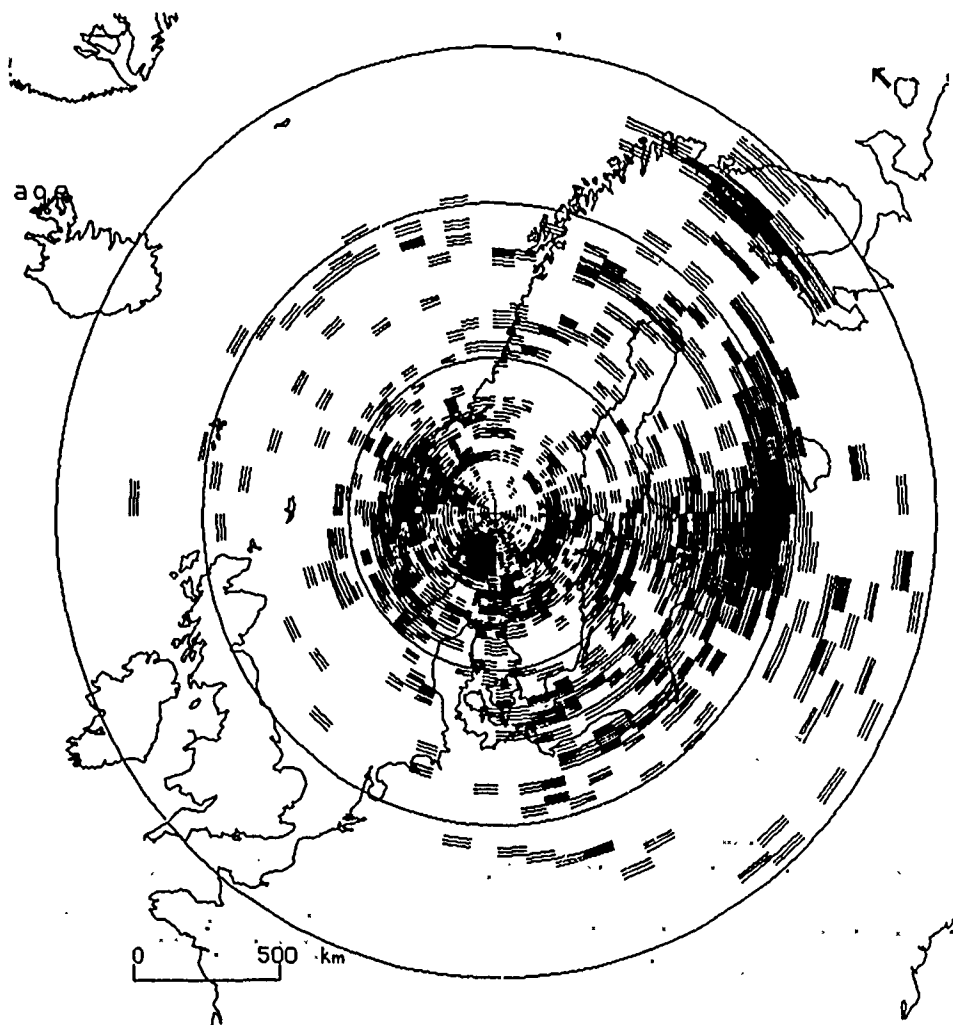
Figure 1. Seismic events (grade A) in the NORESS bulletin from Jan. 1, 1986 - June 30, 1988. The NORESS array is the projection point of the map and the events have been grouped into sector cells with 25 km radial extension and azimuthal coverage of 5 degrees. The relative number of events in each cell is indicated by the degree of shading.
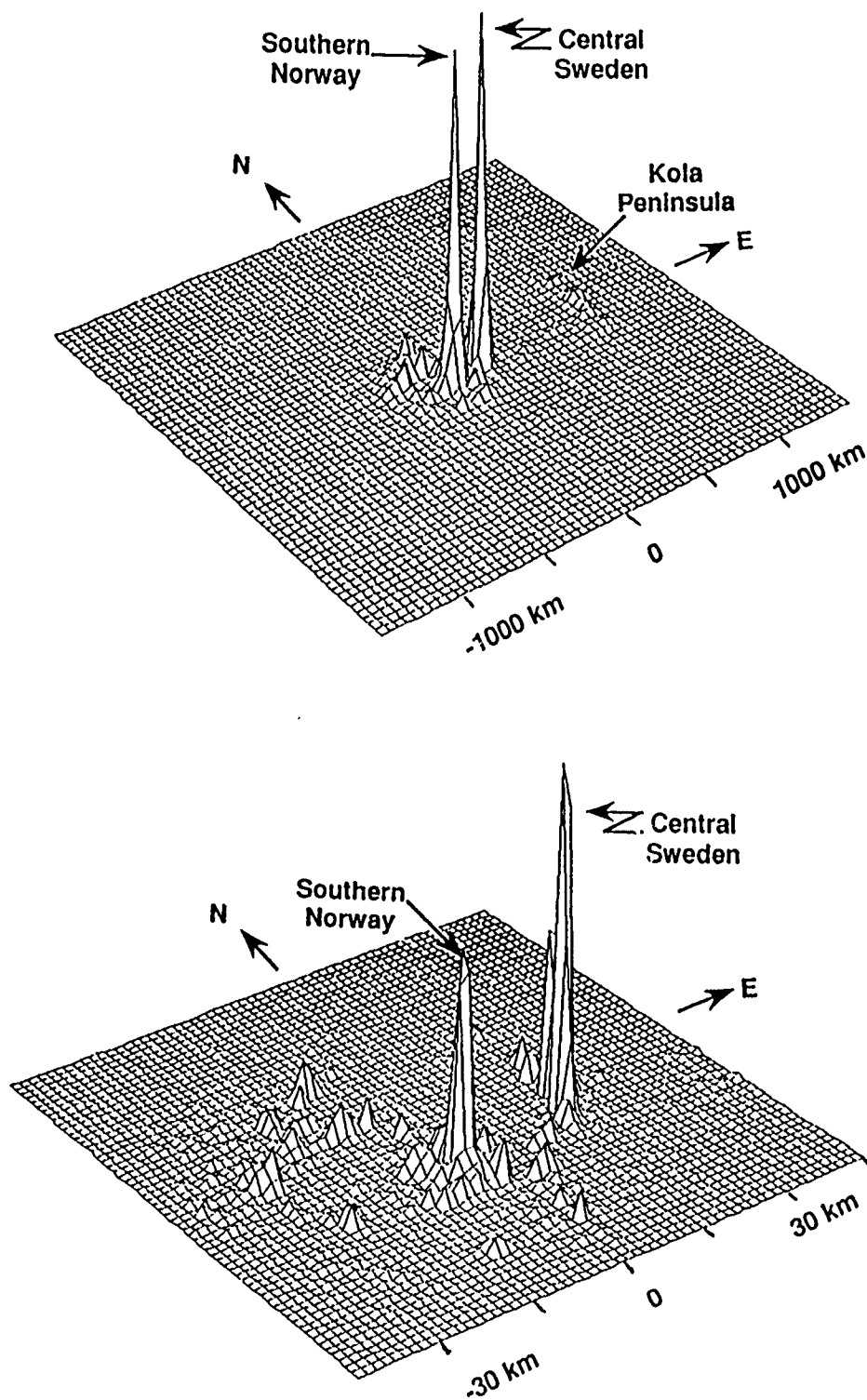
Figure 2. The upper perspective diagram shows the number of events (in all 5946) as a function of geographical location out to 1500 km from the NORESS array, which is located at the center of the co-ordinate plane. The two spikes in the top diagram correspond to events in Southern Norway and Central Sweden. In the lower diagram events out to 450 km from NORESS are shown in a similar way (in all 4899 events).
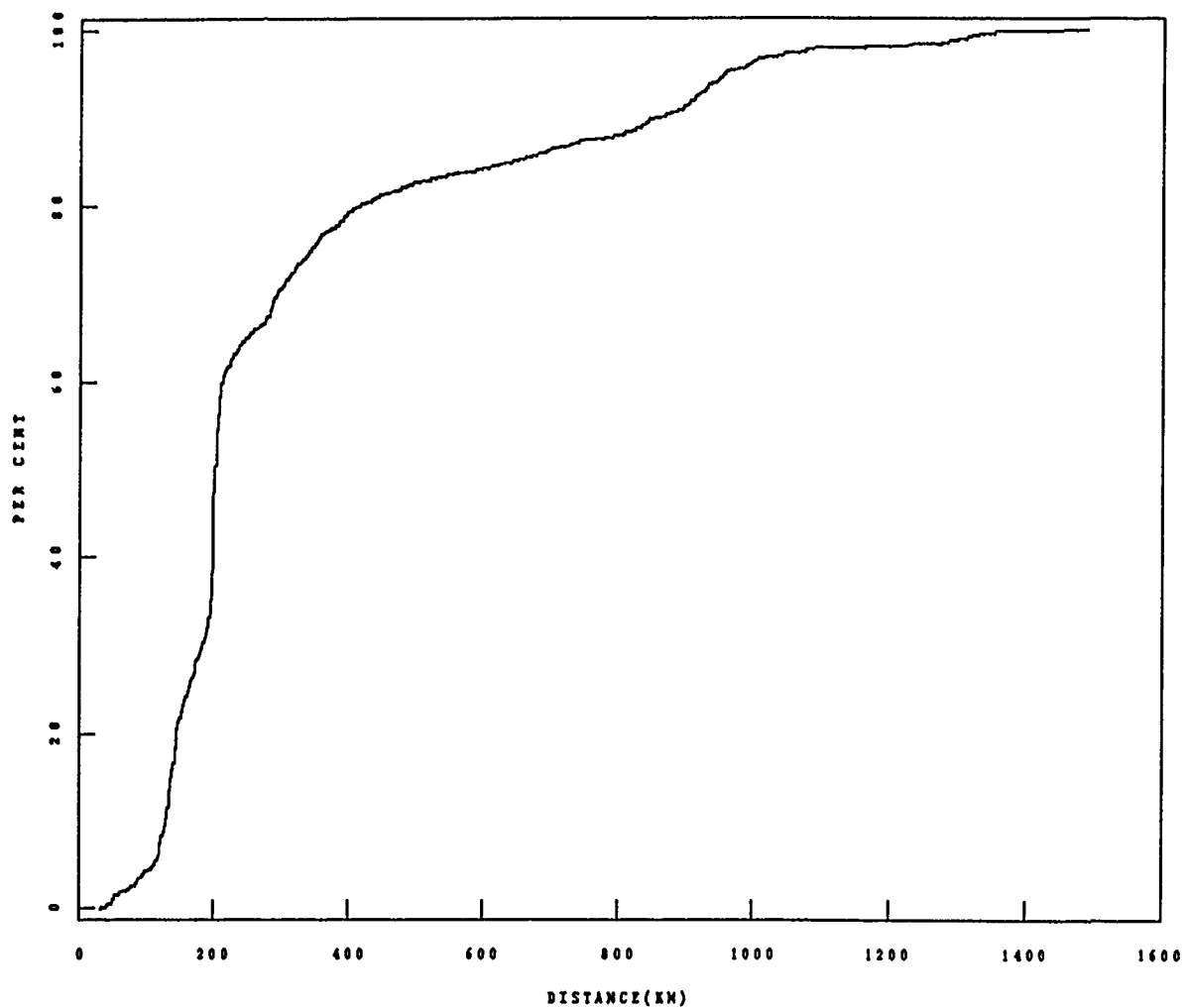
Figure 3. Cumulative distribution of epicentral distance for all events reported by NORESS (in all 5946). The curve shows that about 60% of the events are at distances less than 200 km and 80% are at distances less than 400 km.

1-6
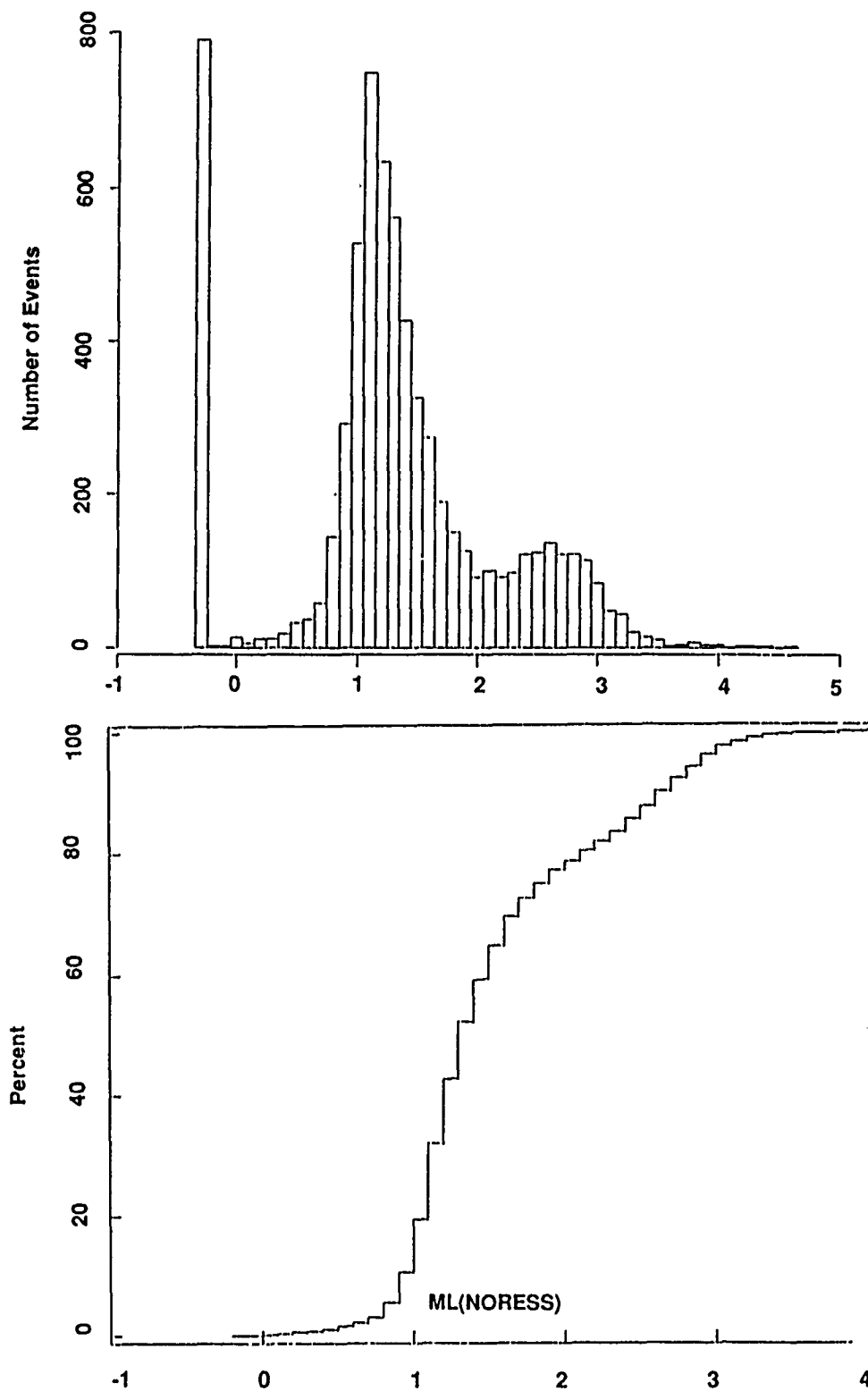
Figure 4. A histogram representation of the frequency distribution of the magnitudes, *ML*, for all events reported by NORESS (above). Empirical cumulative distribution function of event magnitudes, *ML*, for all events reported by NORESS (below). The curve shows that about 80% of the events have a magnitude less than *ML*=2.0, and 15% have a magnitude *ML*≥2.5.
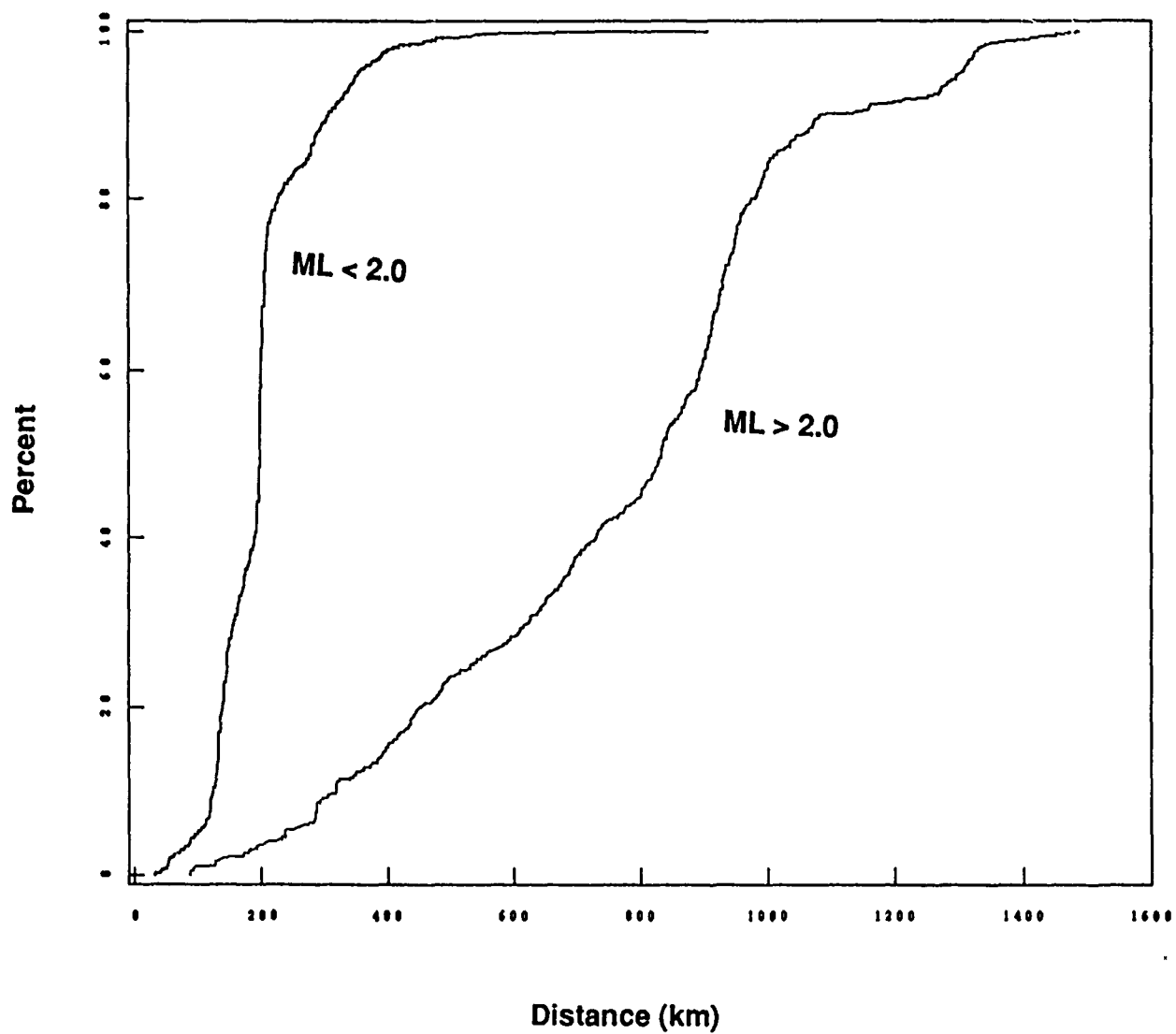
Figure 5. The two curves represent the empirical cumulative distribution functions of the epicentral distance for events with *ML* <2.0 and with *ML*≥2.0 respectively.

Time Variation

Ringdal, (1986) pointed out that there is a large increase in the number of detections during daytime hours due to mining explosions, road work and other cultural sources. In *Figure 6* we see this effect by plotting the number of events as a function of time during the week. Not surprisingly there is a strong cyclic variation, not only with time of day but also with day of week, with few events detected during the weekends.

Regions with main activity

The regions containing most of the seismic activity, based on the perspective representation of the number of events as a function of location in *Figure 2*, are defined by the five areas in *Figure 7*. Data on area and number of events in each region are listed in *Table 1*. The data in the table show that about 50% of all events detected by NORESS are located in Central Sweden or Southern Norway, in an area that is less than 1% of the operative region of the array (circle with 1500 km radius). Taken together, the events in the five regions make up almost 75% of the events that are detected and located by NORESS. The events in Central Sweden are concentrated in a small group of mining districts with over 1000 events or almost 20% of all NORESS events within a rectangular area of 20 by 60 km.

TABLE 1.						
MAIN EVENT REGIONS						
Region	Center Co-ordinates		Area $*10**4$	No. of Events	ML	
-	Lat(N)	Long(E)	(km**2)	-	Median	Std
-					-	-
Central Sweden	60.1	14.8	2.1	1506	1.1	0.20
Southern Norway	59.7	10.5	2.8	1488	1.2	0.31
Western Norway	61.2	6.6	8.3	684	1.5	0.35
Baltic Region	60.5	26.0	49.2	594	2.7	0.33
Kola Peninsula	68.5	32.3	19.0	77	2.7	0.23

The event magnitudes for each region vary within rather limited ranges as summarized in *Table 1*. The magnitudes for each region are approximately normally distributed (*Figure 8*). As pointed out earlier, the vast majority of the events in the NORESS bulletins are chemical explosions for mining and other industrial purposes. The difference of more than one magnitude unit between median values for the Baltic and Kola regions on the one hand ($ML=2.7$) and for the regions in Norway and Sweden on the other ($ML=1.1-1.5$), suggests rather different practices in carrying out explosions with regard to tonnage and/or distribution of charges.
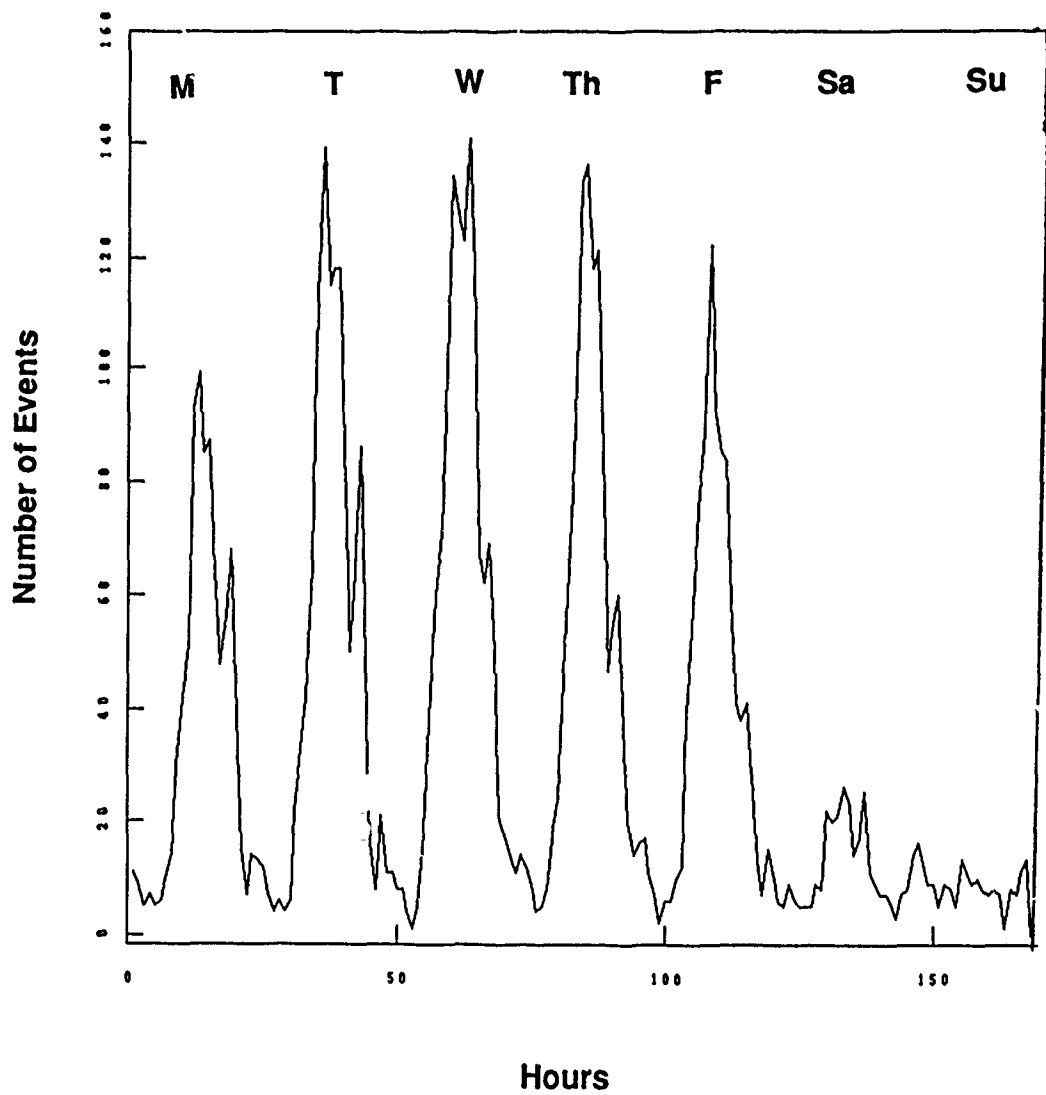
Figure 6. Number of events as a function of hour during the week for all events. The curve shows a clear variation with working hours with peaks during the day and low activity on the weekends.
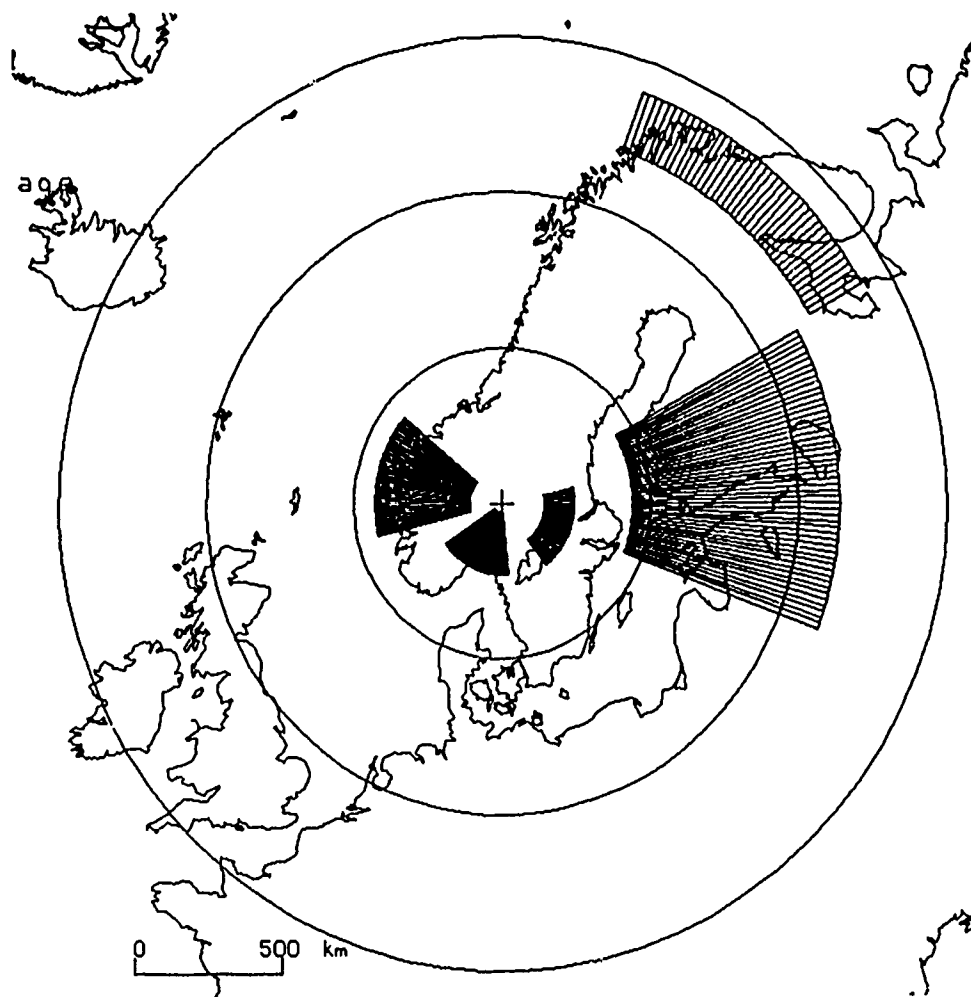
Figure 7. The shaded areas define the event regions discussed in the text: Central Sweden, Southern Norway, Western Norway, the Baltic region, and the Kola Peninsula.
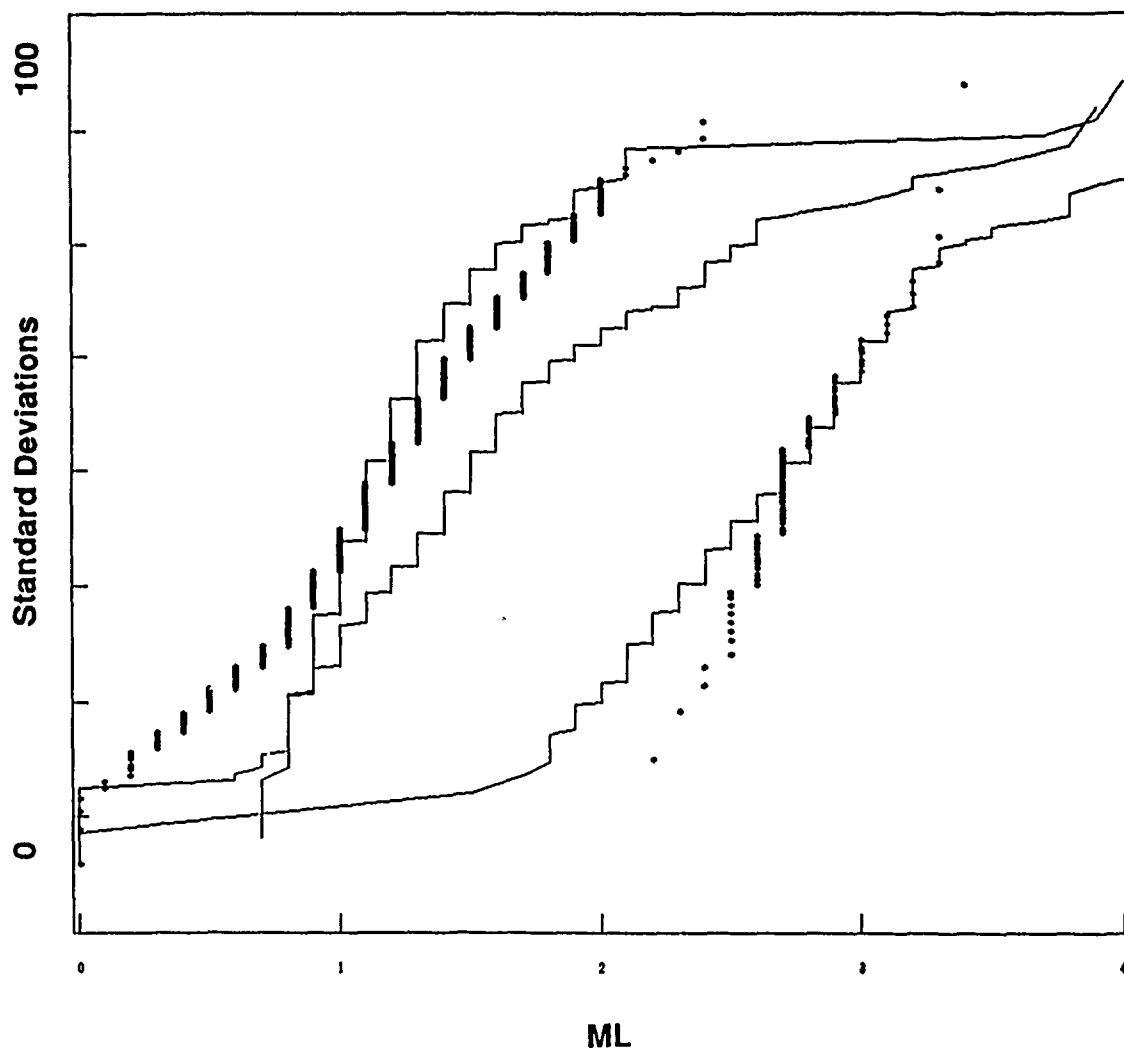
Figure 8. Empirical cumulative distribution functions of event magnitudes, *ML*, for events in the five regions defined in *Figure 7.*

Variations in the number of events as a function of time of week are shown in *Figure 9* for each region separately. Although the cyclic variation during the week is similar for all regions (except for the Kola peninsula) there are also minor differences. The diagram for Central Sweden shows three daytime peaks separated by 6-8 hours, which may reflect the working shifts in the mines. The activity in Central Sweden and Western Norway peaks on Tuesdays, whereas the peak occurs on Wednesdays in Southern Norway and Fridays in the Baltic region. The daily peaks for the Baltic are sharper than the other three regions, which may be an effect of more rigorous time schedules. The weekly curve for the Kola Peninsula is somewhat different than those of the other regions. The peak activity occurs on Sunday morning around 0300 GMT (i.e. 0500 local time). The fact that few explosions are reported for the working days may be due to the higher seismic noise level at NORESS during the normal working hours.

1.1.3 NORESS Detection And Location Capabilities

Events in the NORESS bulletin are defined from detection of P_n and L_g phases (Mykkeltveit, 1985). An event epicenter is defined by the distance obtained from the L_g - P_n arrival time difference and by the backazimuth obtained from f-k analysis of the L_g phase. For each event the bulletin also includes a local magnitude calculated from the maximum L_g amplitude with a distance correction for Scandinavia.

Phase and Event Detection Capability

Several studies have been carried out on NORESS detection capabilities for the P_n, S_n, and L_g phases. For example, Sereno and Bratt (1988) have approximated analytical expressions to the detection probabilities of P_n and of L_g as a function of magnitude, *ML*, and epicentral distance, *r*, (in km):

$$P_i(r,ML) = \Phi\left(\frac{D_i(r) + \alpha_i \cdot ML}{\sigma_i}\right)$$

with

$$D_i(r) = a_i + b_i \cdot \log_{10}(r)$$

Here Φ is the standardized normal distribution function, and α, a, b, and σ are constants and parameters with values characteristic of each phase, $i = P_n$, and L_g. The formulas were obtained for the distance interval 300-1400 km, and they are graphically illustrated in *Figure 10*. The smallest of the 50% thresholds for P_n is below $ML = 2.5$ over this interval. This can be compared with results of Ringdal (1986),
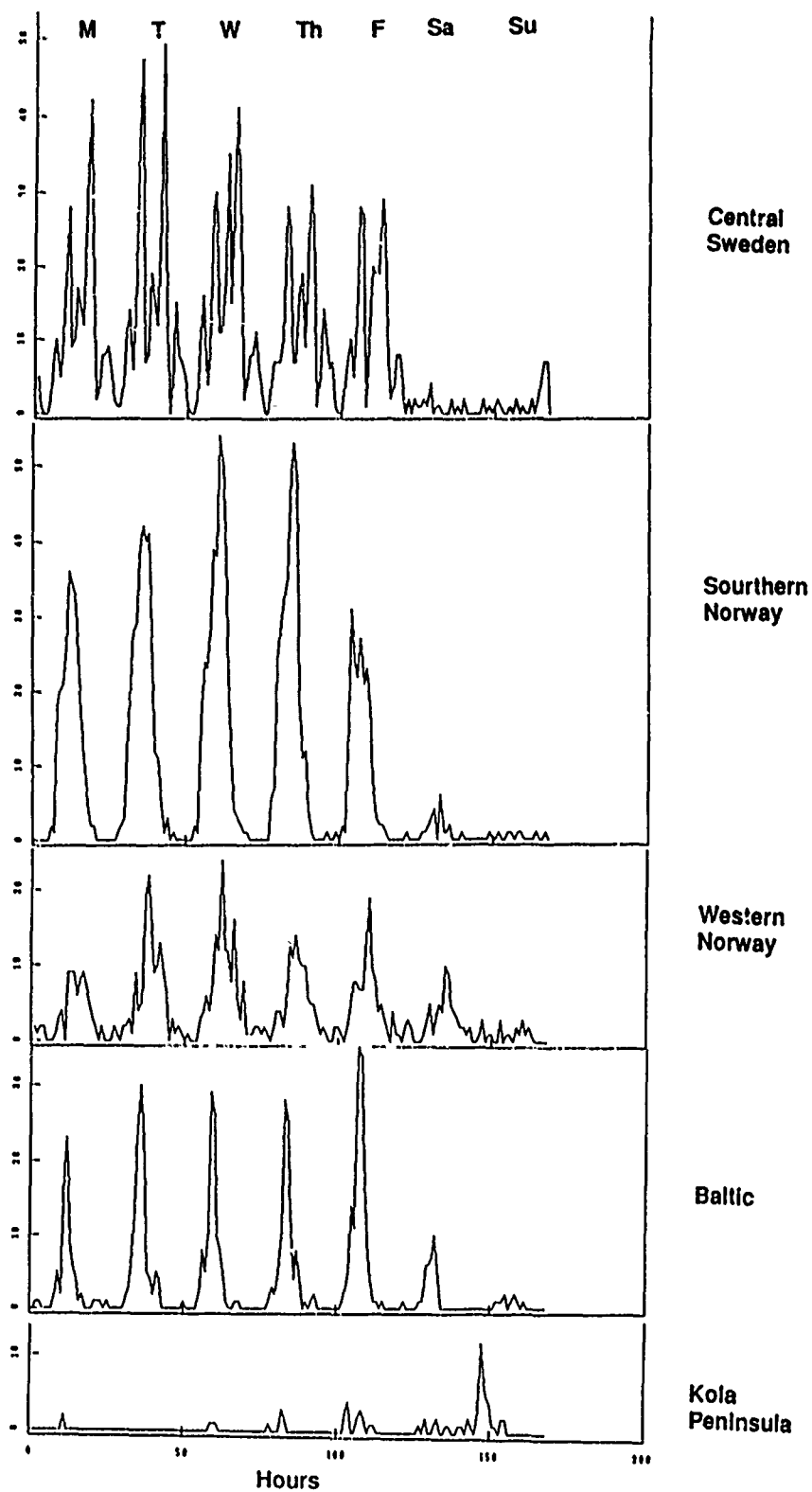
Figure 9. Number of events as a function of hour during the week for each of the five regions separately.
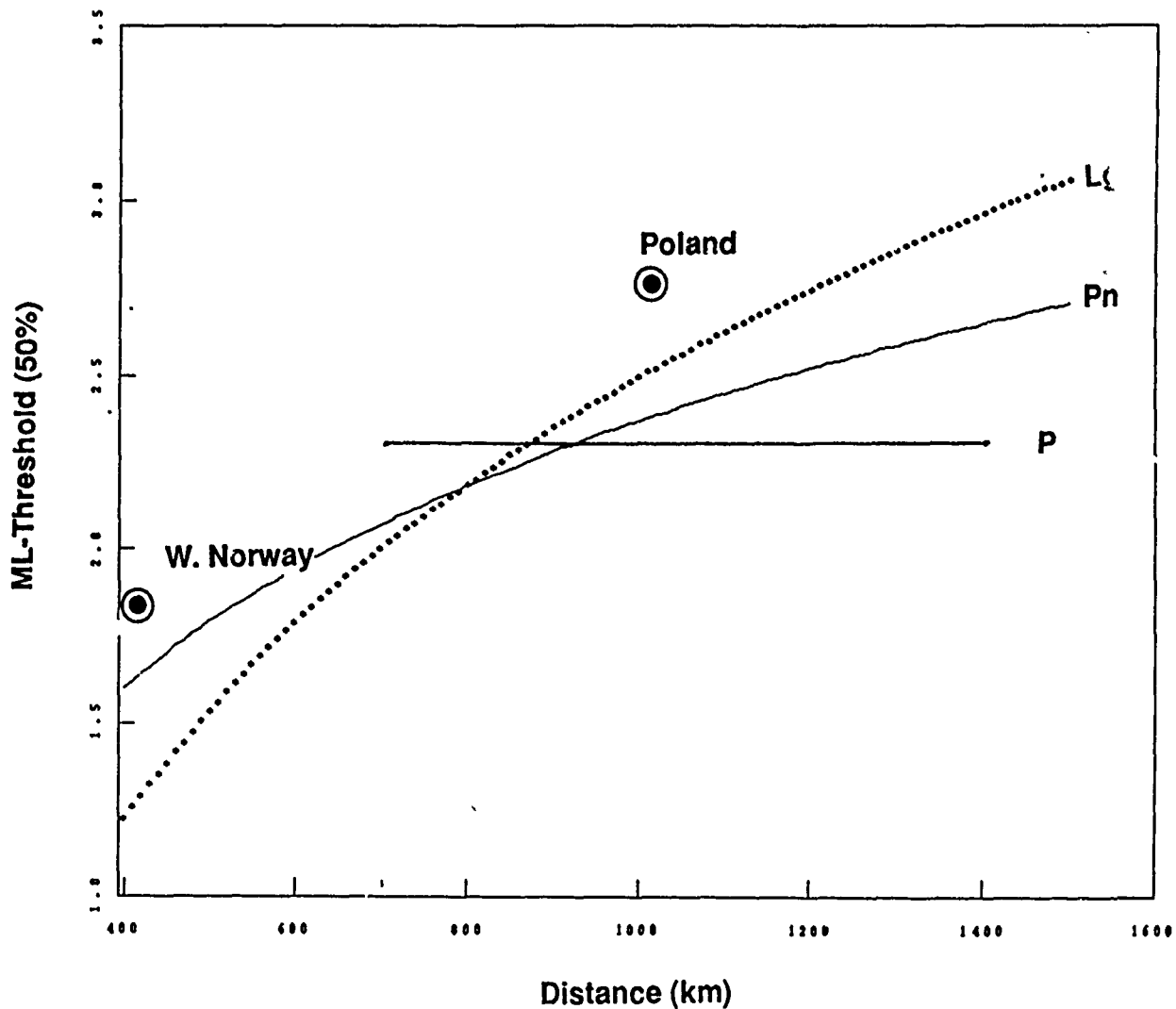
Figure 10. The curves represent 50% magnitude (ML) detection thresholds for P_n (line) and L_g (dotted) at NORESS according to analytical expressions by Sereno and Bratt (1988). The threshold at $ML=2.4$ for P waves estimated from a comparison with Network detections and locations of events east of NORESS in the distance range 700-1400 km was obtained by Ringdal (1986). The 50% threshold at ML=1.8 at 400 km was obtained by Mykkeltveit (1986) and relates to events in Western Norway. Finally the $ML=2.7$ threshold was defined by Gibowicz (1987) for mining events in the Lubin basin in Poland at about 1000 km from NORESS. A precise threshold could not defined and the value in the figure represents an approximate limit. It can be noted that the Lubin basin is located behind the Tornquist line from NORESS in a tectonically disturbed area.

who found that the detection capability of NORESS appeared to be better than $ML=2.3$ out to at least 1400 km distance.

The probability of detecting a seismic event, $P_e(r,ML)$, can be obtained from these phase detection probabilities if we assume that detections of P_n and L_g are independent:

$$P_e(r,ML)=P_{P_n} \cdot P_{L_g}$$

For given values of the probability $P_e(r,ML)$ and epicentral distance the ML threshold can be obtained from this non-linear equation.

In a similar way the probability for the detection of at least one of the two phases P_n and L_g is:

$$P_{P_n}+P_{L_g}-P_{P_n} \cdot P_{L_g}$$

Again the ML threshold can be calculated from this expression for a given probability and distance.

Figure 11 shows the event magnitudes plotted as a function of epicentral distance for events at distances greater than 400 km. The data points are compared with the event detection thresholds at 10, 50, and 90% probability obtained from the non-linear equation above. The thresholds for 10 and 90% range over about one magnitude unit. This difference is partly caused by a significant variation of the seismic noise with time at NORESS (Fyen, 1986). The difference in noise amplitude is about 10 dB (in power, i.e., 0.5 magnitude unit) from weekend lows to mid-day highs during working days, in the 2-16 Hz frequency band of detection (Kvaerna and Mykkeltveit, 1986). It can be seen that a significant number of events are indeed detected at or even below the 10% detection threshold. The events on the Kola Peninsula were mainly detected during weekends, which usually have low noise levels.

Annual Activity Levels

The events in the NORESS bulletin can be used to describe the number of events occurring within a given region as a function of magnitude, during a given period of time. This is an important characteristic for seismic monitoring systems. Since we are dealing with chemical explosions, the standard methods of earthquake seismology cannot be used, and we therefore use a straightforward descriptive approach. We define the event activity as the number of events with magnitude above a certain value, ML, that occur per unit time and per unit area. The event activity can be obtained for events in the NORESS bulletin above the magnitude
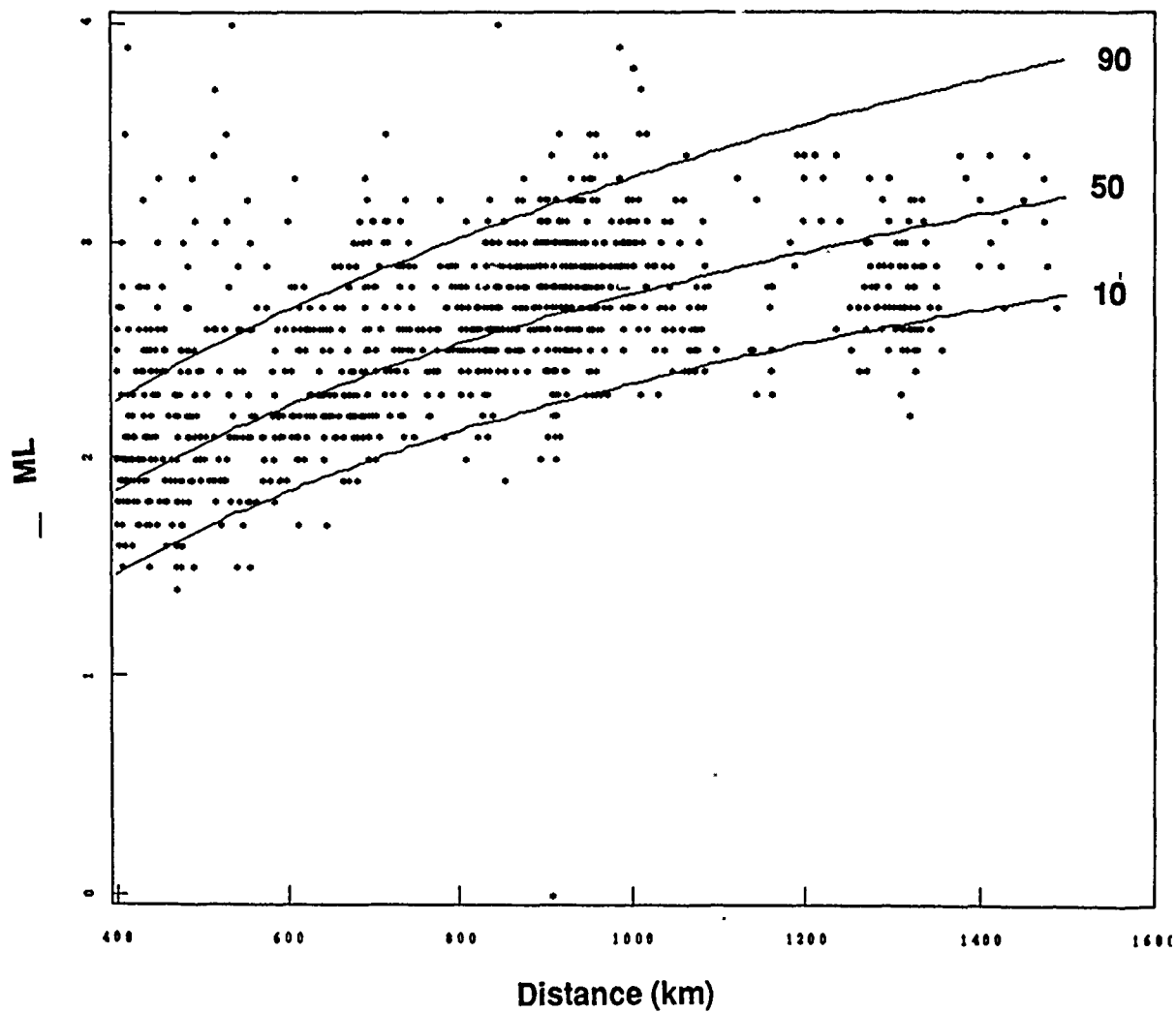
Figure 11. Event magnitudes as a function of epicentral distance for all events beyond 400 km from NORESS. The three curves represent the magnitude detection thresholds at 10, 50, and 90% probability as defined in the text.

threshold for which NORESS has more or less complete detection. We use the magnitude values of low magnitude thresholds that have been discussed for test ban monitoring with internal station networks. Hannon (1983) defined a network of stations with a 90% magnitude threshold equal to or below 3.0 throughout the Soviet Union as adequate, but considered the even lower magnitude range 2-3 to be of potential interest for this type of monitoring network.

The 90% ML threshold for NORESS is equal to or below 3.0 out to a distance of about 800 km *(Figure 11)*. On average 24 events per year with $ML \geq 3.0$ were detected and located within 800 km of NORESS according to the NORESS bulletin for the period analyzed here. This corresponds to an annual average of 12 events/million km^2 with $ML \geq 3.0$. If we assume in a similar way that complete detection of events with $ML \geq 2.0$ is obtained at distances less than 400 km (which seems somewhat optimistic according to *Figure 11)*, we get from the NORESS bulletin an annual average of 48 events/ million km^2 with $ML \geq 2.0$. However, a somewhat larger annual average, 76 events/ million km^2, as actually reported for the entire operative area of NORESS (here defined as distances less than 1500 km). If these event activities (12 and 76 events/million km^2) were representative of the seismic activity in the Soviet Union (area of about 22.3 million km^2), they would correspond to about 250 and 1500 events annually on Soviet territory with $ML \geq 3.0$ and $ML \geq 2.0$ respectively. Hannon (1983) estimated that the annual number of Soviet *earthquakes* with magnitude greater than 3 and greater than 2 would be about 1000 and 5000 respectively. That is to say that the event rates for chemical explosions are about a factor of 3-4 smaller than those estimated for natural earthquakes. The number of events with $ML \geq 2.0$ and $ML \geq 3.0$ as a function of geographical location in relation to NORESS are shown in *Figure 12*. The larger events are concentrated in the Baltic region and the Kola Peninsula with few events scattered in other parts of the operative area of NORESS.

Location Capability

A NORESS epicenter estimate is defined as the point at a distance obtained from the difference between L_g and P_n arrival times and at a backazimuth obtained from L_g. The estimated azimuths are compared with those calculated from epicenter determinations by local networks in Western Norway (BER) and Finland (HEL) in *Figure 13*. The empirical distribution functions of the azimuth error, η, are shown both for regionalized and non-regionalized data. Here η is defined as the difference between the azimuth reported by NORESS and that calculated from the BER and HEL determinations. Medians and standard deviations of η are summarized in *Table 2*. The errors have similar distributions for all data sets and are approximately normal with no bias (zero mean) and a standard deviation of around 7 °. This value can be compared with $\sigma_\eta = 10°$ used by Bratt and Bache (1988) in theoretical simulations of NORESS mislocations. Furthermore, Harris *et al.* (1986) obtained
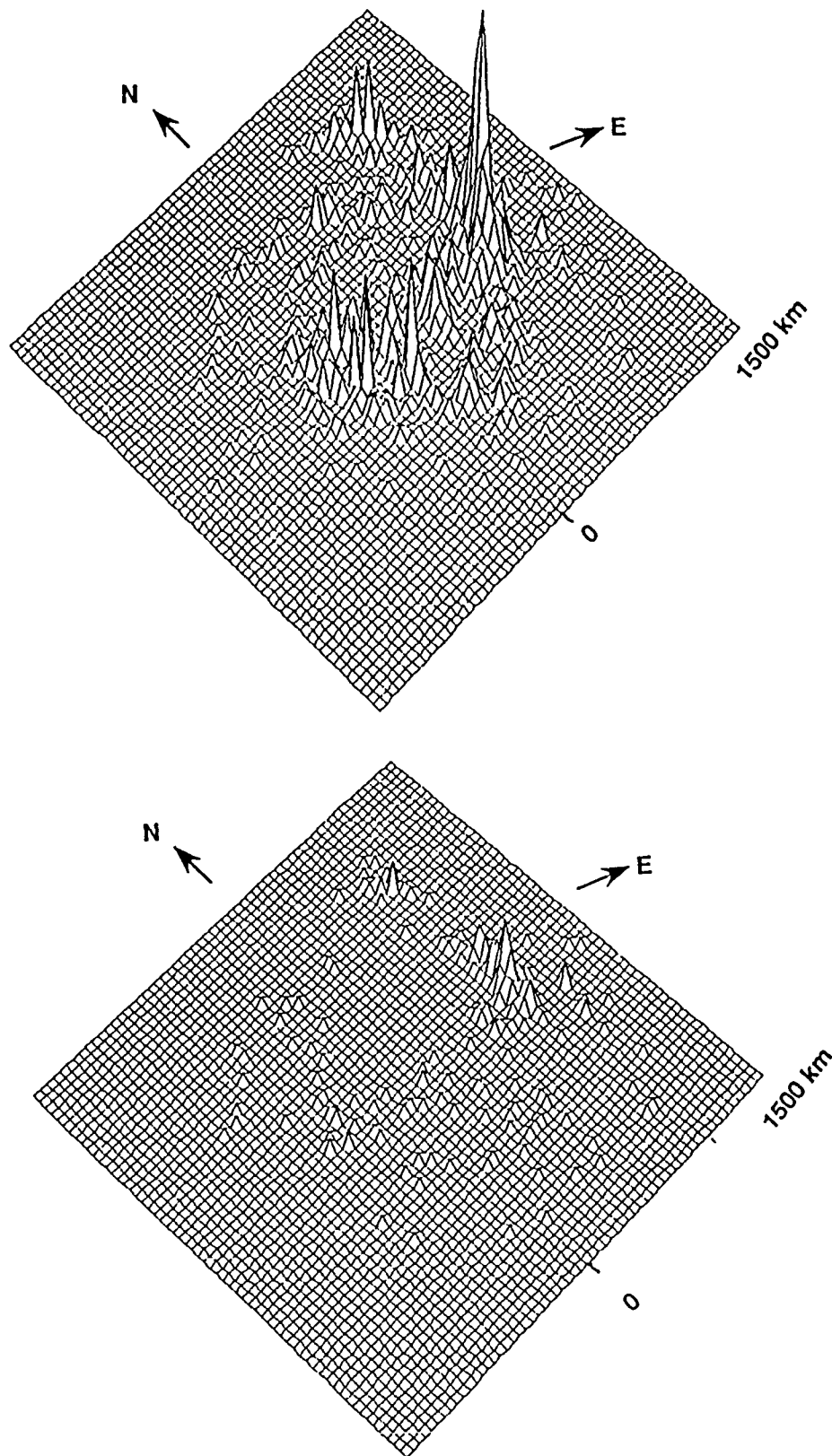
Figure 12. Number of events with magnitude $ML \geq 2.0$ and $ML \geq 3.0$ as a function of geographical location in relation to NORESS out to 1500 km. The maximum density in the diagram is 40 events/ 15 km^2.
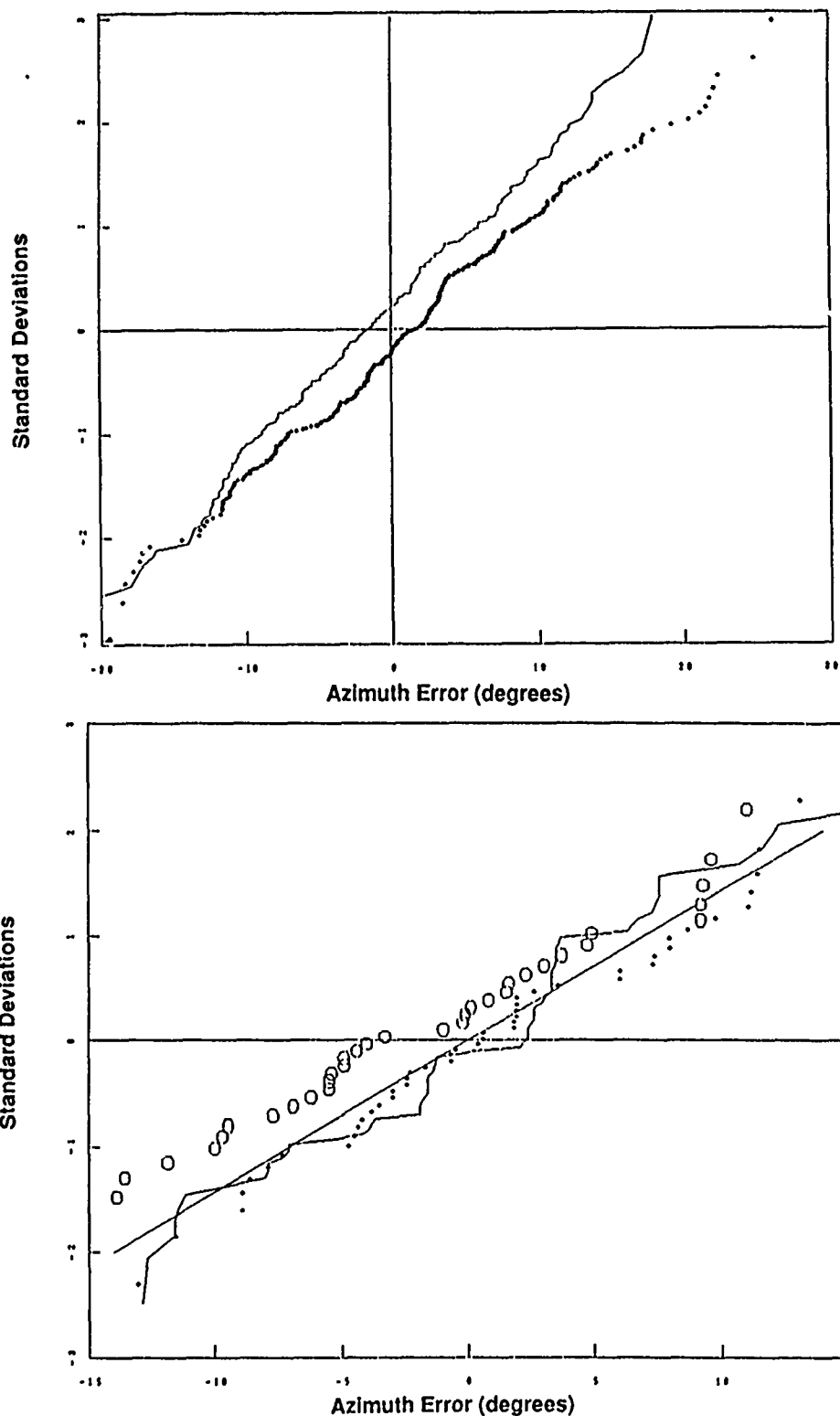
Figure 13. Cumulative distribution function of error in backazimuth for NORESS events that were also reported by local networks in Western Norway (BER) and Finland (HEL). There were 347 and 383 common events respectively for BER and HEL. The error is defined as the difference between the azimuth reported by NORESS and that calculated from the epicenter determined by BER or HEL.

an rms error of 5.5 ° for a three phase average (P_n, S_n, and L_g) for mining explosions. If we assume that the azimuths of these phases are independent and have equal standard deviations, this corresponds to σ_η=9.2°. Finally, Gibowicz (1987) found that for mining events in the Lubin basin at about 1000 km distance from NORESS the error in backazimuths of P_n and S_n ranged in the interval -14° to 17° and -5° to 4° respectively.

TABLE 2								
ERRORS IN DISTANCE AND BACKAZIMUTH								
Events	Lat(N)	Long(E)	Dist (km)	No of Events	Error			
-	-	-	-	-	Distance		Backazimuth	
-	-	-	-	-	Med	Std	Med	Std
W. USSR	60.5-61.0	28.5-30.5	175	46	20	15	0.5	6.6
W. USSR	59.0-60.0	23.5-25.5	730	36	27	23	-3.7	7.6
S. Norway	60.0-61.0	5.4-5.7	330	71	41	17	2.3	6.2
HEL Events				383	20	41	1.3	7.9
BER Events				347	24	43	-1.8	7.1

The situation for the distance error, ξ, is more complicated, as indicated by the empirical distribution functions for the regionalized data sets in *Figure 14*. The difference, ξ, is defined as the difference (in km) between the distance reported by NORESS and that calculated from the epicenter determinations of BER and HEL. Values of medians and standard deviations are listed in *Table 2*. For all three regions there is a bias (from 20 to 40 km) and the data are approximately normally distributed in only one case. The standard deviations vary between 15 and 23 km. Let σ_i, for $i=P_n$ and L_g, be the standard deviations of the arrival time errors. The standard deviation of epicentral distance, σ_ξ, can be written as:

$$\sigma_\xi = \left(\sigma_{L_g}^2 + \sigma_{P_n}^2\right)^{1/2}/(S_{L_g} - S_{P_n})$$

with S_i being the slowness for P_n and L_g.

For theoretical simulations of mislocations Bratt and Bache (1988) used $\sigma_{P_n} = \sigma_{L_g} = 1.5$, which according to this formula (with S_{P_n} and S_{L_g}, 1/3.5 and 1/8.1 s/km respectively) corresponds to σ_ξ=13 km. This value is in reasonable agreement with the standard deviations for the distance error of the regionalized sets in *Table 2*.

Data for the distance error, ξ, is also plotted as a function of distance in *Figure 14*. There is a large scatter in the data, which also seem to be biased. Some of this
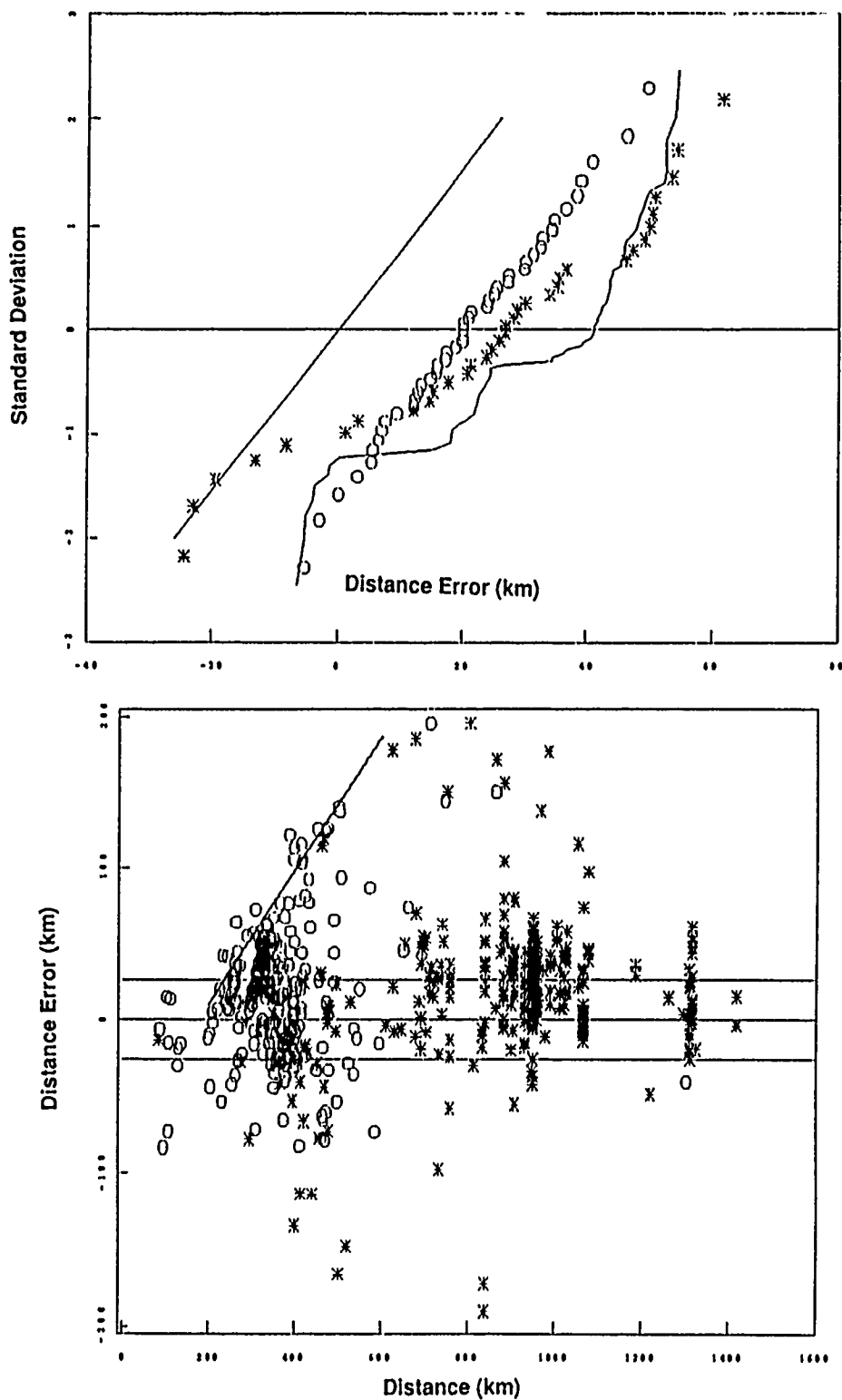
Figure 14. Cumulative distribution of error in distance for NORESS events common with events reported by local networks in Western Norway (BER) and Finland (HEL). The error is defined as the difference between the distance reported by NORESS and that calculated from the epicenter determined by BER or HEL. Data are shown for three regionalized sets defined in Table 2. The straight line represents distance error used in theoretical calculations (Bratt and Bache, 1988).

1-22

bias can be explained by misidentification of the L_g phase as the largest amplitude in the S coda if the maximum actually occurs for S_n, as is often the case for mining explosions in the Lubin area (Gibowics, 1987). This bias caused by using the arrival time of L_g when it really is that of S_n is a function of distance:

$$bias = \frac{(S_{L_g}-S_{S_n})\cdot r - t_{S_n}(0)}{(S_{L_g}-S_{P_n})}$$

with $t_{S_n}(0)$ being the intercept of the travel time formula for S_n (i.e., $t_{S_n}(r)=t_{S_n}(0)+r\cdot S_{S_n}$). With the values of the layered model for crustal velocities used in the NORESS locations the bias is $\approx 0.44\cdot r - 78$ (km). This linear relation is drawn in *Figure 14* and there seems to be a group of events at distances between 200-600 km that cluster around this line.

The mislocation or total error, ς, is defined as the distance between the NORESS epicenter and that determined by BER or HEL. If we assume plane geometry we have approximately:

$$\varsigma^2 = \xi^2 + r^2\cdot\eta^2\cdot\frac{\pi^2}{180}$$

By applying the expectation operator we get:

$$E(\varsigma^2) = \sigma_\xi^2 + E(\xi^2) + r^2\cdot\sigma_\eta^2\cdot\frac{\pi^2}{180}$$

Here $E(\xi^2)$ will depend on the bias of the distance error, which seem to vary between regions.

Even if we assume no bias in the distance error (which can be 20-40 km), the mislocations are significantly larger than the reported epicenter accuracy of 0.1 degree in latitude and longitude.

1.1.4 Concluding Remarks

Seismic events reported in the NORESS bulletin for a period of two and a half years, Jan. 1, 1986 - June 30, 1988 have been analyzed. The events show a strong cyclic variation with time of week. Averaged over the working days, the total number of events for this period corresponds to 9 events per working day.

The geographical distribution of the epicenters has a highly regionalized pattern, with about 80% of the events at distances less than 400 km. Half of the events are from two limited areas within about 200 km from the array, one in Central

Sweden and the other in Southern Norway. About 20% of the events are from a small area (20 by 60 km) in the mining districts of Central Sweden.

The magnitudes for events in a given region are approximately normally distributed with standard deviations between 0.2 - 0.35. The magnitudes for the events in Sweden and Norway have mean values in the range $ML=1.1-1.5$. For the Baltic region and the Kola Peninsula the medians are equal to $ML=2.7$. Clearly, events in the Kola peninsula in the $ML=1-1.5$ range would not be detected by NORESS. Even so, if one assumes that the majority of the events are mining explosions this systematic difference in magnitudes suggests major differences in the use of explosions tonnages and/or distribution in time and space of charges.

The detected events on the Kola peninsula differ from the other regions with regard to the cyclic pattern as a function of the hour of the week. Most Kola events occur on the weekends with a peak early Sunday morning. The fact that few events are reported during working days from the Kola peninsula may be an effect of the strong variation of the seismic noise level with time of week.

Magnitude thresholds for event detection are derived from published phase detection probabilities. The event detection threshold at 50% probability is in the range $ML=1.9-3.3$ for the distance interval 400-1500 km. The threshold varies almost one magnitude unit for probabilities at 10% and 90% for any given distance, and this range may again partly be caused by the variation of the seismic noise at NORESS.

In order to compare the characteristics of the number of events in the NORESS operative area with those of other regions, the NORESS bulletin data was also used to estimate the level of event activity, defined as the number of events above a certain magnitude, ML, per unit time and per unit area. The estimated event activities for $ML \geq 3.0$ and $ML \geq 2.0$ are 12 and 48 events annually/ million km^2. If these activities were uniformly applicable to the Soviet Union, 250 and 1500 mining events would occur annually within Soviet territory with $ML \geq 3.0$ and $ML \geq 2.0$ respectively. These event rates for chemical explosions are about a factor of 3-4 smaller than those estimated for natural earthquakes for the Soviet Union.

Comparisons of epicenters estimated by NORESS and those determined from station network data in Fenno-Scandinavia are used to estimate standard deviations of errors in backazimuth and distance to about 7.5 ° and 15-25 km respectively for regionalized data. The distance errors are also subject to bias due to misidentification of secondary phases.

Hans Israelsson

References

Bratt, S.R. and T.C. Bache (1988). Locating Events with a Sparse Network of Regional Arrays, *Bull. Seism. Soc. Am.*, Vol. 78: pp. 780-798.

CD/43, (1979). Second Report of the Ad Hoc Group of Scientific Experts to consider International Co-operative measures to detect and identify seismic events. *Document of UN Conference of Disarmament, Geneva*

Fyen, J. (1986). NORESS noise spectral studies - noise level characteristics *NORSAR Sci. Report No. 1-86/87:* pp. 103-117.

Gibowicz, S.J. (1987). NORESS Capability for Detection and Location of Mining Tremors in the Lubin Area in Poland, *NORSAR Sci. Report No. 2-86/87:* pp. 91-124.

Harris, D., Dowla, F., and B. Tapley (1986) NORESS Performance in Determining Bearing and Phase Velocity, *In Seismic Monitoring Research Program- Annual Report,* Lawrence Livermore National Laboratory **UCID-20628-86** pp. 48-53.

Kvaerna, T. and S. Mykkeltveit (1986). Optimum beam deployment for NORESS P-wave detection, *NORSAR Sci. Report No. 1-86/87:* pp. 61-76.

Mykkeltveit, S. (1986). NORESS real time processing performance for events in Western Norway and the North Sea, *NORSAR Sci. Report No. 2-85/86:* pp. 40-47.

Mykkeltveit, S. and H. Bungum (1984). Processing of regional seismic events using data from samll-aperture arrays, *Bull. Seism. Soc. Am.*, Vol. 74: pp. 2313-2333.

Ringdal, F. (1985). Initial Results from NORESS Detection Processing, *NORSAR Sci. Report No. 1-85/86:* pp. 40-51.

Ringdal, F. (1986). Regional Event Detection Using the NORESS array, *NORSAR Sci. Report No. 2-85/86:* pp. 21-30.

Sereno, T.J. and S. R. Bratt (1988) Attenuation and Detection Capability of Regional Phases Recorded at NORESS, *Science Applications International Corp., Semiannual Report No. 3* **AFGL-TR-88-0095, ADA196568**

2.1 SPECTRAL CHARACTERISTICS OF HIGH FREQUENCY SEISMIC NOISE AT NORESS AND KKL

ABSTRACT

In this note we compare power spectra of seismic noise recorded during *quiet* periods at the high-frequency element of the NORESS array and the NRDC high-frequency station at Karkaralinsk, KKL, in the Soviet Union. Between 2 and 40 Hz the power spectrum of the vertical component surface noise at NORESS is up to 10 dB quieter than that of KKL. Outside this band the spectrum at KKL is clearly lower (up to 10 dB) than the NORESS spectrum. The decay of the power spectra with frequency does not follow a simple power law. For example, the NORESS spectrum has a pronounced minimum at 4 Hz, which can be utilized as a window for signal detection. Below 10 to 20 Hz, both NORESS and KKL quiet spectra are less than (by at most 10 dB) or equal to levels predicted by the NORSAR noise model. At higher frequencies they are up to 10 dB larger than the NORSAR model. The spectra of the horizontal components are, in general, lower than those of the vertical components at frequencies between 25 to 50 Hz. Borehole instruments provide approximately 6 dB noise reduction relative to surface instruments in the frequency band from 10 to 30 Hz. The spectra of all instrument components are dominated by a suite of 15 to 20 narrow peaks. Many peaks occur at frequencies that can be described by the formula for a geometric series. Most of these peaks seem to be generated by non-linear mechanical and electrical processes of the instruments and their recording systems. Even if such peaks do not obscure many broadband signals of interest, they impose limits on the detection of weak signals of interest in test ban monitoring.

2.1.1 Introduction

Interest in high-frequency seismology for monitoring underground nuclear explosions has resulted in studies of the ambient ground noise at frequencies up to 100 Hz at the NORESS array in Norway (Fyen, 1987) and at NRDC experimental stations in the Soviet Union (Berger et al., 1988). Collecting high-frequency seismic noise data requires highly sensitive instruments and recording systems. In fact, Berger et al. (1988) conclude from their data collected in the Soviet Union, that two instruments are necessary for observing the ambient seismic noise over the frequency band 1-100 Hz, (they use two different Teledyne Geotech seismometers, a GS-13 for frequencies below 10 Hz and a 54100 for frequencies above 10 Hz). At NORESS, data have been collected in the 1 to 50 Hz band with only one instrument (GS-13 seismometers; initially Teledyne Geotech S-3 seismometers were used for about half a year, Fyen, 1987).

In this note we compare power spectral density functions of seismic noise recorded at the high-frequency element of NORESS and at the NRDC stations in the Soviet Union. As the ambient noise at high-frequencies is usually strongly dependent on cultural activities and wind conditions, attempts are made to select data recorded at *quiet* periods for this comparison.

2.1.2 Stations and Recording Characteristics

The technical characteristics of the high-frequency element of the NORESS array and the NRDC stations have been described by Kromer (1985) and Berger et al. (1988) respectively. The high-frequency element at NORESS consist of a three-component set of Teledyne Geotech GS-13 seismometers placed in a surface vault at the NRAO site of the array. The NRDC data were limited to recordings at the station in Karkaralinsk, KKL, which was equipped with Teledyne Geotech 54100 three-component borehole seismometers in a 60 m borehole and three componenent GS-13 seismometers in a surface vault. The 54100 borehole seismometer houses S-750 feedback accelerometers, the output of which are shaped with line drivers to achieve a response that is flat to ground velocity. For the sake of brevity, we refer to the borehole instruments as S-750 in the following. Amplitude response curves obtained from analytical expressions of the nominal response of the instruments with associated recording equipment (after Durham, 1986 and Berger et al., 1988) are drawn in *Figure 1*. All responses are flat to ground velocity. The operational frequency band of the NORESS station is 10 to 50 Hz, while the KKL bands cover frequencies from 1 to 80 Hz. The NORESS response has a resolution (in counts/nm/s) that is over 20 dB higher than the resolutions of the KKL responses.

Instrument and recording equipment noise are summarized and compared with the instrument noise levels for the RSTN stations (Rodgers et al., 1987) and the Lajitas LTX station (Herrin, 1982 and Li et al., 1984) in *Figure 2*. The self-noise for the
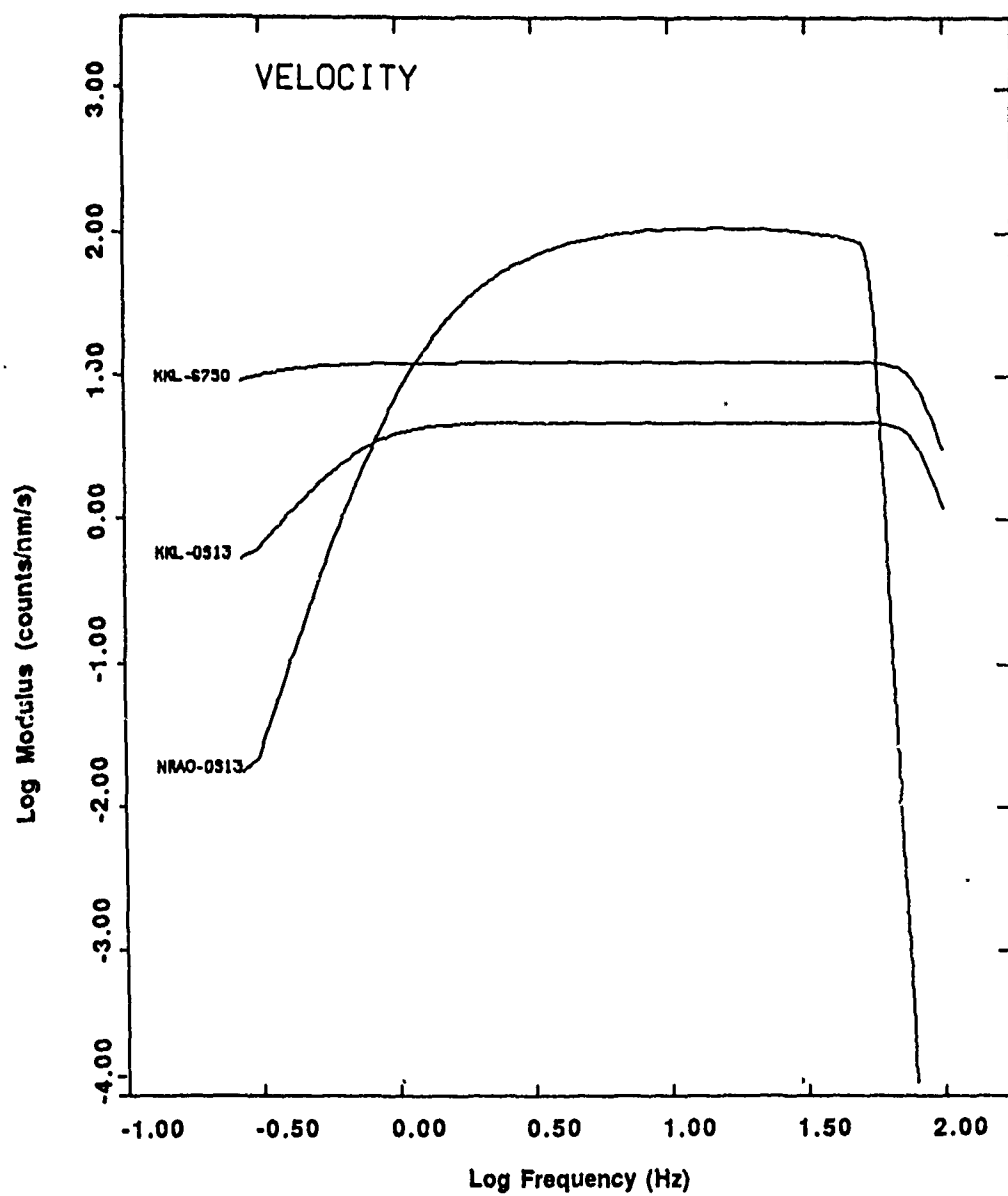
Figure 1. Amplitude response curves of the instruments at KKL and NORESS.
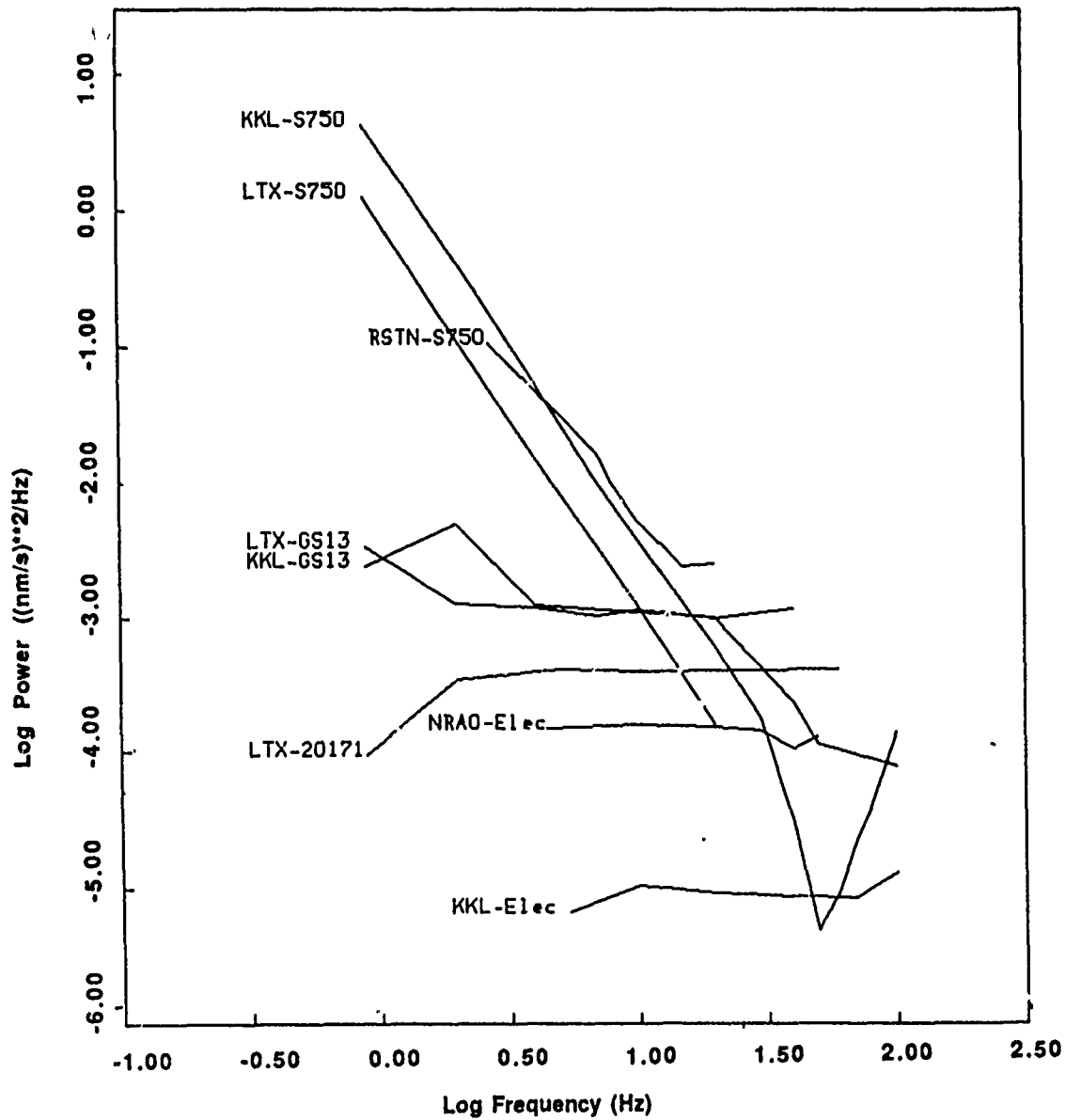
Figure 2. System noise reported in the literature for the NORESS and NRDC data. For comparison, data for the RSTN stations (after Rodgers *et al.*, 1987) and the station Lajitas, LTX, (after Li *et al.*, 1984) are included.

S-750 seismometer (the theoretical instrument noise given by the manufacturer) is flat in acceleration with a clear minimum around 50 Hz. The self noise of the GS-13 seismometer (including the electronic system) of the NRDC stations is flat in velocity between 4 and 25 Hz. The measurement was obtained with the seismometer mass clamped (Berger et al., 1988). The noise of the NRDC and the NORESS recording electronics were obtained by replacing the seismometer with an impedance matching that of the seismometer (Kromer, 1985; Berger et al., 1988). The self-noise of the LTX seismometer (Teledyne Geotech 20171) including the low noise amplifier (Teledyne 43310) is flat in velocity above about 2 Hz. Bias of estimated power density functions for ambient seismic noise caused by quantization noise has been studied theoretically and experimentally for seismic noise data (Bungum and Mykkeltveit, 1985; Rodgers et al., 1987). The power of quantization noise is $1/12 \cdot counts^2/Hz$, which for sampled seismic data introduces a bias in the power spectral density function of $\Delta t \cdot 1/12 counts^2/Hz$, where Δt is the sampling interval in seconds (Rodgers et al., 1987). The quantization sensitivity at NORESS and KKL shown in *Figure 1* is sufficient for such bias to be neglected.

2.1.3 Data

Clear seasonal, weekly, and diurnal variations of the noise level (power spectral density) at the NORESS array have been documented (Fyen, 1987). At higher frequencies, the noise level correlates with the industrial activity in the area, and the diurnal variation can vary from 5 to 15 dB at frequencies above 2 Hz. Furthermore, the nighttime minima during weekends are lower than those during working days. Seasonal variations have also been noted that correlate with water flow related to snow melting in nearby and distant rivers at frequencies above 1.5 Hz. Noise related to industrial activity seems to be less pronounced at frequencies above 20 Hz than at frequencies in the 2 to 20 Hz band (Fyen, 1987). Locally generated wind noise (due to wind speeds of the order of 10 m/s) can usually be neglected below 10 Hz, but may contribute 5 to 15 dB between 20 and 30 Hz (Bungum and Mykkeltveit, 1985). For the purpose of this study, 19 noise segments, each consisting of 2 minutes of data, were selected from data recorded on Jan 4 (a Sunday), 1987. The onsets of the segments were separated by 10 minutes and were taken from data that were recorded between 1 and 4 a.m. local time. These times represent periods with quiet noise conditions. The power spectral densities (estimated as described below) are shown at various frequencies from 1 to 40 Hz as a function of local time in *Figure 3.* The variation about the segment averages is usually less than 5 dB.

Due to the limited recording period, the time variation of the noise level at the NRDC stations was not studied in detail. It has been noted that at the earth's surface, the noise level at frequencies above 20 Hz can increase about 10 dB with an increase in the local wind speeds from 0.5 m/s to 5.8 m/s. For borehole
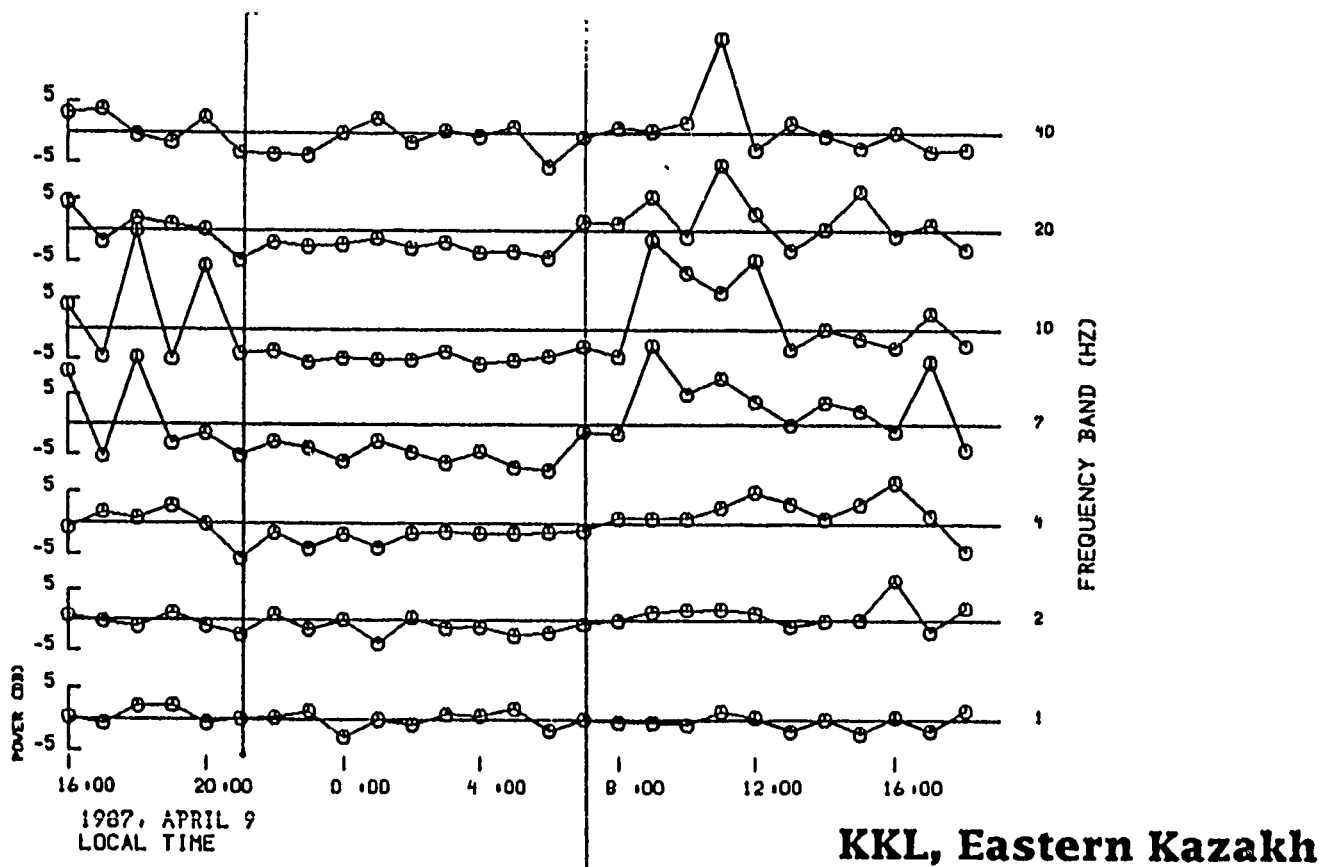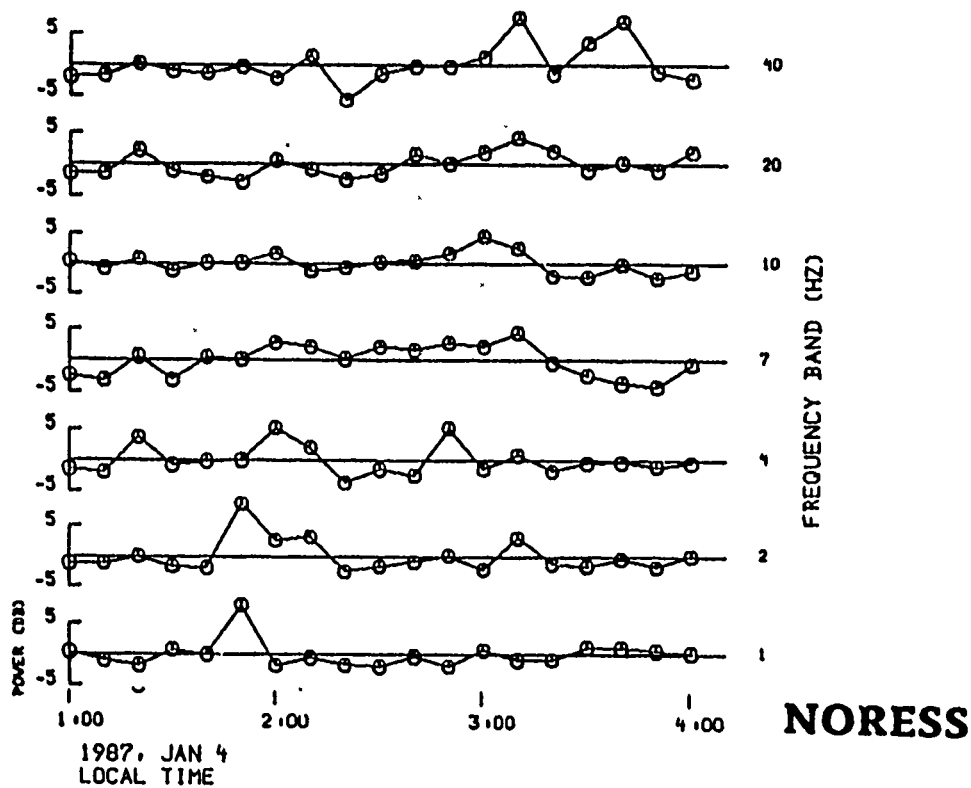
Figure 3. Relative noise power in narrow frequency bands as a function of time for the noise segments at NORESS and KKL. All segments for NORESS were used, whereas only the 11 segments marked in the diagram for KKL were included in the analysis.

instruments (60 m below the surface) this increase is less pronounced (Berger *et al.*, 1988). The noise data recorded at the NRDC station KKL that was used for this study consists of 90 s segments from a suite of noise recordings collected at one hour intervals from the 9th through the 11th of April, 1987 (*Figure 3*). Eleven segments with quiet noise conditions (indicated in the figure) were selected for the subsequent analysis. The data show the power spectral density at various frequencies from 1 to 70 Hz. The selected noise segments were obtained between 9 p.m. and 7 a.m. local time. During that time period, the noise level in all frequency bands stayed fairly constant with a variation less than 5 dB from the average.

2.1.4 Power Spectral Density Functions

Power spectral density functions, $p_x(f)$, of the noise segments were estimated with standard procedures assuming that a recorded noise segment, $x_i(t)$, ($i=1,...,I$) is a realization of a stationary stochastic process. Each noise segment, $x_i(t)$, was divided into J consecutive blocks, $x_{ij}(t)$, ($j=1,...,J$) with an equal number of data points n, in each block. n is an integer power of 2, ($n=2^k$). k=9 and 10 correspond to 4.1 seconds of data for NORESS and NRDC respectively.

For each sample block, any DC bias present was removed and the data were tapered with cosine tapers of 0.5 sec length. The discrete Fourier transform was calculated in the usual manner:

$$X_{ij}(f) = \frac{1}{\sqrt{n}} \sum_{t=0}^{n-1} x_{ij}(t) \cdot e^{-2 \cdot \pi \cdot t \cdot f / n}$$

The block estimates were averaged for each noise segment:

$$\hat{p}_i(f) = \frac{\Delta t}{J} \sum_{j=1}^{J} X_{ij} X_{ij}^*$$

where Δt is equal to the increment between data points in seconds (1/125 and 1/250 s for NORESS and KKL respectively). These averages, $\hat{p}_i(f)$, were then averaged over the segments i.e., $\hat{p}(f) = \sum_{i=1}^{I} \hat{p}_i(f)/I$. The final average estimate of the power density, $\hat{p}(f)$, for each instrument component was based on 418 and 242 block spectral estimates for NORESS and KKL respectively. The average spectra corrected for instrument response (ground velocity), $\hat{p}(f)$, are shown in *Figure 4* for the vertical components of the three instruments. The system noise spectra, $p_s(f)$, from *Figure 2* are included for comparison. The system noise spectra are well below the estimated spectra, $\hat{p}(f)$, for each instrument. Berger *et al.* (1988) found that the GS-13 seismometer noise) approaches the ambient ground noise at KKL (during quiet conditions) at about 30 Hz. The theoretical seismometer noise for the S-750
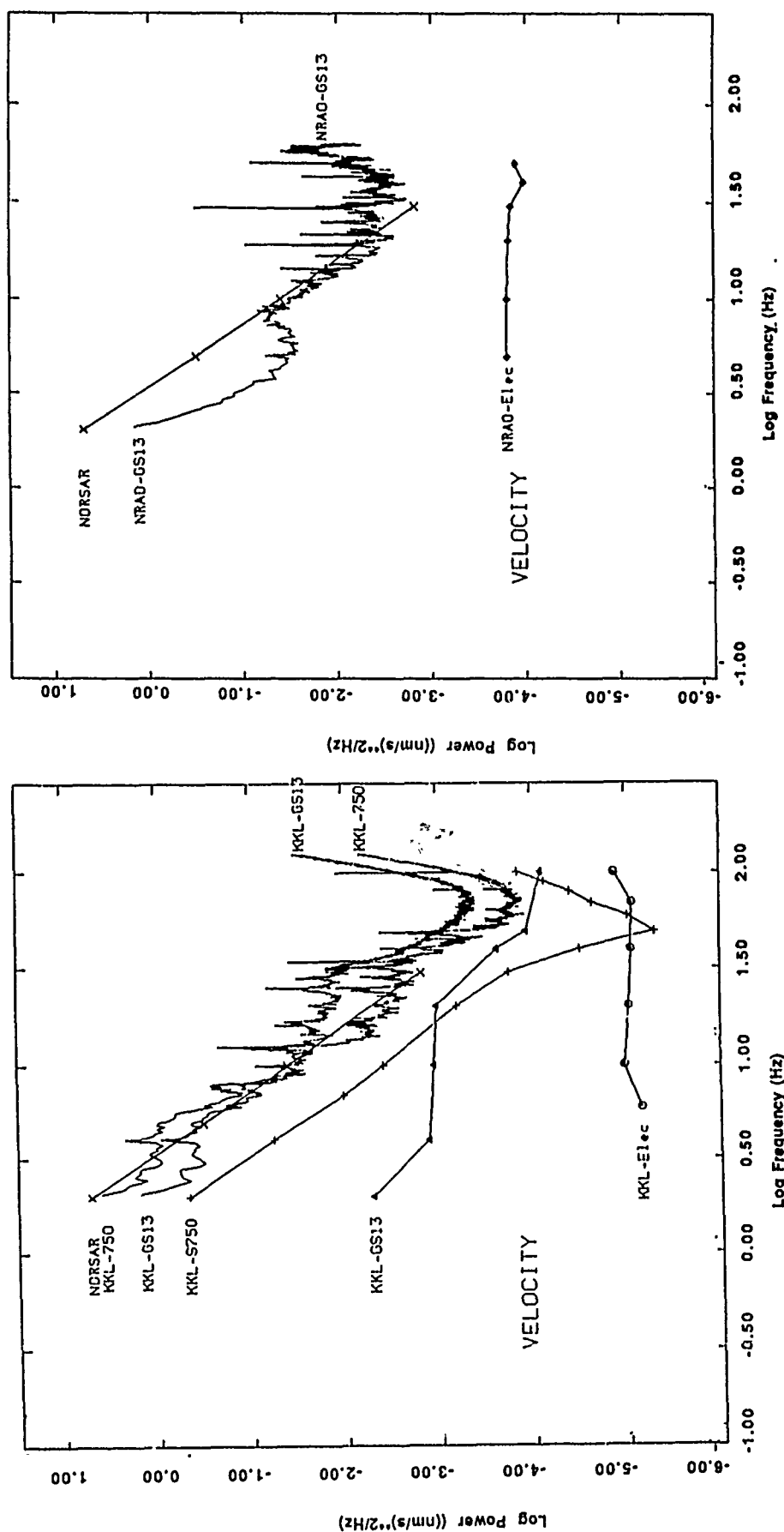
Figure 4. Average power spectral density functions of the vertical component data from KKL and NORESS. System noise reported in the literature and i ` > NORSAR noise model (Bungum and Mykkeltveit, 1985) are included for comparison.

instrument at KKL is fairly close to the average ambient noise spectra for the GS-13 instrument at frequencies around 2 Hz. Berger *et al.* (1988) therefore composed the quiet noise spectrum from that of the GS-13 instrument for frequencies below 10 Hz and that of the S-750 above 10 Hz. The two ambient noise spectra at KKL cross over at about 10 Hz in *Figure 4*. The curve representing the minimum of the two KKL spectra in *Figure 4* would thus represent the ambient noise at KKL according to the procedure used by Berger *et al.* (1988).

In *Figure 5* the "ambiant noise-to-system noise ratio" defined as ambient noise plus system noise over system noise, i.e., $\hat{p}(f)/p_s(f)$, is plotted as a function of frequency for the two instruments at KKL. The surface instrument has the largest noise-to-noise ratio for frequencies below 35 Hz, and above 70 Hz the two instruments have about the same values. The large maximum for the borehole instrument in a band around 50 Hz is an effect of the minimum of the theoretical noise and possibly self noise from the 50 Hz power line of the S-750 instrument. That is to say, the apparently large noise-to-noise ratio in this band is probably strongly biased. Between 10-20 Hz the noise-to-noise ratio for the borehole instrument is about the level of the noise-to-noise ratio for the surface instrument at frequencies above 50 Hz.

Surface and Bore Hole Instruments

Figure 6 compares the power spectra at the surface (GS-13) and in the borehole (S-750) of the KKL site. The ratio of the power spectra is plotted as a function of frequency between 1 and 80 Hz. The power spectra were corrected for the system noise, i.e., the ratio is defined as: $\left[\hat{p}(f)-p_s(f)\right]_{GS-13}\Big/\left[\hat{p}(f)-p_s(f)\right]_{S-750}$. The ratio in *Figure 6* shows that the noise level is about the same at 10 Hz; below 10 Hz it is lower for the surface instrument; and above 10 Hz it is higher for the surface instrument. Between 10 and 30 Hz the ratio is about 6 dB, and above 30 Hz the ratio stays fairly constant around 4 dB except in a narrow band around 50 Hz, where it drops below 0 dB. For the data analyzed here, the borehole environment provide the largest noise reduction in the band from 10 to 30 Hz. This is in general agreement with results for the NORESS high-frequency element. Fyen (1987) reports clear differences for frequencies above 6 Hz, with a 6-7 dB higher noise level at the surface (GS-13 in shallow vault) than in the borehole (a Teledyne Geotech S-3 bore hole seismometer at a depth of 60 m). However, Berger *et al.* (1988) found little improvement in noise levels at the quieter NRDC sites for the borehole instruments for frequencies below 40 Hz. Above 40 Hz the improvements were only marginal.
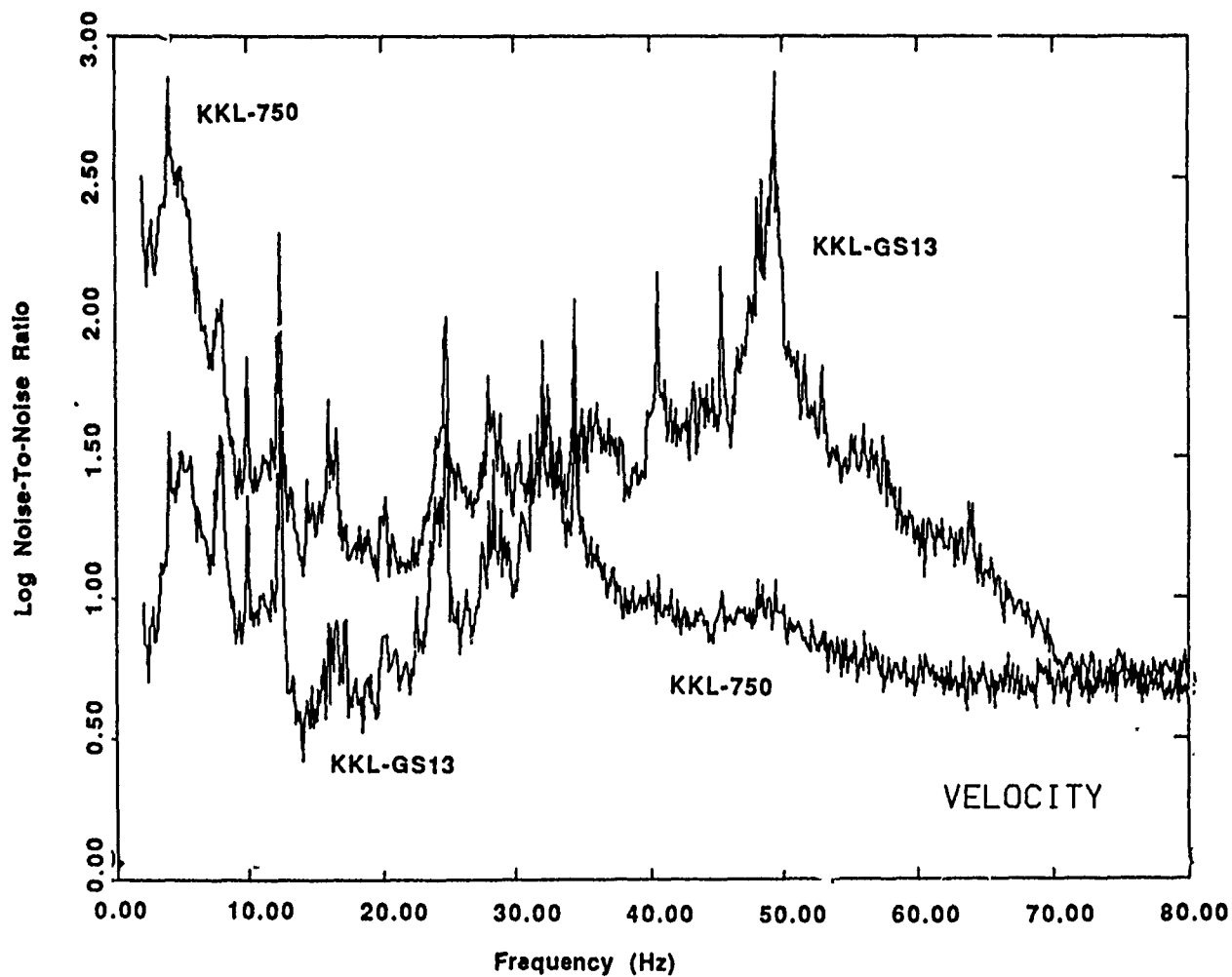
Figure 5. Noise-to-noise ratio defined as ambient noise plus system noise divided by system noise for the vertical component data from KKL.

2-10
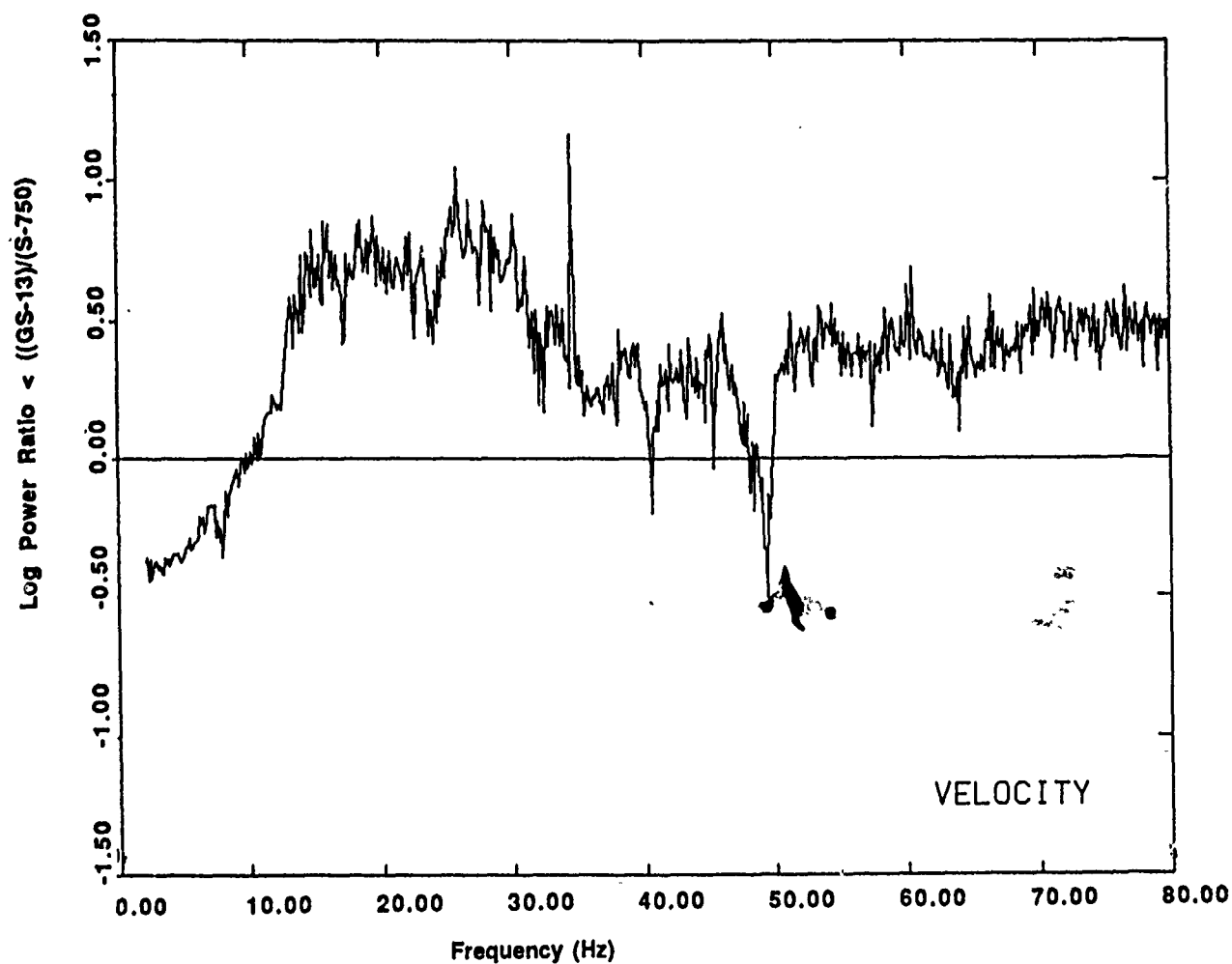
Figure 6. The ratio of the power spectra of the GS-13 and S-750 vertical component data recorded at KKL.

Decay Rate with Frequency

Power spectra of ground noise displacement are usually decaying more or less monotonically with frequency, f, above some low frequency value and various power law models have been used to describe this effect. For example, the NORSAR model, which is based on noise data from Southern Norway, assumes that the power of the displacement above 1 Hz is proportional to f^{-5} (Bungum and Mykkelteit, 1985). Another model, based on data from the Lajitas, Texas, station LTX, assumes that the acceleration power density above 2 Hz is independent of frequency (white noise process), which means that the spectrum of the displacement would fall off like f^{-4} (Li *et al.*, 1984).

In *Figure 7* the average spectra at NORESS and KKL are compared with the NORSAR model, i.e., the ratio: $\hat{p}(f)/f^{-5}$ is plotted as a function of frequency. The spectrum for KKL is represented by that of the surface vault (GS-13) to allow comparison with the NORESS spectrum. Neither of the average spectra fit the NORSAR model particularly well. In fact, no simple power law, f^{-n}, describes the data spanning the frequency bands covered by the two spectra. However, the KKL spectrum decreases steadily over its frequency band, and decays approximately like f^{-4} between 2 and 30 Hz. The average spectra follow the NORSAR model closely only over narrow bands (8 to 20 Hz for NORESS, and 4 to 10 Hz for KKL). At higher frequencies (above 20 Hz for NORESS and above 10 Hz for KKL) the spectra decay slower than f^{-5}. The NORESS average spectrum has a pronounced minimum at 4 Hz which provides a window with high potential for signal detection.

In the 2 to 40 Hz band the NORESS spectrum is equal to or smaller (by at most 10 dB) than that for KKL. The KKL spectrum is clearly smaller (up to about 10 dB) than the NORESS spectrum outside this band at lower, as well as at higher, frequencies. The NORESS spectrum is also equal to or below the NORSAR model for frequencies less than 20 Hz. Above 20 Hz the NORESS spectrum increases relative to the NORSAR model and at 50 Hz there is about a 10 dB difference. The KKL spectrum is equal to or below the NORSAR model at lower frequencies, and becomes larger than the NORSAR model at about 10 Hz.

Horizontal Components

The analysis so far has only been concerned with noise of the vertical components. The average spectral ratios of the horizontal components to the vertical component (i.e., $\hat{p}_{EW}(f)/\hat{P}_Z(f)$ and $\hat{p}_{NS}(f)/\hat{p}_Z(f)$) of NORESS are plotted in *Figure 8*. Apart from narrow peaks, which are discussed in the following paragraph, the ratios for the two horizontals are quite similar. There is slightly more power in the horizontal components than in the vertical component up to 25 Hz. Beyond 25 Hz the horizontal levels are smaller than the vertical level, and at 50 Hz they are almost a

COMPARISON OF NORESS AND KKL
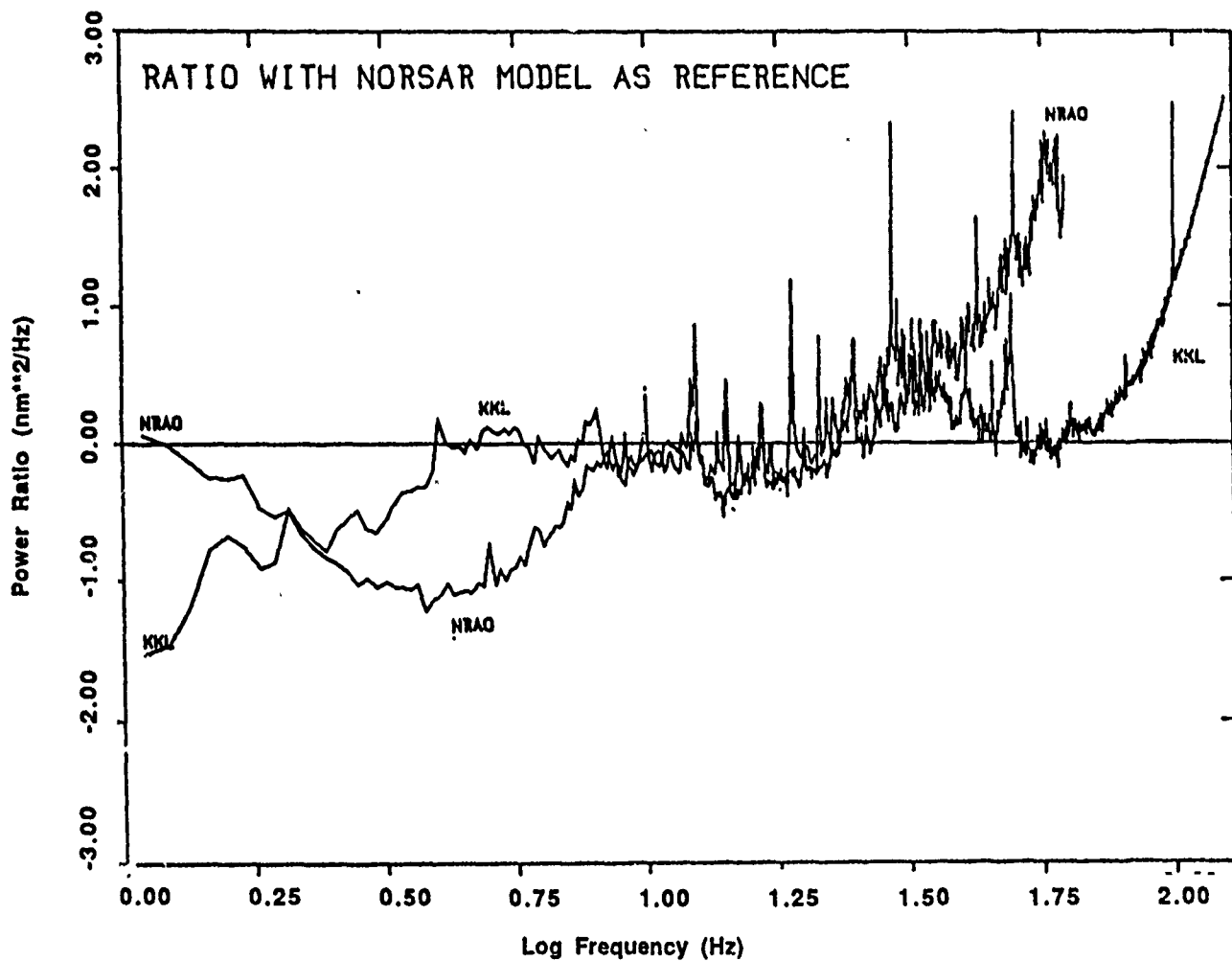
Figure 7. Power spectra from GS-13 data at NORESS and KKL divided by the NOR-SAR noise model.
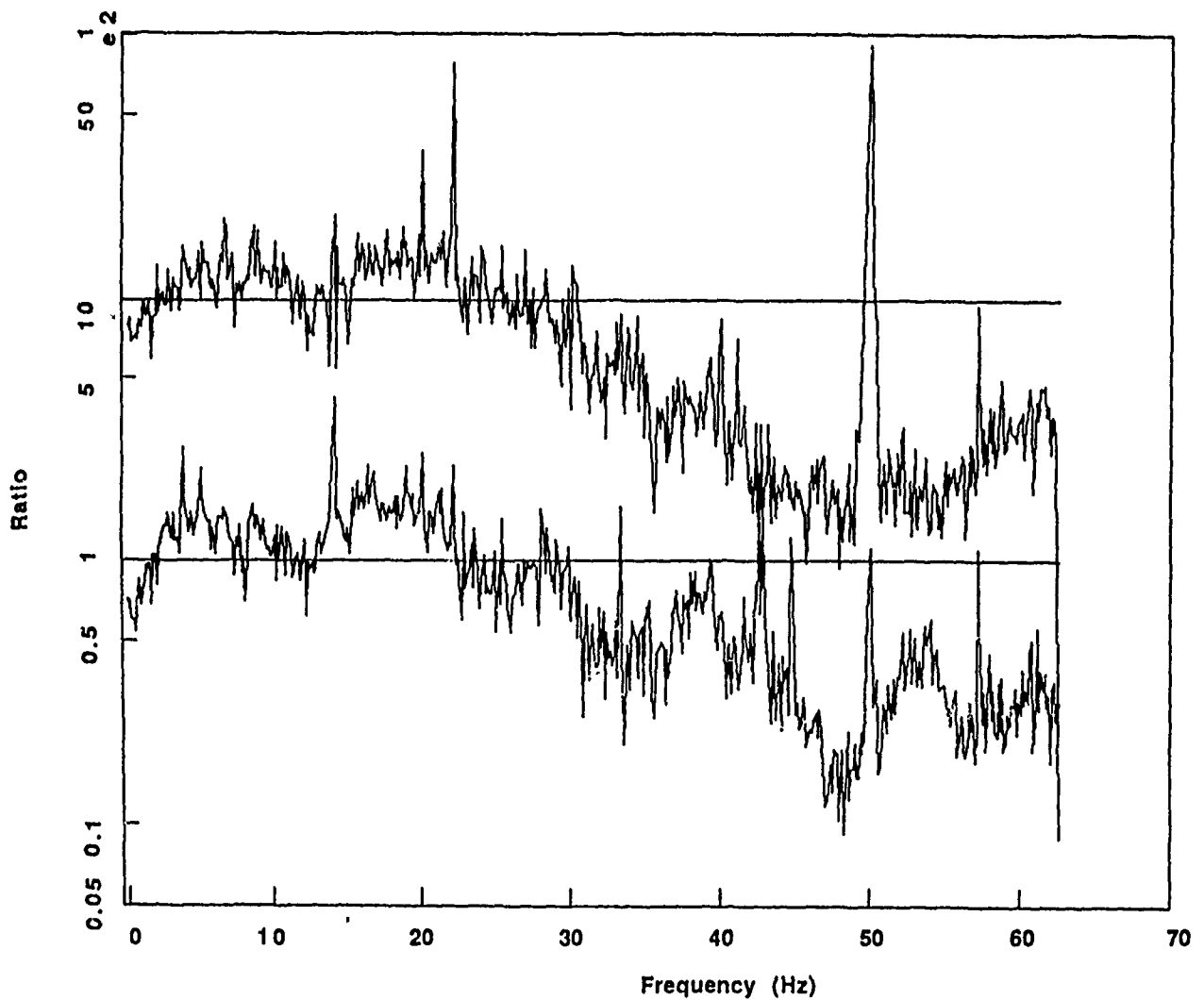
Figure 8. Ratios of the horizontal-to-vertical component power spectra from data recorded at NORESS. The E/Z ratio is offset + 10 dB relative to the N/Z ratio for clarity.

2-14

factor of ten below that of the vertical.

The horizontal-to-vertical ratios for the surface instruments at KKL (*Figure 9*) are similar to the NORESS ratios, but after reaching a minimum around 40 Hz, the difference becomes smaller with increasing frequency. At 80 Hz (corner frequency of the anti-aliasing filters) the ratios are close to one.

The power spectra (ground velocity) of the the horizontal component data from the borehole instruments are constant (white noise) above 30 Hz (see *Figure 10)*, and they are therefore assumed to have a high system noise in this frequency band.

Narrow Peaks

One of the most significant features of the average power spectra is a suite of narrow peaks. The number of peaks varies between 15 and 20 among the instrument components analyzed here. Such narrow peaks in the noise spectrum are often observed at frequencies above 1 Hz. Berger *et al.* (1988) noted that some peaks of the NRDC stations were persistent over time, whereas others appeared to come and go. The peaks here represent averages over 4 to 12 hours. Noise peaks are seldom analyzed in detail since it is felt that they should not in general obscure broadband signals of interest. The peaks are mostly associated with instrumental effects. For example, studies of peaks in noise spectra at the RSTN stations based on comparisons between surface and downhole sites lead to the conclusion that the source of many of these peaks might be related to unknown vibrations of the equipment at the site itself (Rodgers *et al.*, 1987). However, peaks with frequencies around 5 Hz and below have also been related to actual ground motion generated by nearby hydroelectric power plants (Hjortenberg and Risbo, 1975).

Using the the spectrum from the S-750 vertical data at KKL in *Figure 11* as a starting point, we discuss briefly the nature of the spectral peaks of the data analyzed here for NORESS and KKL. Some of the peaks can be related to the 50 Hz power lines, which seems to give rise to a series of peaks at lower and higher frequencies. The frequencies of the series can be summarized by the formula for a geometric series: $f_n = f_0 \cdot 2^{n-1}$, with $f_0 = 6.25$ and $n = 1,...,5$. Only one of the nine instrumental components (the vertical GS-13 at KKL) is free from a 50 Hz peak in the spectrum. For the S-750 data, other similar series of peaks can be identified with $f_0 = 2$; $n = 1,...,6$; and $f_0 = 10$; $n = 1,...,4$. The origin of these series is less obvious, but it seems reasonable to assume that it is caused by instrumental resonances rather than actual ground motion. In fact, 14 peaks of the spectrum in *Figure 11* are described by these three series. There are only three other prominent peaks that are not described by any of these series. These peaks occur at 28 and 34 Hz (seen also in the GS-13 data at KKL; *Figure 12)* and at 45 Hz (not seen in the GS-13 data;
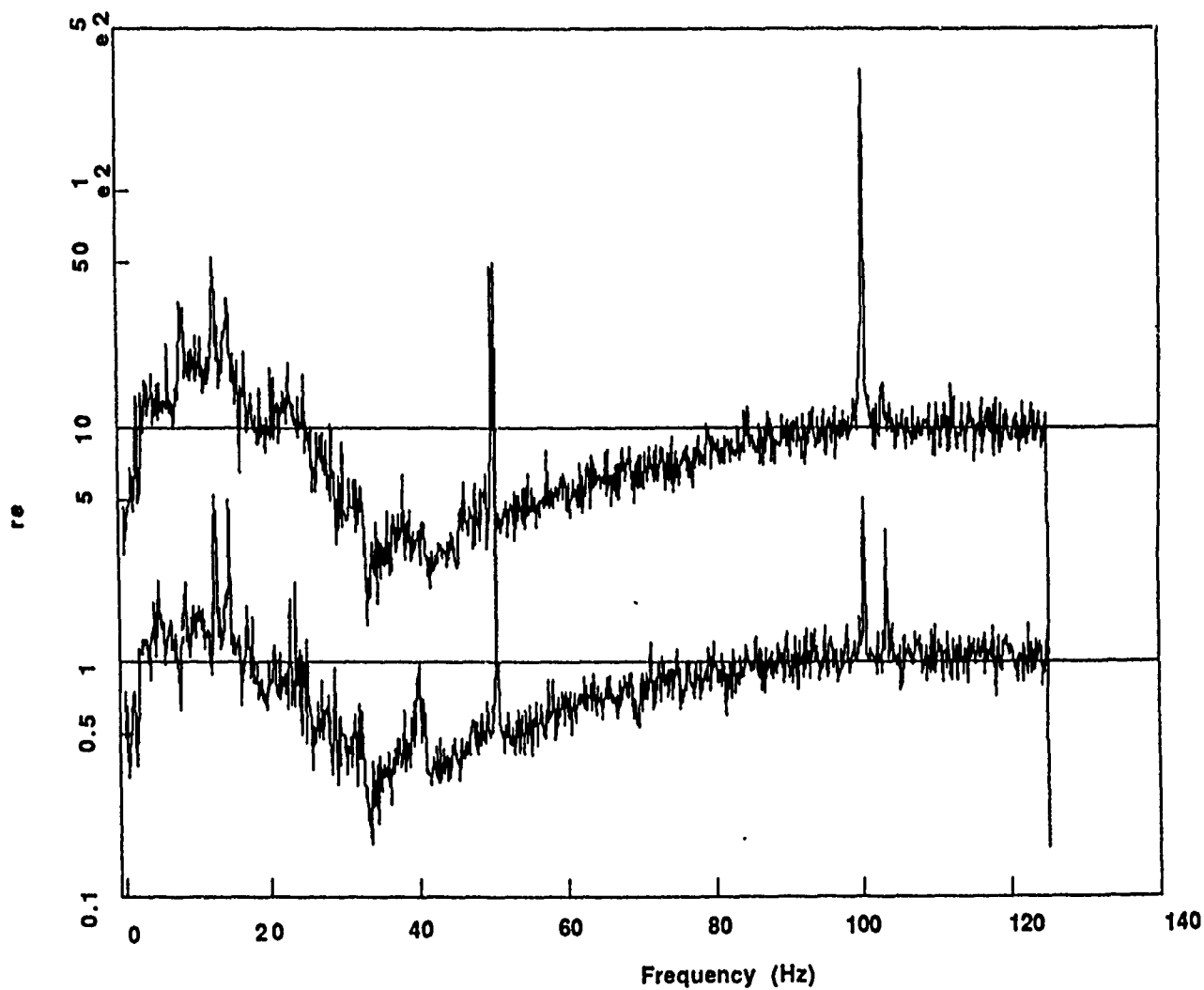
Figure 9. Ratios of the horizontal-to-vertical component power spectra from GS-13 data recorded at KKL. The E/Z ratio is offset + 10 dB relative to the N/Z ratio for clarity.

Figure 10. The power spectra of horizontal and vertical component data from the S-750 instruments at KKL. The spectra for the horizontals are essentially flat beyond 30 Hz.

Narrow peaks at frequencies: $f_n = f_0 \cdot 2^n$

Figure 11. The average power spectrum of the S-750 vertical component data at KKL. Frequencies of the geometric series $f_n = f_0 \cdot 2^n$ for $f_0 = 2, 6.25, 10$ Hz are marked as vertical lines.

COMPARISON OF PEAKS

Figure 12. Average power spectra of all components at KKL and NORESS displayed in the frequency band 4 to 55 Hz for comparison of frequencies of spectral peaks. Spectra are offset for clarity.

Figure 12). The 28 and 34 Hz peaks could be due either to resonances of the recording system, which is common to the KKL instruments, or to ground vibrations. The peak at 45 Hz can probably be related to the S-750 instrument itself, since if it were caused by ground motion, such a prominent amplitude should have appeared on the nearby surface vault instruments also. None of these three peaks are observed in the NORESS noise spectra (see *Figure 12*).

Peak series with frequencies described by the doubling formula with $f_0=2$ and 10 do not appear in the NORESS spectra, which contain three dominant peaks at frequencies of 19, 29, and 43 Hz. These peaks, "unique" to NORESS, have been associated with electronic interference of the fans in the surface vault, but they have also been noticed on noise spectra of the early borehole installation at NORESS (Fyen, 1987). Two of the peaks of the NORESS spectra (14 and 17 Hz) are also found in the spectra of the horizontal data from the GS-13 and S-750 instruments at KKL, but cannot be seen in the spectra of the vertical component S-750 at KKL. In addition, less prominent peaks at 20 and 40 Hz are common to all horizontals (including those of the S-750) of the two stations. There appear to be no peaks that are specific to the GS-13 instruments.

In conclusion, it appears that many of the narrow peaks, which constitute a dominant feature of the noise spectra, are generated by non-linear mechanical and electrical process of the instruments and the recording systems. This is indicated by the occurrence of clear peaks at the 50 Hz power line frequencies and the associated suite of subharmonic peaks. Period doubling phenomena have been observed for a variety of dynamical systems. Such period doubling starts out with oscillations at a fundamental frequency, and as some system parameter is changed the period of the oscillations is doubled (Moon, 1987).

2.1.5 Concluding Remarks

In this note we compare power spectra of seismic noise recorded during *quiet* periods at the high-frequency element of NORESS and the NRDC high-frequency station KKL in the Soviet Union.

- The power spectrum of the vertical component surface noise data at NORESS is equal to or smaller than that of KKL in the frequency band 2 to 40 Hz. The largest difference between the two stations is about 10 dB and occurs at around 4 Hz. At frequencies below 2 Hz and above 40 Hz the KKL spectrum is up to 10 dB below that at NORESS. Both spectra are equal to or smaller than the NORSAR noise model, f^{-5}, at frequencies less than 10-20 Hz. At higher frequencies the two spectra are up to 10 dB above the NORSAR model.

- The decay of the power spectra with frequency does not follow a simple power law throughout the instrumental bands. For example, the NORESS spectrum has a pronounced minimum at 4 Hz, which may be utilized as a window for

signal detection.

- The power spectra of the horizontal component noise data are found to be lower than those of the vertical components at frequencies between 25 to 50 Hz.

- The borehole instrument at KKL seems to provide the largest noise reduction (6 dB or so) relative to the surface instrument at frequencies in the band from 10 to 30 Hz.

- The noise spectra from data for all instrument components are dominated by 15-20 narrow peaks at frequencies above 1 Hz. Many of these peaks can be described by the formula for a geometric series and appear to be generated by non-linear mechanical and electrical processes of the instruments and their recording systems. Such peaks impose limits for detection of weak signals of interest in test ban monitoring.

Hans Israelsson

References

Berger, J., H. Eissler, F.L. Vernon, I.L. Nersesov, M.B. Gokhberg, O.A. Stolyrov, and N.D. Tarasov, (1988). Studies of High-Frequency Seismic Noise in Eastern Kazakhstan *Bull. Seism. Soc. Am.*, Vol. 78, pp. 1744-1758.

Bungum, H., S. Mykkeltveit, and T. Kvaerna (1985). Seismic Noise in Fennoscandia, with emphasis on high frequencies, *Bull. Seism. Soc. Am.* Vol. 75, pp. 1489-1513.

Durham, H. B. (1986). Response estimates for GS13 or S3 seismometers plus EDME digitizer, *Sandia National Laboratories, 0311 6 March 1986*

Fyen, Jan (1987). NORESS noise spectral studies - Noise level characteristics, *Semi-annual Technical Summary 1 October 1986 - 31 March 1987*, pp 46-58.

Herrin, Eugene (1982). The resolution of seismic instruments used in treaty verification, *Bull. Seism. Soc. Am.* Vol. 72, pp. S61-S68.

Hjortenberg, E., and T. Risbo (1975). Monochromatic Components of the Seismic Noise in the NORSAR Area, *Geophys. J. R. astr. Soc.* Vol. 42, pp. 547-554.

Kromer, R. P. (1985) An overview of the NRSA high-frequency seismic element (HFSE), *Sandia National Laboratories, Systems Research Division 311 Aug 1985*

Li, T.M.C., J.F. Ferguson, E. Herrin, H.B. Durham (1984). High frequency seismic noise at Lajitas, Texas, *Bull. Seism. Soc. Am.* Vol. 74, pp. 2015-2033.

Moon, Francis, (1987) Chaotic Vibrations, *John Wiley & Sons, New York, 309 pp.*

Rodgers, Peter W., Steven R. Taylor, and Keith K.Nakanishi (1987) System Noise in the Regional Seismic Test Network from 0.1 to 20 Hz, *Bull. Seism. Soc. Am.* Vol. 77, pp. 663-678.

3.1 ESTIMATING SPECTRAL SCALING OF SOURCE SPECTRA

3.1.1 Introduction

A frequently used simplified model for the amplitude displacement spectrum of an earthquake recording in the far field is characterized by a constant level at low frequencies (equal to the seismic moment, M_0 at zero frequency) up to a corner frequency, beyond which it drops fast with increasing frequency.

Several models have been proposed to represent the spectral rolloff at higher frequencies and the scaling of corner frequency with seismic moment. Chael (1987) and Chael and Kromer (1988) used a forward-modelling approach to select a model that best fit observations from earthquake suites in New Brunswick and Western Norway. Spectral ratios for observations were compared with a few theoretical models. Although such comparisons show convincing support for models with a rolloff proportional to frequency squared, it may not be possible to make a clear choice between models for different scaling of the corner frequency (Chael, 1987).

In this note we present an approach to *estimate* the rolloff and the scaling parameter directly from the data rather than trying to *choose* from comparisons with a few theoretically calculated models. We use the ratio model introduced by Chael (1987) as a basis and formulate the estimation problem as a non-linear weighted least squares procedure. The procedure is also tested on some synthetic examples with varying degrees of noise added.

3.1.2 Source Models

Following Chael (1987) the amplitude displacement of the source spectrum can be written as:

$$|S(\omega)| = \frac{b \cdot M_0}{\left[1 + \left(\frac{\omega}{\omega_0}\right)^2\right]^{\gamma/2}}$$

where b is a constant and M_0 the seismic moment. Rolloff values of $\gamma=2$ and 3 have been used in the literature. The corner frequency, ω_0, scales with the seismic moment as:

$$\omega_0 = \frac{k}{M_0^{1/\delta}}$$

k is a constant, which depends on the value of δ, which in turn is assumed to be 3 and 4 for constant and increasing stress drop models respectively.

The ratio of the power spectra of events with seismic moments M_{01} and M_{02} and with the same source model can be written as:

$$R_{21}(\omega) = \left(\frac{M_{02}}{M_{01}}\right)^2 \cdot \left[\frac{\left\{1+\left(\frac{\omega}{\omega_{01}}\right)^2\right\}}{\left\{1+\left(\frac{M_{02}}{M_{01}}\right)^{2/\delta} \cdot \left(\frac{\omega}{\omega_{01}}\right)^2\right\}}\right]^\gamma$$

Here ω_{01} is the corner frequency of event with moment M_{01}. Using a suite of events with different moments at the same hypocenter we formulate a procedure to estimate the parameters γ and δ. We assume that we know only the moment of the largest event. This means that in addition to the rolloff and scaling parameter, the corner frequency of the largest event and the moments of the other events are estimated as well.

3.1.3 Weighted Least Squares Formulation

We assume that we have a suite of J events and then calculate the spectral ratios, r_{ij}, with $j=1,...J-1$ between the reference event (J) and the $J-1$ unknown events for frequencies ω_i with $i=1,...,I$. For each ratio value there is also a weighting factor, w_{ij} which is equal to 1 if the signal to noise ratios for the two amplitude spectra of the ratio are greater than a certain preset threshold, otherwise it is equal to 0.

We also assume that we know the moment of the largest event (M_{0J}) in the suite of events that is considered. Now we form the least squares sum:

$$Q = \frac{1}{\sum\limits_{i=1,j=1}^{I,J-1} w_{ij}} \cdot \sum_{i=1,j=1}^{I,J-1} w_{ij} \cdot \left(\log(r_{ij}) - \log f(\delta,\gamma,\omega_{0J},m_{0J},\omega_i)\right)^2$$

where:

$$\log f(\delta,\gamma,\omega_{0J},m_{0J},\omega_i) = 2\cdot\log(m_{0J})\cdot\gamma\cdot\left(\log\left[1+\left(\frac{\omega_i}{\omega_{0J}}\right)^2\right] - \log\left[1+m_{0J}^{2/\delta}\cdot\left(\frac{\omega_i}{\omega_{0J}}\right)^2\right]\right)$$

Here ω_{0J} is the corner frequency of the largest event, and the parameters:

$$m_{0j} = \frac{M_{0j}}{M_{0J}}$$

We try to find values of $\delta, \gamma, \omega_{0J}$, and m_{0j} so that Q is minimized. These values are then our estimates.

In order to minimize Q, we use an IMSL algorithm based on the quasi-newton method (zxmwd: see IMSL, 1982) to find the values of the parameters that are estimated for a global minimum of Q with constraints on the parameter values.

3.1.4 Examples With Synthetic Data

The algorithm described above was applied to some examples of synthetic data. The moment of the main event was set to $2.4 \cdot 10^{24}$ dyne-cm and moment ratios of this event to three other smaller events were assumed to be 0.5, 0.2, and 0.1. Noise generated with a Gaussian random number generator was added to spectra prior to forming the ratios. Spectra were computed for $\gamma=2,3$ and for $\delta=3,4$. The ratios for these four cases are shown in *Figures 1-4*

Using the frequency band of 1-30 Hz with ratio values every 0.1 Hz the following estimated values were obtained:

COMPARISON OF TRUE AND ESTIMATED VALUES

Parameter	True	Estimated			
-	Value	2-3	2-4	3-3	3-4
ω_{0J}	0.70	0.690	0.675	0.723	0.689
m_{01}	0.20	0.196	0.195	0.205	0.197
m_{02}	0.10	0.097	0.097	0.102	0.098
m_{03}	0.05	0.048	0.048	0.049	0.048
γ		2.008	1.934	3.159	2.959
δ		2.993	3.814	3.161	3.932
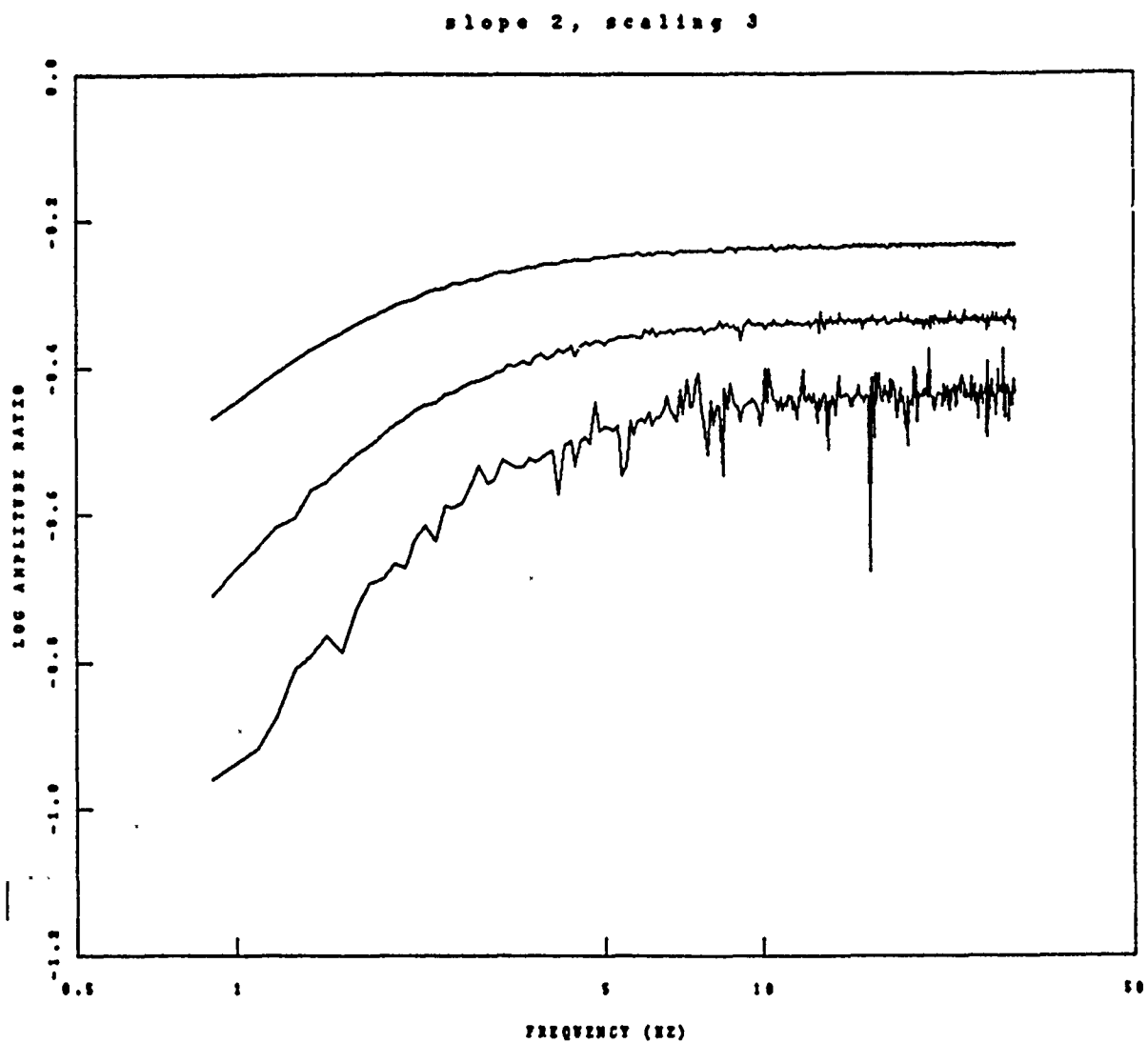
Figure 1. Spectral ratios for five events with rolloff 2 and scaling factor 3. The moment of the largest event, $2.4 \cdot 10^{24}$ dyne-cm, and the ratios to the smaller events are 0.5, 0.2, and 0.1. Random noise has been added to the power spectra before forming ratios.
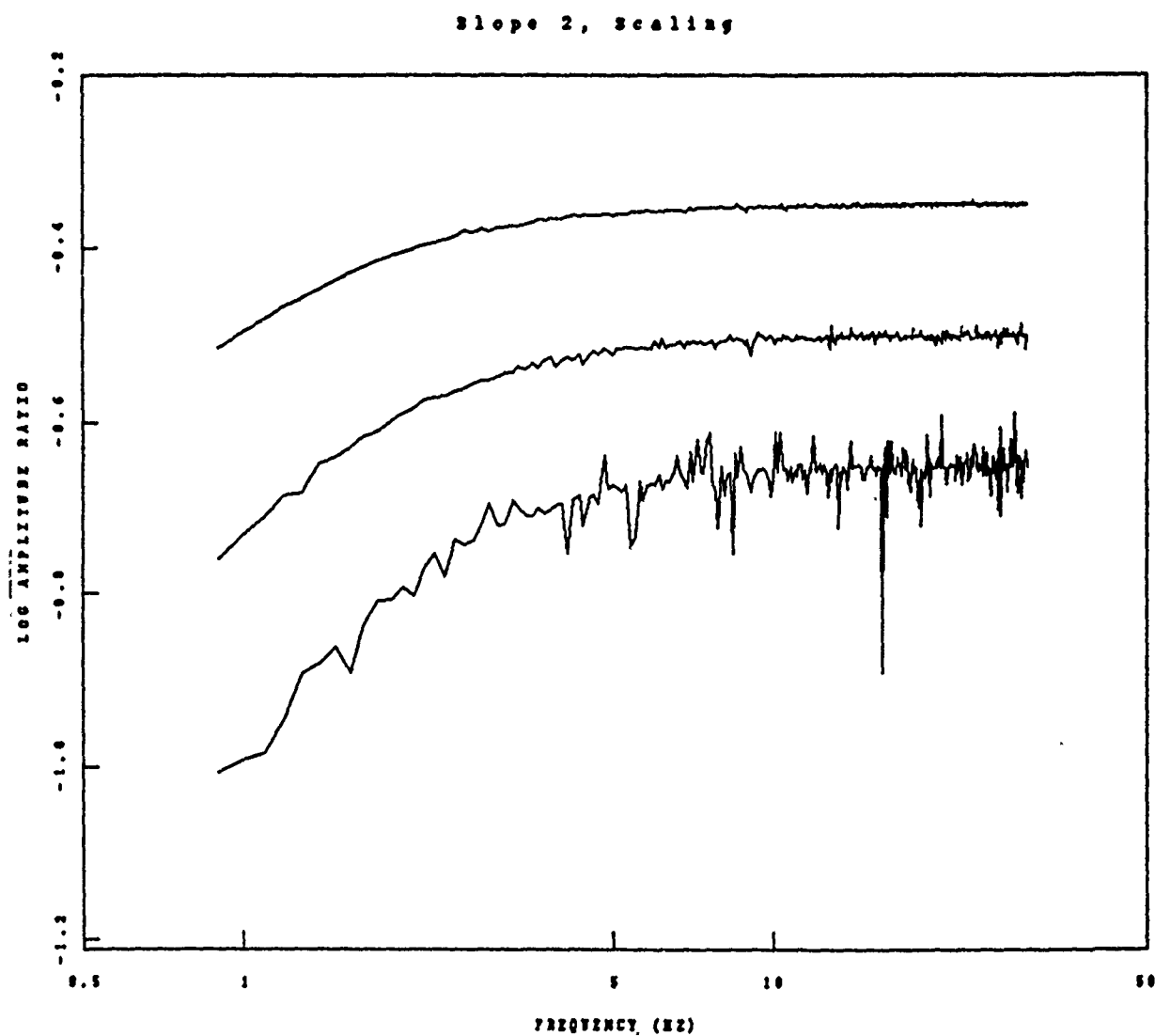
Figure 2. Spectral ratios for five events with rolloff 2 and scaling factor 4. The moment of the largest event $2.4 \cdot 10^{24}$ dyne-cm, and the ratios to the smaller events are 0.5, 0.2, and 0.1. Random noise has been added to the power spectra before forming ratios.
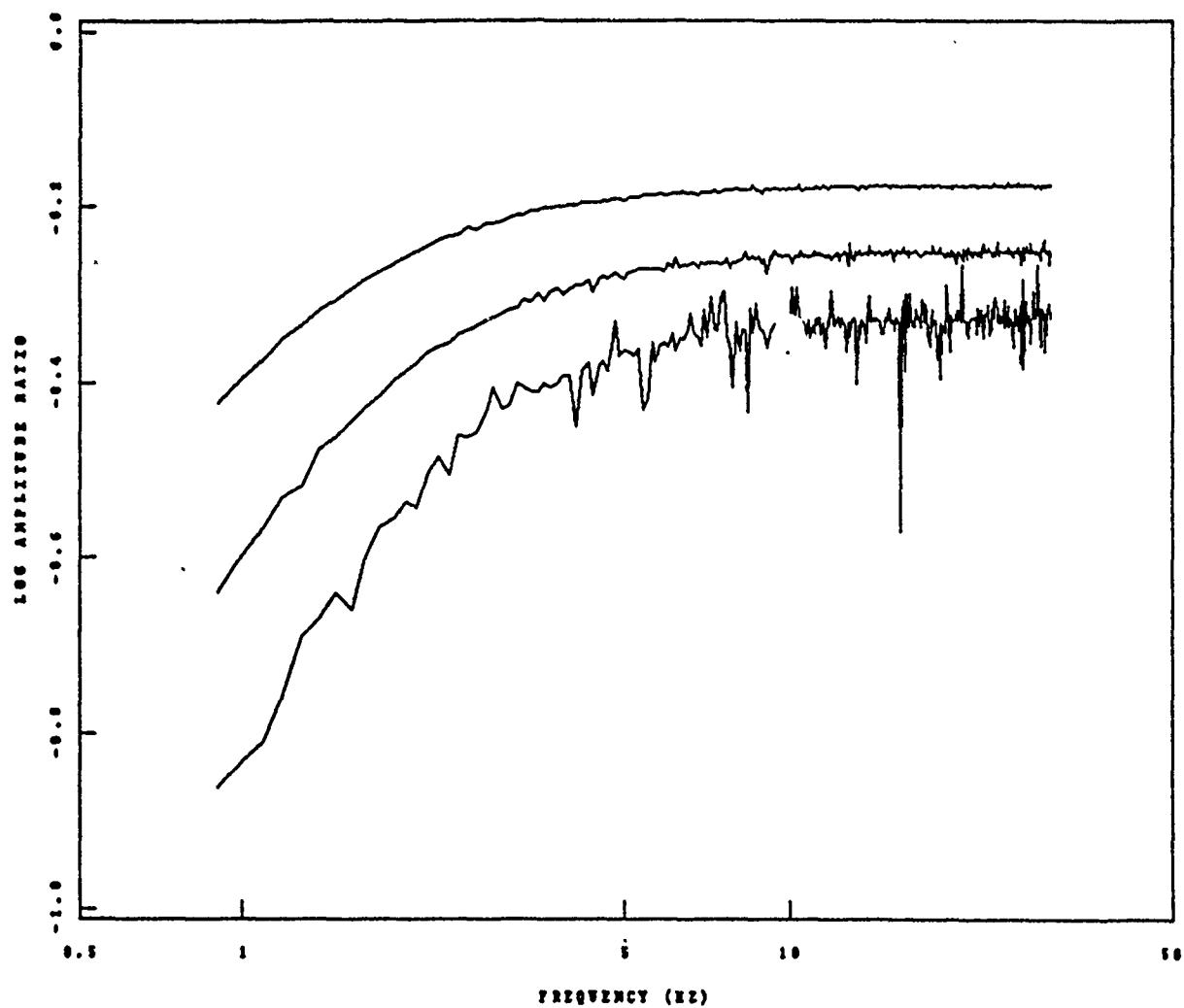
Figure 3. Spectral ratios for five events with rolloff 3 and scaling factor 3. The moment of the largest event $2.4{\cdot}10^{24}$ dyne-cm, and the ratios to the smaller events are 0.5, 0.2, and 0.1. Random noise has been added to the power spectra before forming ratios.

3-6
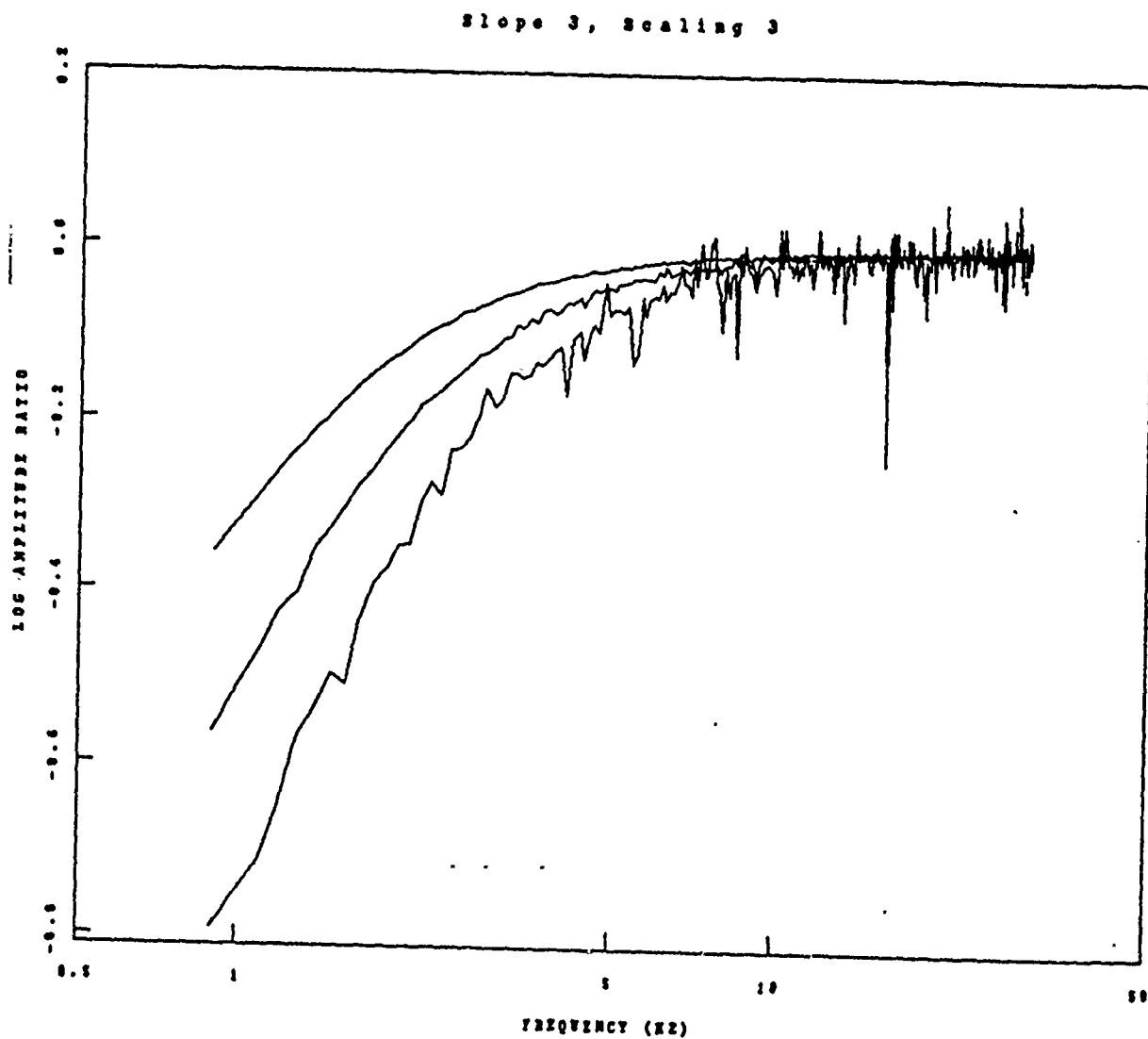
Figure 4. Spectral ratios for five events with rolloff 3 and scaling factor 4. The moment of the largest event $2.4 \cdot 10^{24}$ dyne-cm, and the ratios to the smaller events are 0.5, 0.2, and 0.1. Random noise has been added to the power spectra before

3-7

3.1.5 Comments

In this note we presented a procedure to estimate the rolloff and scaling parameter for corner frequency-seismic moment from spectral ratios of a suite of events at the same location and of the same type of source function. If the seismic moment of one (usually the largest event) is known, seismic moments for the other events can be estimated, as well as the corner frequency for the event with known moment. Corner frequencies for the other events can be obtained directly from the other estimated parameters.

Hans Israelsson

References

Chael, Eric P. (1987) Spectral Scaling of Earthquakes in the Miramichi region of New Brunswick *Bull. Seism. Soc. Am.* Vol. 77, pp. 347-365.

Chael, Eric P. and Richard P. Kromer (1988) High Frequency Spectral Scaling of a Main Shock/Aftershock Sequence near the Norwegian Coast *Bull. Seism. Soc. Am.* Vol. 78, pp. 561-570.

IMSL, (1982) IMSL Library LIB-009 Houston, Texas.

4.1 WAVEFORM CORRELATION OF CLOSELY SPACED REGIONAL EVENTS

4.1.1 Introduction

In regional seismic monitoring one sometimes distinguishes between *model* based and *case* based approaches to identify seismic events (Dysart and Pulli, 1987). The model based approach aims at defining some discriminant from the recorded waveforms that will in general identify events regardless of region. The discriminant should also relate to the physics of various seismic source types, like the ratio of radiated P and S wave energy. In spite of a number of studies, no single model based method has so far been defined that performs successfully regardless of region.

In contrast, the case based approach attempts to take advantage of the repeatability of records from events in the same source area for location and identification. Similarities of waveforms recorded from closely spaced sources have been reported for several regions in the literature. For example, seismograms recorded at NORESS from several events events at the Titania mine (400 km distance) showed remarkable similarity in time history (Jurkevics, 1987). Records are not only consistent for a particular area, but may also be distinct from those at nearby locations. In the western USSR (about 1000 km from NORESS) marked differences have been observed between records at NORESS of events at neighboring mines only 25 km apart (Suteau-Henson and Bache, 1988). From visual inspection of recordings of mining explosions, experienced analysts have even been able to pinpoint the particular mine of origin. The case based approach is thus based on knowledge acquired from the recordings of many events from a particular area, and a new event is identified by waveform comparisons with events previously recorded in the region.

Even if waveform repeatability has been observed in several cases, it seems that the case based approach has not yet been fully explored. In particular, if one considers that the number of observations used to demonstrate repeatability is usually quite small (i.e., a handful compared to the total number of regional events detected and located). The NORESS array, for example, reports an average about 30 events on a working day. The purpose of this note is to study repeatability and patterns of regional records from a fairly large number of events within a small area. An attempt is made to utilize automatic procedures to compare and group seismic waveforms.

4.1.2 Effects and Waveform Data

The seismic events used in this study were all located within a small region, 50 by 200 km, in Central Sweden. In fact, this region has the highest density of events

detected and located by NORESS. Most of the events are located in mining districts and are presumed to be ripple fired quarry blasts.

The High Frequency Element

Because of the current interest in high frequency recordings and short epicentral distances (around 200 km), data recorded at the high frequency element of NORESS were selected for the analysis. Two types of instruments have so far been used for high frequency recordings, and the analysis here is based on data recorded with only one of them, Teledyne Geotech GS-13 seismometers installed in a surface vault at the central elements (NRAO) of the array. These inst...ᵉnts with associated recording systems have responses that are essentially flat to ground velocity in the frequency band 2-50 Hz, and the data sampling rate was 125/sec.

Evert Selection

A total of about 1500 events were detected and located by NORESS in central Sweden between January 1, 1986 and June 30, 1988. About 1000 of these were detected when the GS-13 instruments were in operation, and digital data were available at the NORESS high frequency waveform database at the Center for Seismic Studies for about 700 of these events. Waveform data for 222 events were selected from the database and reviewed with regard to data quality. In order to minimize tape handling, this selection was based on the number of events available on each tape of the database. In the review process 85 events were rejected for various reasons (e.g., insufficient SNR, spikes in the data, uncertainties about horizontal components). This left 137 events to be used in the analysis.

Epicenters and magnitudes, *ML*, reported in the NORESS bulletin for these events are listed in *Table 1*. The relative locations of the events are illustrated in the perspective diagram of *Figure 1*. None of the events were reported in seismic bulletins based on local station networks in Fennoscandia, and the epicentral accuracy is limited by the location accuracy of the array. The uncertainty of a NORESS location is in turn determined by the uncertainties in the backazimuth and distance determinations, discussed in the following section. The magnitude distribution of the events is shown by a histogram and normal distribution plot in *Figure 2*, which indicates that *ML* has a median of 1.2, ranges between 0.8-2.1, and is approximately normally distributed for *ML*<1.5. For comparison, relative P and S wave amplitudes in the 2.5-4.0 Hz frequency band are plotted in *Figure 2* as well. There is some scatter in the P/S wave amplitude ratio, which ranges almost over half an order of magnitude, indicating considerable variation among the waveforms.

TABLE 1									
	Date			Time		Epicenter		ML	Event
Year	Month	Day	Hour	Min	Sec	Lat(N)	Long(E)	-	#
86	12	17	11	47	39.1	59.9	14.7	1.3	1
86	12	17	16	29	40.7	59.9	14.7	1.1	2
86	12	17	19	13	49.4	59.9	14.9	1.2	3
86	12	18	2	2	5.4	60.0	14.8	1.5	4
86	12	18	11	48	26.9	59.9	14.7	1.6	5
86	12	18	11	52	30.4	60.3	15.0	1.3	6
86	12	30	10	22	6.6	59.9	14.7	1.2	7
86	12	˙0	11	43	9.7	59.9	14.8	1.3	8
86	12	30	18	26	25.4	59.7	14.5	1.2	9
86	12	30	18	45	12.0	60.3	15.0	1.1	10
87	1	22	9	27	19.6	60.3	15.1	1.0	11
87	1	22	11	35	29.4	60.1	15.0	1.1	12
87	1	22	15	0	13.2	59.8	14.5	1.0	13
87	1	22	19	5	14.4	59.9	14.7	1.4	14
87	2	18	11	55	31.7	60.0	14.7	1.4	15
87	2	18	19	8	32.5	60.3	15.1	1.0	16
87	3	3	11	53	41.1	59.9	14.8	1.3	17
87	3	3	19	16	20.8	60.0	14.7	1.0	18
87	3	3	22	50	34.8	60.0	14.9	1.0	19
87	3	4	2	3	56.3	59.9	14.7	1.2	20
87	3	4	11	55	1.5	59.9	14.7	1.6	21
87	3	4	12	57	23.7	60.8	15.1	2.1	22
87	3	4	15	27	27.7	59.9	14.7	1.2	23
87	3	6	1	58	58.6	60.3	15.1	1.2	24
87	3	6	14	56	53.2	60.1	14.9	1.1	25
87	3	6	18	40	0.8	60.7	15.1	1.0	26
87	3	6	19	3	42.6	59.9	14.7	1.0	27
87	3	13	6	1	22.0	60.2	14.9	1.3	28
87	3	13	7	10	44.3	59.9	14.7	1.1	29
87	3	13	11	34	58.1	59.8	14.7	1.3	30
87	3	13	17	22	15.0	59.9	14.8	1.0	31
87	3	13	17	28	28.9	60.2	14.9	1.0	32
87	3	17	9	56	8.6	60.7	15.2	1.2	33
87	3	17	10	15	57.1	61.0	15.2	1.4	34
87	3	17	15	5	59.9	60.1	14.8	1.6	35
87	3	17	15	23	14.1	59.9	14.7	1.2	36
87	3	24	23	31	31.5	60.1	15.0	0.9	37
87	4	21	9	36	45.8	60.8	15.1	1.9	38
87	4	21	14	23	10.4	60.7	15.2	1.1	39
87	4	21	17	10	8.1	59.9	14.7	1.1	40
87	4	24	6	58	48.1	60.2	15.1	1.1	41
87	4	24	10	31	13.8	59.8	14.7	1.1	42
87	4	24	17	41	53.3	60.0	14.8	0.8	43
87	4	29	16	32	9.6	59.7	14.4	1.1	44
87	5	19	7	23	19.5	60.7	15.3	1.1	45
87	5	19	23	9	30.8	60.0	14.9	1.2	46

TABLE 1 (Cont.)									
	Date			Time			Epicenter		ML
Year	Month	Day	Hour	Min	Sec	Lat(N)	Long(E)	.	Event #
87	5	22	10	27	3.7	59.9	14.7	1.3	47
87	5	22	10	43	16.0	60.2	14.9	1.2	48
87	6	9	10	42	2.3	60.2	15.1	1.2	49
87	6	9	11	44	18.7	60.8	15.1	2.1	50
87	6	9	16	32	41.3	59.8	14.6	1.1	51
87	6	9	18	9	31.2	59.9	14.7	1.3	52
87	6	16	3	16	22.7	59.6	14.3	1.3	53
87	6	16	10	37	9.0	60.0	15.0	1.4	54
87	6	16	16	54	3.6	59.9	14.8	1.1	55
87	6	15	18	15	56.3	59.9	14.7	1.2	56
87	6	24	0	10	13.3	59.7	14.5	1.3	57
87	6	24	17	59	26.2	59.9	14.8	1.0	58
87	6	24	19	32	45.5	60.0	14.9	1.0	59
87	6	25	6	24	43.1	60.0	14.8	1.4	60
87	6	25	10	37	24.1	59.9	14.9	1.2	61
87	8	3	13	55	55.8	60.0	14.7	1.2	62
87	8	3	14	21	55.4	60.1	14.9	1.0	63
87	8	3	16	18	27.9	60.3	15.0	0.9	64
87	8	3	21	58	43.4	60.1	14.9	1.0	65
87	8	20	0	27	55.3	59.9	14.7	1.0	66
87	8	20	10	29	5.8	59.9	14.7	1.0	67
87	8	20	17	49	25.9	60.0	14.7	1.1	68
87	8	20	22	35	27.8	60.0	14.8	1.1	69
87	8	27	9	26	6.0	60.1	14.9	1.2	70
87	8	27	15	33	57.3	59.9	14.7	0.9	71
87	8	27	17	52	49.3	60.0	14.8	1.1	72
87	8	27	23	0	37.6	60.2	15.0	0.9	73
87	8	28	16	27	6.2	60.1	14.9	1.1	74
87	8	28	17	9	12.7	60.0	14.8	1.2	75
87	9	1	14	27	41.7	59.9	14.7	1.1	76
87	9	1	18	11	27.1	60.3	15.1	1.2	77
87	9	7	14	10	19.3	60.4	15.2	1.0	78
87	9	7	17	17	28.6	59.9	14.7	1.1	79
87	9	7	18	7	35.2	60.3	15.0	1.3	80
87	9	7	18	17	28.6	59.9	14.9	0.9	81
87	9	9	7	1	51.0	59.9	14.8	1.2	82
87	9	9	10	36	19.4	59.9	14.7	1.2	83
87	9	9	17	32	23.8	60.1	14.9	1.0	84
87	9	9	23	0	58.8	60.4	15.1	1.0	85
87	9	10	5	12	49.3	59.9	14.7	1.2	86
87	9	10	10	37	13.2	59.9	14.8	1.1	87
87	9	10	16	26	48.2	60.1	14.3	1.0	88
87	9	10	23	39	18.9	60.1	14.8	1.1	89
87	9	29	1	56	35.1	60.1	14.9	1.0	90
87	9	29	11	31	46.0	61.0	15.2	1.3	91
87	9	29	12	12	20.5	61.0	15.3	1.2	92

	TABLE 1 (Cont.)								
	Date			Time			Epicenter		ML	Event
Year	Month	Day	Hour	Min	Sec	Lat(N)	Long(E)	.	#
87	9	29	19	8	23.3	59.7	14.5	1.0	93
87	10	1	15	39	23.3	59.8	14.5	1.1	94
87	10	1	16	18	36.1	59.8	14.7	1.1	95
87	10	6	11	39	6.1	60.3	15.1	1.4	96
87	10	6	18	58	0.9	60.2	15.0	1.2	97
87	10	30	1	40	6.0	60.0	14.7	1.2	98
87	10	30	19	39	55.3	60.2	15.1	1.1	99
87	11	4	0	27	36.7	60.1	15.0	0.8	100
87	11	4	18	52	48.6	60.2	15.0	1.1	101
87	11	5	1	50	20.3	60.1	14.9	1.0	102
87	11	5	23	27	35.8	59.8	14.5	1.1	103
87	11	10	14	25	26.9	59.9	14.8	1.0	104
87	11	10	22	5	52.9	59.8	14.7	1.1	105
87	11	18	7	50	46.1	59.9	14.7	1.1	106
87	11	18	18	56	34.9	60.0	15.0	1.0	107
87	12	1	7	22	36.5	59.7	14.6	1.2	108
87	12	1	18	46	4.0	60.3	15.0	1.3	109
87	12	16	20	32	35.7	60.3	15.1	1.3	110
87	12	22	11	27	17.2	59.9	14.8	1.3	111
87	12	22	12	45	53.8	60.8	15.1	1.8	112
87	12	22	22	33	50.9	59.8	14.6	1.3	113
87	12	22	23	43	57.6	60.2	14.9	1.1	114
87	12	28	11	17	30.3	60.3	15.0	1.2	115
87	12	28	13	24	51.9	60.2	15.0	1.0	116
87	12	28	18	34	24.5	60.3	15.0	1.1	117
88	1	4	15	25	3.0	60.0	14.9	1.3	118
88	1	4	16	18	24.8	60.3	15.0	1.1	119
88	1	4	18	43	54.0	60.3	15.1	1.1	120
88	1	7	17	21	16.9	60.2	15.1	1.1	121
88	1	27	6	36	51.4	59.8	14.7	1.1	122
88	1	27	15	24	36.6	60.1	15.0	1.1	123
88	2	10	11	17	31.8	60.3	15.0	1.1	124
88	2	10	15	50	56.6	59.8	14.6	1.2	125
88	2	10	18	2	37.1	59.8	14.5	1.2	126
88	2	10	18	49	46.5	60.3	15.0	1.2	127
88	2	10	22	58	29.9	59.9	14.8	1.3	128
88	2	23	7	22	48.8	59.6	14.4	1.3	129
88	2	23	9	57	56.4	61.0	15.3	1.3	130
88	2	23	11	30	40.3	60.3	15.0	1.2	131
88	2	23	16	12	39.0	60.3	15.0	1.1	132
88	2	24	6	1	57.3	60.2	15.0	1.1	133
88	2	24	11	8	7.3	60.8	15.1	1.7	134
88	3	9	16	2	49.2	59.9	14.9	1.1	135
88	3	9	18	34	11.8	60.3	15.0	1.1	136
88	3	9	18	44	10.4	60.3	15.0	1.2	137
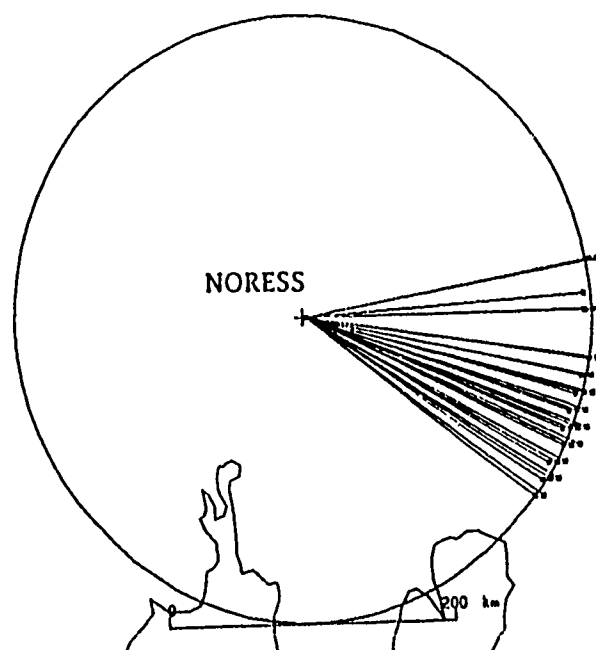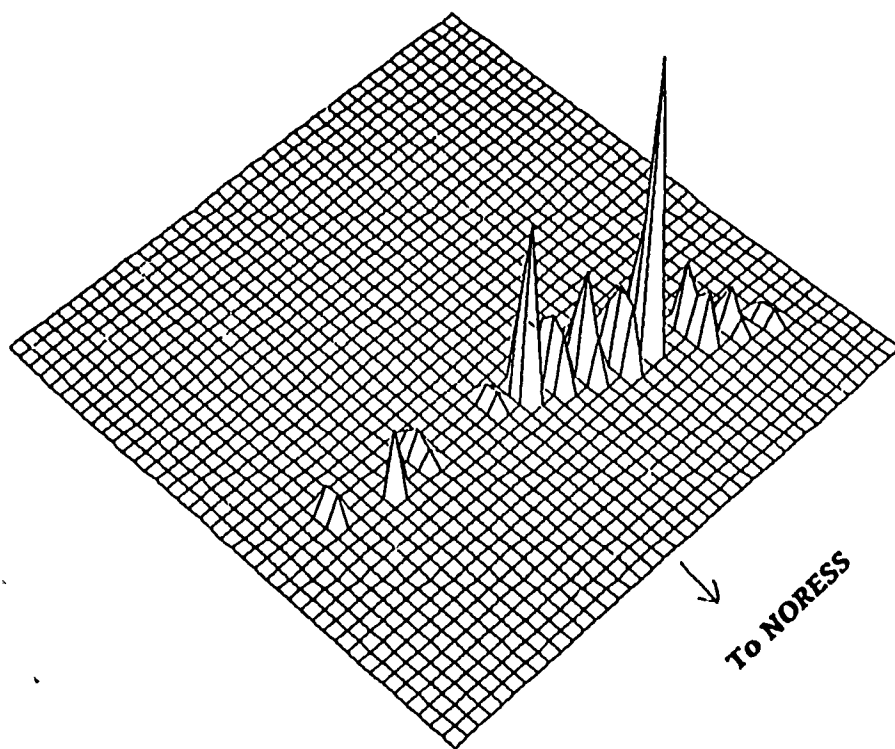
Figure 1. ⅰhe perspective diagram shows the density of the events studied. The maximum is 17 events and the cell spacing is 5 km. The map shows the paths to NORESS from the epicenters.
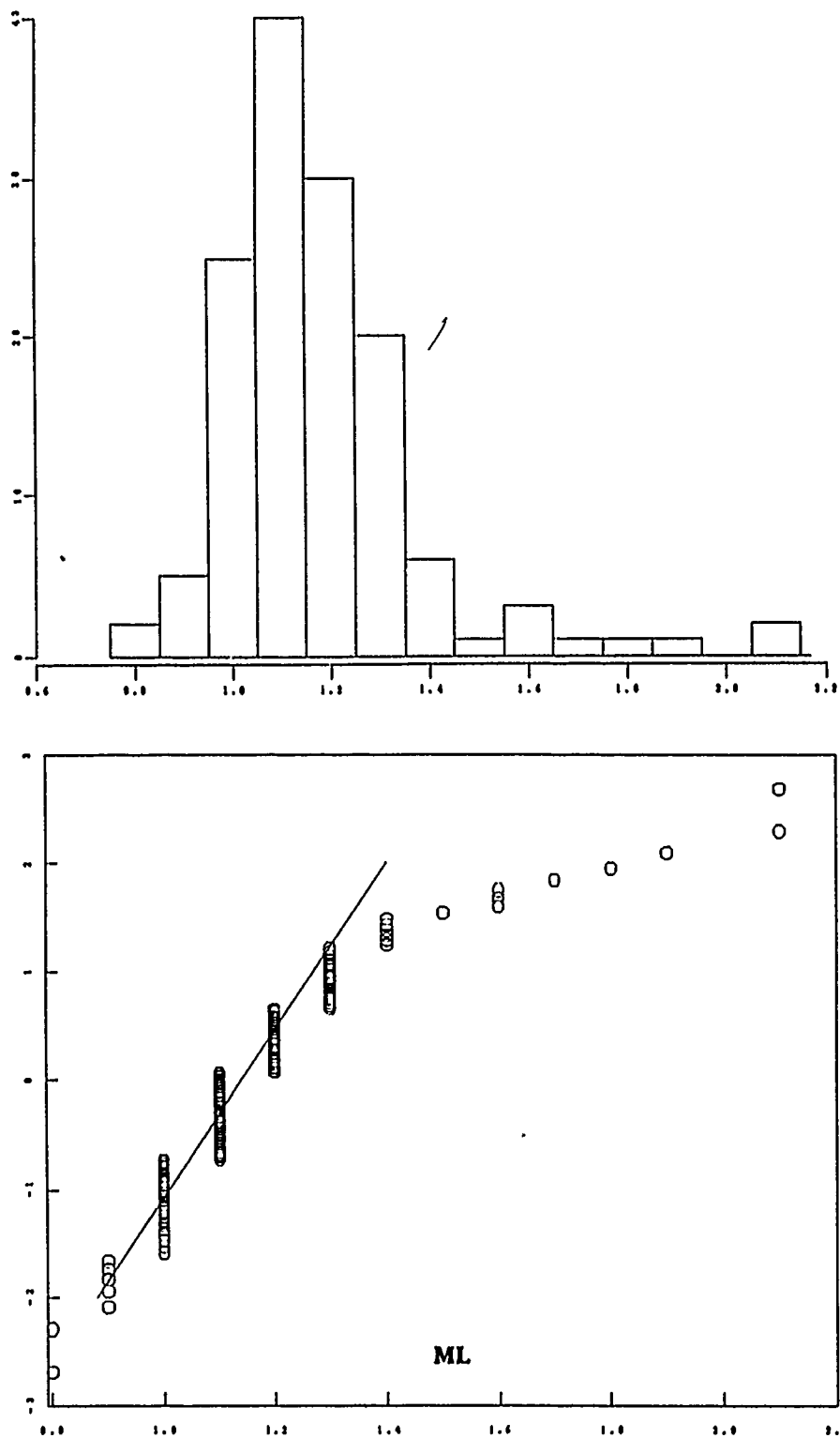
Figure 2. The histogram shows the number of events as function of magnitude. The plot of magnitude as a function of cumulative distribution follows approximates a normal distribution at magnitudes below 1.5. The straight line represents a normal distribution with a mean value of 1.14 and a standard deviation of 0.13 magnitude units. The scatter diagram shows the maximum amplitudes of P and S wave windows of vertical-component recordings in the band 2.5-4.0 Hz.

The Path to NORESS

The paths from the epicenters to NORESS are also shown in *Figure 1*. The phases P_g and P_n, (and also S_g and S_n) have theoretical arrival times within a few seconds for a distance of 200 km. This means that there will be some interference between these phases. Synthetics calculated with the reflectivity method and with the standard flat-layer velocity model used in the NORESS locations (three layers 16, 24, and 15 km thick with P velocities 6.2, 6.7, and 8.1 km/s, overlying a halfspace with velocity 8.23 km/s) for explosive sources close to the surface suggest, however, that P_g and S_g are the most prominent phases in this distance range.

## Signal to Noise Ratio as a Function of Frequency

Since most of the events are in the low magnitude range, attempts were made to define a frequency band with good SNR for the subsequent signal processing. For this purpose the SNR was calculated as a function of frequency for each event. Each record was filtered by a set of narrow bandpass filters that were obtained from low- and high- pass Butterworth (three-pole) filters, at frequency f varying from 0.1 to 50 Hz in increments of 0.1 Hz. The SNR at frequency f was then defined by the ratio:

$$SNR(f) = \frac{\max_{m} |s(m;f)|}{\max_{m} |n(m;f)|}$$

Here $n(m;f)$ is noise prior to signal onset in a time interval of about 12 seconds as shown in *Figure 3*, and $s(m;f)$ denotes the signal segment. The maximum amplitude of the noise and signal segments was determined in the appropriate time intervals. Ratios were calculated as marked in *Figure 3* for the four signal intervals P, P-coda, S, and S-coda.

The $SNR(f)$ for the two events in *Figure 3* are typical of the data, and these functions usually show a pronounced peak at some frequency (peaking frequency). If the peaking frequency were the same for all events, a bandpass at that frequency would thus provide maximum signal-to-noise ratio. The peaking frequencies for P and S wave intervals are plotted in *Figure 4* against the associated SNR (in dB). There is a strong concentration of the peaking frequencies below 5 Hz for both P and S waves. For about 10% of the events the peaking occurs at about 15 Hz or higher. The peaking frequencies scattered above 30 Hz for the S wave data are probably due to instrumental or local disturbances.
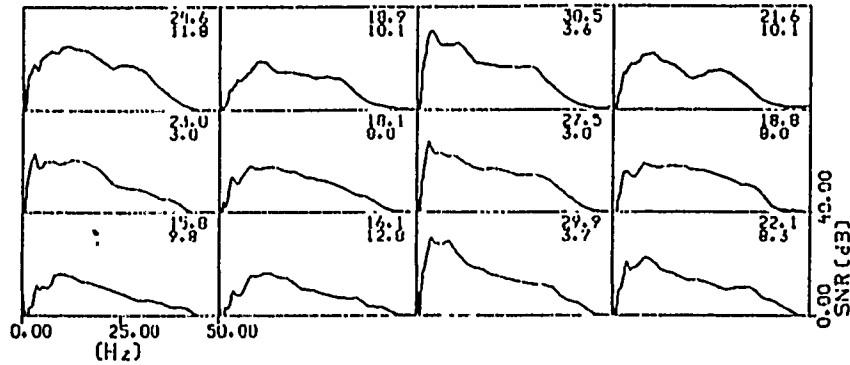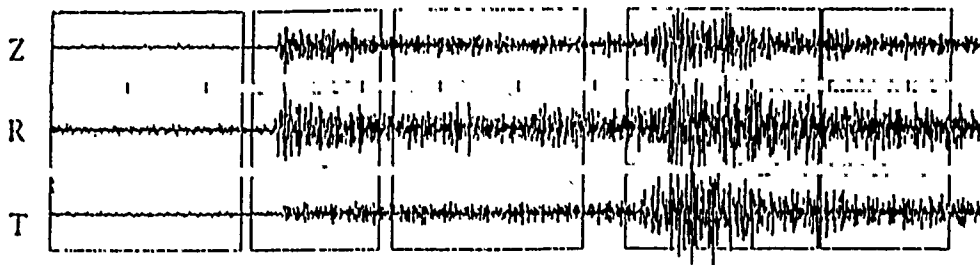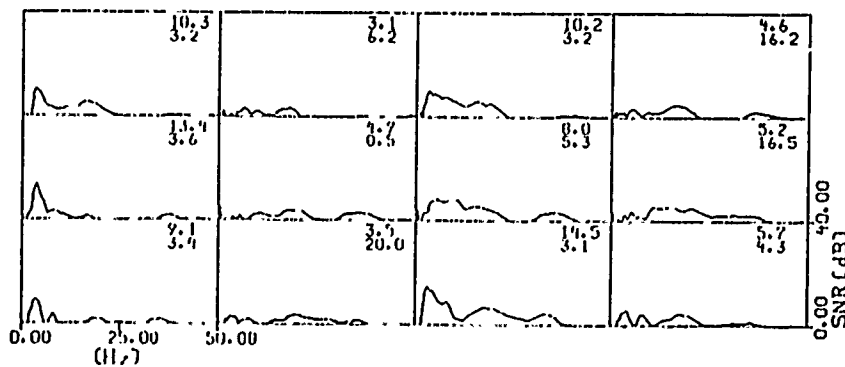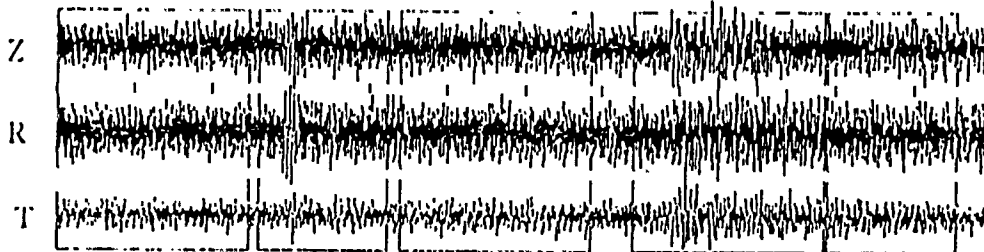
Figure 3. Examples of waveforms for the events analyzed. The horizontal east-west and north-south components have been rotated to the radial and the transverse components. The SNR(f) as a function of frequency for four different segments of the recorded wavetrains as marked in the seismograms are plotted below the seismograms. These functions usually have a pronounced peak for the P and S wave intervals.
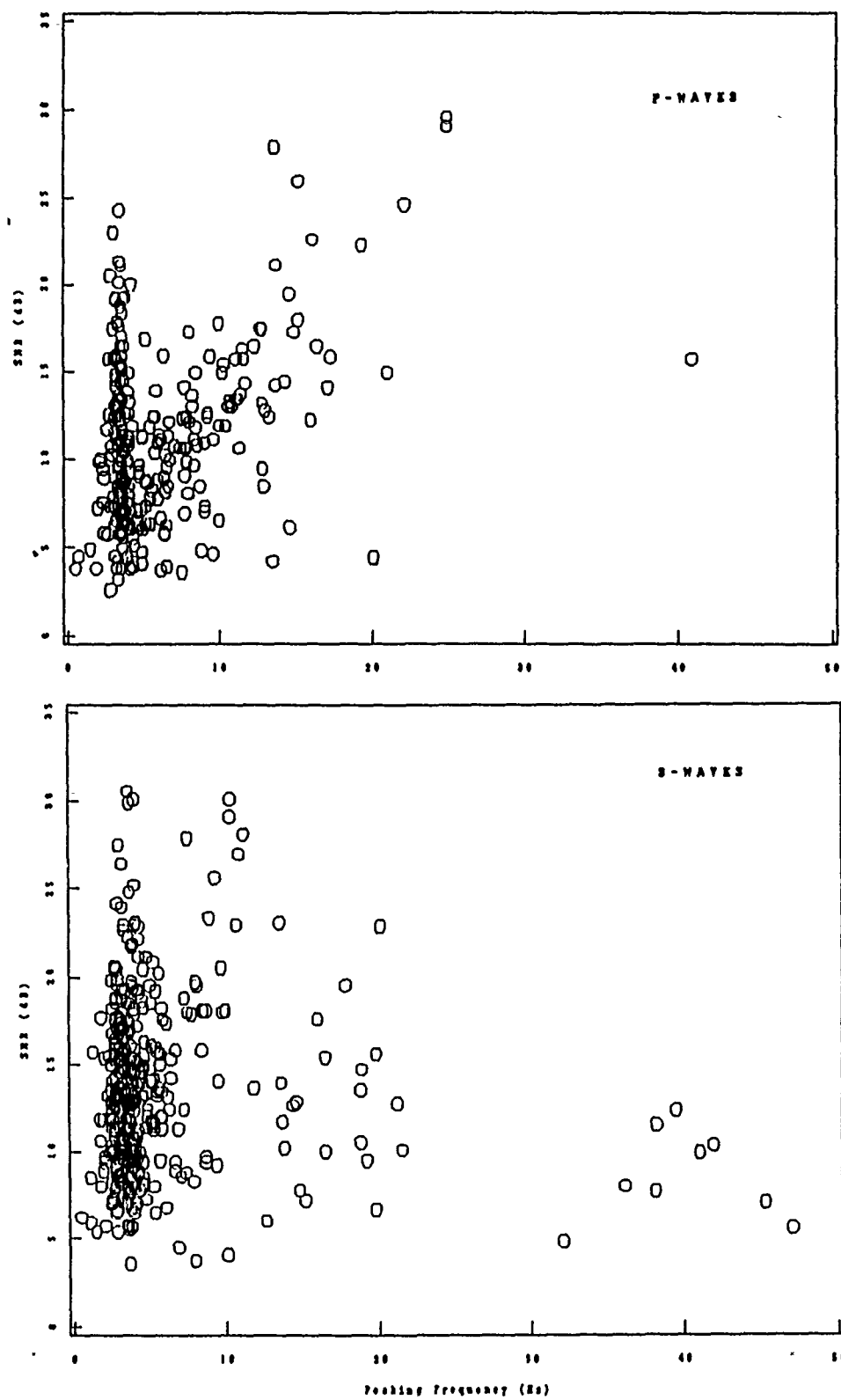
Figure 4. Signal-to-noise ratio at the peaking frequency against the peaking frequency for P and S wave intervals as defined in Figure 3.

In general, a band below 5 Hz provides the best SNR for both P and S waves for this data set, and in *Figure 5* we see the empirical density distributions for P and S waves at frequencies below 10 Hz. These are concentrated in a narrow band between 2.5 and 4.0 Hz, which we will subsequently use for prefiltering of the data.

The fact that the maximum signal-to-noise ratio mostly occurs at such low frequencies could be due to increased daytime high-frequency noise levels when most of the events were recorded. Many of the events are also ripple fired, and delayed firing of shots may reduce the high frequency content (Willis, 1963).

4.1.3 Waveform Similarity

In order to compare the waveforms recorded from the 137 events, we use quantitative measures based on polarization (Jurkevics, 1987) and relative amplitude of the records. In polarization processing, various useful attributes like particle-motion ellipticity and orientation can be extracted from the polarization ellipse, which in turn is defined by the three polarization axes resolved from the covariance matrix of the three components recordings. Rather than use such polarization attributes we employ the approach by Jurkevics (1987) that simply forms particle-motion signatures from the covariance matrix.

Similarity Measures

The band-filtered (2.5-4.0 Hz) seismogram of component i ($i=1,2,3$) for event k is denoted $s_{ik}(m)$. For each event, k, the covariance matrix R_{ijk} of components i and j as a function of time t is defined as follows: .

$$R_{ijk}(t) = \sum_{m=-T/2}^{m=T/2} \frac{(T-2m)}{T} \cdot s_{ik}(t-m) \cdot s_{jk}(t-m)$$

The matrix R_{ijk} is the 3 by 3 matrix of coefficients for a quadratic form, which is an ellipsoid and is symmetric with six unique terms. The three diagonal terms of R_{ijk} are simply the envelopes of the three-component motions as a function of time. The three unique off-diagonal terms are the cross-products between components and they provide important information about the phase and orientation of the particle motion.

According to equation (1) the data are windowed into short overlapping time segments, T seconds wide. The bandwidth of the filtered records and the window length determine the frequency and time resolution. The data window is also tapered, and its width is related to the center frequency of the passband in such a
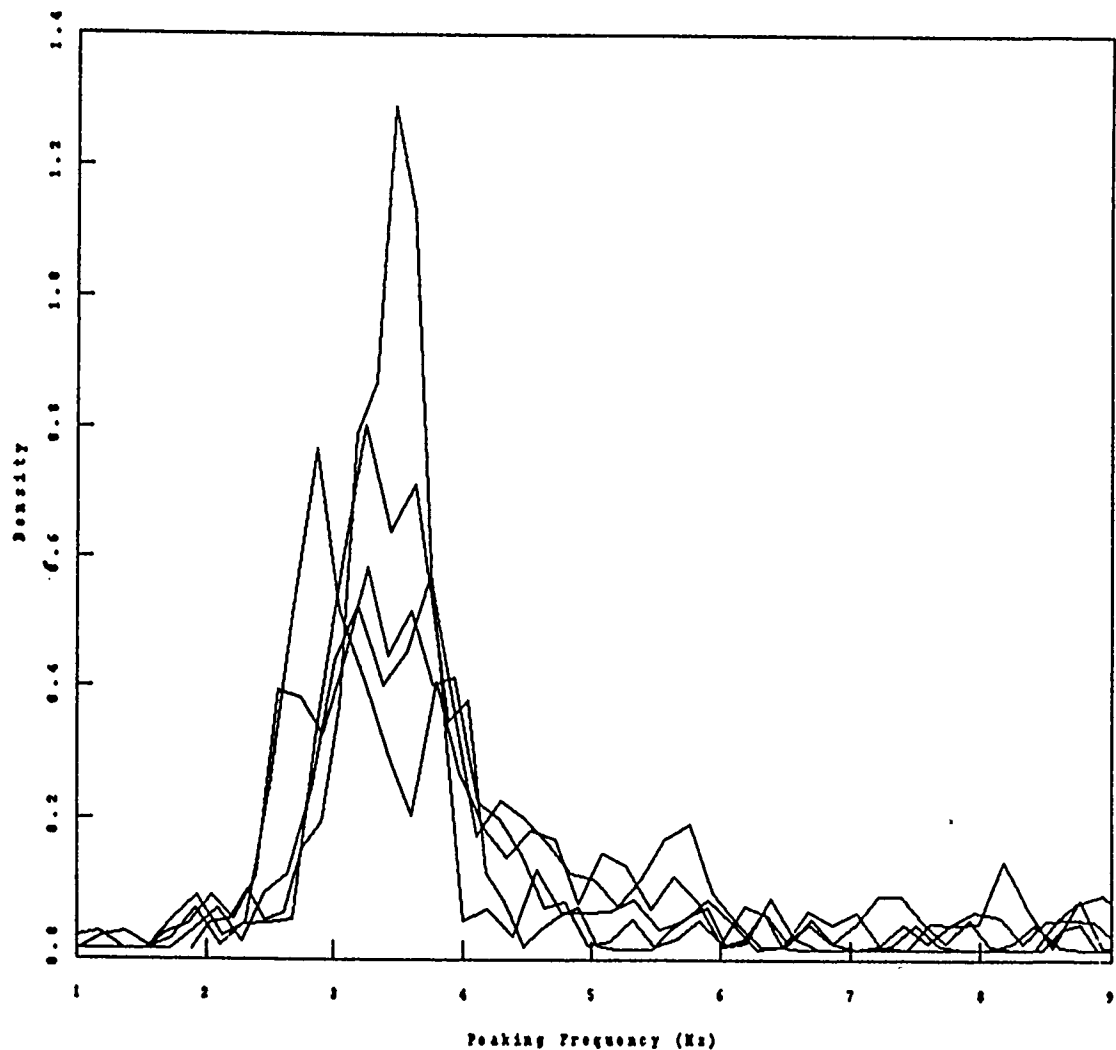
Figure 5. Estimated probability density functions for the peaking frequencies for P radial and vertical components and the S radial, transverse, and vertical components. The curves have been obtained by a non-parametric procedure by Becker and Chambers (1984). The two curves with largest maximum values of the density functions correspond to P (radial and vertical components), and the three curves with smaller maximum density values and somewhat broader densities corresponds to S wave data on the vertical, radial, and transverse components.

way that each frequency component is assumed to be purely polarized over several cycles. The tapered sliding data window has a smoothing effect that will make the signatures less sensitive to minor variations in source and path properties. We use a window length of about $T=1.5$ seconds and move the center of the time window in steps (t) of about 0.5 s. The signature correlations were calculated from a data window covering the entire wavetrain including both P and S phases.

Cross correlations between events k and l are obtained by cross correlating the signature traces R_{ijk} and R_{ijl}. A summation of these cross correlations over the channels i and j is then used to define a similarity measure, $\rho_{kl}(\tau)$:

$$\rho_{kl}(\tau) = \sum_{i \geq j} \left(\sum_t R_{ijk}(t) \cdot R_{ijl}(t-\tau) / \left(\sum_t R_{ijk}^2(t) \cdot \sum_t R_{ijl}^2(t-\tau) \right)^{1/2} \right) \quad (1)$$

In order to account for different amplitudes in the comparison of waveforms we define the maximum amplitude of the three component recordings from the maximum amplitudes (positive or negative) of one of the components (vertical, $i=1$):

$$A_k = \max \left(\max_m (s_{1k}(m)), |\min_m (s_{1k}(m))| \right)$$

The maximum amplitudes defined in this manner can in turn be used to define the following measure of similarity between amplitudes of two recordings:

$$\rho_{kl}(A) = \sqrt{\min \left[A_k/A_l, A_l/A_k \right]} \quad (2)$$

This measure is normalized and is always in the interval (0,1), and because of the square root it is not too different from 1 in cases with minor amplitude differences.

The two correlation measures (equations 1 and 2) are combined to define the total correlation, ρ_{kl}, between waveforms of events k and l:

$$\rho_{kl} = \rho_{kl}(A) \cdot \max_\tau \rho_{kl}(\tau)$$

The total correlation defined in this manner is used in analysis of the events. Examples of particle signatures and correlations are given in *Figure 6* for event pairs
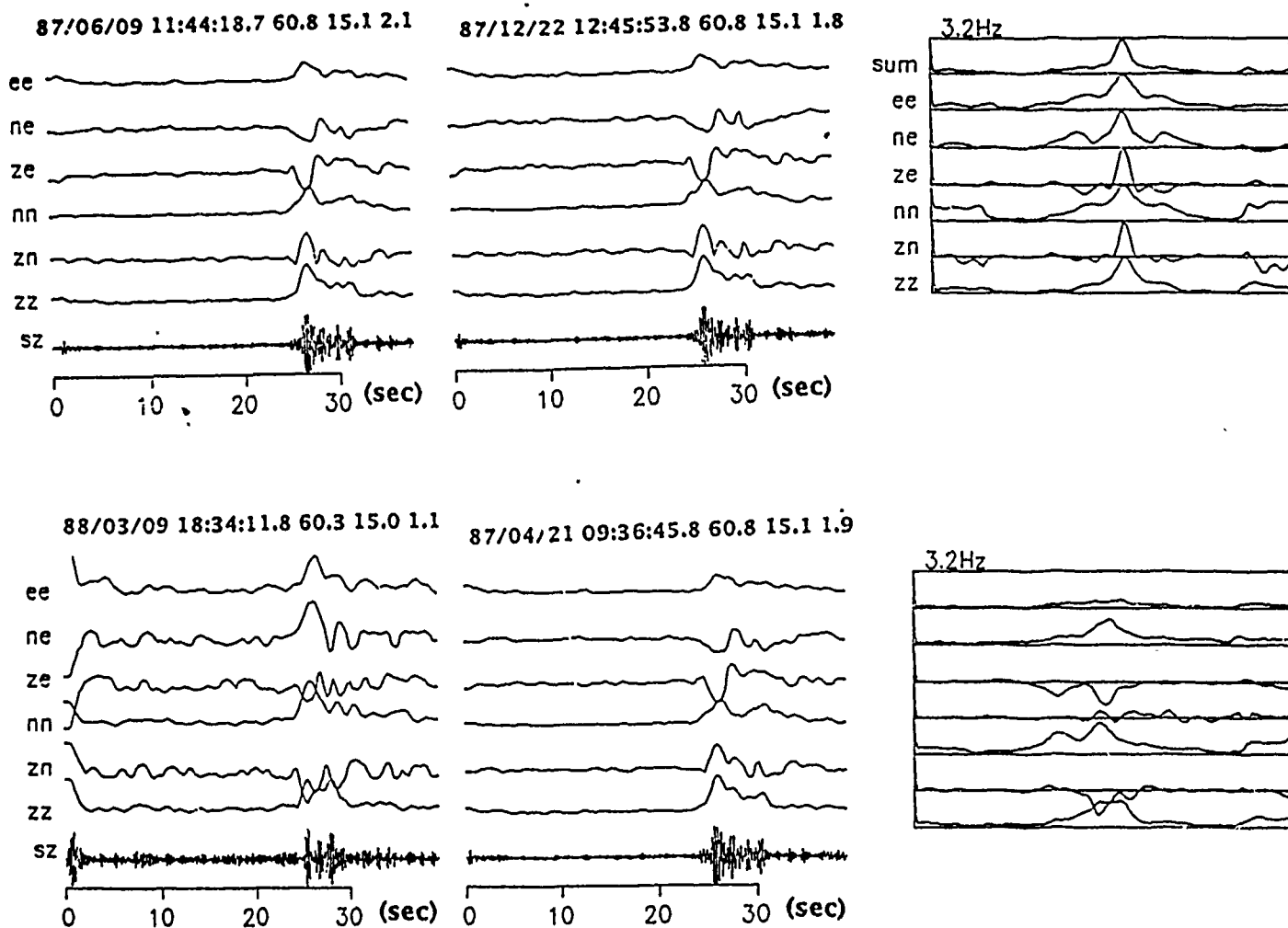
Figure 6. Examples of using the cross-correlation algorithm for three component data for events with high and poor correlation. The vertical component seismograms are plotted in the center of each diagram, and the six unique components of the covariance matrix as a function of time are shown above the vertical component seismograms. The cross correlation functions of the six covariance components and the sum of the cross correlations are displayed below the vertical component seismogram.

with high and low total correlation values, ρ_{kl}.

Correlation Values

Correlation values ρ_{kl} were calculated for all possible event pairs (total of 137·136/2=9,316). The correlation values for all the event pairs are graphically summarized by the image matrix in *Figure 7*.

In order to group similar waveforms we need to specify some cutoff value of ρ_{kl} above which waveforms are considered similar. The correlation ρ_{kl} depends on the signatures of all components and their relation to each other, and will therefore be sensitive to location of the event--in particular backazimuth, since the events are presumed to have similar epicentral distance.

We use the uncertainty of the NORESS estimates of backazimuth to define this cutoff value. The standard deviation of the azimuth error is 6 · 7 ° and we use a minimum of 6.2 ° obtained by comparison with locations of regional station networks for regionalized set of events. In other words, we assume that the error in backazimuth determined by NORESS for a group of events with identical sources and locations would have a standard deviation of 6.2 °, and the difference in backazimuths determined independently of pairs of such events would then have a standard deviation of $\sqrt{2}$·6.2 = 8.8 °. If the events were gradually separated from each other, the standard deviation of the difference in backazimuths would increase, and the correlation between waveforms would drop.

It is reasonable to assume that for the data studied here event pairs with high correlations also have similar locations, and *Figure 8* shows the standard deviation of the azimuth differences as a function of correlation values for all event pairs. The *a priori* value of the standard deviation is indicated by the horizontal line in the diagram. For correlation values above about 0.7 the standard deviation is about the same as this expected value, and at lower correlations it becomes significantly larger. In the subsequent grouping we will therefore use this value as a cutoff for similarity between event pairs.

A value of 0.6 for the cross correlation, based on one component only and defined in an entirely different way, was used by Pechmann and Kanamori (1982) and Thorbjarnardottir and Pechmann (1987) as a cutoff that separated well correlated from poorly correlated events.

We use $\max_{l \neq k} \rho_{kl}$ as an indicator of the similarity of event k with that of the rest of the events. In other words, if this value for a given event k is high there is at least one other event with a similar record, but if it is low the event would appear

Event Number

CORRELATION MATRIX

Event Number
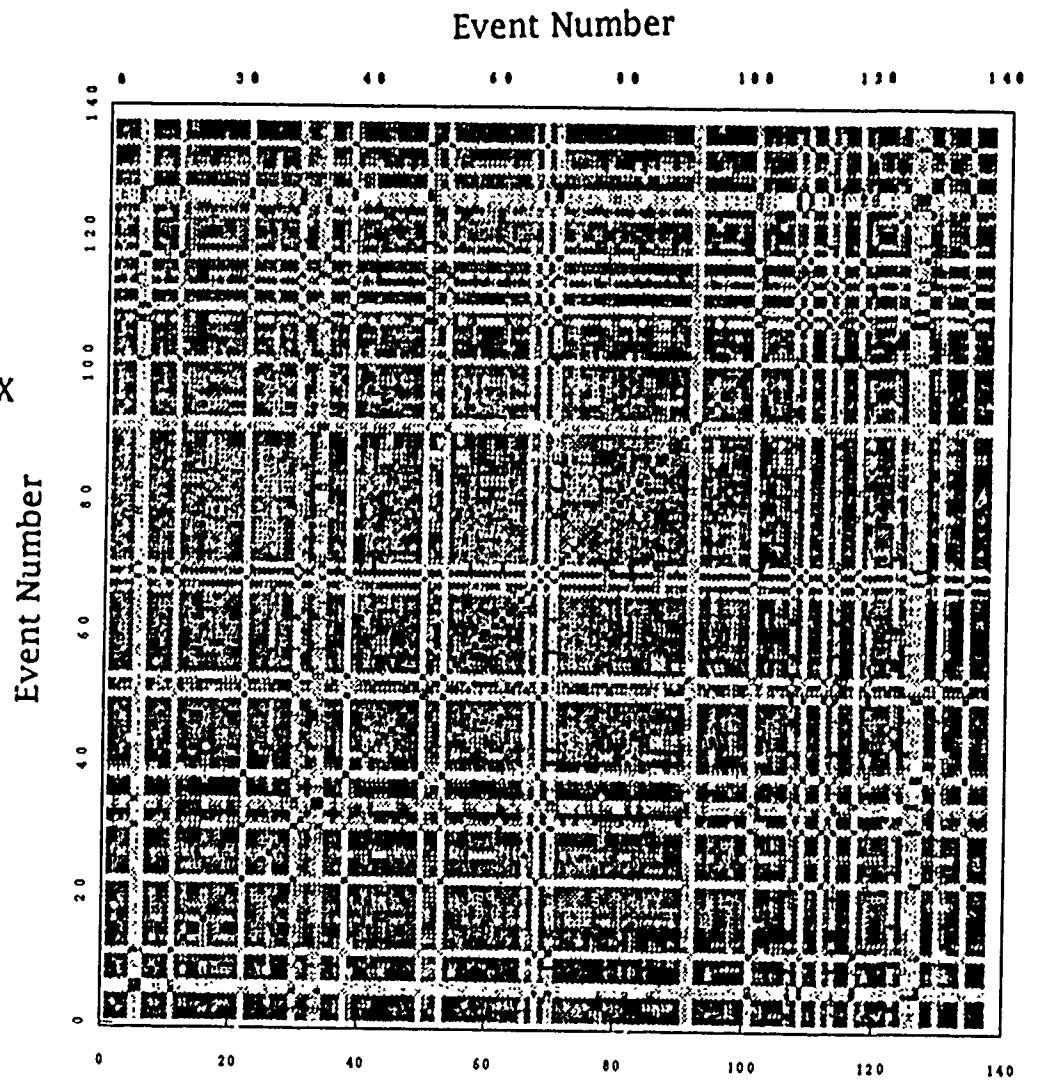
Figure 7. Graphical representation of the matrix of event correlations for all 137 events. The darker the shading, the higher the correlation. The black diagonal represent perfect correlation (1.0) and white areas represent zero correlation. The image, which is symmetric around the black diagonal, contains 18769 elements 9316 of which are unique and or not on the diagonal.
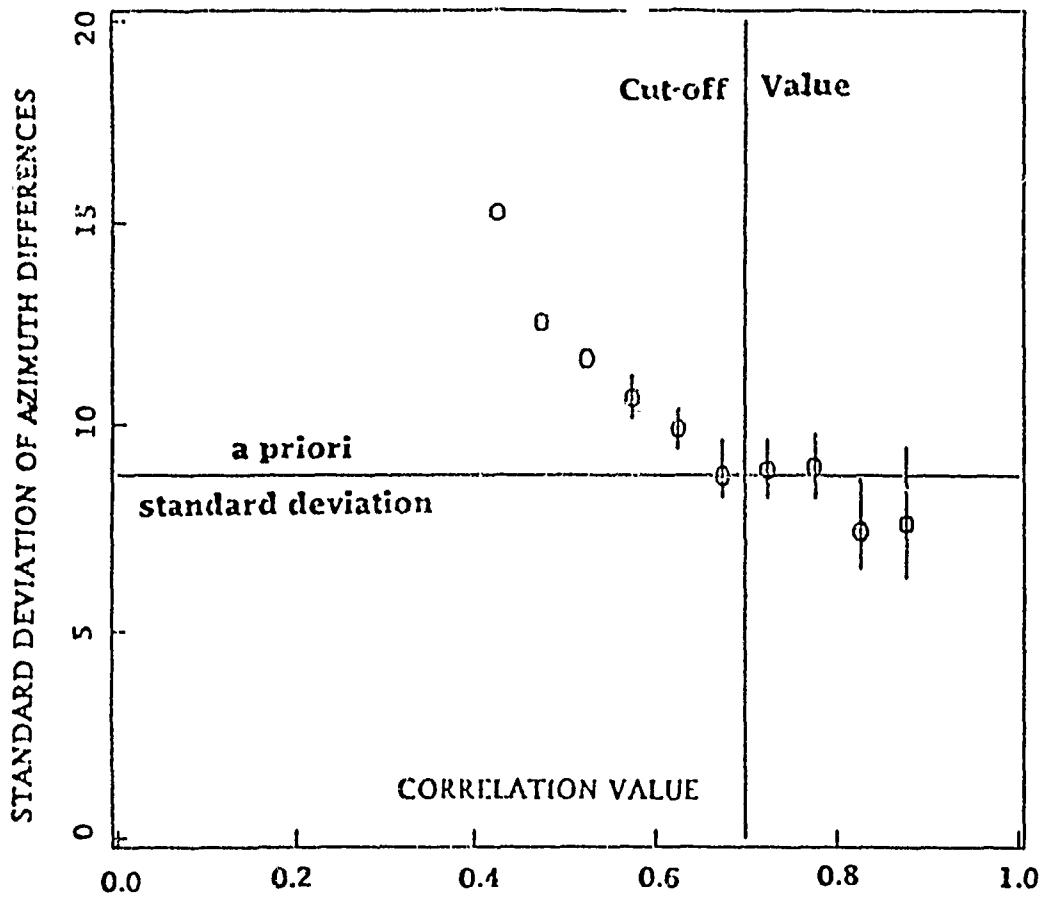
Figure 8. The data points with error bars represents 95% confidence intervals of the standard deviations of the difference in azimuths to epicenters of event pairs located by NORESS ploted against centers of correlation intervals 0.1 units wide. The horizontal line corresponds to an *a priori* standard deviation for differences in the the back azimuth error of pairs of events. The vertical line represents a correlation value 0.7 selected as a cut off value in the event grouping.

as "unique" in the data set. The distribution of these maximum values is shown by the histogram of *Figure 9*. There are 24 events (or about 17% of all events) with $\max_{l \neq k} p_{kl} < 0.7$ that thus would be characterized as unique.

4.1.4 Event Grouping

The locations and source properties for the events studied here are not precisely known, but from a visual inspection of the records it is reasonable to assume that there are a number of events with close locations and similar source characteristics. We can therefore attempt to group the data so that events within groups are similar and unlike those from other groups without assuming anything about the number of such groups This problem can be forma.'y analyzed with clustering analysis techniques (Everitt, 1986).

As a first attempt with this technique we apply hierarchical clustering, which operates on the matrix of pairwise correlations between the event waveforms (graphically illustrated in *Figure 7*). The hierarchical clustering consists of a series of "fusions" of events into groups and in each step of this process events or groups of events that are most similar are fused together. We use the single linkage method, in which the groups initially consist of single events. As the clustering proceeds, groups are fused according to members with highest correlation. The correlation between groups is defined as the highest correlation between members.

The results of this clustering are summarized by a *dendogram* or cluster structure tree in *Figure 10*, which shows the successive fusions of events. If we use 0.7 as a cutoff value between groups, the events can be grouped into one large group with 98 members according to the dendogram. In addition, there are two groups with four and two groups with two members. In the larger group there are also three subgroups with very high correlation (above 0.85) among the members. That is to say that about 80% of the events can be grouped in one way or another, with one large group that contains about 70% of the events.

The hierarchical clustering gives a re-ordering of the events as described by the dendogram. In general, this re-ordering places similar waveforms close to each other on the plot. The vertical-component records of the events have been plotted according to this order in *Figure 11*. The records are plotted with the same amplitude sensitivity as indicated in the figure. The event grouping including the subgrouping of the large group, is also marked in the record sections. There are several examples of waveforms that are nearly identical over the entire length of the records in *Figure 11*. However, most subg. 'ups include only two or three events. and there is no large suite of events with nearly identical waveforms It should be noted that the similarity measure used here depends on the horizontal components as well as vertical, and that it is not a direc' correlation between
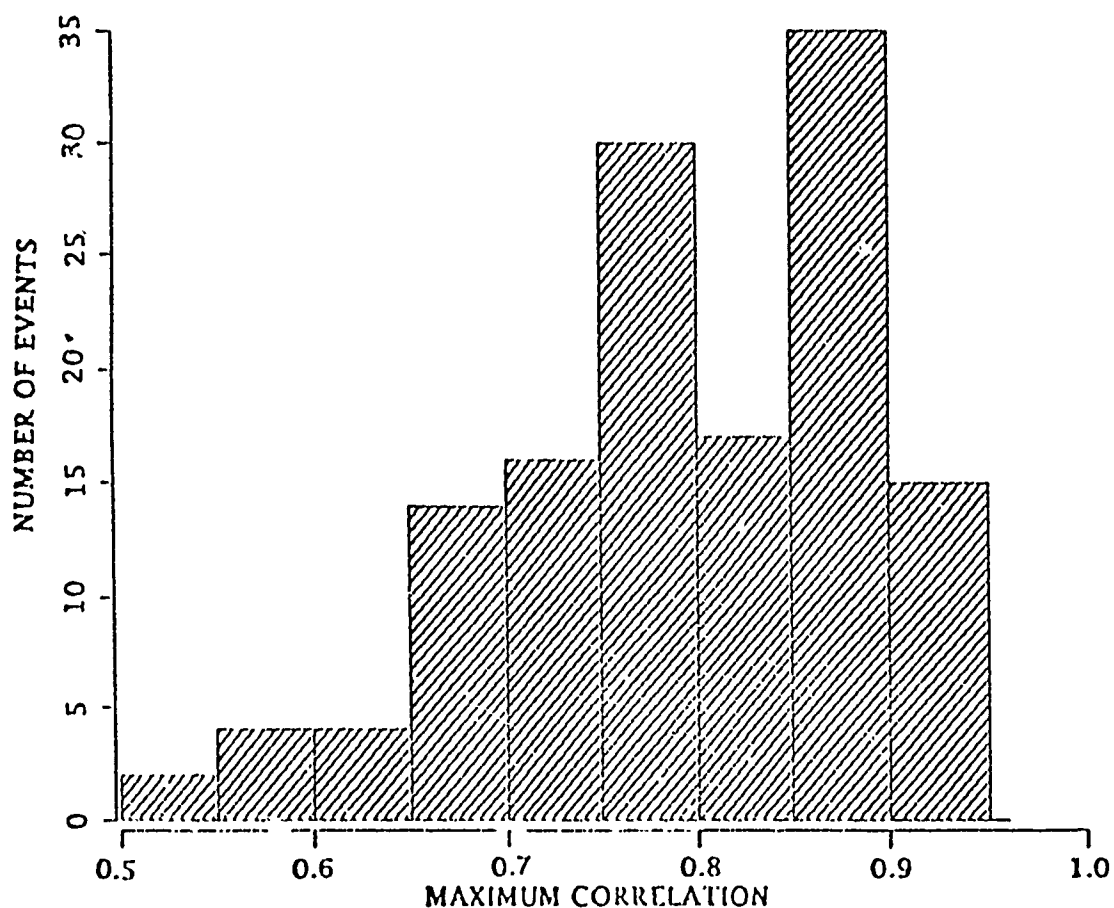
Figure 9. The histogram shows the density of the maximum correlation for the 137 events with that of any other event, i.e., $\max_{l\neq k}\rho_{kl}$, and $k=1,2,...137$. The histogram shows, for example, that 24 events have a maximum correlation with any other events that is less than the cut off value of 0.7.
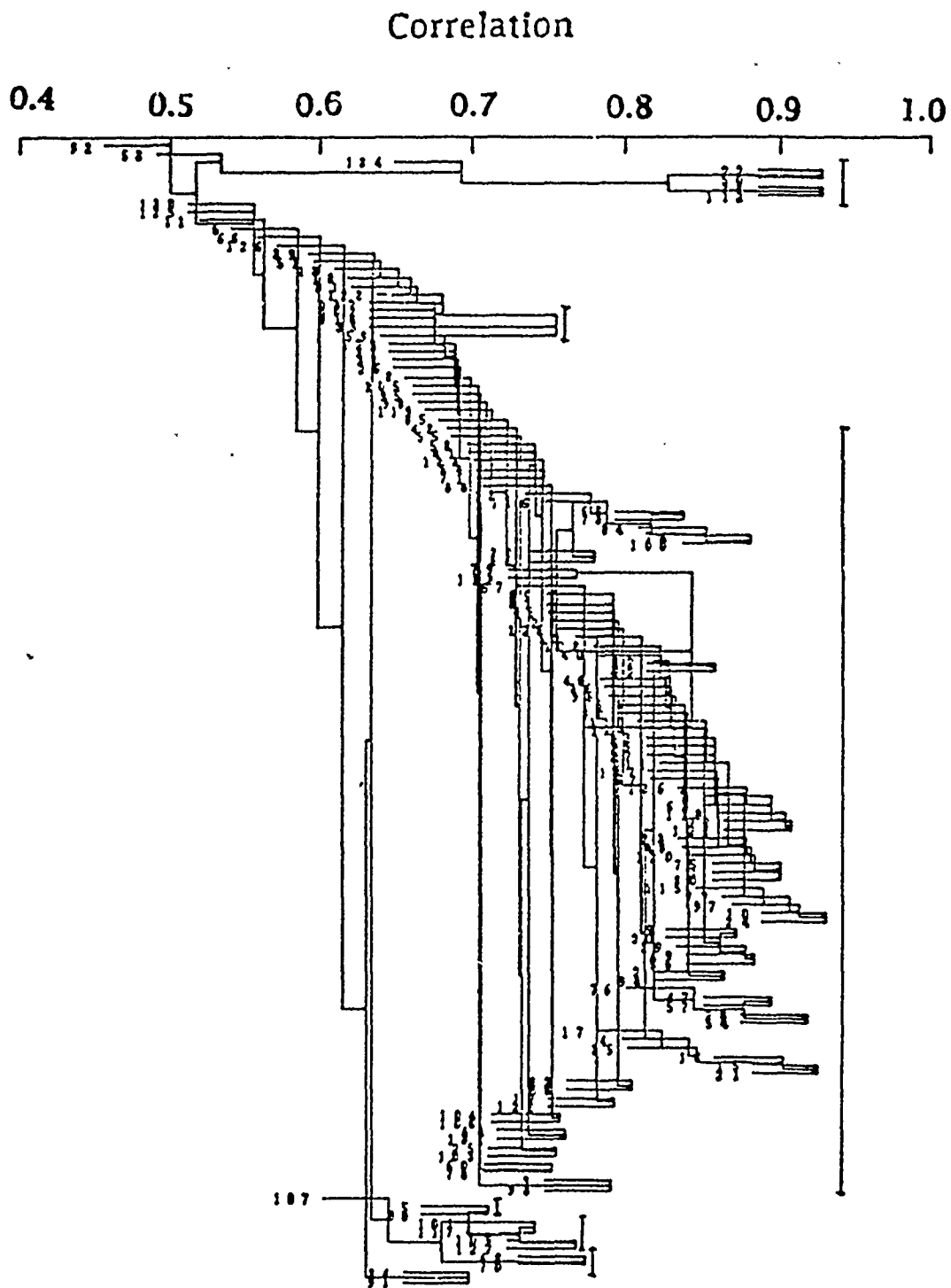
Figure 10. Dendogram or cluster tree structure as a result of hierarchical clustering with the single link method. Above the cut off value of 0.7 the data cluster in one large and a few smaller events.

Figure 11. The filtered vertical component records of the high frequency element at NORESS (site NRAO). The records were aligned according to visually measured first arrival times and are plotted in the order obtained from the hierarchical clustering.

waveforms but with the smoothed envelopes of the seismograms.

Event Group Epicenters

If we assume that events grouped together by the similarity measure also have the same location, an improved estimate of the epicenter can be obtained from the NORESS locations of these events and *a priori* assumptions about the uncertainties in determinations of backazimuth and distance. We assume that the azimuth and distance error are both normally distributed, with zero mean (unbiased) and standard deviations σ_ϕ (6.2 degrees) and σ_r (3.7 km) respectively.

For a group of n events with backazimuth ϕ_i and distance, r_i, the confidence region of the epicenter (specified by uncertainties in distance and azimuth) becomes:

$$\bar{\phi} \pm t_{1-\sqrt{1-\alpha}} \cdot \frac{s_\phi}{\sqrt{n-1}}$$

$$\bar{r} \pm t_{1-\sqrt{1-\alpha}} \cdot \frac{s_r}{\sqrt{n-1}}$$

Here t is the standard t distribution and s_ϕ and s_r are the standard error of the the backazimuth (ϕ_i) and distance (r_i), respectively. If backazimuth and distance determinations are independent, then the confidence level is $1-\alpha$. The point estimates $\bar{r}$ and $\bar{\phi}$ for all event groups and the 95% confidence region for the large event group are shown in *Figure 12* together with the NORESS epicenter determinations of the events. The extent of the confidence region, centered around 60.03^o N and 14.84^o E, is about 10 km. The standard deviation of the epicenter errors due to rounding errors in the NORESS bulletin (latitude and longitude given to 0.1 degree) is about 2 km.

The shape of the confidence region is a circular sector since we approximate with plane geometry, and this approach of obtaining confidence regions for arrays operating at regional distances can be used for single events as well if the t-distribution is replaced by a normal distribution (Cf. confidence ellipses for spherical geometry by Bratt and Bache, 1988).

Confidence regions for the epicenters of the smaller event groups were not calculated since the number of events ranged only between 2 and 4. However, the northernmost group of four events, all with the same NORESS epicenters (60.8N and 15.3E), seems to be at a significantly different location from that of the large event group.
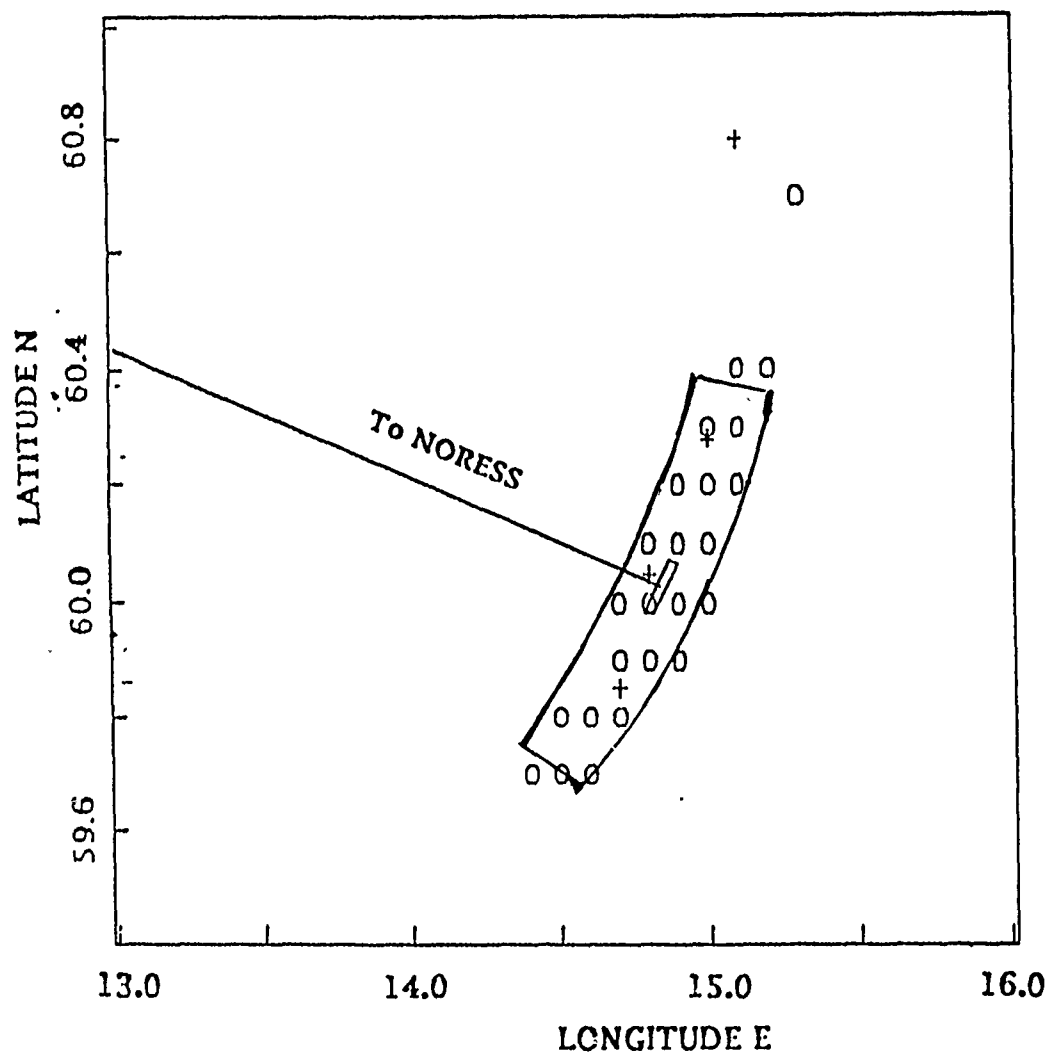
Figure 12. Epicenters of events in large group and confidence region of their epicenter on the assumption that they all have the same epicenter. The direction to NORESS in also indicated.

Similarity as a Function of Source Separation

The degree of waveform similarity between two events recorded at the same instrument is a function of differences in path and source characteristics. For identical source pairs the correlation will be a function only of path differences, which sometimes are approximated with source separation. For example MacLaughlin et al (1983) approximated the correlation of waveforms recorded across an array as a function of array coordinates, with an exponential function of the moduli of the coordinates. If one simplifies further and assumes isotropic conditions, the correlation will have an exponential decay with source (or receiver) separation, d. We write this decay as $e^{-d/a}$, with the constant a being a characteristic distance for the source (or receiver) region. A smoothed curve fit to the cross correlations obtained here as a function of source separation (from the NORESS locations) is shown in *Figure 13*. This curve is almost flat to about 40 km, and at larger distances drops exponentially with different rates for different distance intervals. The flat part of the curve is caused by a bias in distance between event pairs computed from the NORESS locations. With assumptions about the distributions of the errors in backazimuth, ξ_ϕ, and epicentral distance, ξ_r, this bias can be estimated. Let r_i and ϕ_i be the true distance and backazimuth from NORESS for event i. The rounding errors of the latitude (ξ_{yi}) and longitude (ξ_{xi}) reported for event i in the NORESS bulletins can be assumed to be uniformly distributed over the intervals (-5.6,5.6) and (-2.8,2.8) km respectively. The estimated coordinates of the event in a Cartesian plane with NORESS at the center can then be written as:

$$x_i = (r_i + \xi_{ri}) \cdot \sin(\phi_i + \xi_{\phi i}) + \xi_{xi}$$

and

$$y_i = (r_i + \xi_{ri}) \cdot \cos(\phi_i + \xi_{\phi i}) + \xi_{yi}$$

The separation between two events from the epicenters determined by NORESS is:

$$\delta_{ij} = \sqrt{(x_i - x_j)^2 + (y_i - y_j)^2}$$

whereas the true distance is:

$$d_{ij} = \sqrt{r_i^2 + r_j^2 - 2 \cdot r_i \cdot r_j \cdot \cos(\phi_i - \phi_j)}$$

Even if the ξ variables have standard distributions, the δ_{ij} variable does not.

We therefore used random number generators for normal and uniform distributions to generate a sample of observations for this non-standard distribution (9316 observations), with $r_i=r_j=200$ km and $\phi_i=\phi_j=111.0$ degrees. This sample has a skewed distribution and $\delta_{ij}^{1/3}$ fits a normal distribution resonably well. The median value, $E(\delta_{ij})$, for this sample was 21.36 km, which thus would represent the bias in the correlation curve. By subtracting this bias the characteristic distance, a, can now be estimated from:

$$\hat{a}_{ij} = \frac{E(\delta_{ij})-\delta_{ij}}{log(\rho_{ij})}$$

The median value of $\hat{a}_{ij}$ was 8.0 km if the data were limited to $\rho_{ij}>0.6$ (5024 event pairs). Although there is a very considerable scatter in the $\hat{a}_{ij}$ values, the 95% confidence interval (Claerbout, 1976) for the median is limited to 7.0-9.5 km. Similar results were obtained for data with $\rho_{ij}>0.8$ (1032 event pairs). This is in qualitative agreement with the characteristic distance obtained from corrlelations between station pairs of the NORESS array (Cf. *Figure 13*). The correlation of P_g across NORESS in the frequency band 2.4-4.8 Hz, which is fairly close to the one used here, is shown in *Figure 13* with a linear regression fit to an exponential decay $e^{-d/a}$. The characteristic distance, a, estimated from this data is about 10 km. Thorbjanardottir and Pechmann (1987) get correlation values that fall below 0.6 within 0.4 km for the band 1-2 Hz and within 0.2 km for the band 2-4 Hz, which correpond to characteristic distances of about 0.8 and 0.4 km respectively.

Triangulation with the Cross Correlation

If cross correlation as a function of source separation, d, is known, together with the precise epicenters of at least three reference events at different locations, triangulation can be used to estimate epicenters of other events from cross correlations. This of course presumes that the events have the same source characteristics. *Figure 14* shows the results of an example with this approach. This is included only for the sake of illustration; actual locations cannot be made without knowledge of the epicenters of the referenc vents. Three events ($k=1,2,3$) that had high correlation among each other werc selected as reference events. One of these events was then arbitrarily given the center coordinates and one of the two remaining events was placed on the positive x-axis at distance, $-a \cdot log\rho_{12}$ from the center. The coordinates of the third event were obtained from distances to the other two ($-a \cdot log\rho_{13}$ and $-a \cdot log\rho_{23}$) of two possible locations, the one in the first

Bias

Log Correlation

(km)

50 100

$\rho = e^{-d/a}$

Robust estimate
of $a = 10$

Log Correlation

(km)

1   2   3

Decorrelation with
receiver separation
of P_g at NORESS
(Mykkeltveit et al, 1983)
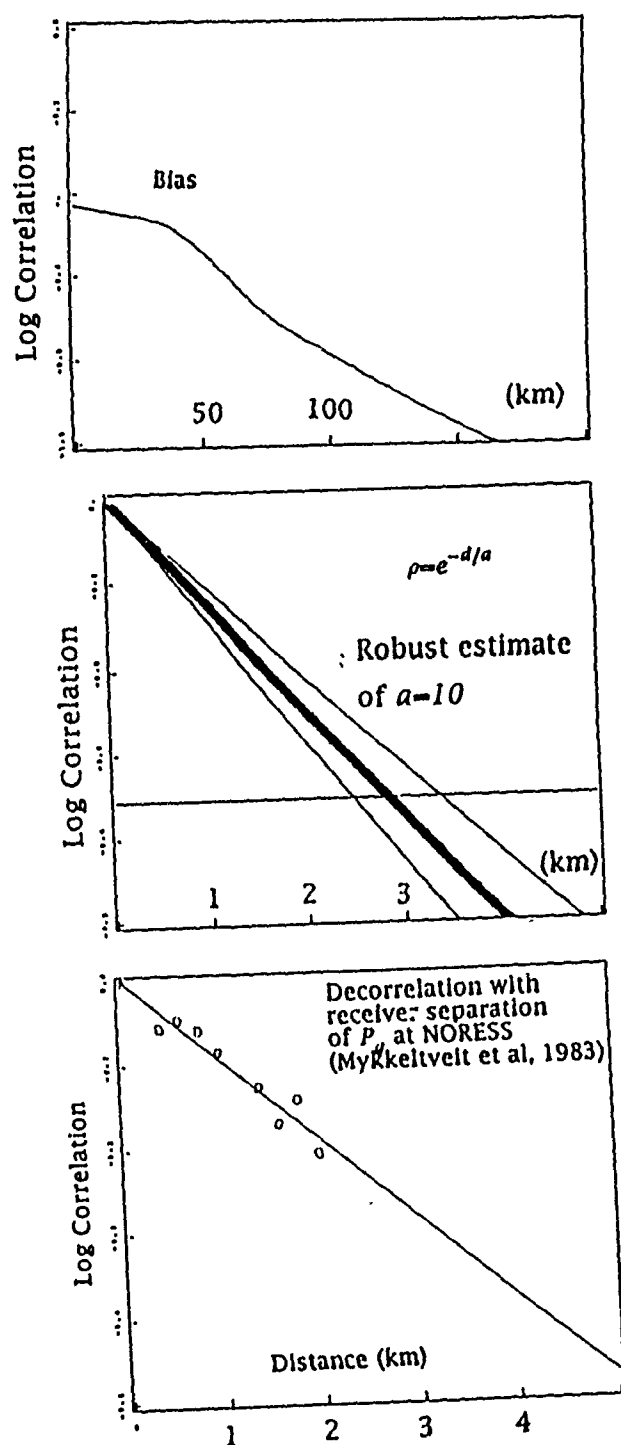
Log Correlation

Distance (km)

1   2   3   4

Figure 13. The correlation above was obtained from the correlation data in this study and represent a smoothed curve based on robust locally weighted regression (Becker and Chambers, 1984). Note that this curve is biased due to errors in the NORESS epicenter determinations. The dark line in the middle represents an exponential decay of the correlation as a function of the source separation obtained from a median estimate of the characteristic distance, a. The thin lines in the same diagram represent the 95% confidence levels of this characteristics. The correlation in the lower part of the figure represent results obtained for the NORESS array of P_g in the band 2.4-4.2 Hz (Mykkeltveit, 1983).
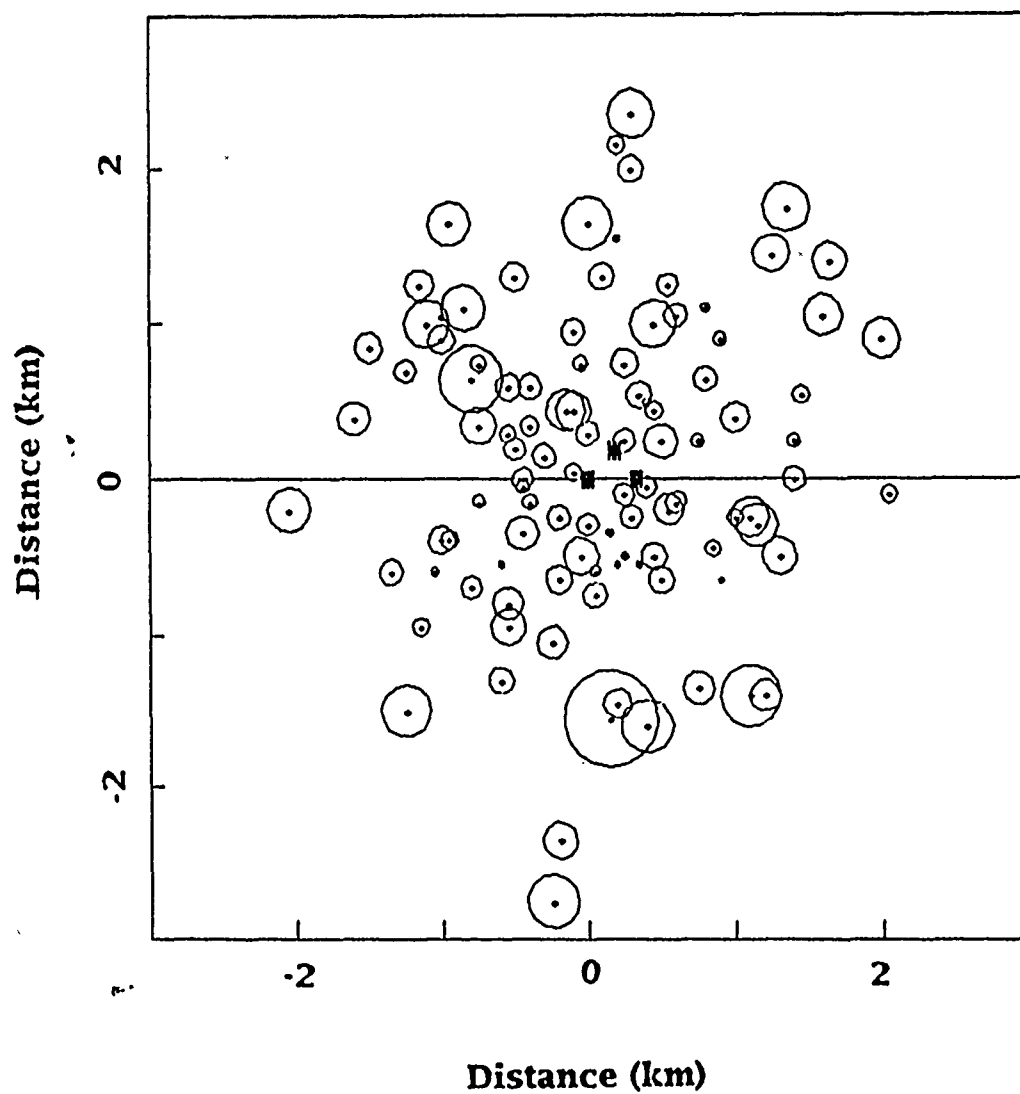
Figure 14. Relative location of events in large event group as obtained in an experiment that illustrates the triangulation method.

quadrant being arbitrarily chosen. Relative location of the remaining events was obtained iteratively. In each step of this process a new event, having the largest number of correlation values with reference events above a certain minimum correlation threshold, ρ_{min}, was added to the set of reference events. In the iteration this threshold was gradually reduced from 0.95 to 0.7. This means that initially, events close to the reference events were added and as the iteration proceeded events further and further away were added. The relative coordinates x and y of a new event, l, is obtained by minimizing the sum:

$$Q = \frac{1}{\Sigma \epsilon_{ij}} \cdot \sum_{i=1}^{l} \epsilon_{ij} \cdot \left(-log(\rho_{ij}) \cdot a - \sqrt{(x_i - x)^2 + y_i - y^2} \right)^2$$

The summation operator, ϵ_{ij}, is 1 if $\rho_{ij} > \rho_{min}$. We also require that $\Sigma \epsilon_{ij} \geq 3$. The circle about each event in *Figure 14* is an indication of the spread in the estimated coordinates, i.e., $\sqrt{Q/(\Sigma \epsilon_{ij} - 1)}$.

Similarity at High Frequencies

The results for waveform correlation presented above are limited to a band with rather low frequencies, 2.5-4.0 Hz, since the SNR is usually low at higher frequencies. There are, as indicated in *Figure 15*, some events with high SNR at high frequencies, like a suite of five events that all have NORESS epicenters at 60.8N and 15.3E. Correlation values based on particle signatures were calculated for these events, for portions of the records that were windowed for P and S waves (Cf. *Figure 3*). Calculated ρ_{kl} in these frequency bands, shown in *Figure 15*, indicate high correlations (0.90 or more) for data up to 20 Hz for P waves and 15 Hz for S wave data.

As a quantitative statement about the spatial clustering of earthquake aftershocks, it has been suggested that events with very similar waveforms at a particular wavelength can be assumed to have source locations within one-quarter of that wave length (Geller and Mueller, 1980). Results for records of mine blasts by Thorbjarnardottir and Pechmann (1987) provide support for this hypothesis. If we use this argument for high-frequency correlations for the group of events near 60.8N and 15.3E, the quarter wavelengths are about 100 m or less (assuming P velocity of 6.2 km/s). The quarter wavelengths obtained for the P and S wave data in *Figure 15*, using a cutoff at 0.9 of the correlation, are fairly consistent with a $\sqrt{3}$ ratio for to P and S wave velocities except for one of the event pairs, for which the S wave correlation drops at about 4 Hz. Source separations derived from the quarter wavelength argument are of course only quantitative in nature. Frankel and Clayton (1986) demonstrate with synthetic examples that a decrease in waveform
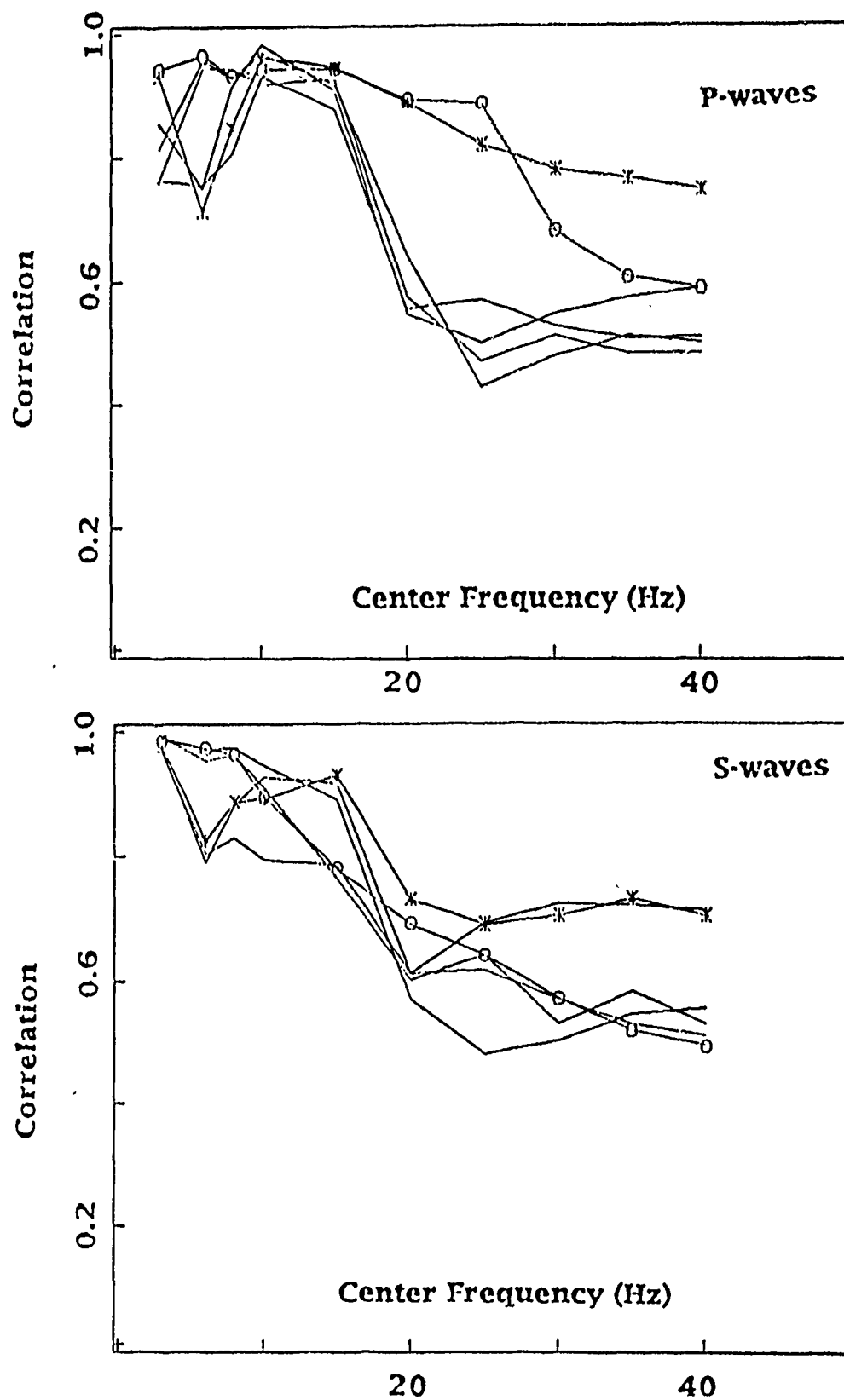
Figure 15. Correlations in different pass bands as a function of center frequency for P and S wave data windows. The curves represent data for a small suite of four events all with the same NORESS location 60.8N and 15.3E.

correlation may also depend on the medium characteristics, and not simply on a fixed fraction of the wavelength.

Considering the 200 km epicentral distance for the five events in *Figure 15*, the frequencies at which their waveforms have strong correlations are high compared to results from other studies. Thorbjarnardottir and Pechmann (1987) study data recorded from mine blasts at about 100 km and get correlations (between two traces) around 0.6 or higher in the frequency band 2-4 Hz, but little or no correlation in higher frequency bands. Geller and Mueller (1980) observed very high correlations for regional earthquake data at less than 100 km for frequencies up to about 5 Hz. Lack of correlation at higher frequencies was attributed to very small scale crustal heterogeneities and scattering.

4.1.5 Concluding Remarks

In this note we have studied waveforms recorded at the high frequency element of the NORESS array, from 137 events in or near the mining districts of Central Sweden at epicentral distance of about 200 km from the array. The 137 events, recorded between Jan 1, 1986 and June 30, 1988, constitute about 10% of all the events that were detected and located in this area by NORESS for this period. None of these events, which are in the magnitude range $ML=0.8-2.1$ has been reported in event bulletins based on local station networks in Norway and Finland, and the epicentral accuracy is therefore limited by the location accuracy of the NORESS array. Even if most events are believed to be ripple fired no explicit information on intrinsic source properties were available in this study. This situation, with uncertainties about both precise epicenters and source characteristics, is somewhat similar to the test ban monitoring case, where stations have to be deployed in an area with which the verifying party has little or no previous experience.

The case-based approach for regional event detection and identification assumes that events can be identified on the basis of similarity with nearly identical waveforms of previously recorded events. Visual inspection of the records analyzed here indicated that there were comparatively few pairs or groups of nearly identical records, and that some variability seemed to be a significant characteristic of the data set. In order to quantify the comparison, waveform correlations were therefore calculated for all event pairs.

Waveform correlations based on the covariance matrices of the three component recordings as introduced by Jurkevics (1987) and the maximum amplitudes of the recordings were calculated from traces filtered between 2.5-4.0 Hz, the bandpass in which the SNR consistently peaked for the events. The correlation defined in this manner is somewhat unsensitive to minor variations in waveforms due to

data smoothing, and is quite sensitive to th   ee-component recordings and thus location of the events in terms of backazim   . Cutoff values of the cross correlations to separate waveforms with poor and good correlation values were defined from the s·atistical uncertainty in backazimuth estimates of the NORESS array.

The events are grouped with hierarchical clustering analysis, using the single-link method, into one large group of 98 events and four smaller groups with 2-4 events each. Several subgroups of 2-5 events could also be identified in the large event group at higher cut-off values. The NORESS epicenters of the events in the large event group were scattered over an area of 20 by 75 km. If one assumes that these events had the same location, the 95% confidence region of the epicenter has an aperture of about 10 km. If the waveform correlation between nearby events is reduced monotonically as a function of source separation in a known manner, relative epicenters between near events can be determined from their correlation values. This approach is illustrated for an exponential decay of the waveform correlation with source separation. A numerical example is provided by a least squares procedure applied to the large event group.

High correlation values were obtained at frequencies above 15 Hz for one of smaller event groups. These frequencies are significantly higher than those reported in other studies, and the quarter wave length argument constrains the epicenters of these events to within 100 m.

Hans Israelsson

References

Becker, Richard A. and John M Chambers (1984). S: An interactive environment for data analysis and graphics. *Wadworth Advanced Book Program, Belmont, California* pp 550.

Bratt, Steven R. and Thomas C. Bache (1988). Locating Events with a Sparse Network of Arrays. *Bull. Seism. Soc. Am.,* Vol. 78, pp. 780-798.

Claerbout, Jon F. (1976). Fundamentals of geophysical data processing. *McGraw Hill.* 274 pp.

Dysart, P. S. and J. J. Pulli (1987). Spectral Study of Regional Earthquakes and Chemical Explosions Recorded at the NORESS array. *Center for Seismic Studies Tech. Rept. C87-03*, pp. 3.21-3.44.

Everitt, Briant (1986). Cluster Analysis. *Halsted Press, Division of John Wiley & Sons, New York* **(2nd Edition),** pp 136.

Frankel, A. and R.W. Clayton (1986). Finite difference simulations of seismic scattering: implications for the propagation of short-period seismic waves in the crust and models of crustal heterogeneity, *J. Geophys. Res.* Vol. 91, pp. 6465-6489.

Geller, R. J. and C. S. Mueller (1980). Four similar earthquakes in central California. *Geophys. Res. Letters* Vol. 7, pp. 821-824.

Jurkevics, Andy (1987). Particle motion signatures for source identification, *Center for Seismic Studies Tech. Rept. C87-01*, pp. 3.1-3.11.

McLaughlin, K. L., L.R. Johnson, and T. V. McEvilly (1983). Two-dimensional array measurements of near source ground accelerations. *Bull. Seism. Soc. Am.*, Vol. 73, pp. 349-375.

Mykkeltveit, S., Astebol, K., Doornbos, D. J., and E. S. Husebye (1983). Seismic array configuration optimization. *Bull. Seism. Soc. Am.*, Vol. 73, pp. 173-186.

Pechmann, J. C. and H. Kanamori (1982). Waveforms and spectra of preshocks and aftershocks of the 1979 Imperial Valley, California, earthquake: evidence for fault heterogeneity? *J. Geophys. Res.* Vol. 87, pp. 10579-10597.

Suteau-Henson, Anne and Thomas C. Bache (1988). Spectral Characteristics of Regional Phases Recorded at NORESS, *Bull. Seism. Soc. Am.*, Vol. 78, pp. 708-725.

Thorbjanardottir, Bergthora S. and James C. Pechmann (1987). Constraints on Relative locations from Cross-Correlation of Waveforms, *Bull. Seism. Soc. Am.*, Vol. 77, pp. 1626-1634.

Willis, D. E. (1963). A note on the effect of ripple firing on the spectra of quarry shots, *Bull. Seism. Soc. Am.*, Vol. 53, pp. 79-85.

4.2 EFFECT OF SCATTER IN DELAYS OF RIPPLE FIRING

4.2.1 Introduction

Several methods with a potential for identifying ripple-fired mine explosions have been suggested in the literature. A summary of studies in this field and the standard seismic source model for ripple-firing, together with its effect on recorded signals and calculated signal spectra, has been given by Baumgardt (1988). That seismic source model was based on the assumption that a series of explosions at the same location are fired one-by-one with equal delay between subsequent shots.

Smith (1988) introduced a factor to account for the spatial distribution of the individual shots, which was also considered by Hedlin *et al.* (1989). However, both Smith and Hedlin *et al.* found that the effect of this factor on the time delays was negligable for the data in their studies.

Although the standard model assumes a regular time spacing between individual shots, it has also been recognized that scatter in the shot delays occurs and that this will primarily suppress the high-frequency harmonics of the spectra of recorded signals. Smith (1988) noted that 20% timing variations had only small effects on the spectral peaks associated with the delay. Hedlin *et al.* (1989) observed that deviations between actual and intended delay times could be as high as 34% for some ripple-fired quarry blasts in the Eastern U.S. They also demonstrated the effect on higher harmonics with a synthetic example for which the standard deviation was 10%.

In this note a model is presented for ripple-firing that includes scatter in the delay times of the individual explosions. Analytical expressions for the resulting modulation of the source spectrum are derived and simulated examples are compared with the analytical solutions. The variation of delay times are discussed for some cases of ripple-firings which have been studied in the literature.

4.2.2 Model

The source function, $x(t)$, as a function of time, t, for a ripple-fired explosion consisting of N equal explosions delayed by τ_k can be written as:

$$x(t) = \sum_{k=0}^{N-1} s(t - \tau_k)$$

$s(t)$ is the source function for the individual explosions. It is assumed that each explosion has the same source function and that the delays between shots are multiples of Δt :

$$\tau_k = k \cdot \Delta t$$

The source function is often represented by its Fourier transform:

$$X(i\omega) = S(i\omega) \cdot M(i\omega)$$

where $M(i\omega)$ is a modulation factor that introduces a scalloping effect on the spectrum of the source function:

$$M(i\omega) = \sum_{k=0}^{N-1} \exp(-i \cdot \omega \cdot k \cdot \Delta t)$$

A stochastic error term, ϵ, is added to the delay time, $\tau_k + \epsilon_k$ so that the Fourier transform of the modulation function becomes:

$$M(i\omega) = \sum_{k=0}^{N-1} \exp\left(-i \cdot \omega \cdot \left(\Delta t \cdot k + \epsilon_k\right)\right)$$

We assume that the error, ϵ_k is gaussian with zero mean and a standard deviation of σ. This means that the scatter in the delay is the same for all delay times regardless of the average length of the total delay, which for shot k is equal to $\Delta \tau \cdot (k-1)$.

The power spectrum of the modulation function can be written as:

$$M(i\omega) \cdot M^*(i\omega) = \left\{\sum_{k=0}^{N-1} \exp\left(-i \cdot \omega (\Delta t \cdot k + \epsilon_k)\right)\right\} \left\{\sum_{k=0}^{N-1} \exp\left(i \cdot \omega \cdot (\Delta t \cdot k + \epsilon_k)\right)\right\}$$

The average value (expectation operator) of the power spectrum becomes:

$$E(M(i\omega) \cdot M^*(i\omega)) = \frac{\left\{(1-\cos(\omega \cdot N \cdot \Delta t)\right\}}{\left\{(1-\cos(\omega \cdot \Delta t))\right\}} \cdot \exp(-(\sigma \cdot \omega)^2) + N \cdot (1-\exp(-(\sigma \cdot \omega)^2)$$

The ϵ_k are assumed to be independent and the concept of characteristic functions are utilized when applying the expectation operator i.e.,

$$E\left\{\exp(-i \cdot \epsilon_k)\right\} = \exp(-\sigma^2/2)$$

The expression for the power spectrum of the modulation function includes two

parts. The first part consists of the standard modulation factor weighted with an exponential decay term, the decay rate of which is proportional to the squared product of the frequency (angular frequency, ω) and the standard deviation (σ) of the delay time. The second term increases with frequency towards the asymptotic value, N, which is equal to the number of shots. At higher frequencies this term adds white noise to the modulation of the spectrum.

Figure 1 compares the average modulation spectrum calculated from the formula above to the average of 1500 simulated spectra with scatter in the delay times. The simulated values were obtained from a random number generator and are in general agreement with the curves derived from the analytical expression above. The ratio of these two average spectra deviates less than about 3% from 1 throughout the frequency band.

In *Figure 2* the modulation function of a series of 5 shots with a delay time of Δt=100 ms is compared with the average value of the modulation function with a 10% scatter in the data i.e., σ=10 ms. The modulation function for the series with no scatter in the delay time is characterized by a reguar pattern of equal amplitude peaks while only 4 peaks can be clearly seen on the average curve for the series with scatter in the delay times. *Figure 3* shows an example of the spectrum of one simulated modulation function for a series with 10% scatter.

4.2.3 Examples

In this section, the effect of 10, 20, and 30% scatter in the time delays for some configurations of ripple-fired explosions that have been studied in the literature are illustrated. The first example comes from Baumgardt and Ziegler (1988) who produced synthetic examples of 30 shots with delay times of 125 ms. They assumed no scatter in the delay times and a maximum frequency of 20 Hz. On the basis of the sharp peaking of the modulation function at frequencies of 8 and 16 Hz they concluded that the number of explosions in the ripple sequences they studied was 4 or less. *Figure 4*, shows the effect of scatter in the delay times for this case. It compares the average amplitude spectrum for 10, 20, and 30% scatter. For 20% scatter the peak at 16 Hz has almost disappeared.

Hedlin *et al.* (1989) discuss a synthetic example with 50 shots having 63 ms delay time and 10% scatter, i.e., σ=6.3 ms. *Figure 5* shows *average* spectra for this case with 10, 20, and 30% scatter in the delay times. Again, the peaks at higher frequencies are strongly suppressed, and for 30% scattering even the first peak at 16 Hz is lowered to 20% of its non-scattered value. The spectral level around the peak is high.

Finally, in *Figure 6* we have calculated the average amplitude spectrum of 16 shots with 50 ms delay to approximate one of the explosions (B) studied by Smith
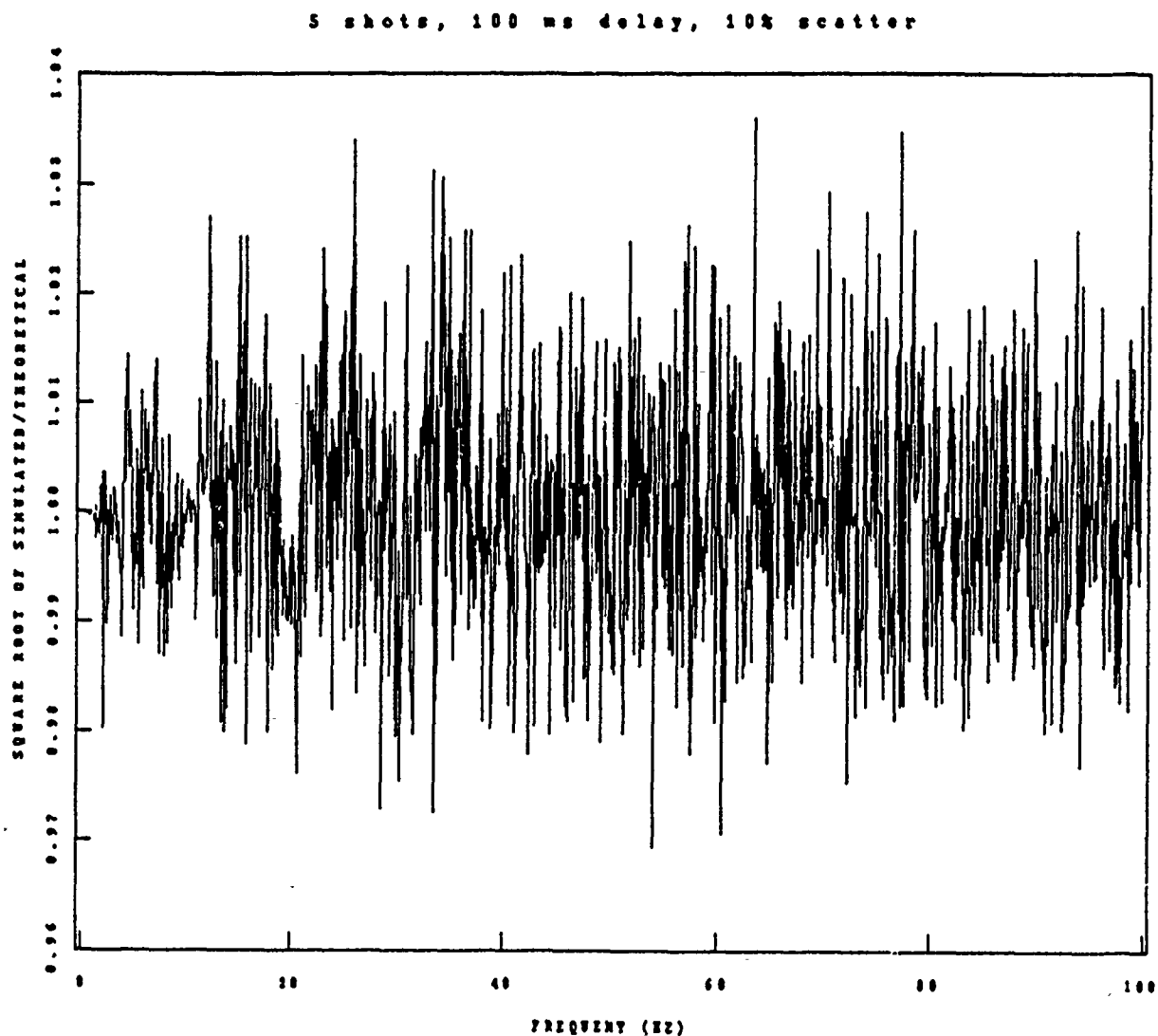
Figure 1. The ratio of the average power spectrum of the modulation function obtained from the analytical expression derived in the text and from 1500 simulations.
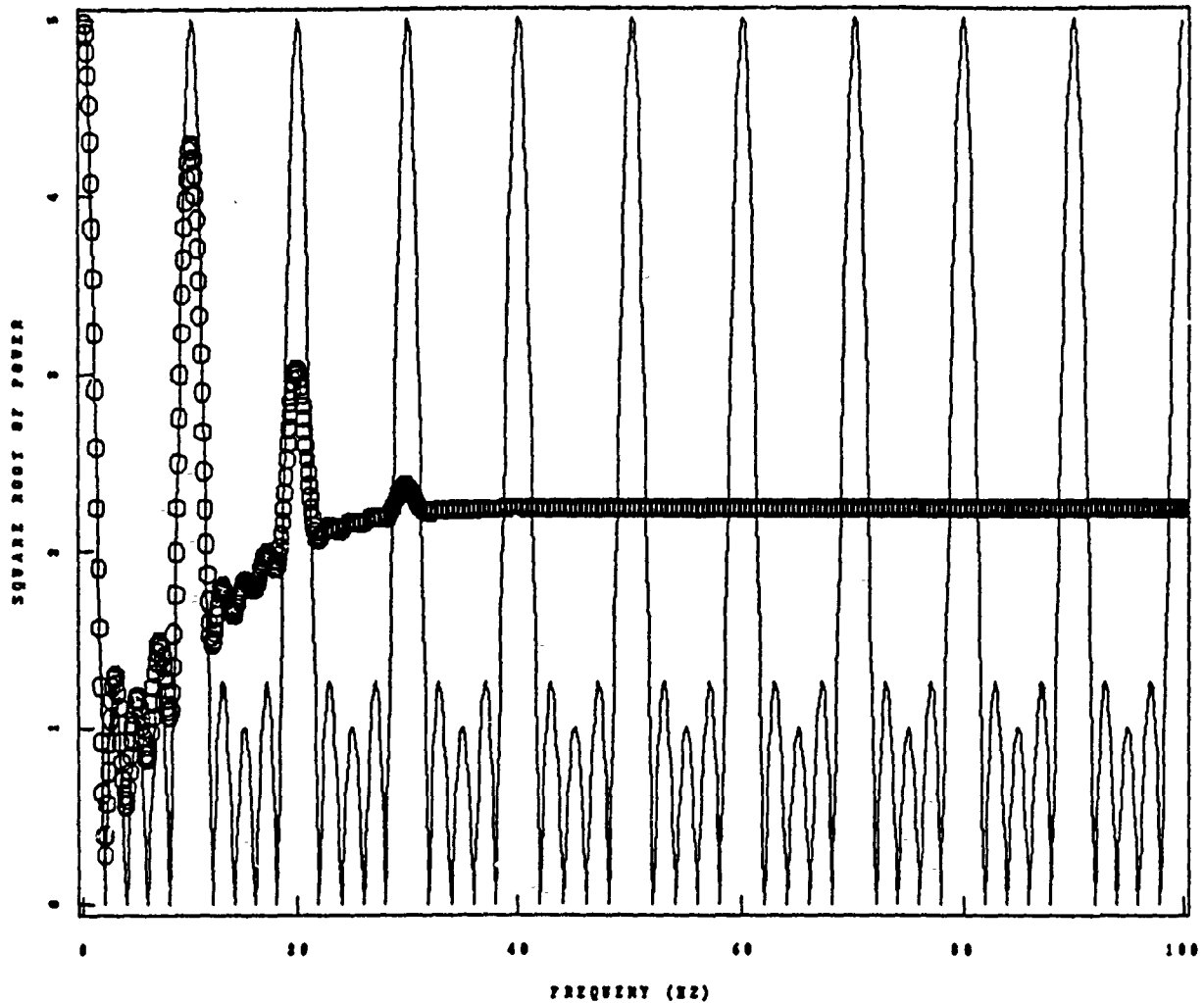
Figure 2. The amplitude spectrum of the modulation function for 5 shots at 100 ms delay and with (circles) and without (lines) scatter in the delay times (10%). The spectrum for the case with scatter represents the average spectrum and was obtained from the formula derived in the text.
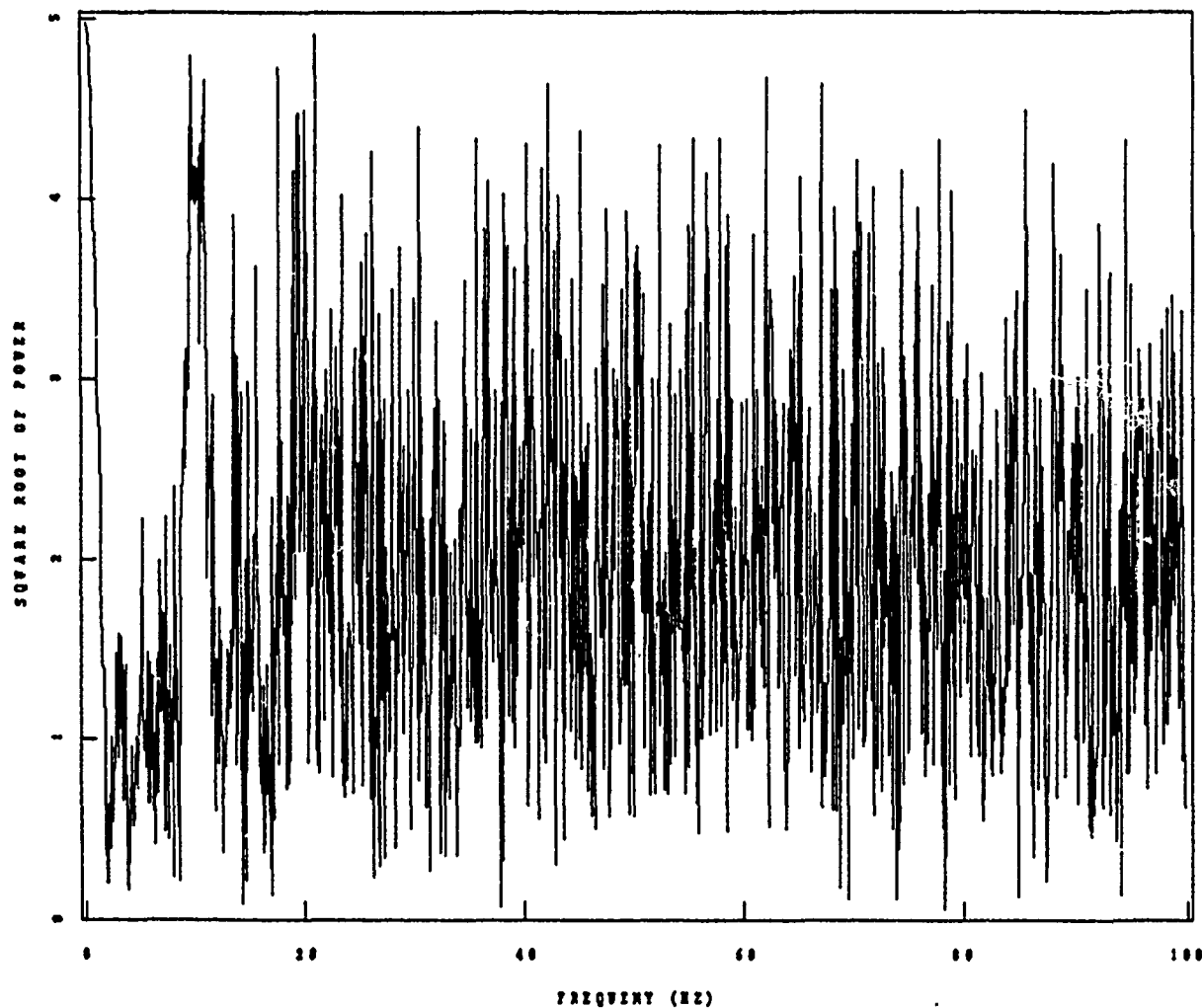
Figure 3. The amplitude spectrum of the modulation function for one simulated ripple firing with 5 shots with 100 ms delay times and 10% scatter in the delay times.
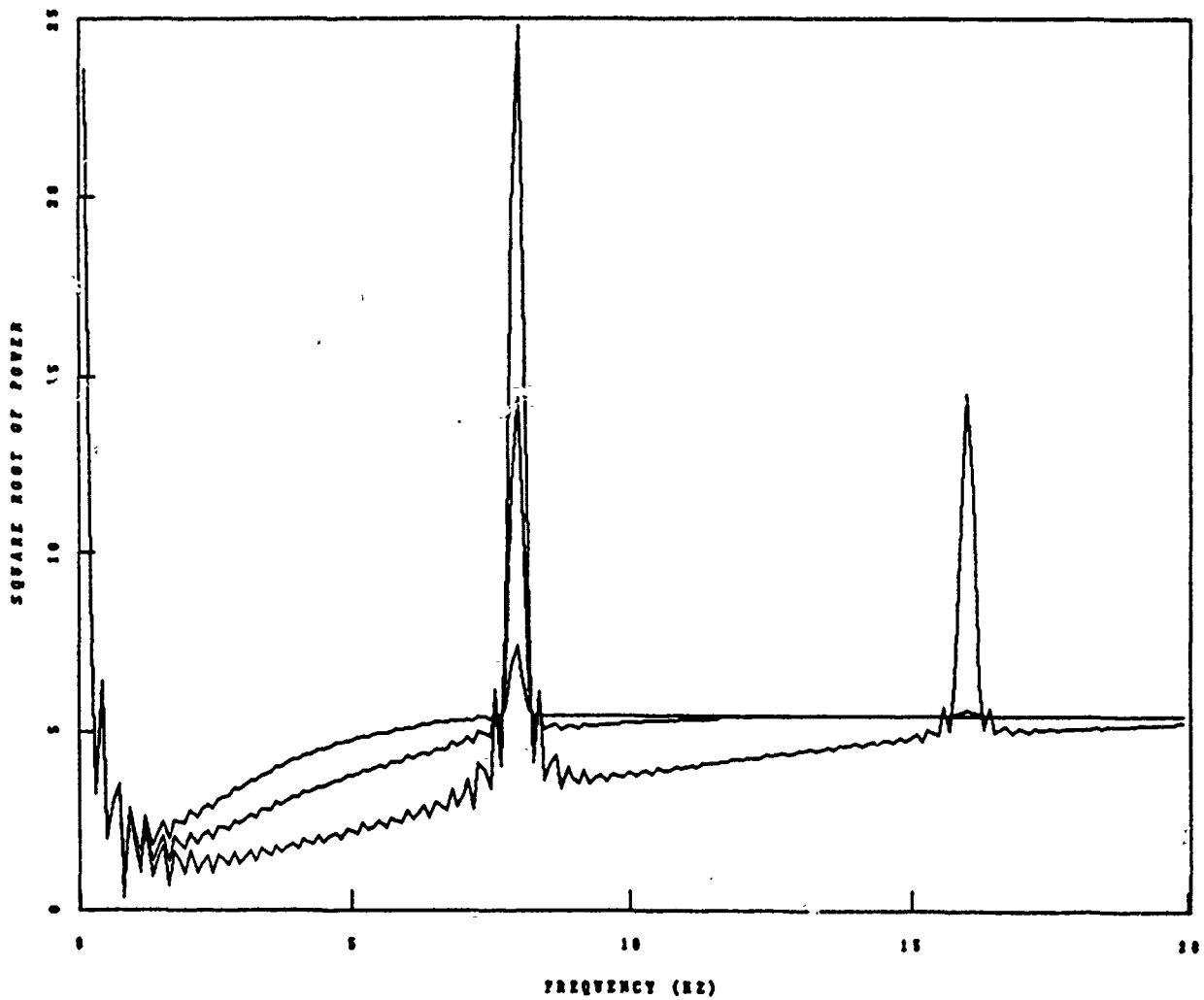
Figure 4. The amplitude spectrum of the modulation function for ripple fire consisting of 30 shots with 125 ms delays and 10, 20, and 30% scatter in the delay times. This is a case studied by Baumgardt and Ziegler (1988).
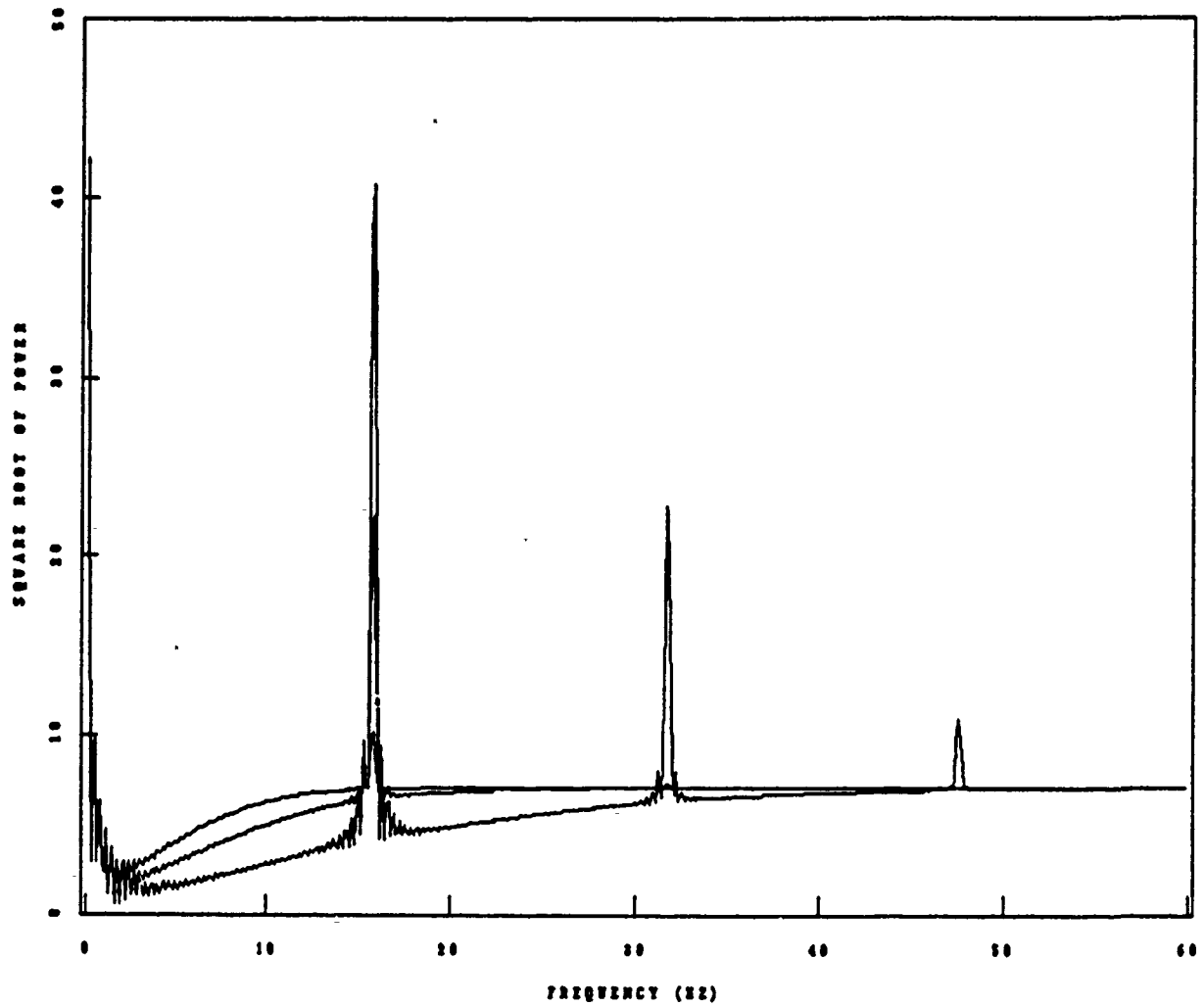
4-39

Figure 5. The amplitude spectrum of the modulation function for ripple fire consisting of 50 shots with 63 ms delays and 10, 20, and 30% scatter in the delay times. This is a case studied by Hedlin et al. (1988).
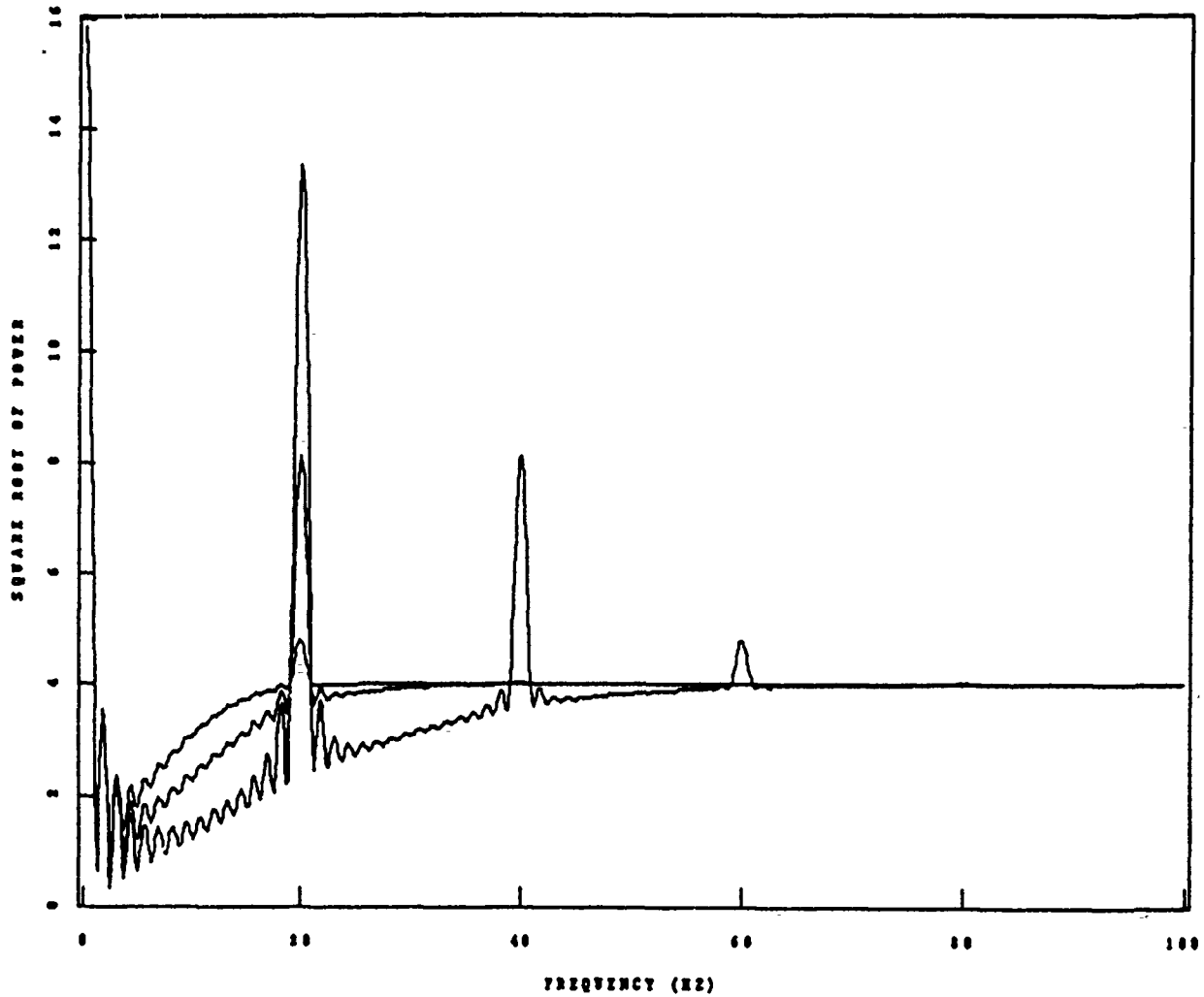
Figure 6. The amplitude spectrum of the modulation functiion for ripple fire con-
sisting of 16 shots with 50 ms delays and 10, 20, and 30% scatter in the delay times.
This approximates a case studied by Smith (1988).

(1989). It can be seen that the "signal-to-noise" ratio of the primary peak for 20% scatter is only about 2. The signal-to-noise ratio of a peak is defined as the amplitude of the peak divided by the level of the power spectrum at frequencies just below and just above the peak.

4.2.4 Conclusions

Simulations of ripple fired explosions with Gaussian delay time errors can be made using an analytical expression for the power spectrum of the modulation function of a standard model for ripple fired explosions. This expression, which accounts for scatter in the delay times, can be used to study the expected effect of spectral peaking and scalloping of the modulation function for various configurations of ripple fired explosions. The computational examples illustrate that a 20% scatter can significantly attenuate the secondary harmonics of the spectrum and reduce the signal-to-noise ratio of the primary peak. This, in turn, makes it more difficult to establish that a recorded seismic signal is from a multiple source through the use of spectral scalloping.

Hans Israelsson

References

Baumgardt, D.R. and K.A. Ziegler (1988). Spectral Evidence for Source Multiplicity in Explosions: Application to regional discrimination of earthquakes and explosions, *Bull. Seism. Soc. Am.*, Vol. 78, pp. 1773-1795.

Hedlin, M. A. H., J. B. Minster and J. A. Orcutt, (1989). The Time and Time-Frequency Characteristics of Quarry Blasts and Chemical Explosions Recorded in Kazakhstan U.S.S.R. *Geophysical Journal*, Vol. 99, pp. 109-122.

Smith, A. T. (1988). High Frequency Seismic Observations and Models of Chemical Explosions: Implications for the Discrimation of Ripple-Fired Mining Blasts. *Bull. Seism. Soc. Am.*, Vol. 79, pp. 1089-1110.

4.3 CHARACTERIZATION OF REGIONAL EVENTS RECORDED AT NORESS AND THE NRDC STATIONS

4.3.1 Introduction

Accurate location and identification of seismic events, and discrimination between various types, such as earthquakes, mine blasts and nuclear explosions depend on our ability to characterize their signals. Characterization of the numerous small events recorded at local and regional distances is complicated by several factors. Low signal-to-noise ratio, complex regional path effects, and interference of various seismic phases contribute to obscure signal characteristics due to source type.

Regional discriminants have been proposed, including P- to S-wave spectral ratios, depth phases, and spectral complexity. The use of signal characteristics to accurately locate and identify repeated events from a given mine or seismic area has also received attention. Recent studies made use of the large database provided by the NORESS regional array. Dysart and Pulli (1988) characterized regional events at NORESS using waveforms, spectra and cepstra. Baumgardt and Ziegler (1988) showed how spectral modulations due to ripple-firing and their corresponding cepstral peaks can help characterize and identify mine explosions. Suteau-Henson and Bache (1988) analyzed series of events at known mines and studied the repeatability of their waveform and spectral characteristics.

Although these methods of event characterization have met with some success, the following questions need to be addressed:

- How does event characterization deteriorate as signal-to-noise ratio (SNR) decreases or epicentral distance increases?

- How do such methods perform for data recorded at a single station without the benefits of array-averaging?

- At NORESS, the analyst can use ancillary information from local seismic networks (operated by Bergen and Helsinki Universities), the location of known mines, and the available knowledge of mining practices. Can characterization techniques help locate and identify events in an "uncontrolled" situation, such as that encountered with data from the NRDC network within the Soviet Union?

In this report we begin to address these questions for events at local and far-regional distance ranges. We characterize events using spectrograms, spanning the frequency range of interest, for a time segment including pre-event noise and the event. We start with a controlled experiment, performed on a dataset of both

earthquakes and mine explosions recorded at NORESS, located at distances of 800 to 1300 km, in a N-NE direction. In a second controlled experiment we analyze calibration shots recorded by the NRDC network of three-component single stations in Eastern Kazakhstan. Then, this technique is tested on a dataset including presumed mine blasts and one earthquake in that area. Finally, recordings at those sites, equipped with instruments from the University of Nevada-Reno (UNR), of the Soviet nuclear explosion from the Joint Verification Experiment (JVE2) are analyzed.

4.3.2 Analysis Technique: Event Spectrograms

The technique used in this report to characterize regional events combines the advantages of waveform and spectral techniques, since it makes it possible to view and analyze the entire seismic wavefield, before and throughout the event, in both time and frequency. Previously, it has been demonstrated that events often show significant characteristics when viewed as a set of bandpass filtered single-channel waveforms or steered beams (Dysart and Pulli, 1988). Baumgardt and Ziegler (1988) use a display showing a set of incoherent beams, filtered in a series of narrow frequency bands. They point out that such incoherent beamforming in the time domain is equivalent to array-averaging in the spectral domain. Alternatively, spectra (and cepstra) of pre-event noise and individual seismic phases for a given event can bring up useful spectral characteristics (Dysart and Pulli, 1988; Suteau-Henson and Bache, 1988).

A concise and powerful display of signal characteristics is provided by a "spectrogram," which shows the variation of spectral content as a function of time for a data segment containing the event. In this report, such spectrograms are displayed as 3-D perspective plots. Such plots can be particularly useful to an analyst because of the amount of visual information present. Other possible displays include contour, half-tone and contour color-fill plots, such as the half-tone displays used by D. Harris (LLNL; work described by K. Nakanishi at 30 November 1988 AFTAC research review).

Spectra are calculated for non-overlapping fixed-length time windows covering pre-event noise and the event itself. In this study we use window lengths of 3 to 5 seconds. The technique of spectral analysis is similar to that used by Suteau-Henson and Bache (1988). Amplitude spectra are calculated for the vertical channel (in the case of single-station data), or for each vertical channel and then averaged over all channels for array data. Then, the amplitude spectra are corrected for the instrument response. The logarithmic amplitude spectra are smoothed. An estimate of pre-event noise is obtained by averaging the logarithmic amplitude spectra over a time segment preceding the event. Finally, this noise spectrum is subtracted to obtain noise-corrected amplitude spectra for each time window. Examples of spectrograms obtained in this way will be given in the following sections.

Analysis of NORESS Events

The Dataset

Our first dataset includes events recorded at the regional array NORESS. All were detected by the Helsinki network, and the Helsinki bulletin also listed their local magnitude, and indicated that most were explosions from known mines. They were located at distances ranging from 800 to 1300 km from NORESS, and in a N-NE direction. They provide a set of events at far-regional distances, with a continental path, and with magnitudes from 2.0 to 3.6. Although the effects of source corner frequency may be significant for the few larger events, we do not attempt any source correction in this qualitative study. Such a correction would not significantly affect the results concerning spectral complexity.

The event information is given in *Table 1*. Locations of the earthquakes and mines are shown in *Figure 1*. About three years of seismic activity have now been recorded at NORESS, providing sequences of repeated events from individual mines and seismic areas. Of particular interest are a set of earthquakes with magnitudes of 2.9 and above from a seismic area in Northern Sweden, and a set of 16 explosions from a nearby mine (designated as "R1" in the Helsinki bulletin). Since these events are located in the same area, spectral differences due to regional path effects are not expected to be dominant, and source effects can easily be observed.

Processing Parameters

Figures 2 through *5* show spectrograms of the events, calculated using the technique described in the previous section. Frequencies range from 0 to 20 Hz. The 50-second long noise segment used to correct for noise starts one minute before the first arrival. The total time segment displayed is 6-minutes long. The window length used for spectral calculation is 5 seconds.

R1 Spectrograms

A set of 16 explosions at mine R1, located about 800 km from NORESS, with Helsinki magnitudes ranging from 2.0 to 2.7 were analyzed. *Figure 2* shows spectrograms for one large and one small event in this set. The others are shown in *Figure A1* in Appendix I. All events have characteristic spectral modulations that last throughout the entire wavetrain. Such distinctive patterns could help an analyst identify an event as an R1 explosion.

The spectrograms show the evolution of spectral content as a function of time for that part of the signal which is above the noise level. The S_n spectral content is very similar to that of P_n for the entire coda. L_g, on the other hand, is characterized by significantly lower frequencies. For larger events, the S_n phase arrives in the P_n coda, therefore, some frequencies are contaminated by P-type signal. A worse contamination occurs for L_g, which arrives in the P_n / S_n coda. Typically, for

Table I: NORESS Events

Event	Date	Origin Time	Lat.(N)	Lon.(E)	Magnitude	Type
85347	12/13/85	16:59:07.	67.1	20.6	2.5	R1
85350	12/16/85	16:44:36.	67.1	20.6	2.5	R1
86010	01/10/86	16:29:35.	67.1	20.6	2.5	R1
86023	01/23/86	16:33:23.	67.1	20.6	2.5	R1
86037	02/06/86	16:29:55.	67.1	20.6	2.7	R1
86045	02/14/86	16:44:08.	67.1	20.6	2.6	R1
86076	03/17/86	16:34:40.	67.1	20.6	2.6	R1
87105	04/15/87	16:34:56.	67.1	20.6	2.0	R1
87156	06/05/87	16:37:42.	67.1	20.6	2.3	R1
87238	08/26/87	16:29:46.	67.1	20.6	2.2	R1
87302	10/29/87	18:33:42.	67.1	20.6	2.0	R1
88025	01/25/88	18:30:19.	67.1	20.6	2.2	R1
88027	01/27/88	16:00:03.	67.1	20.6	2.5	R1
88043	02/12/88	18:30:18.	67.1	20.6	2.1	R1
88060	02/29/88	18:49:42.	67.1	20.6	2.2	R1
88062	03/02/88	18:30:25.	67.1	20.6	2.0	R1
87109	04/19/87	12:39:49.6	67.74	19.45	3.6	earthquake
87147	05/27/87	02:48:02.7	67.74	22.52	2.9	earthquake
87360	12/26/87	08:29:08.7	67.86	19.59	3.4	earthquake
86038	02/07/86	11:00:01.	64.7	30.7	3.1	V10
86049	02/18/86	12:45:50.	64.7	30.7	2.6	V10
88072	03/12/88	09:59:59.	64.7	30.7	2.9	V10
87051	02/20/87	08:51:10.	67.7	33.7	2.6	K1
87081	03/22/87	05:25:12.	67.7	33.7	2.7	K1
87319	11/15/87	03:55:58.	67.7	33.7	3.2	K1

the time segment containing L_g, the low frequencies (less than about 3 Hz) include mostly L_g energy, the high frequencies (above 6 Hz) include mostly energy from the S_n coda, and for the intermediate frequencies the signal is a superposition of both S_n and L_g. Such contamination is observed as well for other mines and earthquakes, as will be shown below. Contamination of L_g by S_n in particular has been recognized as a source of bias for measurements based on spectral estimates, such as inversion for attenuation (Sereno and Bratt, 1988). This effect should be taken into account when using spectra calculated in a time window containing L_g to measure source discriminants (such as cepstral peaks, or P to L_g spectral ratios). For each seismic arrival, the spectrogram can help the analyst identify those parts of the wavetrain (as areas in the time-frequency domain) which are the least
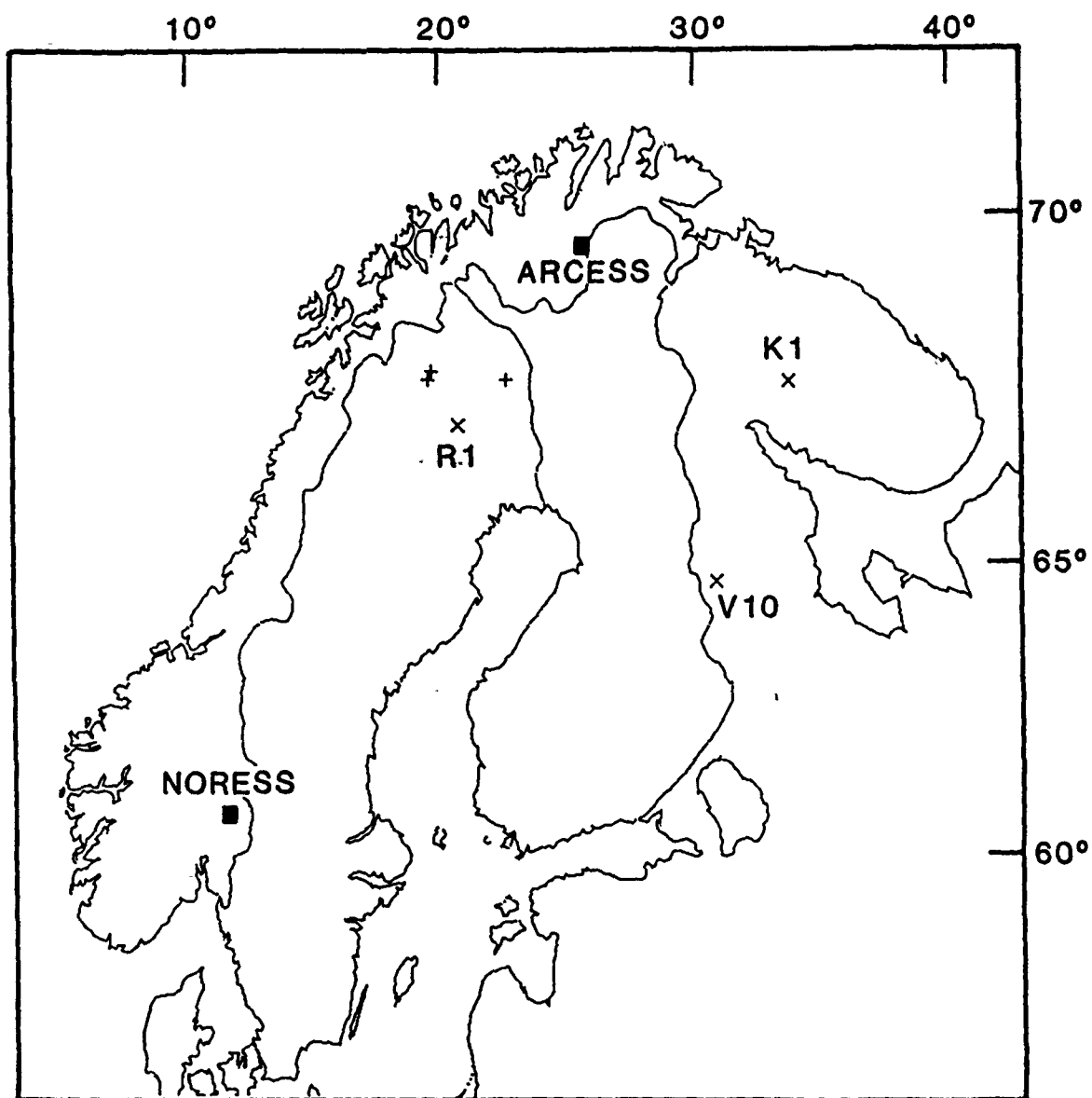
Figure 1. The locations of earthquakes and mines used in this study are shown for the NORESS events listed in *Table I.*
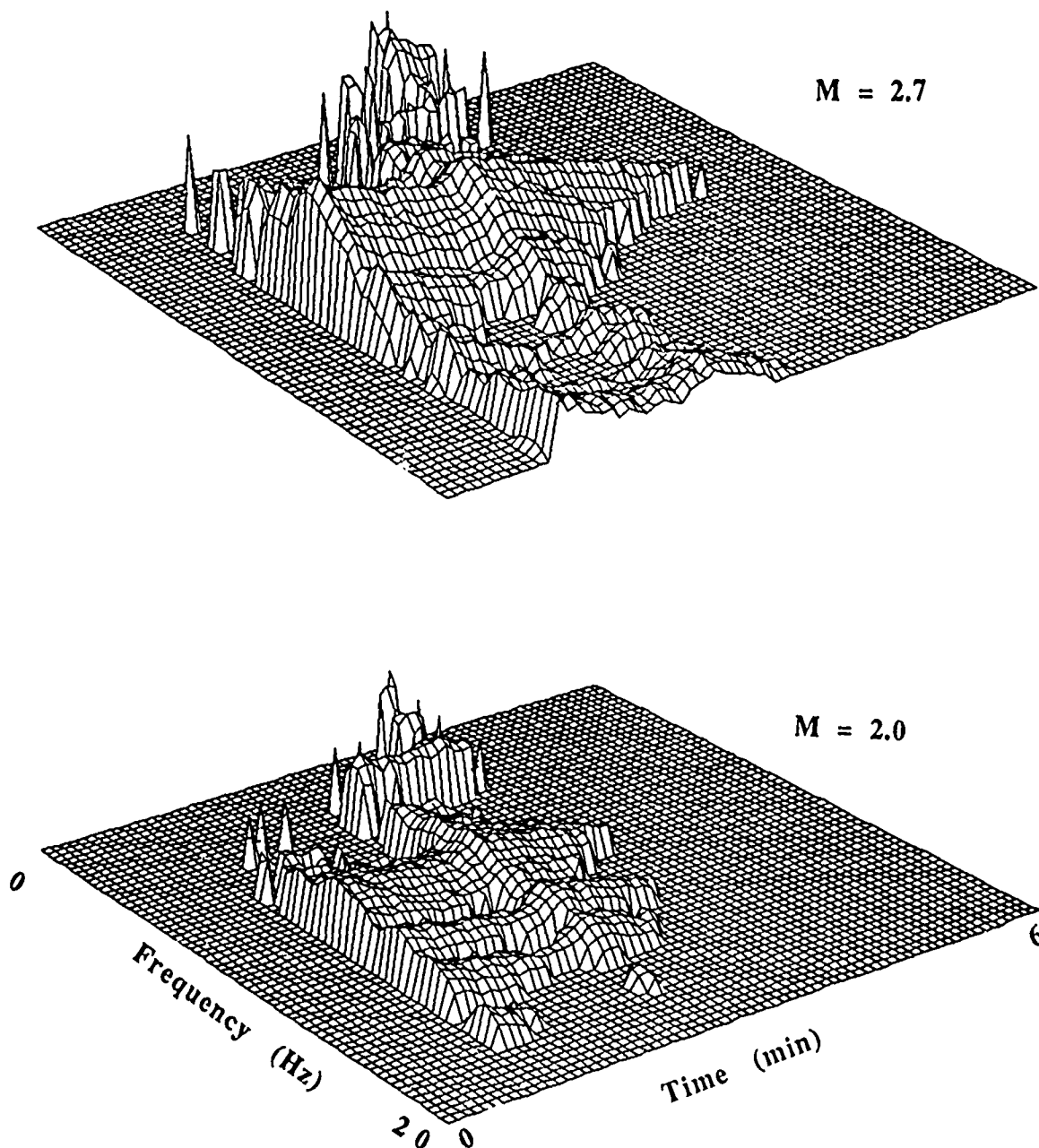
RI Explosions at NORESS

Figure 2. Spectrograms of two explosions from mine R1 (listed in *Table I*) at NORESS -- 86037 (Top) and 87302 (Bottom). The frequency scale is linear, from 0 to 20 Hz; the time scale includes one minute before the P-wave and five minutes after. A logarithmic scale is used for the spectral values, which represent instrument- and noise-corrected spectral amplitudes. Frequencies below 0.5 Hz are masked to avoid spurious peaks due to noise non-stationarity.

Earthquakes at NORESS

M = 3.6

M = 3.4
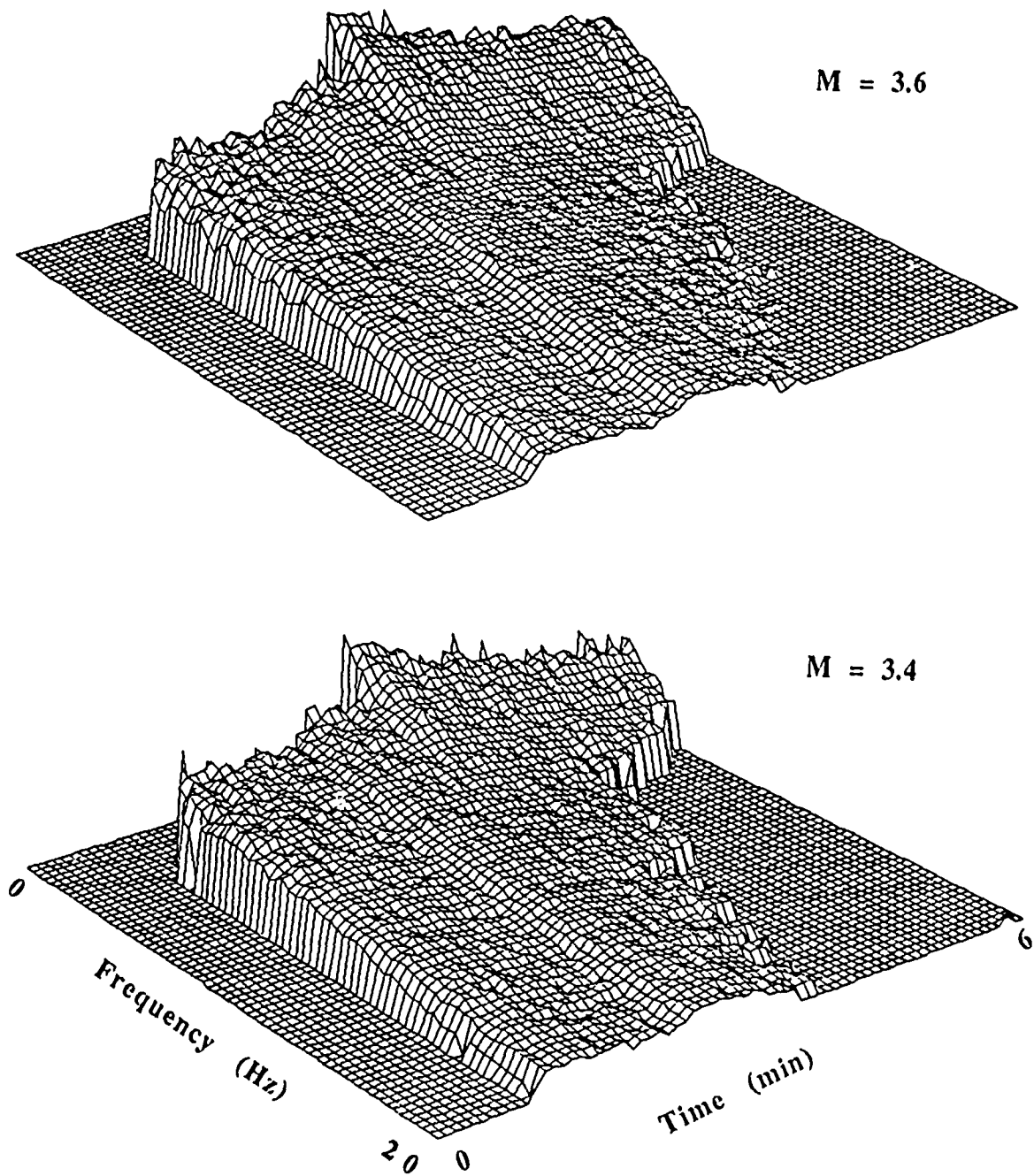
Figure 3. Spectrograms of two Northern Sweden earthquakes (listed in *Table 1*) at NORESS -- 87109 (Top) and 87360 (Bottom). The scale and parameters are the same as in *Figure 2.*
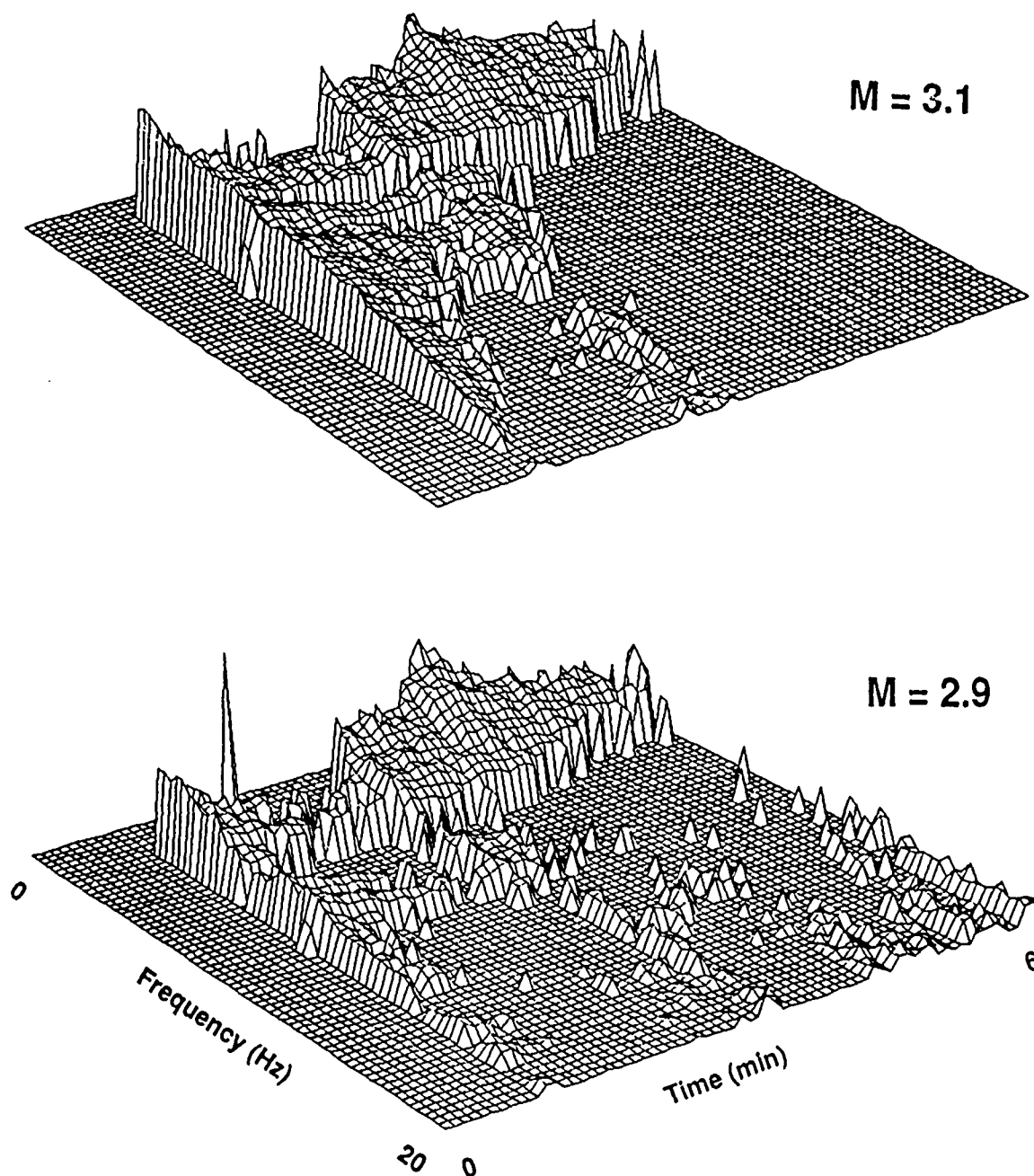
Figure 4. Spectrograms of two V10 explosions (listed in *Table 1*) at NORESS -- 86038 (Top) and 88072 (Bottom). The scale and parameters are the same as in *Figure 2*. High-frequency noise bursts contaminate the spectrogram of event 88072.

K1 Explosions at NORESS

M = 3.2

M = 2.7

Frequency (Hz)

Time (min)
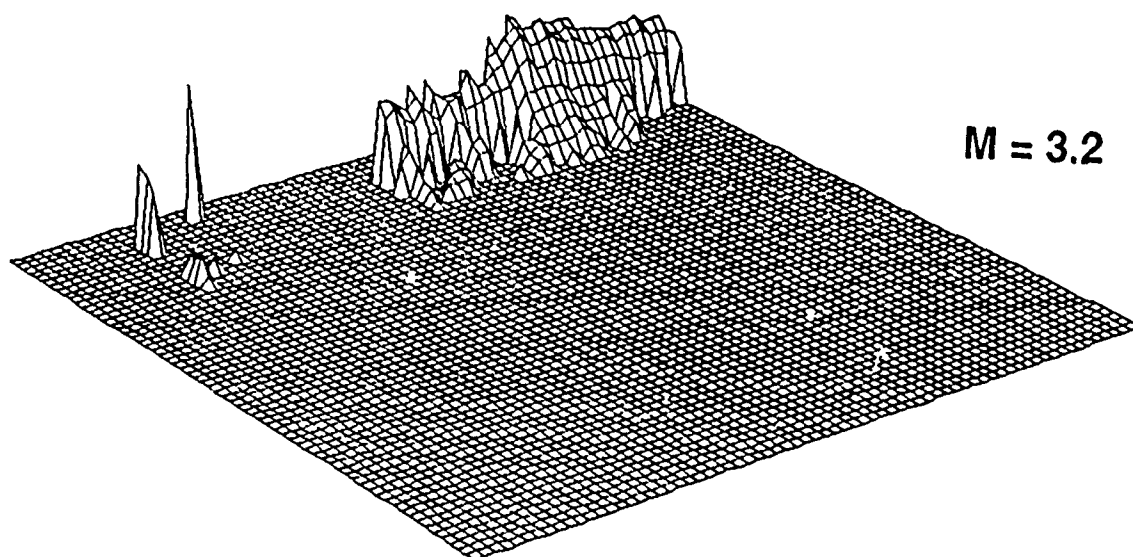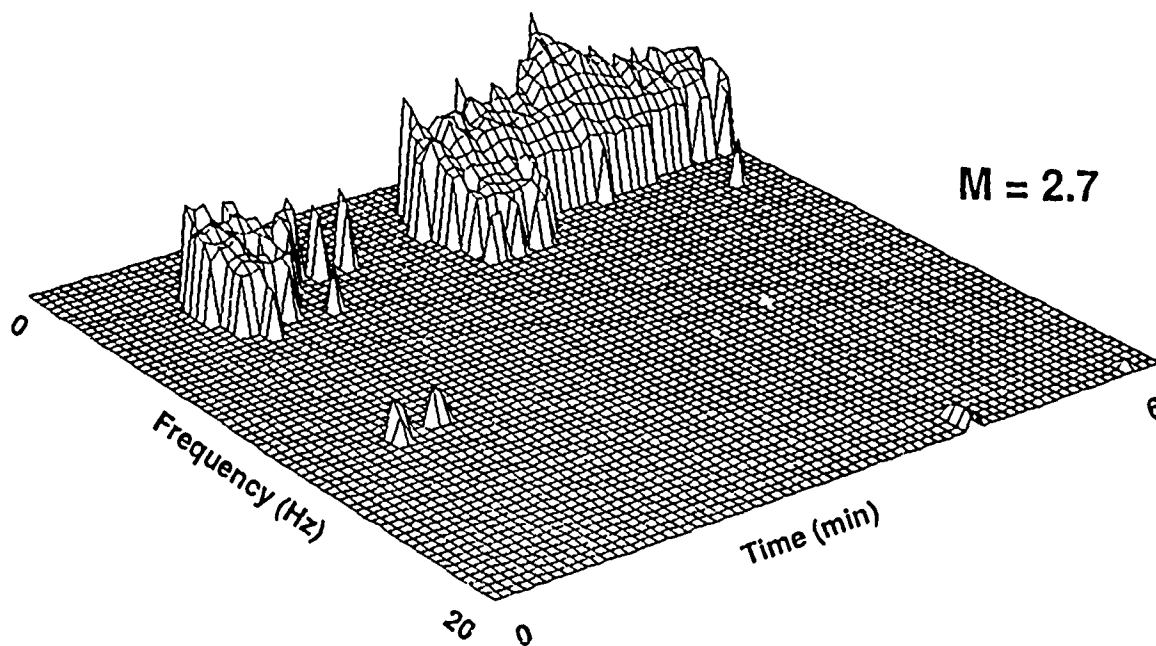
Figure 5. Spectrograms of two K1 explosions (listed in *Table I*) at NORESS -- 87319 (Top) and 87081 (Bottom). The scale and parameters are the same as in *Figure 2*. The low SNR for the large event 87319 is due to high noise conditions.

contaminated by interfering signal from other phases. Such information can then be used for optimal spectral and/or cepstral measurements of potential discriminants.

As expected, the characteristic patterns on the spectrograms become less visible as the magnitude (and SNR) decreases, although they can still be observed for R1 events with Helsinki magnitude as low as 2.0. The effect of varying SNR on the error estimates attached to various discriminants is beyond the scope of this preliminary study.

Earthquake Spectrograms

The spectrograms for two events identified as earthquakes in the Helsinki bulletin are shown in *Figure 3*. Another is displayed in *Figure A2*. As for R1 events, the S_n and P_n spectral contents are very similar for the entire coda, while L_g has much lower frequencies. Also, each secondary phase is contaminated by coda energy from previous arrivals, especially so for larger events. Apart from this, although these earthquakes are located close to mine R1, their signal characteristics, as observed on the spectrograms, are remarkably different from those for R1 explosions. First, the ratio of P to S energy is significantly smaller, as expected. Second, the spectrograms do not show any spectral modulations and are generally lacking in character. They are similar for events 87109 and 87360, located only 14 km apart by the Helsinki network. This is an example of repeated events exhibiting very similar temporal and spectral character.

Spectrograms of Other Explosions

Figures 4 and *5* show s,.ectrograms for events from mine V10 (about 1100 km from NORESS) and mine K1 (about 1300 km), respectively. Others are displayed in *Figure A3*. At V10, some modulations are present for event 88072, but not for the larger event, 86038. At K1, the available signal bandwidth is so narrow, due to strong attenuation of higher frequencies, that spectral modulations such as those at R1 could not be observed. Clearly. for events in the magnitude range of interest, increasing epicentral distance decreases our ability to observe spectral modulations. A similar analysis for V10 and K1 events recorded at ARCESS (at closer range) would provide an interesting comparison. Therefore, along with noise, attenuation due to propagation over large distances (beyond 1000 km) significantly limits our ability to characterize mine explosions using spectral modulations. A quantitative estimation of this effect on characterization parameters and discriminants awaits further study.

The Dataset

In the previous section, we showed how spectrograms could be used to recognize spectral modulations in NORESS events, when not limited by low SNR and/or small bandwidth due to large epicentral distance. In this section we evaluate the use of this technique for events recorded at one or two single stations. The first experiment still represents a controlled situation, i.e., the event type is known. The second experiment is performed on events of unknown type, but presumed to be either earthquakes or mine blasts, based on information provided in the Center database (routine analysis by F. Ryall and R. Baumstark). Also, spectrograms were calculated for the "JVE2" nuclear explosion at the Semipalatinsk Test Site, recorded by UNR at the NRDC sites. *Table II* gives the event information. The NRDC network that operated in 1987 in Eastern Kazakhstan near the Soviet Test Site consisted of three-component seismic stations at Karkaralinsk (KKL), Karasu (KSU) and Bayanaul (BAY). In this study we did not use station KSU, because of a pronounced resonance peak due to near-receiver structure. *Figure 6* shows the locations of the stations and events studied here.

Table II: NRDC/UNR Events

| Event	Date	Origin Time	Lat.(N)	Lon.(E)	Type
710	08/22/87	00:21:39.8	43.79	86.05	earthquake?
763	08/24/87	09:06:54.339	51.55	74.49	blast?
847	08/27/87	10:11:25.738	50.93	73.28	blast?
883	08/28/87	13:33:02.837	51.60	74.80	blast?
886	08/28/87	14:22:27.412	51.58	74.06	blast?
987	09/02/87	07:00:00.001	50.28	72.17	calibration shot
998	09/02/87	08:58:34.834	51.82	75.58	blast?
1001	09/02/87	09:27:05.315	50.03	77.19	calibration shot
1024	09/03/87	07:00:00.001	50.28	72.17	calibration shot
JVE2	09/14/88	04:00:00.	49.87	78.82	nuclear explosion
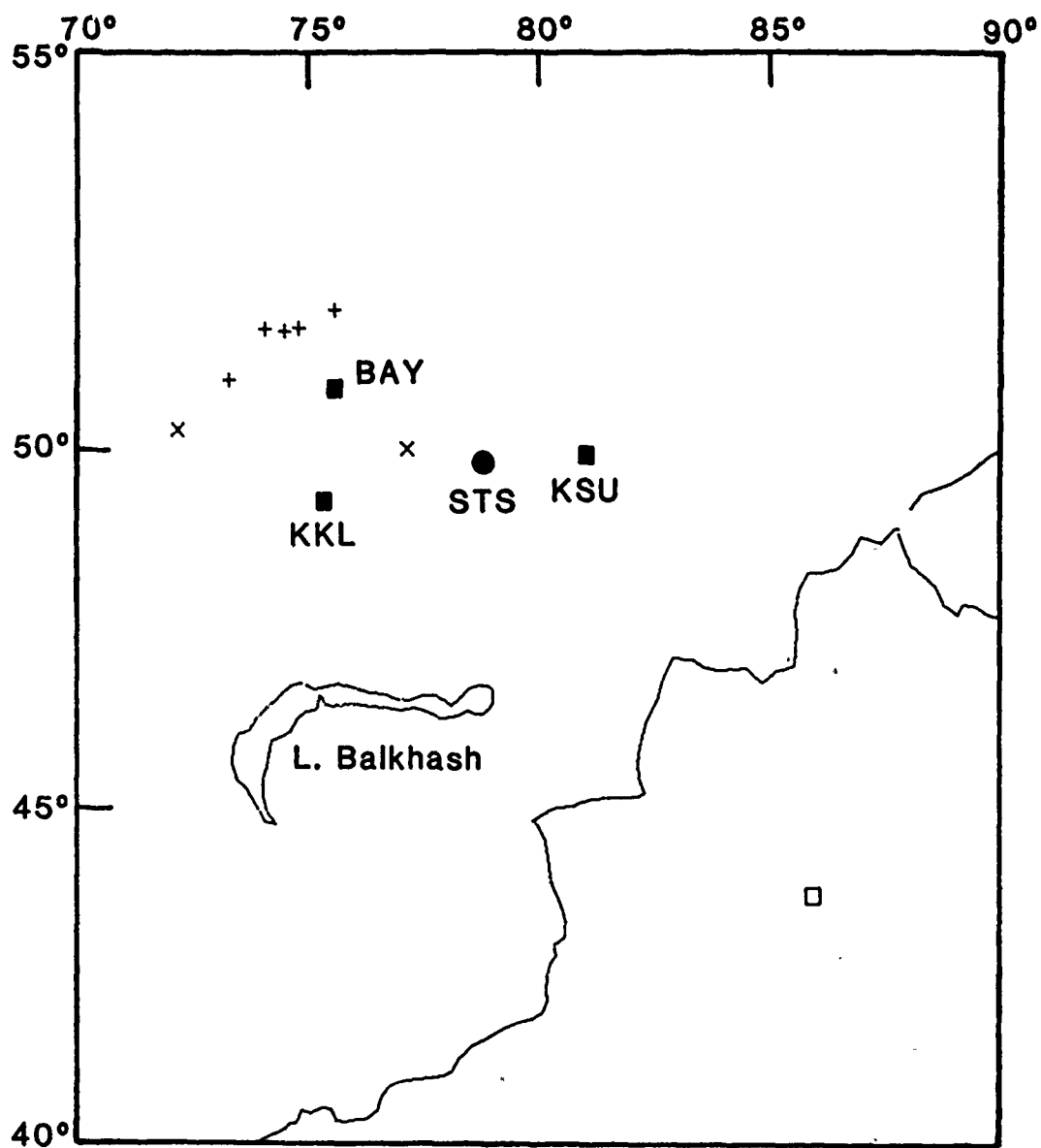
Figure 6. The locations of the Eastern Kazakhstan events used in this study (and listed in *Table II*) are shown. Crosses represent calibration shots; pluses, presumed mine blasts; and the open square, a possible earthquake. "BAY", "KKL" and "KSU" denote the three NRDC stations. "STS" denotes the location of the Semipalatinsk Test Site.

Processing Parameters

The NRDC short-period, high-gain data we used were sampled at 250 samples/second, corresponding to a Nyquist frequency of 125 Hz. In practice, we found that the useful frequency range could be limited to half of that, i.e., 62.5 Hz. Most events were within 200 km of the recording stations, and the amplitude spectra were calculated over 3-second windows (4 seconds for event 710 at larger distance). Frequencies below 1 Hz are masked, because of noise contamination at lower frequencies. Also, since continuous data are not available, the amount of noise preceding the event and the length of recording vary from event to event.

The UNR short-period data were sampled at 100 samples/second at BAY and 200 samples/second at KKL. To facilitate the comparison with the NRDC data, we plotted the UNR spectrograms for frequencies up to 62.5 Hz (padding to zero frequencies above 50 Hz for BAY). The instrument correction applied is the same as for NRDC, except for a nominal free period of 1 second.

Spectrograms of the Calibration Shots

Figure 7 shows the spectrograms obtained at stations BAY and KKL for a known H.E. calibration shot that occurred in September 1987. *Figure A4* in Appendix I shows the spectrograms for two other shots. These shots are single explosions, as opposed to multiple explosions produced by "ripple-firing" in mines such as Swedish mine R1. As expected, no spectral modulations are observed. In spite of the smoothing applied to the spectra, there are many noise peaks. Since no array-averaging could be performed, the non-stationarity of the noise produces such peaks. Also, the scatter in the spectrograms is significantly larger than for NORESS events, increasing the uncertainty attached to our characterization technique.

Spectrograms of Unidentified Events

Next, we calculated spectrograms for a set of unidentified events. Identification hypotheses can be made, however, based on location, origin time, P to S amplitude ratio, and the presence of an R_g phase. *Figure 8* shows spectrograms for a presumed mine blast, at both stations BAY and KKL. More are given in *Figure A5* in Appendix I. As for the calibration shots, these events are located within 2.5 ° from the stations. Some of them show spectral modulations (event 883 has similar modulations at both BAY and KKL, and events 763 and 847 at BAY), but others do not. Hedlin *et al.* (1988) report observing such modulations for explosions recorded at the NRDC stations. The spectrograms for a presumed earthquake at about 1000 km from both stations are shown in *Figure 9*. They have no complex character, as expected.

Calibration Shot at NRDC

BAY
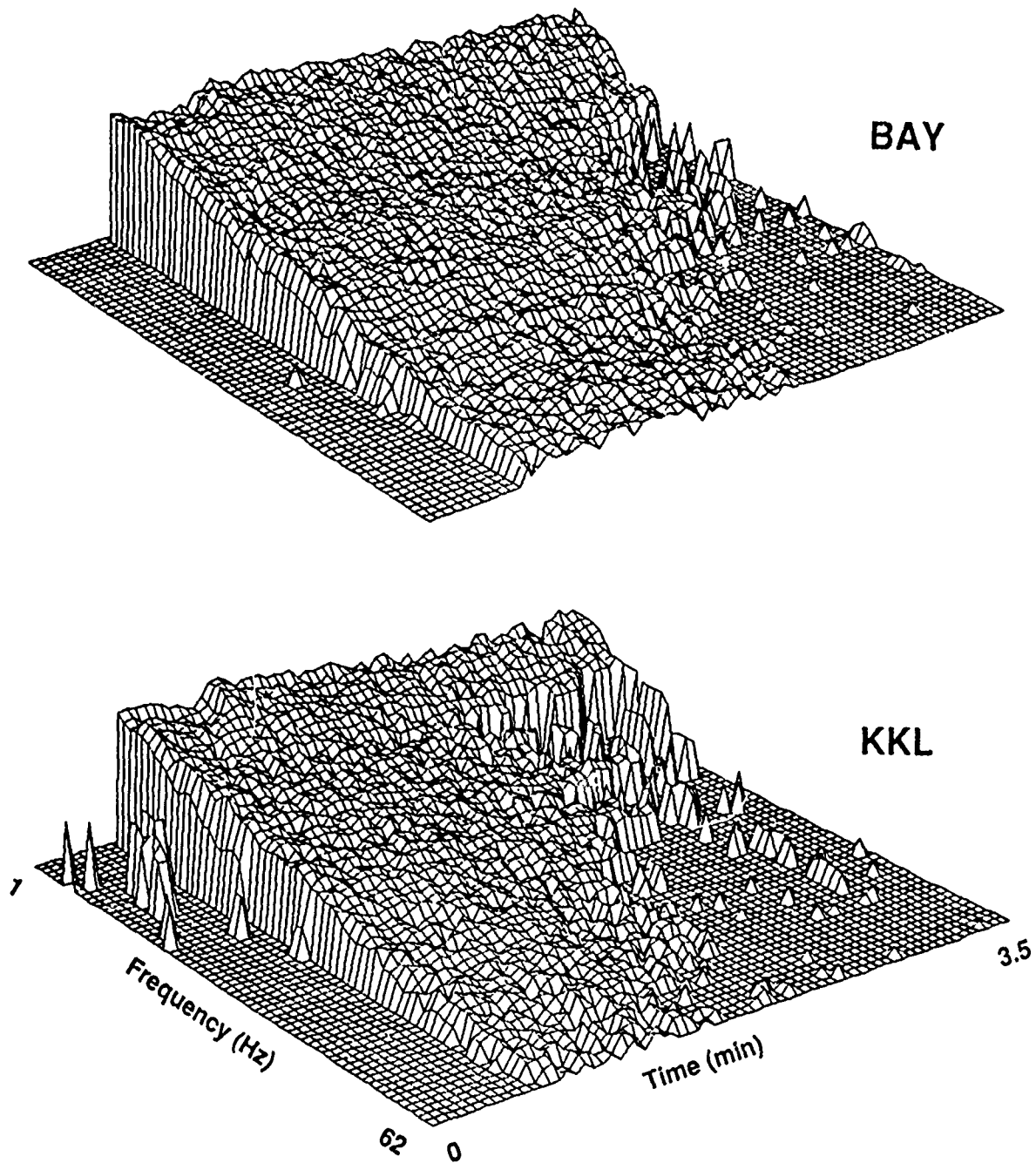
KKL

Frequency (Hz)

Time (min)

1

3.5

62 0

Figure 7. Spectrograms of an NRDC calibration shot (event 987, *Table II*) at stations BAY and KKL are plotted, for frequencies ranging from 1 to 62 Hz. The time segment is 3.5-minute long. A logarithmic scale is used for the spectral values, which represent instrument- and noise-corrected spectral amplitudes.
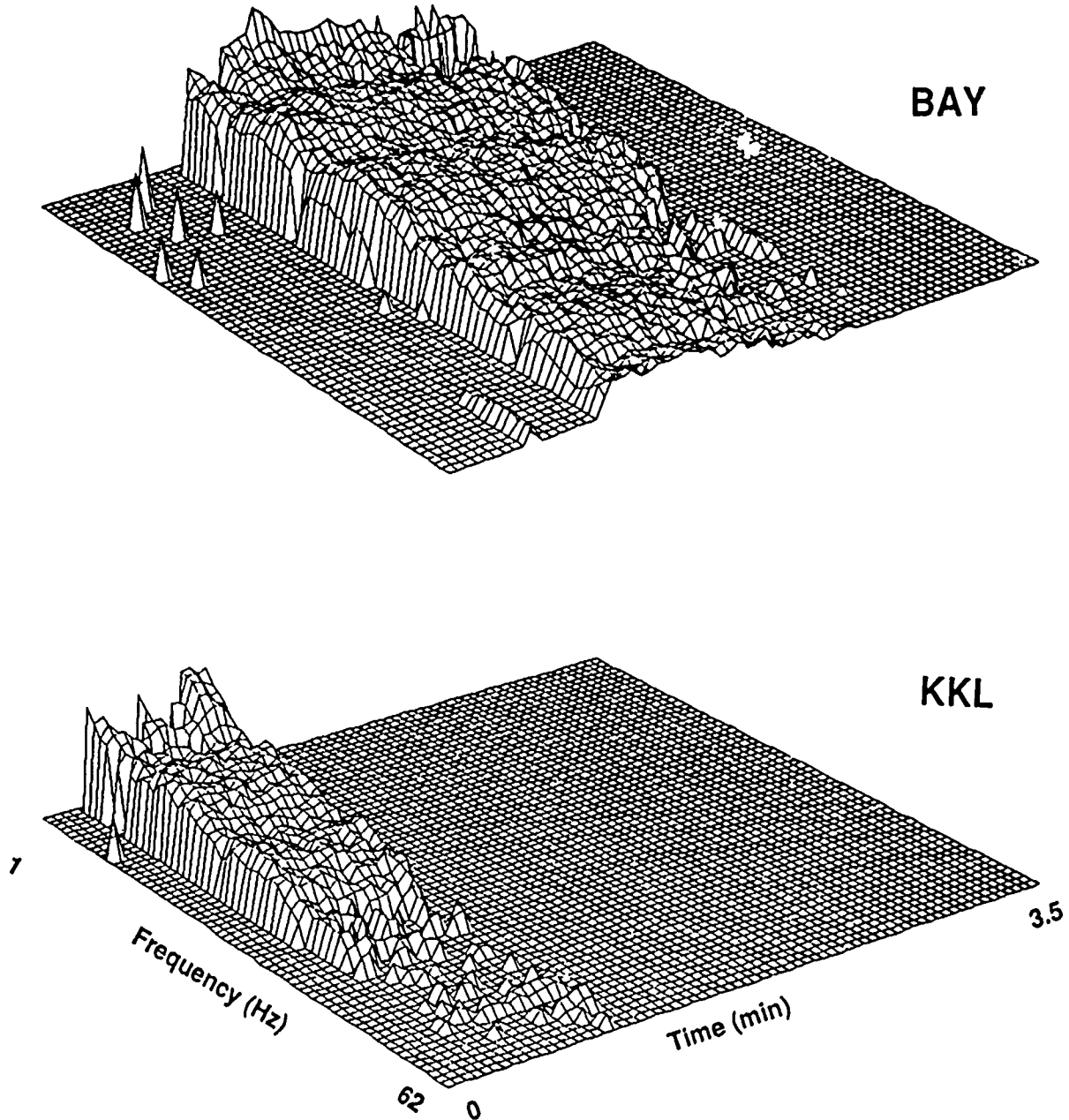
BAY

KKL

Frequency (Hz)

Time (min)

Figure 8. Spectrograms of a presumed mine blast (event 883, *Table II*) at stations BAY and KKL. The scale and parameters are the same as in *Figure 7.* Times beyond the end of the recorded data are masked.

Earthquakes at NRDC

BAY

KKL

Frequency (Hz)

Time (min)
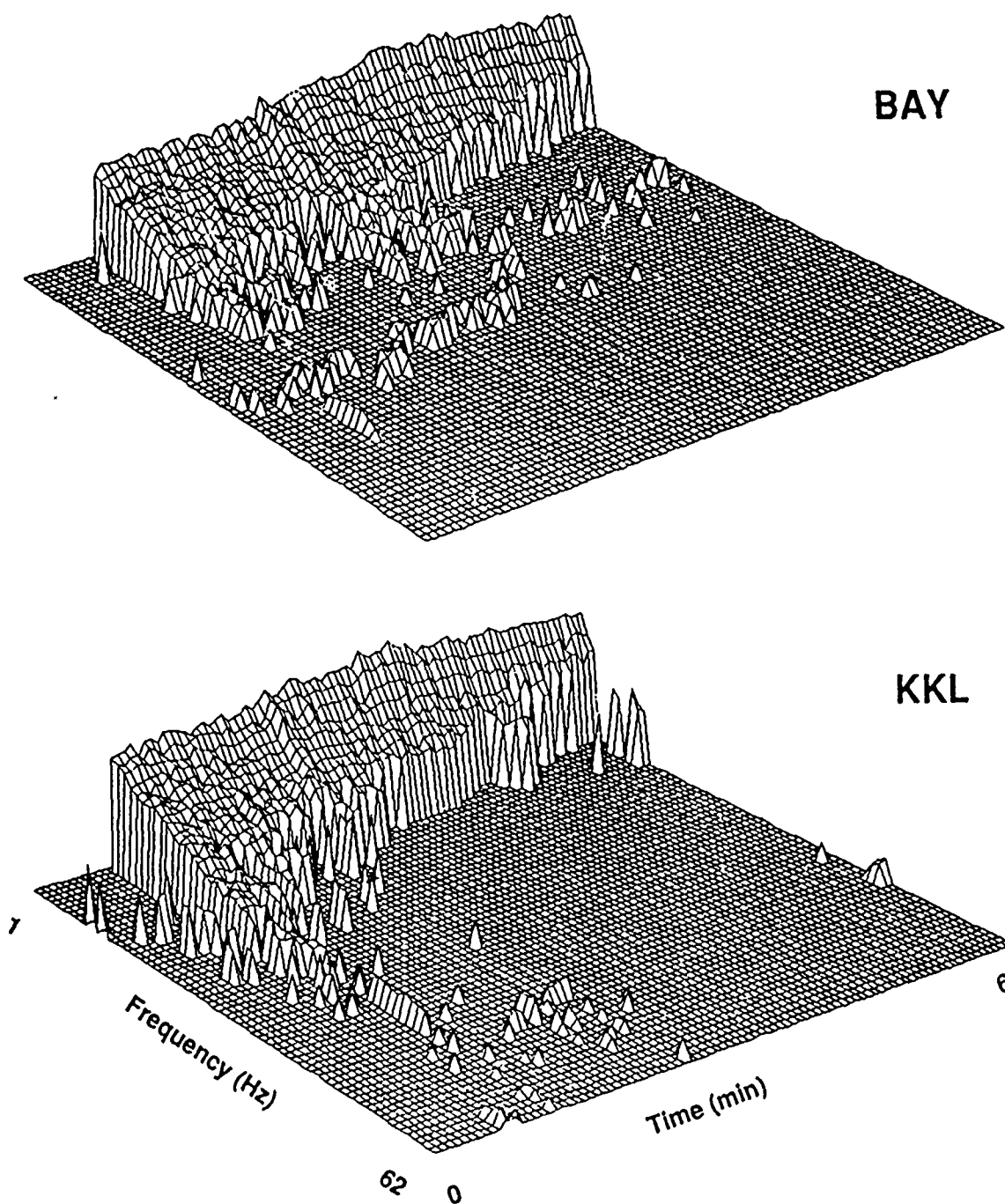
Figure 9. Spectrograms of a presumed regional earthquake (event 710, *Table II*) at stations BAY and KKL. Six minutes of data are shown. Other parameters are the same as in *Figure 7.*

The presence of spectral modulations can be used to confirm or establish the identification of an event as an explosion, although the scatter in the data increases the uncertainty on such an estimation. If distinctive spectral modulations are not observed, no conclusion can be drawn as to the event type.

Spectrograms of JVE2 Nuclear Explosion

Last, we obtained spectrograms for a nuclear explosion, the JVE2 event at the Soviet Test Site, recorded at stations BAY and KKL using UNR instruments. They are shown in *Figure 10*. As can be seen in *Figure 6*, the epicentral distance is about the same for both stations, and very similar to that for the calibration shots 987 and 1024. As expected, no spectral modulations are observed. Above about 30 Hz, the spectral amplitude (when above noise level) remains roughly constant, instead of continuing to decay, as it does for the calibration shots (see *Figures 7* and *A4*). This is observed at both BAY and KKL, and on all three components, and seems to indicate some noise contamination. *Figure 11a* compares the unfiltered data on the vertical at KKL and the same data highpass filtered above 30 Hz. The filtered data follow the envelope of the unfiltered data (except for the long-period R_g), indicating a correlation between the high-frequency part of the data (above 30 Hz) and the seismic signal. However, a closer look (*Figure 11b*) shows that the filtered data are composed of spikes. These correlate with the main pulses in the unfiltered data. This is consistently observed on all components at both stations. The character of the data above 30 Hz seems to indicate an instrument-related artifact, correlated with the actual signal. We cannot ascertain at this time that the source of the JVE2 event was particularly rich in higher frequencies.

4.3.3 Summary

A preliminary investigation of the use of spectrograms for characterization of regional events has been presented. Spectrograms were displayed as 3-D perspective plots. We have shown how they can be a useful tool to characterize events, especially during an analyst review. Spectral analysis methods performed on "time slices" around a secondary arrival have shortcomings and limitations, due to signal contamination with coda of previous arrivals in some frequency ranges. The use of spectrograms can help overcome these limitations.

This method was used in a controlled experiment for events recorded at NORESS and located at source-receiver distances of 800-1300 km. For a large set of explosions from Swedish mine R1, very distinctive patterns of modulations were present on the spectrograms, down to local magnitudes of 2.0. Such patterns were not usually observed for western U.S.S.R. mines V10 and K1, at larger distances, although more data should be analyzed before definite conclusions can be reached. Along with low SNR, small bandwidth due to attenuation of high frequencies limits the usefulness of spectral modulations as a discriminant at distances beyond 1000
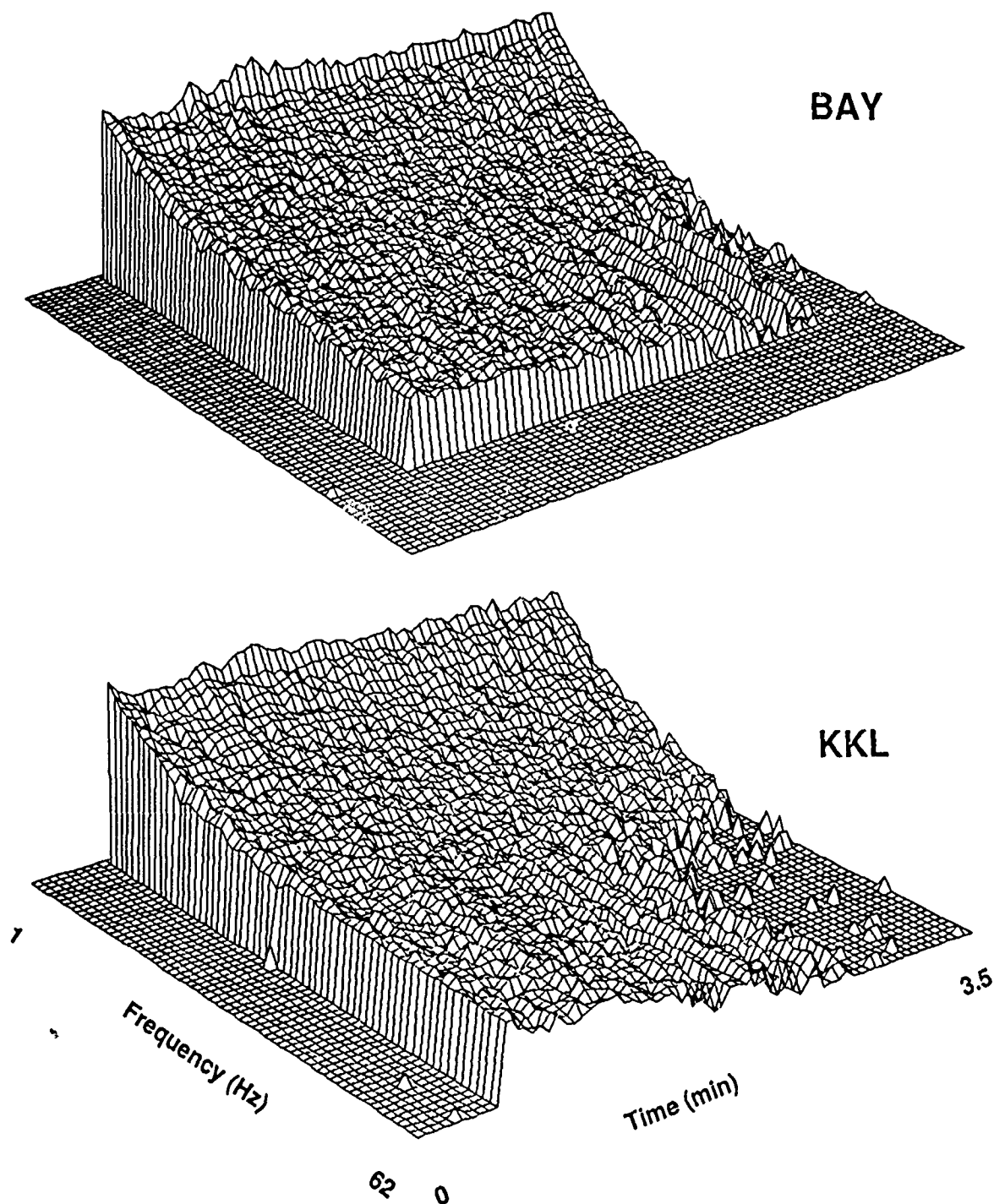
Figure 10. Spectrograms of the JVE2 nuclear explosion at the Semipalatinsk Test Site (Event JVE2, *Table II*), recorded at stations BAY and KKL by the University of Nevada-Reno. The scale and parameters are the same as in Figure 7. The BAY data are masked beyond their Nyquist frequency of 50 Hz.
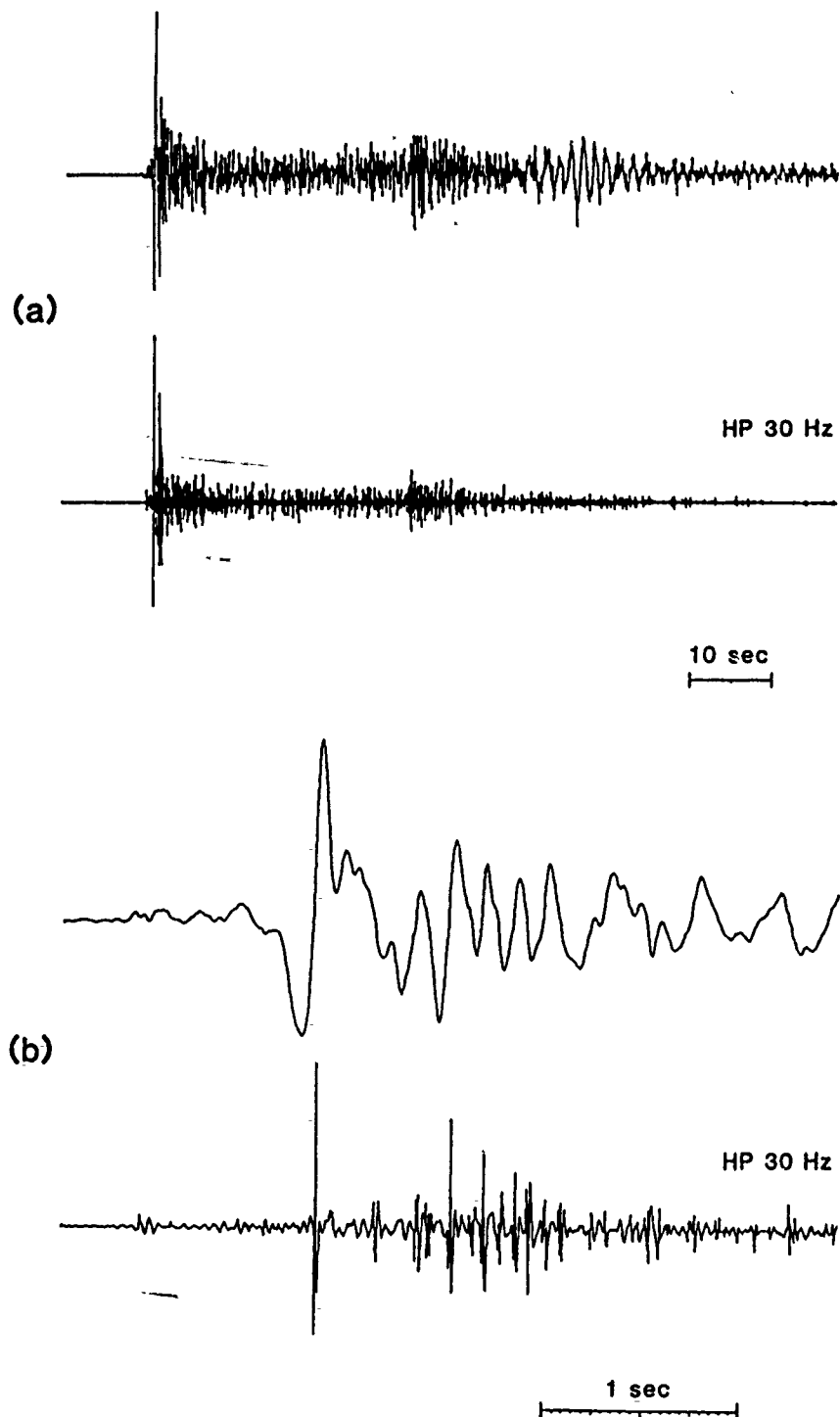
Figure 11. (a): Vertical recording of the JVE2 event at station KKL: unfiltered (Top) and 30 Hz highpass filtered (Bottom). The filtered data have an envelope similar to that of the unfiltered short-period data. The amplification factor for the filtered data is 10.7. (b): Same as (a), except the beginning of the event is blown up. The filtered data show spikes, correlated with the main pulses in the seismic signal.

km, although events with magnitude larger than 2.6 can still be detected and located by an array such as NORESS.

Events (mostly local) recorded at NRDC stations BAY and KKL in Eastern Kazakhstan were analyzed. The scatter in the spectrograms is larger than at NORESS, due to the lack of array-averaging. Three H.E. calibration shots do not show any spectral modulations, as expected for single shots. Some presumed mine blasts show spectral modulations due to ripple-firing, while some do not. A presumed regional earthquake has the expected smooth spectral character. Therefore, spectrograms can still be used as part of event identification at single stations, when no information from independent networks is available. The presence of spectral modulations indicates that a given event is a mine blast, while their absence is inconclusive. We also analyzed UNR recordings of the JVE2 nuclear explosion at stations BAY and KKL. Their spectrograms do not show any spectral modulations.

To better evaluate the usefulness of this characterization method, we plan to analyze more data, in particular ARCESS data. The use of interactive graphics by an analyst, to compare spectrograms of unidentified and reference events, and measure characterization parameters using carefully selected parts of the spectrogram, will also be evaluated.

Anne Suteau-Henson

REFERENCES

Baumgardt, D. R. and K. A. Ziegler (1988). "Spectral Evidence for Source Multiplicity in Explosions: Application to Regional Discrimination of Earthquakes and Explosions," *Bull. Seism. Soc. Am.*, vol. 78, pp. 1773-1795.

Dysart, P. S. and J. J. Pulli (1988). "Waveform and Spectral Characteristics of Regional Earthquakes and Chemical Explosions Recorded at the NORESS Array," in *Center for Seismic Studies Tech. Rept. C87_03*, 35 pp.

Hedlin, M. A. H., J. B. Minster and J. A. Orcutt (1988). "The Time and Time-Frequency Characteristics of Quarry Blasts and Chemical Explosions Recorded in Kazakhstan U.S.S.R. (abstract)," *EOS, Trans. Am. Geophys. Union*, vol. 69, p. 1331.

Sereno, T., S. Bratt, and T. Bache, (1988). "Simultaneous inversion of Regional Wave Spectra for Attenuation and Seismic Moment in Scandinavia", *J. Geophys. Res.*, vol. 93, pp. 2019-2035.

Suteau-Henson, A. and T. C. Bache (1988). "Spectral Characteristics of Regional Phases Recorded at NORESS," *Bull. Seism. Soc. Am.*, vol. 78, pp. 708-725.

APPENDIX I

Spectrograms of Other Events
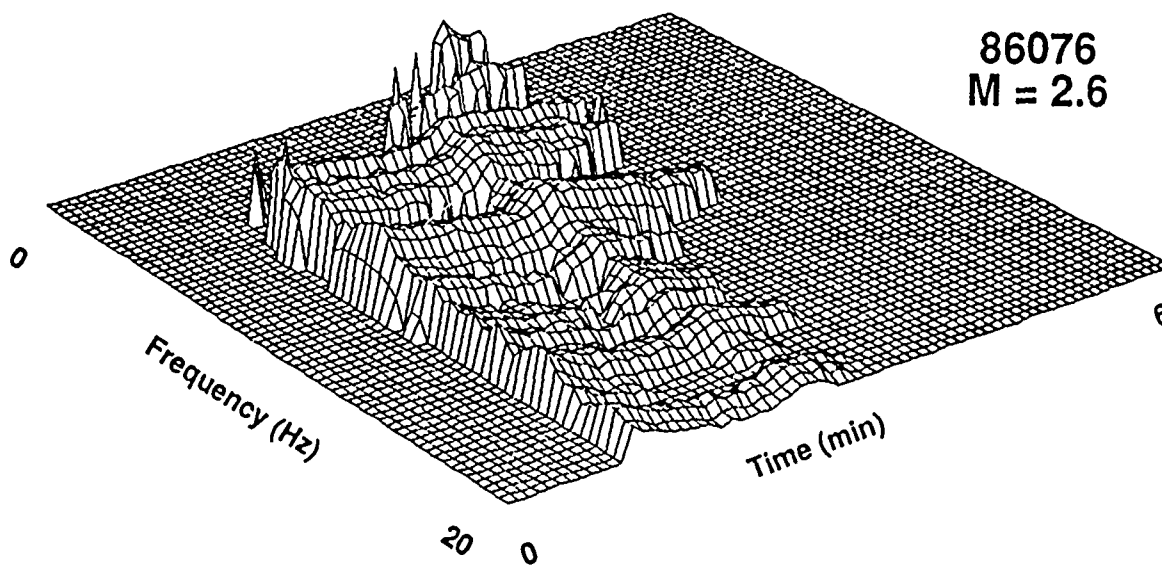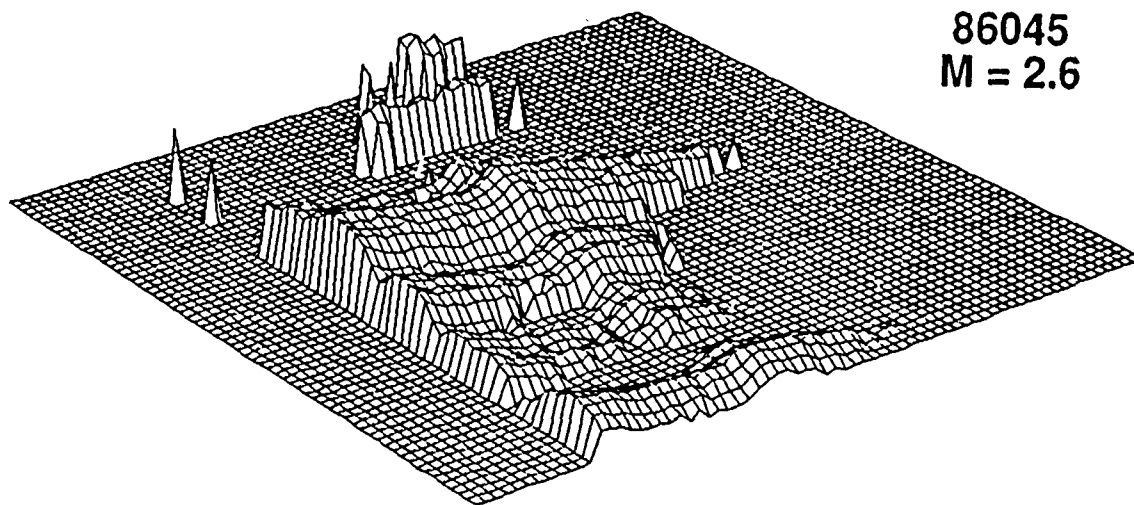Listed in *Tables I and II*

R1 Explosions at NORESS

Figure A1. Spectrograms of R1 explosions (listed in *Table 1*) at NORESS. The scale and parameters are the same as in *Figure 2*.
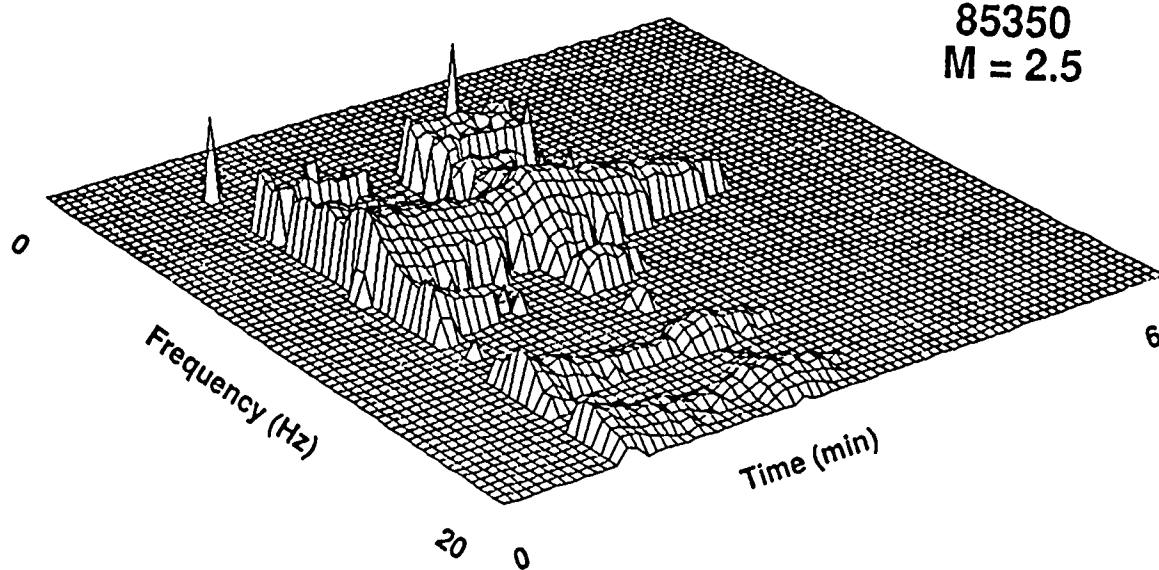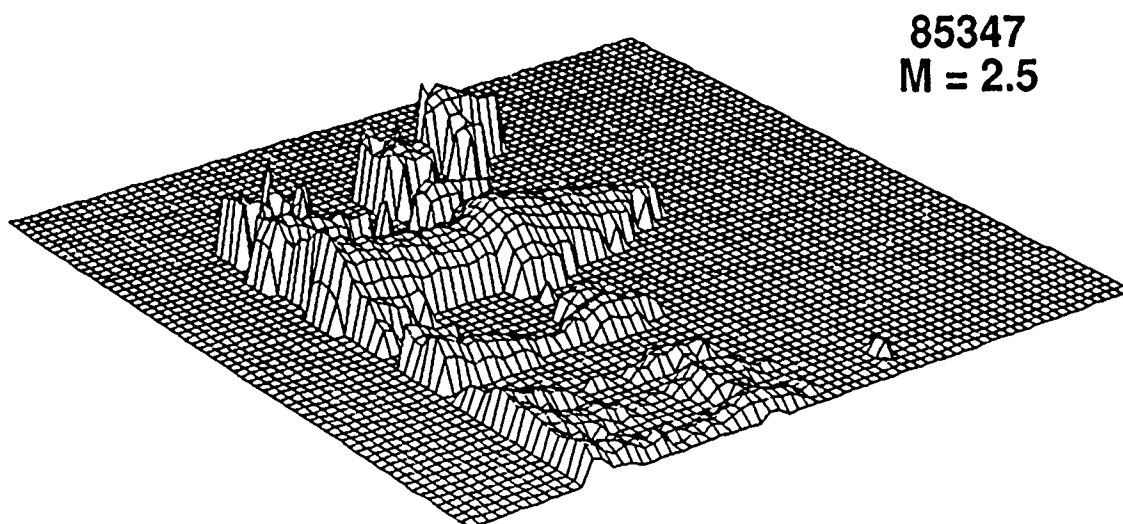
85347
M = 2.5

85350
M = 2.5
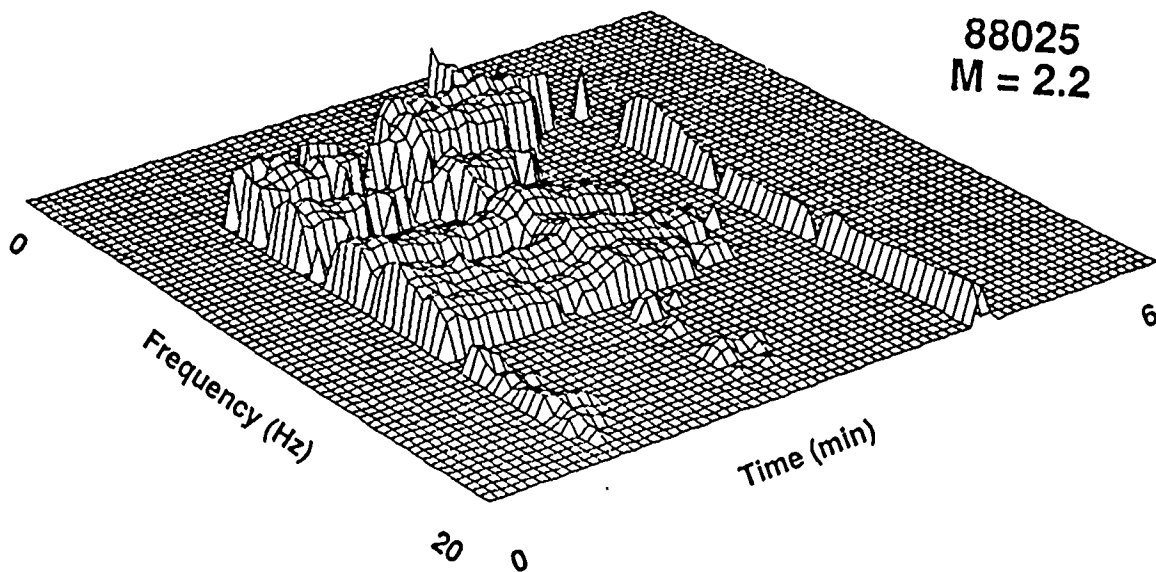
0

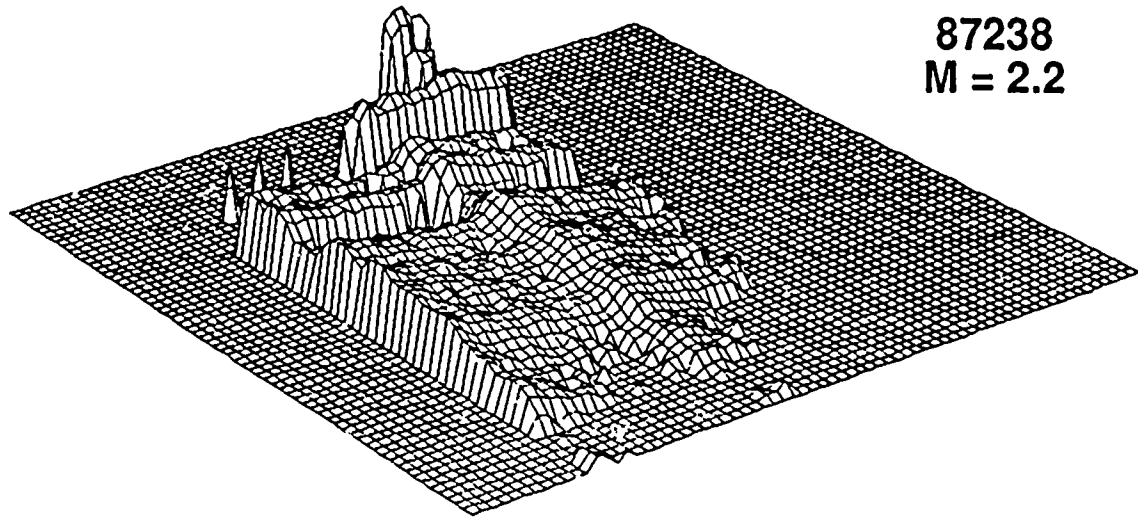Frequency (Hz)

6

Time (min)

20   0

Figure A1 -- (Continued)

R1 Explosions at NORESS

86010
M = 2.5
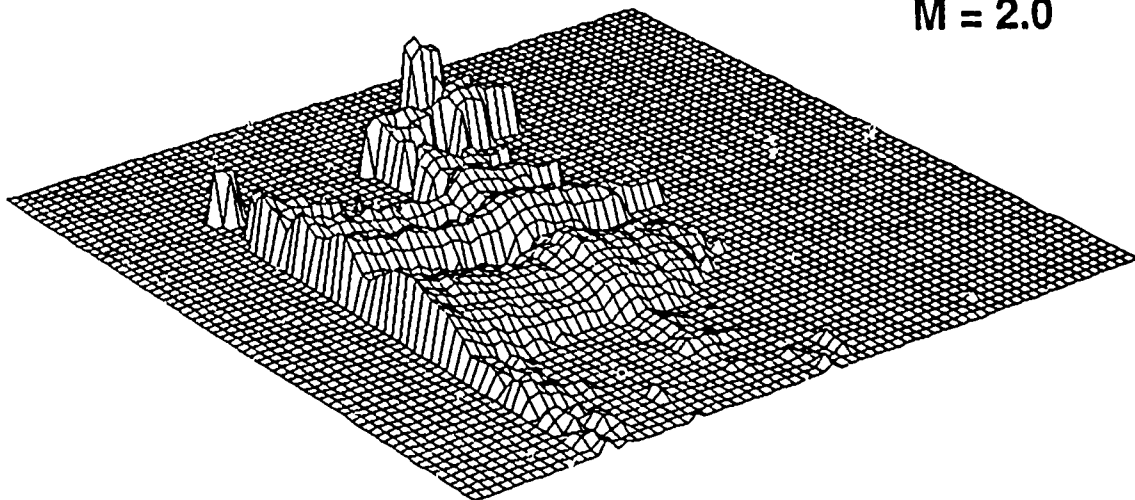
86023
M = 2.5

Figure A1 -- (Continued)

Figure A1 -- (Continued)

87238
M = 2.2

88025
M = 2.2

Frequency (Hz)

Time (min)

0

6

20   0

Figure A1 -- (Continued)

Figure A1 -- (Continued)

87105
M = 2.0

88062
M = 2.0

Frequency (Hz)

Time (min)

0

20   0

0

6

Figure A1 -- (Continued)

M = 2.9

Frequency (Hz)
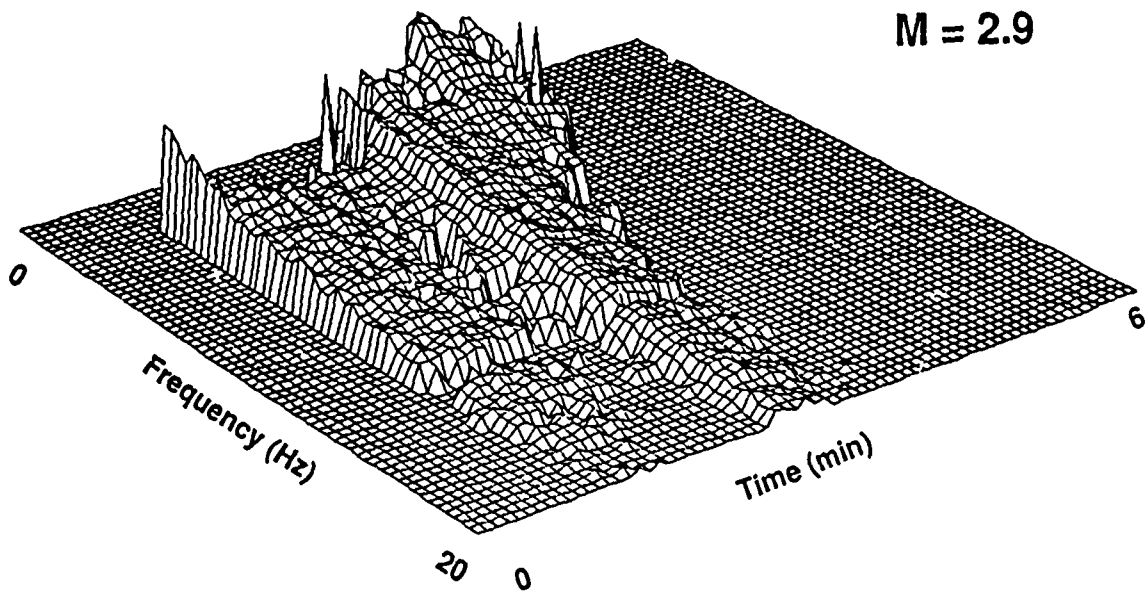
Time (min)

0

20   0

6
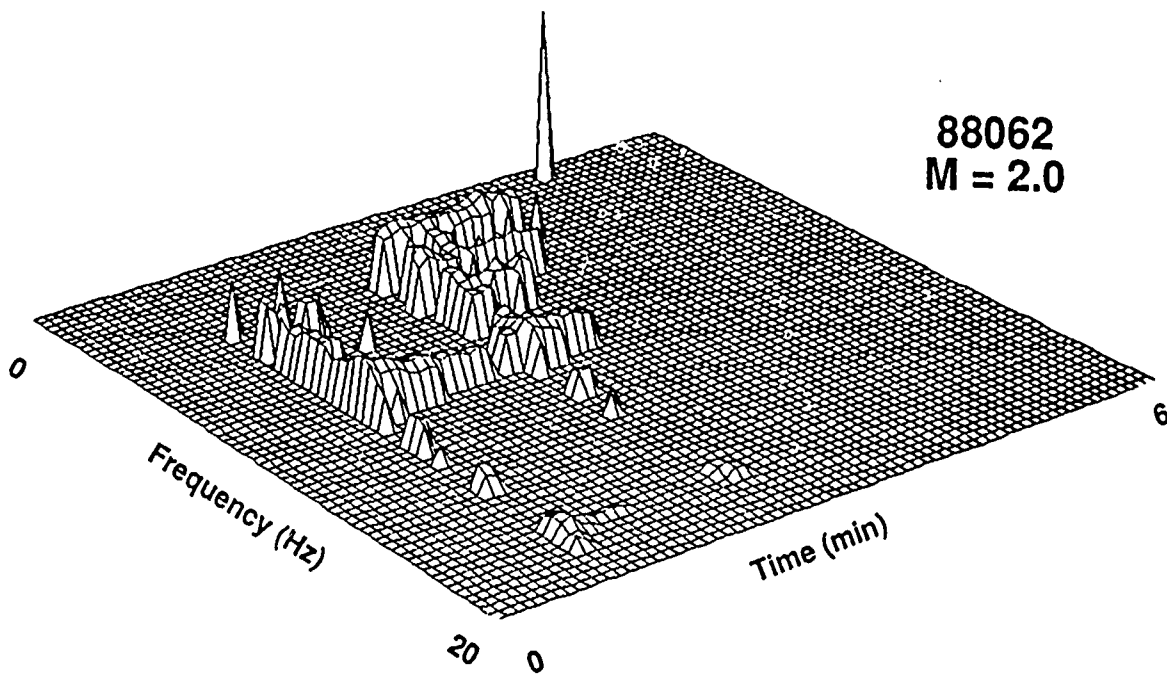
Figure A2. Spectrogram of a Northern Sweden earthquake (event 87147, Table I) at NORESS. The scale and parameters are the same as in Figure 2.

Mine Explosions at NORESS

V10
M = 2.6

K1
M = 2.6

Frequency (Hz)

Time (min)

0

6

0

20

0

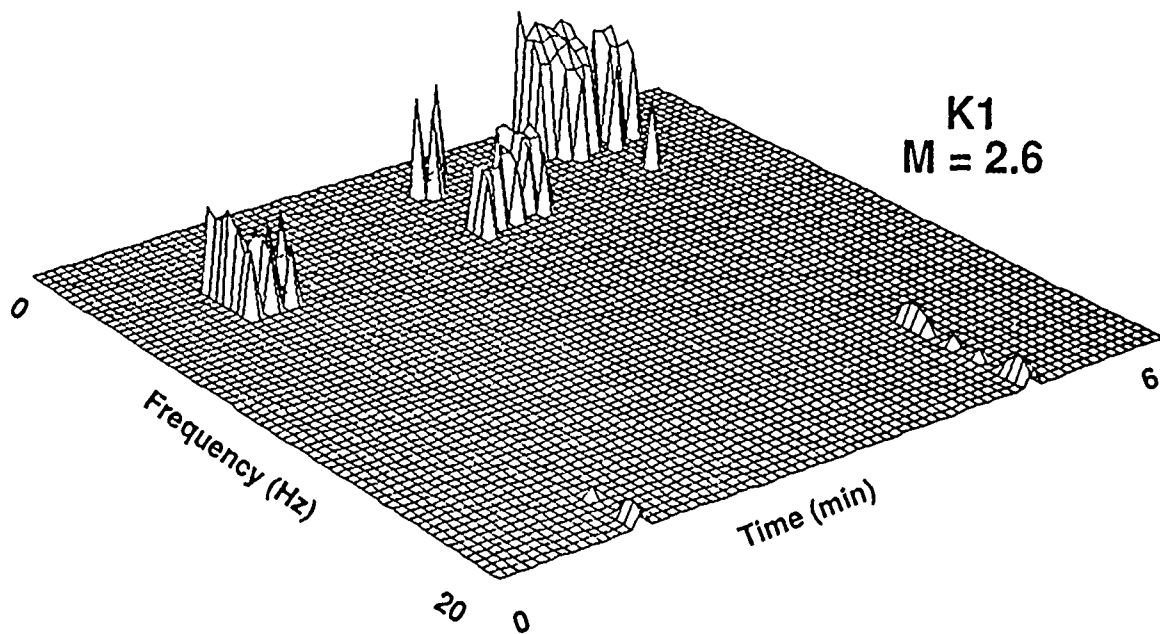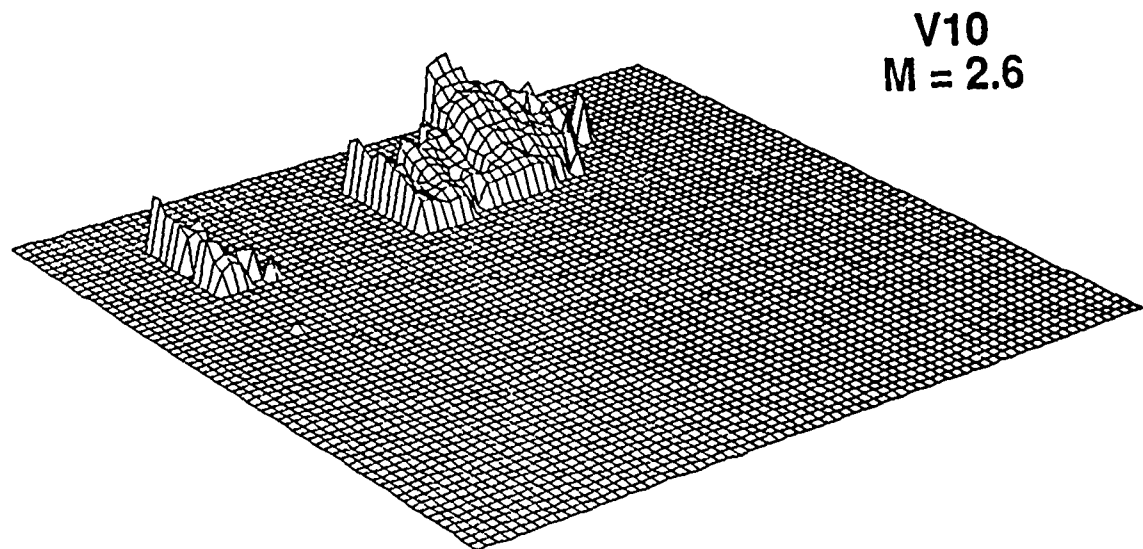*Figure A3.* Spectrograms of two mine explosions (listed in *Table I*) at NORESS -- 86049 (Top) and 87052 (Bottom).

Calibration Shot at NRDC

**1001
BAY**

KKL

Figure A4. Spectrograms of calibration shots (listed in Table II) at NRDC stations BAY and KKL. The scale and parameters are the same as in Figure 7.

1024 BAY

KKL

Frequency (Hz)

Time (min)

1

3.5

62   0
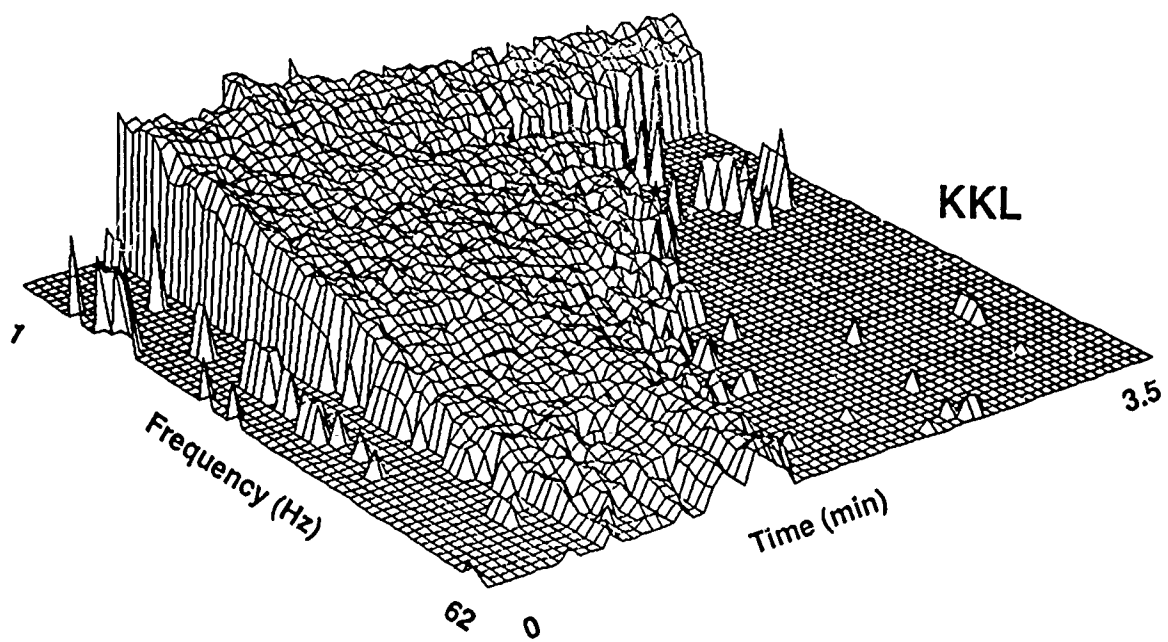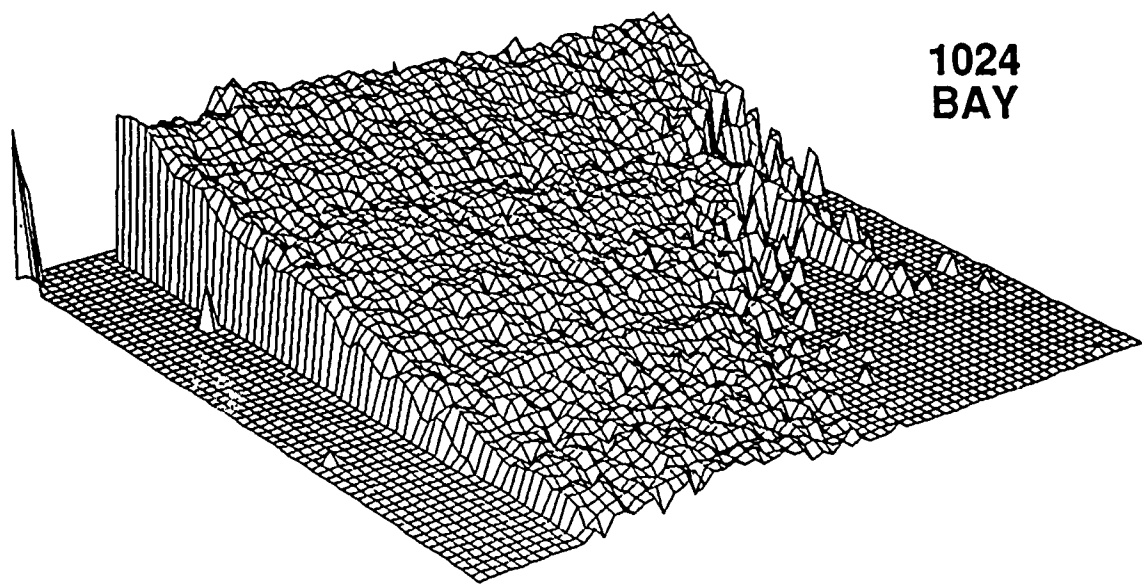
Figure A4. -- (Continued)

Mine Explosions (?) at NRDC

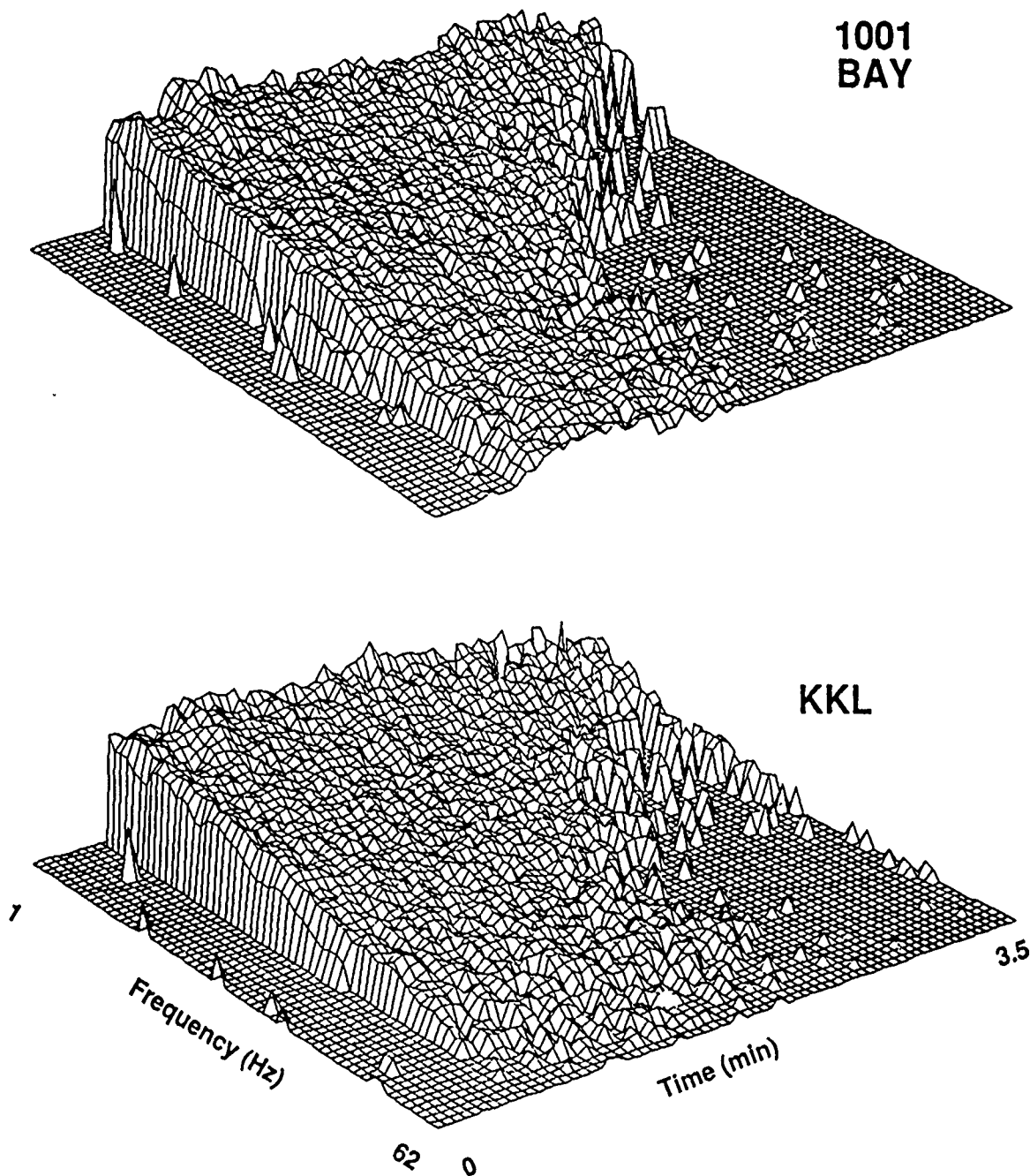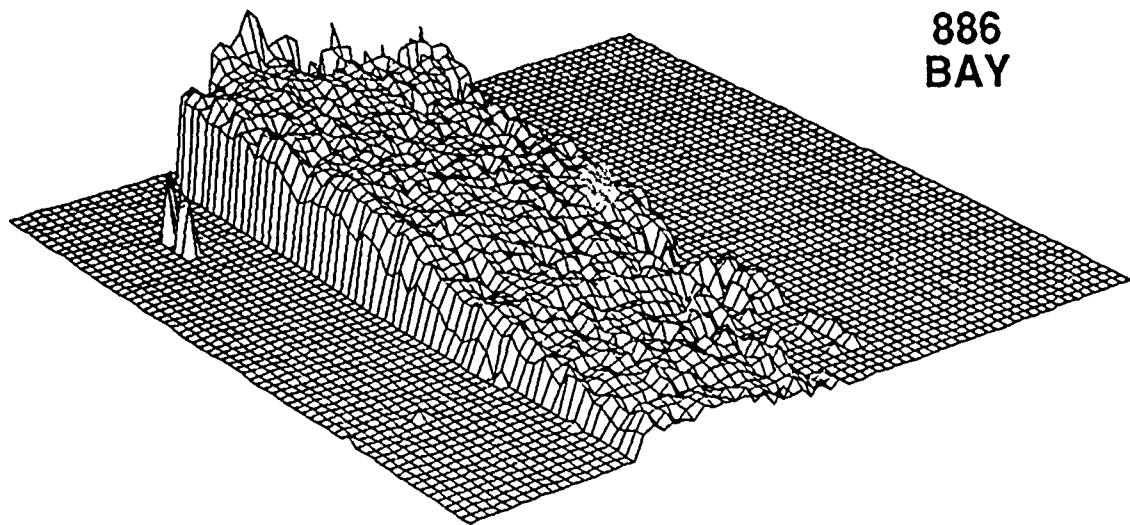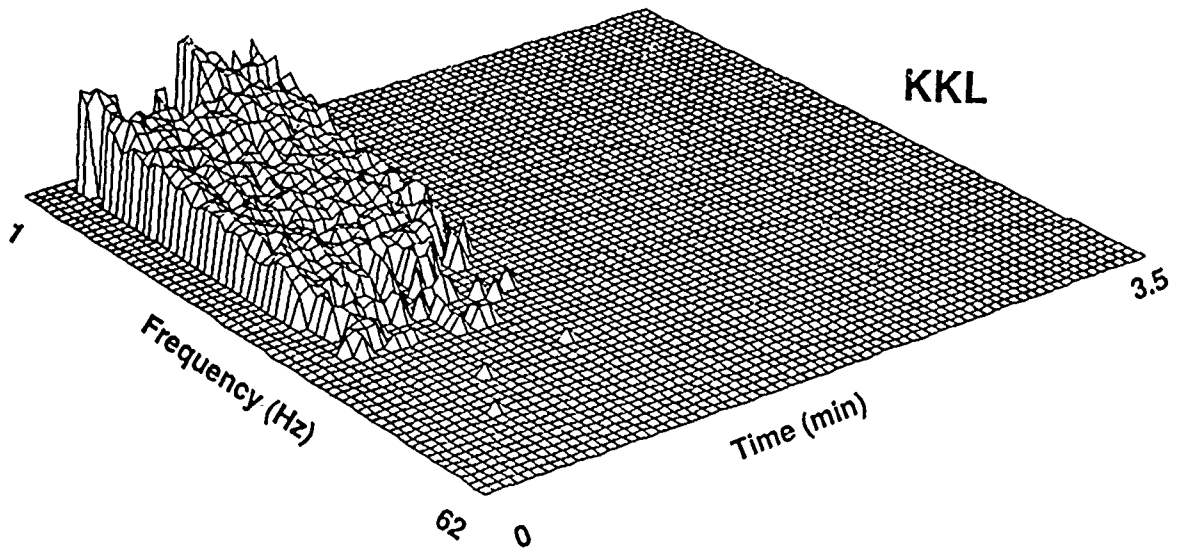

Figure A5. Spectrograms of presumed mine blasts (listed in *Table II*) at NRDC stations BAY and/or KKL. The scale and parameters are the same as in *Figure 7.* Times beyond the end of the recorded data are masked. Event 998 is mixed with a local event arriving in its coda.

Mine Explosions (?) at NRDC

998
BAY

KKL

1

Frequency (Hz)

3.5

Time (min)

62   0

Figure A5. -- (Continued)

**763
BAY**

**847
KKL**

Frequency (Hz)

Time (min)

1

62

0

3.5

Figure A5 -- (Continued)

5.1 COMPARISON OF SDCS AND NRDC INSTRUMENT CHARACTERIS-TICS

Conflicting estimates of m_b bias between explosions set off in hard rock at the Nevada and Eastern Kazakh test sites have been reported in the literature. These estimates have been based on data recorded by instruments with different charac-teristics. Recent estimates for the Eastern Kazakh test site are based on high fre-quency stations by the Natural Resources Defense Council (NRDC) near the test range in 1987 and 1988. Estimates for granite at the Nevada Test S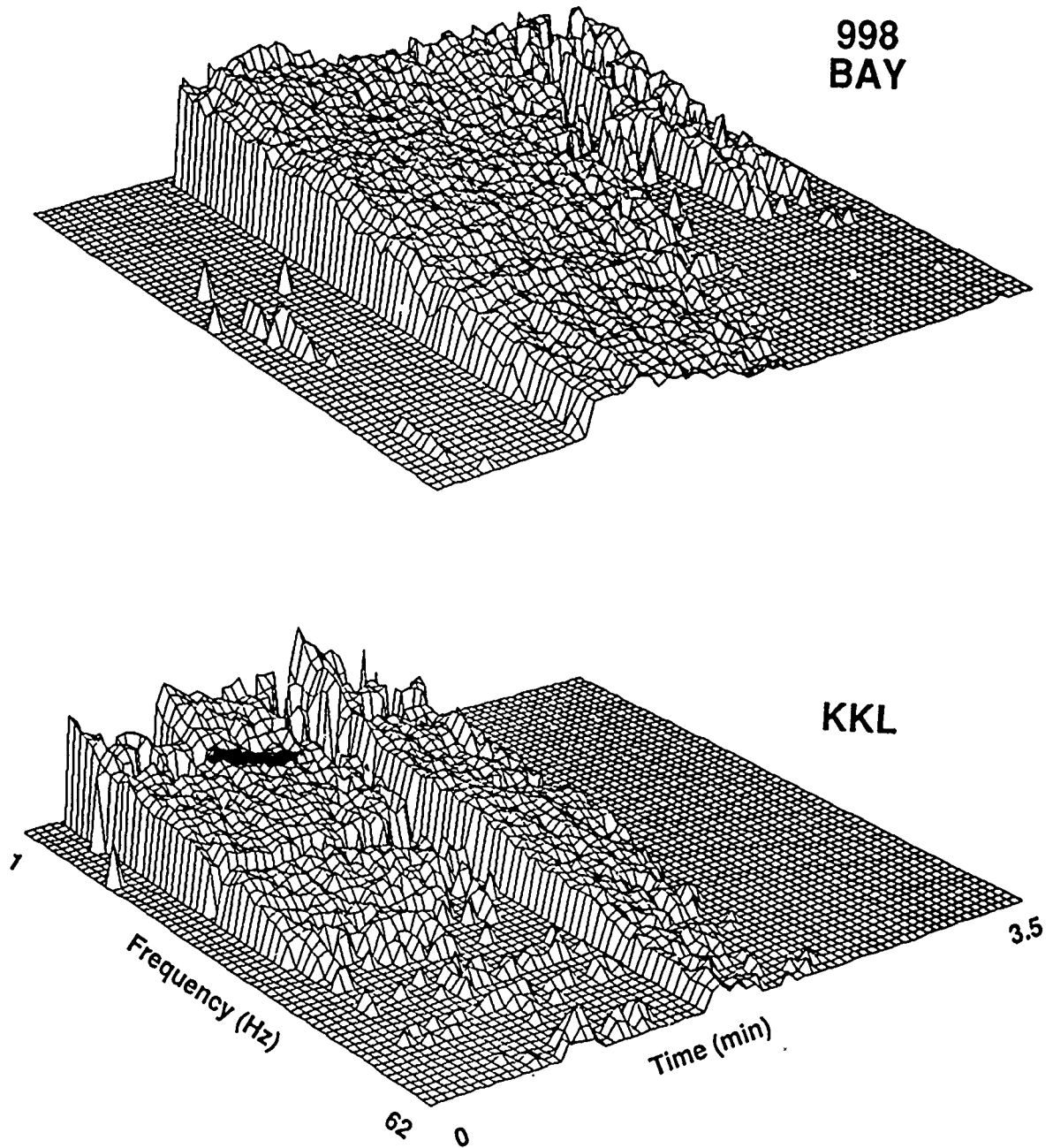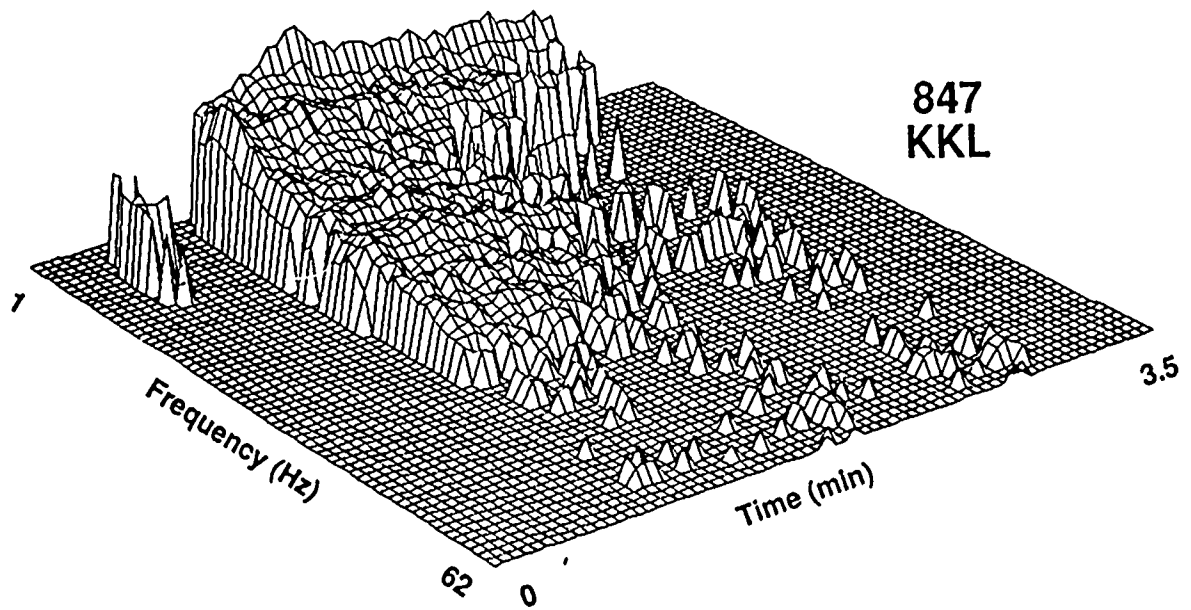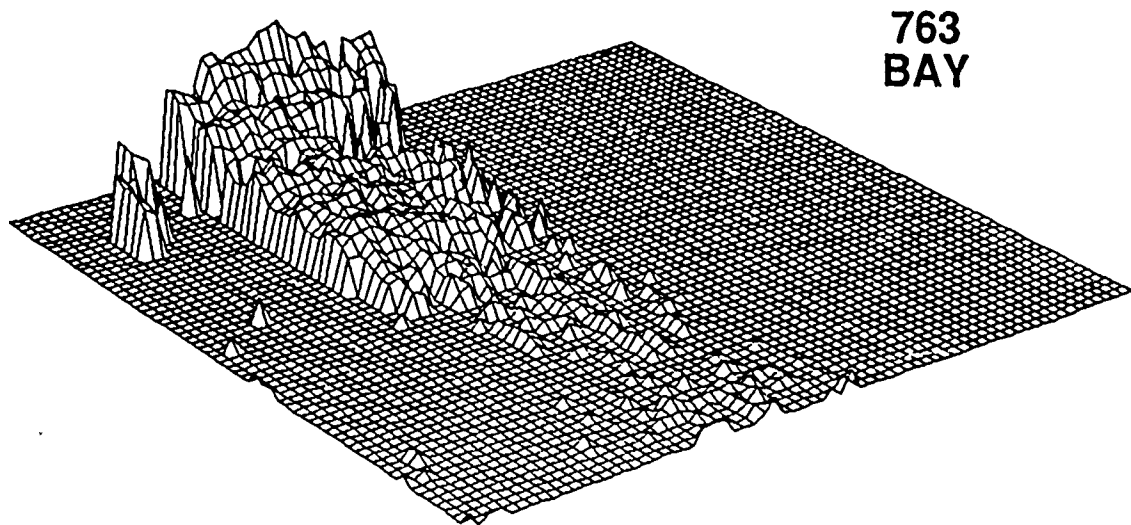ite are based on the short-period Special Data Collection System (SDCS). In this note we illustrate the effect on magnitude estimates of the two different instruments, by comparing amplitude and frequency responses.

The characteristics of the NRDC instruments have been specified with poles and zeros for the various components of the recording system by Berger *et al.* (1987). Similar characteristics for the short period SDCS instruments have been made available by Starkey (personal communication, 1987).

The amplitude and phase characteristics of the two response curves are given and compared in *Figures 1 and 2.*

As can be seen from these diagrams, the amplitude ratio stays fairly constant in the teleseismic frequency band form 1 to 3 Hz, where the range of variation is about 0.13 logarithmic units. The phase shift difference changes about 2 radians in this band. The response of the two instruments are similar in the teleseismic fre-quency band and magnitudes obtained with these instruments can be compared directly as long as only large effects are of interest. However, if high accuracies are required, a correction for differences in the instrument responses may be neces-sary. This is particularly the case if there is significant energy at frequencies lower than 1 Hz or higher than 3 Hz.

Hans Israelsson

References

Berger, J., H. Eissler, F.L. Vernon, I.L. Nersesov, M.B. Gokhberg, O.A. Stolyrov, and N.D. Tarasov, (1988). Studies High Frequency Seismic Noise in Eastern Kazakhstan, *Bull. Seism. Soc. Am.,* Vol. 78, pp. 1744-1758.
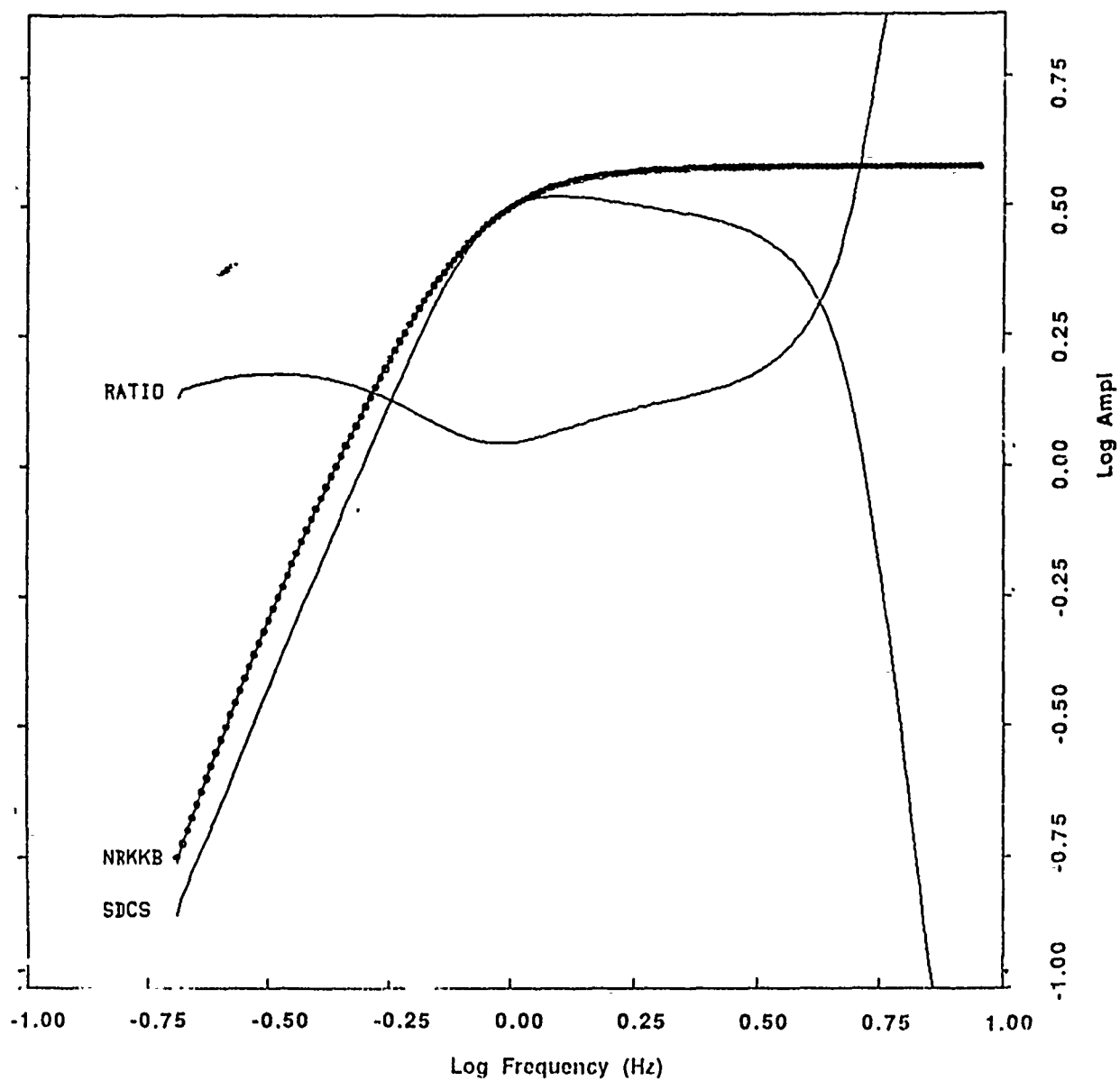
Figure 1. The amplitude response curves for NRDC and SDCS instruments and their ratio.
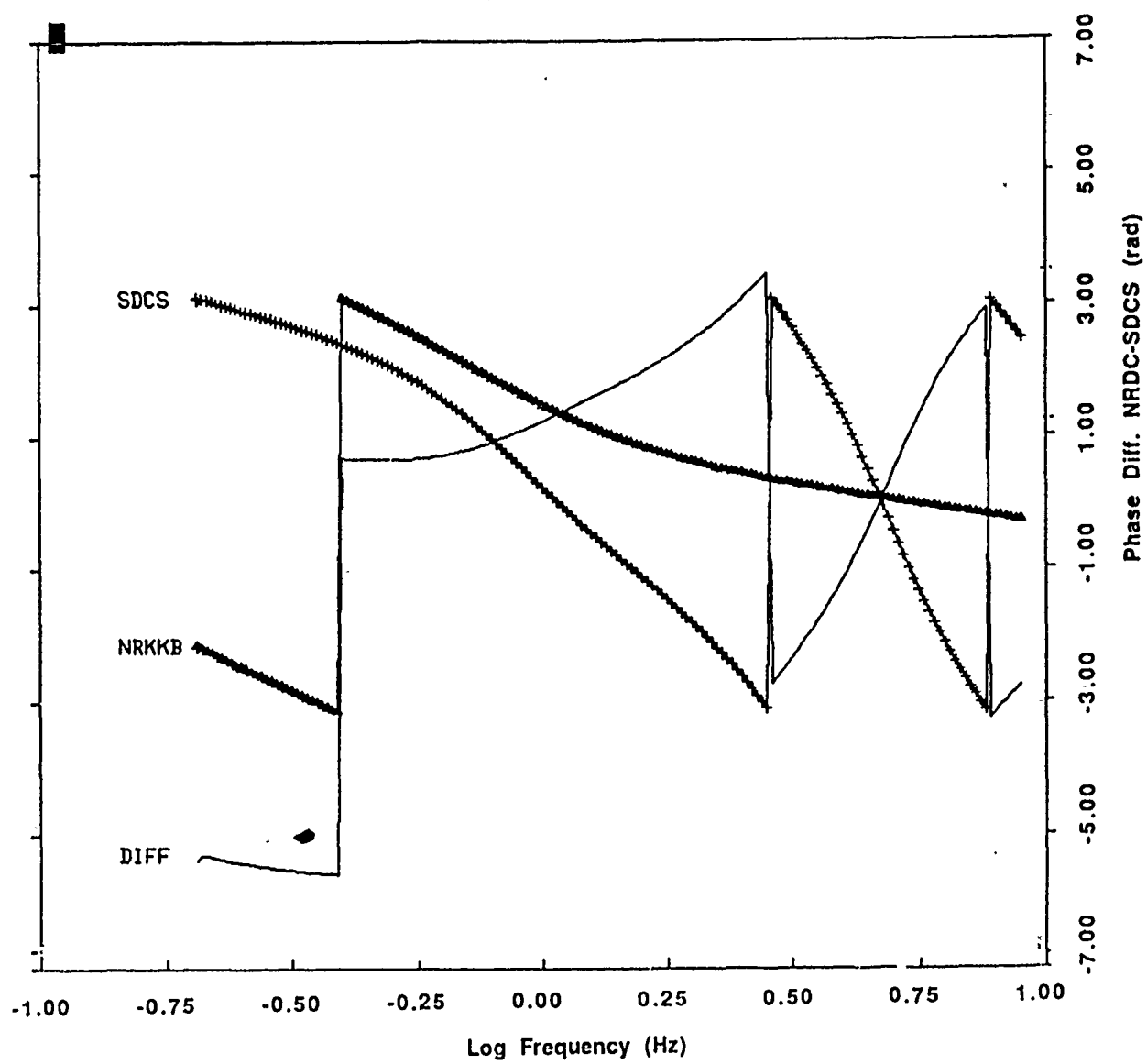
Figure 2. The phase response curves for NRDC and SDCS instruments and their difference.

Prof. Thomas Ahrens
Seismological Lab, 252-21
Division of Geological & Planetary Sciences
California Institute of Technology
Pasadena, CA 91125

Prof. Charles B. Archambeau
CIRES
University of Colorado
Boulder, CO 80309

Dr. Thomas C. Bache, Jr.
Science Applications Int'l Corp.
10260 Campus Point Drive
San Diego, CA 92121   (2 copies)

Prof. Muawia Barazangi
Institute for the Study of the Continent
Cornell University
Ithaca, NY 14853

Dr. Douglas R. Baumgardt
ENSCO, Inc
5400 Port Royal Road
Springfield, VA 22151-2388

Prof. Jonathan Berger
IGPP, A-025
Scripps Institution of Oceanography
University of California, San Diego
La Jolla, CA 92093

Dr. Lawrence J. Burdick
Woodward-Clyde Consultants
566 El Dorado Street
Pasadena, CA 91109-3245

Dr. Jerry Carter
Center for Seismic Studies
1300 North 17th St., Suite 1450
Arlington, VA 22209-2308

Dr. Karl Coyner
New England Research, Inc.
76 Olcott Drive
White River Junction, VT 05001

Prof. Vernon F. Cormier
Department of Geology & Geophysics
U-45, Room 207
The University of Connecticut
Storrs, CT 06268

Professor Anton W. Dainty
Earth Resources Laboratory
Massachusetts Institute of Technology
42 Carleton Street
Cambridge, MA 02142

Prof. Steven Day
Department of Geological Sciences
San Diego State University
San Diego, CA 92182

Dr. Zoltan A. Der
ENSCO, Inc.
5400 Port Royal Road
Springfield, VA 22151-2388

Prof. John Ferguson
Center for Lithospheric Studies
The University of Texas at Dallas
P.O. Box 830688
Richardson, TX 75083-0688

Dr. Mark D. Fisk
Mission Research Corporation
735 State Street
P. O. Drawer 719
Santa Barbara, CA 93102

Prof. Stanley Flatte
Applied Sciences Building
University of California
Santa Cruz, CA 95064

Dr. Alexander Florence
SRI International
333 Ravenswood Avenue
Menlo Park, CA 94025-3493

Prof. Henry L. Gray
Vice Provost and Dean
Department of Statistical Sciences
Southern Methodist University
Dallas, TX 75275

Dr. Indra Gupta
Teledyne Geotech
314 Montgomery Street
Alexandria, VA 22314

Prof. David G. Harkrider
Seismological Laboratory
Division of Geological & Planetary Sciences
California Institute of Technology
Pasadena, CA 91125

Prof. Donald V. Helmberger
Seismological Laboratory
Division of Geological & Planetary Sciences
California Institute of Technology
Pasadena, CA 91125

Prof. Eugene Herrin
Institute for the Study of Earth and Man
Geophysical Laboratory
Southern Methodist University
Dallas, TX 75275

Prof. Bryan Isacks
Cornell University
Department of Geological Sciences
SNEE Hall
Ithaca, NY 14850

Dr. Rong-Song Jih
Teledyne Geotech
314 Montgomery Street
Alexandria, VA 22314

Prof. Lane R. Johnson
Seismographic Station
University of California
Berkeley, CA 94720

Dr. Richard LaCoss
MIT-Lincoln Laboratory
M-200B
P. O. Box 73
Lexington, MA 02173-0073   (3 copies)

Prof Fred K. Lamb
University of Illinois at Urbana-Champaign
Department of Physics
1110 West Green Street
Urbana, IL 61801

Prof. Charles A. Langston
Geosciences Department
403 Deike Building
The Pennsylvania State University
University Park, PA 16802

Prof. Thorne Lay
Institute of Tectonics
Earth Science Board
University of California, Santa Cruz
Santa Cruz, CA 95064

Prof. Arthur Lerner-Lam
Lamont-Doherty Geological Observatory
of Columbia University
Palisades, NY 10964

Dr. Christopher Lynnes
Teledyne Geotech
314 Montgomery Street
Alexandria, VA 22314

Prof. Peter Malin
University of California at Santa Barbara
Institute for Crustal Studies
Santa Barbara, CA 93106

Dr. Randolph Martin, III
New England Research, Inc.
76 Olcott Drive
White River Junction, VT 05001

Prof. Thomas V. McEvilly
Seismographic Station
University of California
Berkeley, CA 94720

Dr. Keith L. McLaughlin
S-CUBED
A Division of Maxwell Laboratory
P.O. Box 1620
La Jolla, CA 92038-1620

Prof. William Menke
Lamont-Doherty Geological Observatory
of Columbia University
Palisades, NY 10964

Stephen Miller
SRI International
333 Ravenswood Avenue
Box AF 116
Menlo Park, CA 94025-3493

Prof. Bernard Minster
IGPP, A-025
Scripps Institute of Oceanography
University of California, San Diego
La Jolla, CA 92093

Prof. Brian J. Mitchell
Department of Earth & Atmospheric Sciences
St. Louis University
St. Louis, MO 63156

Mr. Jack Murphy
S-CUBED, A Division of Maxwell Laboratory
11800 Sunrise Valley Drive
Suite 1212
Reston, VA 22091 (2 copies)

2

Prof. John A. Orcutt
IGPP, A-025
Scripps Institute of Oceanography
University of California, San Diego
La Jolla, CA 92093

Prof. Keith Priestley
University of Cambridge
Bullard Labs, Dept. of Earth Sciences
Madingley Rise, Madingley Rd.
Cambridge CB3 OEZ, ENGLAND

Dr. Jay J. Pulli
Radix Systems, Inc.
2 Taft Court, Suite 203
Rockville, MD 20850

Prof. Paul G. Richards
Lamont Doherty Geological Observatory
 of Columbia University
Palisades, NY 10964

Dr. Wilmer Rivers
Teledyne Geotech
314 Montgomery Street
Alexandria, VA 22314

Prof. Charles G. Sammis
Center for Earth Sciences
University of Southern California
University Park
Los Angeles, CA 90089-0741

Prof. Christopher H. Scholz
Lamont-Doherty Geological Observatory
of Columbia University
Palisades, NY 10964

Thomas J. Sereno, Jr.
Science Application Int'l Corp.
10260 Campus Point Drive
San Diego, CA 92121

Prof. David G. Simpson
Lamont-Doherty Geological Observatory
of Columbia University
Palisades, NY 10964

Dr. Jeffrey Stevens
S-CUBED
A Division of Maxwell Laboratory
P.O. Box 1620
La Jolla, CA 92038-1620

Prof. Brian Stump
Institute for the Study of Earth & Man
Geophysical Laboratory
Southern Methodist University
Dallas, TX 75275

Prof. Jeremiah Sullivan
University of Illinois at Urbana-Champaign
Department of Physics
1110 West Green Street
Urbana, IL 61801

Prof. Clifford Thurber
University of Wisconsin-Madison
Department of Geology & Geophysics
1215 West Dayton Street
Madison, WS 53706

Prof. M. Nafi Toksoz
Earth Resources Lab
Massachusetts Institute of Technology
42 Carleton Street
Cambridge, MA 02142

Prof. John E. Vidale
University of California at Santa Cruz
Seismological Laboratory
Santa Cruz, CA 95064

Prof. Terry C. Wallace
Department of Geosciences
Building #77
University of Arizona
Tucson, AZ 85721

Dr. William Wortman
Mission Research Corporation
735 State Street
P. O. Drawer 719
Santa Barbara. CA 93102

Dr. Monem Abdel-Gawad
Rockwell International Science Center
1049 Camino Dos Rios
Thousand Oaks, CA 91360

Prof. Keiiti Aki
Center for Earth Sciences
University of Southern California
University Park
Los Angeles, CA 90089-0741

Prof. Shelton S. Alexander
Geosciences Department
403 Deike Building
The Pennsylvania State University
University Park, PA 16802

Dr. Kenneth Anderson
BBNSTC
Mail Stop 14/1B
Cambridge, MA 02238

Dr. Ralph Archuleta
Department of Geological Sciences
University of California at Santa Barbara
Santa Barbara, CA 93102

Dr. Jeff Barker
Department of Geological Sciences
State University of New York
at Binghamton
Vestal, NY 13901

Dr. Susan Beck
Department of Geosciences, Bldg # 77
University of Arizona
Tucson, AZ 85721

Lr. T.J. Bennett
S-CUBED
A Division of Maxwell Laboratory
11800 Sunrise Valley Drive, Suite 1212
Reston, VA 22091

Mr. William J. Bes.
907 Westwood Drive
Vienna, VA 22180

Dr. N. Biswas
Geophysical Institute
University of Alaska
Fairbanks, AK 99701

Dr. G.A. Bollinger
Department of Geological Sciences
Virginia Polytechnical Institute
21044 Derring Hall
Blacksburg, VA 24061

Dr. Stephen Bratt
Center for Seismic Studies
1300 North 17th Street
Suite 1450
Arlington, VA 22209

Michael Browne
Teledyne Geotech
3401 Shiloh Road
Garland, TX 75041

Mr. Roy Burger
1221 Serry Road
Schenectady, NY 12309

Dr. Robert Burridge
Schlumberger-Doll Research Center
Old Quarry Road
Ridgefield, CT 06877

Dr. W. Winston Chan
Teledyne Geotech
314 Montgomery Street
Alexandria, VA 22314-1581

Dr. Theodore Cherry
Science Horizons, Inc.
710 Encinitas Blvd., Suite 200
Encinitas, CA 92024 (2 copies)

Prof. Jon F. Claerbout
Department of Geophysics
Stanford University
Stanford, CA 94305

Prof. Robert W. Clayton
Seismological Laboratory
Division of Geological & Planetary Sciences
California Institute of Technology
Pasadena, CA 91125

Prof. F. A. Dahlen
Geological and Geophysical Sciences
Princeton University
Princeton, NJ 08544-0636

Prof. Adam Dziewonski
Hoffman Laboratory
Harvard University
20 Oxford St
Cambridge, MA 02138

Prof. John Ebel
Department of Geology & Geophysics
Boston College
Chestnut Hill, MA 02167

Eric Fielding
SNEE Hall
INSTOC
Cornell University
Ithaca, NY 14853

Prof. Donald Forsyth
Department of Geological Sciences
Brown University
Providence, RI 02912

Dr. Cliff Frolich
Institute of Geophysics
8701 North Mopac
Austin, TX 78759

Dr. Anthony Gangi
Texas A&M University
Department of Geophysics
College Station, TX 77843

Dr. Freeman Gilbert
IGPP, A-025
Scripps Institute of Oceanography
University of California
La Jolla, CA 92093

Mr. Edward Giller
Pacific Sierra Research Corp.
1401 Wilson Boulevard
Arlington, VA 22209

Dr. Jeffrey W. Given
SAIC
10260 Campus Point Drive
San Diego, CA 92121

Prof. Stephen Grand
University of Texas at Austin
Department of Geological Sciences
Austin, TX 78713-7909

Prof. Roy Greenfield
Geosciences Department
403 Deike Building
The Pennsylvania State University
University Park, PA 16802

Dan N. Hagedorn
Battelle
Pacific Northwest Laboratories
Battelle Boulevard
Richland, WA 99352

Dr. James Hannon
Lawrence Livermore National Laboratory
P. O. Box 808
Livermore, CA 94550

Prof. Robert B. Herrmann
Dept. of Earth & Atmospheric Sciences
St. Louis University
St. Louis, MO 63156

Ms. Heidi Houston
Seismological Laboratory
University of California
Santa Cruz, CA 95064

Kevin Hutchenson
Department of Earth Sciences
St. Louis University
3507 Laclede
St. Louis, MO 63103

Dr. Hans Israelsson
Center for Seismic Studies
1300 N. 17th Street, Suite 1450
Arlington, VA 22209-2308

Prof. Thomas H. Jordan
Department of Earth, Atmospheric
  and Planetary Sciences
Massachusetts Institute of Technology
Cambridge, MA 02139

Prof. Alan Kafka
Department of Geology & Geophysics
Boston College
Chestnut Hill, MA 02167

Robert C. Kemerait
ENSCO, Inc.
445 Pineda Court
Melbourne, FL 32940

William Kikendall
Teledyne Geotech
3401 Shiloh Road
Garland, TX 75041

Prof. Leon Knopoff
University of California
Institute of Geophysics & Planetary Physics
Los Angeles, CA 90024

Prof. L. Timothy Long
School of Geophysical Sciences
Georgia Institute of Technology
Atlanta, GA 30332

Dr. Gary McCartor
Department of Physics
Southern Methodist University
Dallas, TX 75275

Prof. Art McGarr
Mail Stop 977
Geological Survey
345 Middlefield Rd.
Menlo Park, CA 94025

Dr. George Mellman
Sierra Geophysics
11255 Kirkland Way
Kirkland, WA 98033

Prof. John Nabelek
College of Cceanography
Oregon State University
Corvallis, OR 97331

Prof. Geza Nagy
University of California, San Diego
Department of Ames, M.S. B-010
La Jolla, CA 92093

Dr. Keith K. Nakanishi
Lawrence Livermore National Laboratory
L-205
P. O. Box 808
Livermore, CA 94550

Dr. Bao Nguyen
GL/LWH
Hanscom AFB, MA 01731-5000

Prof. Amos Nur
Department of Geophysics
Stanford University
Stanford, CA 94305

Prof. Jack Oliver
Department of Geology
Cornell University
Ithaca, NY 14850

Dr. Kenneth Olsen
P. O. Box 1273
Linwood, WA 98046-1273

Howard J. Patton
Lawrence Livermore National Laboratory
L-205
P. O. Box 808
Livermore, CA 94550

Prof. Robert Phinney
Geological & Geophysical Sciences
Princeton University
Princeton, NJ 08544-0636

Dr. Paul Pomeroy
Rondout Associates
P.O. Box 224
Stone Ridge, NY 12484

Dr. Jay Pulli
RADIX System, Inc.
2 Taft Court, Suite 203
Rockville, MD 20850

Dr. Norton Rimer
S-CUBED
A Division of Maxwell Laboratory
P.O. Box 1620
La Jolla, CA 92038-1620

Prof. Larry J. Ruff
Department of Geological Sciences
1006 C.C. Little Building
University of Michigan
Ann Arbor, MI 48109-1063

Dr. Richard Sailor
TASC Inc.
55 Walkers Brook Drive
Reading, MA 01867

6

Dr. Susan Schwartz
Institute of Tectonics
1156 High St.
Santa Cruz, CA 95064

John Sherwin
Teledyne Geotech
3401 Shiloh Road
Garland, TX 75041

Dr. Matthew Sibol
Virginia Tech
Seismological Observatory
4044 Derring Hall
Blacksburg, VA 24061-0420

Dr. Albert Smith
Lawrence Livermore National Laboratory
L-205
P. O. Box 808
Livermore, CA 94550

Prof. Robert Smith
Department of Geophysics
University of Utah
1400 East 2nd South
Salt Lake City, UT 84112

Dr. Stewart W. Smith
Geophysics AK-50
University of Washington
Seattle, WA 98195

Donald L. Springer
Lawrence Livermore National Laboratory
L-205
P. O. Box 808
Livermore, CA 94550

Dr. George Sutton
Rondout Associates
P.O. Box 224
Stone Ridge, NY 12484

Prof. L. Sykes
Lamont-Doherty Geological Observatory
of Columbia University
Palisades, NY 10964

Prof. Pradeep Talwani
Department of Geological Sciences
University of South Carolina
Columbia, SC 29208

Dr. David Taylor
ENSCO, Inc.
445 Pineda Court
Melbourne, FL 32940

Dr. Steven R. Taylor
Lawrence Livermore National Laboratory
L-205
P. O. Box 808
Livermore, CA 94550

Professor Ta-Liang Teng
Center for Earth Sciences
University of Southern California
University Park
Los Angeles, CA 90089-0741

Dr. R.B. Tittmann
Rockwell International Science Center
1049 Camino Dos Rios
P.O. Box 1085
Thousand Oaks, CA 91360

Dr. Gregory van der Vink
IRIS, Inc.
1616 North Fort Myer Drive
Suite 1440
Arlington, VA 22209

Professor Daniel Walker
University of Hawaii
Institute of Geophysics
Honolulu, HI 96822

William R. Walter
Seismological Laboratory
University of Nevada
Reno, NV 89557

Dr. Raymond Willeman
GL/LWH
Hanscom AFB, MA 01731-5000

Dr. Gregory Wojcik
Weidlinger Associates
4410 El Camino Real
Suite 110
Los Altos, CA 94022

Dr. Lorraine Wolf
GL/LWH
Hanscom AFB, MA 01731-5000

7

Prof. Francis T. Wu
Department of Geological Sciences
State University of New York
at Binghamton
Vestal, NY 13901

Dr. Gregory B. Young
ENSCO, Inc.
5400 Port Royal Road
Springfield, VA 22151-2388

Dr. Eileen Vergino
Lawrence Livermore National Laboratory
L-205
P. O. Box 808
Livermore, CA 94550

J. J. Zucca
Lawrence Livermore National Laboratory
P. O. Box 808
Livermore, CA 94550

8

Dr. Ralph Alewine III
DARPA/NMRO
1400 Wilson Boulevard
Arlington, VA 22209-2308

Mr. James C. Battis
GL/LWH
Hanscom AFB, MA 01731-5000

Dr. Robert Blandford
AFTAC/TT
Center for Seismic Studies
1300 North 17th St., Suite 1450
Arlington, VA 22209-2308

Eric Chael
Division 9241
Sandia Laboratory
Albuquerque, NM 87185

Dr. John J. Cipar
GL/LWH
Hanscom AFB, MA 01731-5000

Cecil Davis
Group P-15, Mail Stop D406
P.O. Box 1663
Los Alamos National Laboratory
Los Alamos, NM 87544

Mr. Jeff Duncan
Office of Congressman Markey
2133 Rayburn House Bldg.
Washington, DC 20515

Dr. Jack Evernden
USGS - Earthquake Studies
345 Middlefield Road
Menlo Park, CA 94025

Art Frankel
USGS
922 National Center
Reston, VA 22092

Dr. Dale Glover
DIA/DT-1B
Washington, DC 20301

Dr. T. Hanks
USGS
Nat'l Earthquake Research Center
345 Middlefield Road
Menlo Park, CA 94025

Paul Johnson
ESS-4, Mail Stop J979
Los Alamos National Laboratory
Los Alamos, NM 87545

Janet Johnston
GL/LWH
Hanscom AFB, MA 01731-5000

Dr. Katharine Kadinsky-Cade
GL/LWH
Hanscom AFB, MA 01731-5000

Ms. Ann Kerr
IGPP, A-025
Scripps Institute of Oceanography
University of California, San Diego
La Jolla, CA 92093

Dr. Max Koontz
US Dept of Energy/DP 5
Forrestal Building
1000 Independence Avenue
Washington, DC 20585

Dr. W.H.K. Lee
Office of Earthquakes, Volcanoes,
& Engineering
345 Middlefield Road
Menlo Park, CA 94025

Dr. William Leith
U.S. Geological Survey
Mail Stop 928
Reston, VA 22092

Dr. Richard Lewis
Director, Earthquake Engineering & Geophysics
U.S. Army Corps of Engineers
Box 631
Vicksburg, MS 39180

James F. Lewkowicz
GL/LWH
Hanscom AFB, MA 01731-5000

9

Mr. Alfred Lieberman
ACDA/VI-OA'State Department Bldg
Room 5726
320 - 21st Street, NW
Washington, DC 20451

Stephen Mangino
GL/LWH
Hanscom AFB, MA 01731-5000

Dr. Robert Masse
Box 25046, Mail Stop 967
Denver Federal Center
Denver, CO 80225

Art McGarr
U.S. Geological Survey, MS-977
345 Middlefield Road
Menlo Park, CA 94025

Richard Morrow
ACDA/VI, Room 5741
320 21st Street N.W
Washington, DC 20451

Dr. Carl Newton
Los Alamos National Laboratory
P.O. Box 1663
Mail Stop C335, Group ESS-3
Los Alamos, NM 87545

Dr. Kenneth H. Olsen
Los Alamos Scientific Laboratory
P. O. Box 1663
Mail Stop D-406
Los Alamos, NM 87545

Mr. Chris Paine
Office of Senator Kennedy
SR 315
United States Senate
Washington, DC 20510

Colonel Jerry J. Perrizo
AFOSR/NP, Building 410
Bolling AFB
Washington, DC 20332-6448

Dr. Frank F. Pilotte
HQ AFTAC/TT
Patrick AFB, FL 32925-6001

Katie Poley
CIA-ACIS/TMC
Room 4X16NHB
Washington, DC 20505

Mr. Jack Rachlin
U.S. Geological Survey
Geology, Rm 3 C136
Mail Stop 928 National Center
Reston, VA 22092

Dr. Robert Reinke
WL/NTESG
Kirtland AFB, NM 87117-6008

Dr. Byron Ristvet
HQ DNA, Nevada Operations Office
Attn: NVCG
P.O. Box 98539
Las Vegas, NV 89193

Dr. George Rothe
HQ AFTAC/TTR
Patrick AFB, FL 32925-6001

Dr. Alan S. Ryall, Jr.
DARPA/NMRO
1400 Wilson Boulevard
Arlington, VA 22209-2308

Dr. Michael Shore
Defense Nuclear Agency/SPSS
6801 Telegraph Road
Alexandria, VA 22310

Mr. Charles L. Taylor
GL/LWG
Hanscom AFB, MA 01731-5000

Dr. Larry Turnbull
CIA-OSWR/NED
Washington, DC 20505

Dr. Thomas Weaver
Los Alamos National Laboratory
P.O. Box 1663, Mail Stop C335
Los Alamos, NM 87545

GL/SULL
Research Library
Hanscom AFB , MA 01731-5000 (2 copies)

Defense Intelligence Agency
Directorate for Scientific & Technical Intelligence
Attn: DT1B
Washington, DC 20340-6158

Secretary of the Air Force
(SAFRD)
Washington, DC 20330

AFTAC/CA
(STINFO)
Patrick AFB, FL 32925-6001

Office of the Secretary Defense
DDR & E
Washington, DC 20330

TACTEC
Battelle Memorial Institute
505 King Avenue
Columbus, OH 43201 (Final Report Only)

HQ DNA
Attn: Technical Library
Washington, DC 20305

DARPA/RMO/RETRIEVAL
1400 Wilson Boulevard
Arlington, VA 22209

DARPA/RMO/Security Office
1400 Wilson Boulevard
Arlington, VA 22209

Geophysics Laboratory
Attn: XO
Hanscom AFB, MA 01731-5000

Geophysics Laboratory
Attn: LW
Hanscom AFB, MA 01731-5000

DARPA/PM
1400 Wilson Boulevard
Arlington, VA 22209

Defense Technical Information Center
Cameron Station
Alexandria, VA 22314 (5 copies)

Dr. Ramon Cabre, S.J.
Observatorio San Calixto
Casilla 5939
La Paz, Bolivia

Prof. Hans-Peter Harjes
Institute for Geophysik
Ruhr University/Bochum
P.O. Box 102148
4630 Bochum 1, FRG

Prof. Eystein Husebye
NTNF/NORSAR
P.O. Box 51
N-2007 Kjeller, NORWAY

Prof. Brian L.N. Kennett
Research School of Earth Sciences
Institute of Advanced Studies
G.P.O. Box 4
Canberra 2601, AUSTRALIA

Dr. Bernard Massinon
Societe Radiomana
27 rue Claude Bernard
75005 Paris, FRANCE   (2 Copies)

Dr. Pierre Mecheler
Societe Radiomana
27 rue Claude Bernard
75005 Paris, FRANCE

Dr. Svein Mykkeltveit
NTNF/NORSAR
P.O. Box 51
N-2007 Kjeller, NORWAY   (3 copies)

Dr. Peter Basham
Earth Physics Branch
Geological Survey of Canada
1 Observatory Crescent
Ottawa, Ontario, CANADA K1A 0Y3

Dr. Eduard Berg
Institute of Geophysics
University of Hawaii
Honolulu, HI 96822

Dr. Michel Bouchon
I.R.I.G.M.-B.P. 68
38402 St. Martin D'Heres
Cedex, FRANCE

Dr. Hilmar Bungum
NTNF/NORSAR
P.O. Box 51
N-2007 Kjeller, NORWAY

Dr. Michel Campillo
Observatoire de Grenoble
I.R.I.G.M.-B.P. 53
38041 Grenoble, FRANCE

Dr. Kin Yip Chun
Geophysics Division
Physics Department
University of Toronto
Ontario, CANADA M5S 1A7

Dr. Alan Douglas
Ministry of Defense
Blacknest, Brimpton
Reading RG7-4RS, UNITED KINGDOM

Dr. Roger Hansen
NTNF/NORSAR
P.O. Box 51
N-2007 Kjeller, NORWAY

Dr. Manfred Henger
Federal Institute for Geosciences & Nat'l Res.
Postfach 510153
D-3000 Hanover 51, FRG

Ms. Eva Johannisson
Senior Research Officer
National Defense Research Inst.
P.O. Box 27322
S-102 54 Stockholm, SWEDEN

Dr. Fekadu Kebede
Seismological Section
Box 12019
S-750 Uppsala, SWEDEN

Dr. Tormod Kvaerna
NTNF/NORSAR
P.O. Box 51
N-2007 Kjeller, NORWAY

Dr. Peter Marshall
Procurement Executive
Ministry of Defense
Blacknest, Brimpton
Reading FG7-4RS, UNITED KINGDOM

Prof. Ari Ben-Menahem
Department of Applied Mathematics
Weizman Institute of Science
Rehovot, ISRAEL 951729

Dr. Robert North
Geophysics Division
Geological Survey of Canada
1 Observatory Crescent
Ottawa, Ontario, CANADA K1A 0Y3

Dr. Frode Ringdal
NTNF/NORSAR
P.O. Box 51
N-2007 Kjeller, NORWAY

Dr. Jorg Schlittenhardt
Federal Institute for Geosciences & Nat'l Res.
Postfach 510153
D-3000 Hannover 51, FEDERAL REPUBLIC OF
GERMANY